



**HAL**  
open science

## 3D printing of conductive bionanocomposites and blends

Nour Alhoda Masarra

► **To cite this version:**

Nour Alhoda Masarra. 3D printing of conductive bionanocomposites and blends. Materials. IMT - MINES ALES - IMT - Mines Alès Ecole Mines - Télécom, 2023. English. NNT : 2023EMAL0001 . tel-03980449

**HAL Id: tel-03980449**

**<https://theses.hal.science/tel-03980449>**

Submitted on 9 Feb 2023

**HAL** is a multi-disciplinary open access archive for the deposit and dissemination of scientific research documents, whether they are published or not. The documents may come from teaching and research institutions in France or abroad, or from public or private research centers.

L'archive ouverte pluridisciplinaire **HAL**, est destinée au dépôt et à la diffusion de documents scientifiques de niveau recherche, publiés ou non, émanant des établissements d'enseignement et de recherche français ou étrangers, des laboratoires publics ou privés.

**THÈSE POUR OBTENIR LE GRADE DE DOCTEUR  
DE L'INSTITUT MINES-TELECOM (IMT) –  
ÉCOLE NATIONALE SUPÉRIEURE DES MINES D'ALÈS (IMT MINES ALÈS)**

**En Chimie et Physico-Chimie des matériaux**

**École doctorale SCB – Sciences Chimiques Balard**

**Unité de recherche PCH – Polymères Composites et Hybrides**

**3D Printing of Conductive Bionanocomposites and  
Blends**

**Présentée par Nour-Alhoda MASARRA**

**Le 17 Janvier 2023**

**Sous la direction de José-Marie LOPEZ-CUESTA et Roland EL-HAGE**

**Devant le jury composé de**

**Mustapha KACI, Professeur, Laboratoire LPMA, Université A. Mira, Bejaia, Algérie**

**Cécile NOUVEL, Professeure, Laboratoire LRGP, Université de Lorraine**

**Luca FAMBRI, Professeur, Département d'ingénierie, Université de Trento, Italie**

**Henri VAHABI, Maître de Conférences, HDR, Laboratoire LMOPS, Université de Lorraine**

**Monica PUCCI, Maître-Assistante, Centre des Matériaux, IMT Mines Alès**

**José-Marie LOPEZ-CUESTA, Professeur, Centre des Matériaux, IMT Mines Alès**

**Roland EL HAGE, Professeur, Laboratoire LCPM, Université Libanaise**

**Jean-Christophe QUANTIN, Maître-Assistant, Centre des Matériaux, IMT Mines Alès**

**Marcos BATISTELLA, Ingénieur de recherche, Centre des Matériaux, IMT Mines Alès**

**Rapporteur**

**Présidente du jury**

**Examinateur**

**Examinateur**

**Examinatrice**

**Directeur de thèse**

**Co-directeur de thèse**

**Encadrant de thèse**

**Invité**



# Trainings, publications, and projects

During these years, I took part in several trainings, projects, publications, and conferences that enriched my professional experiences.

## 1. List of trainings

- Writing your first paper step by step (20 h)
- Summer school 2019 "Labex ChemiSyst" (One week)
- Popularize the research (6 h)
- Writing a scientific article (7 h)
- Structuring a long document with word (6 h)
- Dealing with the scientific literature (20 h)
- Eye catching visuals: the discreet charm of the perfect Power Point (21 h)
- Exploiting the scientific literature (14 h)
- Advanced course on photoelectronic X Ray Spectroscopy (XPS) (12 h)

## 2. List of publications and conferences

- "Fabrication of PLA/PCL/Graphene Nanoplatelets (GNP) Electrically Conductive Circuit Using the Fused Filament Fabrication (FFF) 3D Printing Technique": Materials 2022, 15(3), 762, <https://doi.org/10.3390/ma15030762>
- "Influence of polymer processing on the double electrical percolation threshold in PLA/PCL/GNP nanocomposites" (submitted to MDPI, sensors- **accepted**)
- Oral presentation in the second international conference on the additive manufacturing of composites (23-24 Nov 2021)
- Poster presentation in EPF European Polymer Congress (Prague, Czech Republic, 26 June-1 July 2022)

### 3. Significant industrial projects in parallel with this PhD

- Superior technician, IMT Mines Ales- France (04/2021-05/2022)
  - ❖ Studying the fire behavior of biodegradable polymers filled with fly ashes and flame retardants (**LAFARGE HOLCIM**)
  - ❖ Twin-screw extrusion of biopolymer composites followed by injection moulding into cone calorimeter and tensile test samples
  - ❖ Five polymer matrices were used: PLA, PBAT, PS, PA6, and PA11 for the extrusion (100 extrusions) and injection moulding experiments (150 injection mouldings)
- Research engineer, IMT Mines Ales- France (09/2020-09/2021)
  - ❖ Research project for irrigation materials (**IrriFrance**): Study of the mechanical behaviour of PE/CB composites subjected to accelerated UV ageing and natural ageing processes
  - ❖ Injection moulded samples were characterized by: FTIR, SEM, AFM, rheology, tensile tests, Charpy impact tests, DSC, TGA, and CB percentage estimation by electrical tube furnace (ISO6964)
  - ❖ Aged samples were subjected to abrasion tests to quantify the mass loss and study the surface aspect by the aid of a rugosimeter

# Acknowledgements

I would like to thank Professor Roland El Hage from the Lebanese University for facilitating the contact with Professor José-Marie Lopez-Cuesta who made it possible for me to travel to France to accomplish my dream and to start my codirected PhD. Both guided me during my PhD work in addition to Drs Jean-Christophe Quantin, Marcos Batistella, and Monica Pucci. These professors gave me the assistance and guidance throughout the PhD years. Also, when something unpredictable happened (my Lebanese scholarship was stopped in my second year due to the economic crisis in my country), Professor Lopez-Cuesta found for me funding to be able to stay in France. This was through working on other research projects in parallel with my PhD. These projects gave me a lot of experience and strengthened my mental abilities and my efficiency. And the mission although seemed impossible at the beginning, but with my directors' support and with my determination I was able to finish all my projects with good results.

In the second place I would like to thank Mrs. Solange Madec (Administrative assistant of the lab) who was always responsive to help me in finalizing my administrative papers which were sometimes complicated due to the numerous research contracts I was committed to.

In the third place, I would like to thank the technicians and research engineers of the lab and especially Jean-Claude Roux, Sylvain Buonomo, and Romain Ravel who helped me during all this period in my various projects. And without their help, the experiments would not have taken place. In the fourth place, I would like to thank Sithiprumnea Dul (was working in the University of Trento, Italy) who helped us to construct the four probes setup for the electrical resistance measurements.

Also, I would like to thank professors Cécile Nouvel (University of Lorraine, France), Luca Fambri (University of Trento, Italy), Mustapha Kaci (University of A. Mira, Algeria), Henri Vahabi (University of Lorraine, France) for accepting to review and evaluate my work and to be members of my defense jury.

Finally, I gratefully thank Nans Daurat for his encouragement and support during the writing period and my beloved family for their continuous support during these years.



# Table of contents

<b>GENERAL INTRODUCTION .....</b>	<b>5</b>
<b>CHAPTER I: STATE OF ART .....</b>	<b>9</b>
1. GLOSSARY .....	10
2. BIOPLASTICS.....	12
2.1. <i>Biopolyesters</i> .....	14
3. GRAPHENE.....	21
4. BIOPOLYMER BLEND NANOCOMPOSITES.....	24
4.1. <i>Nanocomposites</i> .....	25
4.2. <i>Microstructure</i> .....	26
4.3. <i>Manufacturing methods-FFF</i> .....	27
4.4. <i>PLA/PCL blends</i> .....	30
4.5. <i>PLA/PBAT blends</i> .....	38
5. ELECTRICAL CONDUCTIVITY OF POLYMER COMPOSITES .....	43
5.1. <i>Double electrical percolation</i> .....	47
5.2. <i>FFF-printed carbon based electrically conductive composites</i> .....	51
6. CONCLUSION.....	54
7. BIBLIOGRAPHY.....	55
<b>CHAPTER 2: MATERIALS AND METHODS IMPLEMENTATION .....</b>	<b>69</b>
1. INTRODUCTION.....	69
2. PROPERTIES OF THE DIFFERENT GNP GRADES .....	69
2.1. <i>Objective</i> .....	69
2.2. <i>Materials</i> .....	69
2.3. <i>Characterizations</i> .....	70
2.4. <i>Results and discussion</i> .....	72
3. GNP GRADES INTERACTION WITH THE PLA MATRIX .....	77
3.1. <i>Objective</i> .....	77
3.2. <i>Materials</i> .....	78
3.3. <i>Experimental procedure</i> .....	78
3.4. <i>Characterizations</i> .....	81
4. CHARACTERIZATION OF THE SELECTED MATERIALS .....	84
4.1. <i>SEM</i> .....	84
4.2. <i>XRD</i> .....	86

4.3.	<i>Tensile properties of the injection moulded and 3D printed samples</i> .....	88
4.4.	<i>Two-probes electrical resistance measurements and SEM observations</i> .....	91
5.	PLA/PCL RATIO SELECTION.....	93
5.1.	<i>Objective</i> .....	93
5.2.	<i>Materials</i> .....	93
5.3.	<i>Experimental procedure</i> .....	93
5.4.	<i>Characterizations</i> .....	95
5.5.	<i>Blend selection and characterization</i> .....	95
6.	DIFFERENT GNP GRADES IN PLA80/PCL20 BLENDS .....	98
6.1.	<i>Objective</i> .....	98
6.2.	<i>Materials</i> .....	98
6.3.	<i>Experimental procedure</i> .....	98
6.4.	<i>Characterizations</i> .....	99
6.5.	<i>Results and discussion</i> .....	101
7.	CONCLUSION.....	111
8.	BIBLIOGRAPHY .....	112
<b>CHAPTER 3: FABRICATION OF PLA/PCL/GRAPHENE NANOPATELETS (GNP) ELECTRICALLY CONDUCTIVE CIRCUIT USING THE FUSED FILAMENT FABRICATION (FFF) 3D PRINTING TECHNIQUE .....</b>		<b>120</b>
1.	GRAPHICAL ABSTRACT.....	120
2.	ABSTRACT.....	120
3.	INTRODUCTION .....	121
4.	MATERIALS AND METHODS.....	124
4.1.	<i>Materials</i> .....	124
4.2.	<i>Nanocomposites preparation</i> .....	124
5.	CHARACTERIZATION TECHNIQUES .....	127
5.1.	<i>Contact angle measurements</i> .....	127
5.2.	<i>Scanning electron microscopy (SEM)</i> .....	129
5.3.	<i>Atomic force microscopy (AFM)</i> .....	129
5.4.	<i>Rheological measurements</i> .....	130
5.5.	<i>Thermogravimetric analysis (TGA)</i> .....	130
5.6.	<i>Differential scanning calorimetry (DSC)</i> .....	130
5.7.	<i>Tensile tests</i> .....	131
5.8.	<i>Electrical resistance measurements</i> .....	131
6.	RESULTS AND DISCUSSION .....	133
6.1.	<i>Contact angle measurements</i> .....	133

6.2. Microscopy- SEM and AFM .....	135
7. CONCLUSION .....	156
8. BIBLIOGRAPHY .....	158
<b>CHAPTER 4: INFLUENCE OF POLYMER PROCESSING ON THE DOUBLE ELECTRICAL PERCOLATION THRESHOLD IN PLA/PCL/GNP NANOCOMPOSITES .....</b>	<b>166</b>
1. GRAPHICAL ABSTRACT .....	166
2. ABSTRACT .....	166
3. INTRODUCTION .....	167
4. MATERIALS AND METHODS .....	169
4.1. Materials .....	169
4.2. Nanocomposite blends preparation .....	169
4.3. Compression moulding .....	171
4.4. Filament preparation .....	171
4.5. Fused filament fabrication (FFF) .....	172
5. CHARACTERIZATION TECHNIQUES .....	172
5.1. Scanning electron microscopy (SEM) .....	172
5.2. Atomic force microscopy (AFM) .....	172
5.3. Solvent extraction method .....	173
5.4. Electrical resistance measurements .....	174
5.5. Rheological measurements .....	175
5.6. Differential Scanning Calorimetry (DSC) .....	175
5.7. Thermogravimetric analysis (TGA) .....	176
6. RESULTS AND DISCUSSION .....	176
6.1. Selective localization of graphene in the PCL phase in compression moulded samples .....	176
6.2. Theoretical prediction of the co-continuity .....	180
6.3. Experimental prediction of the co-continuity range in the compression moulded samples .....	183
6.4. Influence of annealing time during compression moulding on the co-continuity .....	194
6.5. Influence of the extrusion protocol .....	196
6.6. Influence of GNP content on the co-continuity .....	198
6.7. Influence of 3D printing on the co-continuity .....	201
7. CONCLUSION .....	203
8. BIBLIOGRAPHY .....	205
9. SUPPLEMENTARY INFORMATION .....	214

**ANNEX: PRELIMINARY STUDY OF DOUBLE ELECTRICAL PERCOLATION IN PLA/PBAT/GNP NANOCOMPOSITE**

<b>BLENDS .....</b>	<b>220</b>
1. GRAPHICAL ABSTRACT .....	220
2. ABSTRACT.....	220
3. INTRODUCTION .....	221
4. EXPERIMENTAL PROCEDURE .....	223
4.1. <i>Materials</i> .....	223
4.2. <i>Nanocomposites and blends preparation</i> .....	223
5. CHARACTERIZATION TECHNIQUES .....	225
5.1. <i>Contact angle measurements</i> .....	225
6. RESULTS AND DISCUSSION .....	229
6.1. <i>Microstructure of pure PLA/PBAT blends</i> .....	229
6.2. <i>Theoretical and experimental localization of GNP in PLA/PBAT blends</i> .....	231
6.3. <i>PLA/PBAT/GNP nanocomposites electrical performance</i> .....	237
7. CONCLUSION.....	239
8. BIBLIOGRAPHY .....	241
<b>GENERAL CONCLUSIONS AND FUTURE PERSPECTIVES .....</b>	<b>247</b>
<b>LIST OF FIGURES.....</b>	<b>251</b>
<b>LIST OF TABLES .....</b>	<b>257</b>
<b>ABSTRACT .....</b>	<b>259</b>
<b>RÉSUMÉ.....</b>	<b>260</b>

## **General Introduction**

Owing to their interesting properties, polymer nanocomposites present a great potential in a broad range of applications such as automobiles, aerospace, energy-storage devices and sensors, biomedical devices, electronics, packaging, and others. And like other composite materials they are comprised of two components: polymer matrix and the nanofillers having at least one dimension in the nanometric range. Thermoplastic polymer nanocomposites are fabricated by solution blending, in-situ polymerization, and melt blending. Melt blending is the most used technique due to its eco-friendliness, easy processability, and cost effectiveness.

Most of the polymer matrices are electrically insulators and mixing them with electrically conductive materials can improve their electrical properties. For this purpose, metals, metal oxides, and metal sulfides have been used. Adding these fillers at high concentrations causes brittleness of the polymer matrix as well as processing difficulties. Tailoring the morphology of the polymeric matrices can cause the reduction of the electrical percolation threshold which is the required filler content necessary to transform the matrix from electrically insulating to electrically conductive. Morphological transformation can occur in immiscible polymer blends by changing the components proportions which will have impact on the viscosity ratio of the blend. Controlling the distribution of the conductive nanofillers either in one polymer phase or at the interphase of the polymer blend can govern the morphology evolution and can form dense conductive network. To ensure the continuity of this network, the polymers should be co-continuous. These two conditions, the co-continuity of the polymer phases and the selective localization of the nanofiller in the blend system, can yield to what is called double electrical percolation threshold. Lots of work have succeeded to implement this phenomenon in carbon nanotubes (CNT), carbon black (CB), graphene based, and carbon fibers (CF) filled systems using melt blending followed by conventional methods such as compression moulding. So far, there has been a scarcity in the works that aimed to achieve this threshold in samples prepared by fused filament fabrication (FFF) 3D printing. FFF is the process of building objects in a layer-by-layer pattern based on a computer aided design (CAD) and starting from a thermoplastic pure polymer or blend or composite filament. This technique grabs tremendous industrial and

academic attention nowadays and the development of functional polymer composite materials using this process has been extensively researched.

Therefore, the objective of this PhD work is the development of graphene nanoplatelets (GNP)-based nanocomposites using FFF 3D printing technique. The introduction of graphene nanofiller within polylactic acid (PLA)/poly caprolactone (PCL) and PLA/poly butylene adipate terephthalate (PBAT) matrices is aimed to improve their properties and mainly their electrical ones based on the concept of the double electrical percolation.

Melt blending technique using twin-screw extrusion is used to mix GNP and the polymers. This step is followed by single-screw extrusion to manufacture calibrated filaments to feed the 3D printer. To study the effect of the process, conventional methods such as injection moulding and compression moulding are employed.

The present work is carried out through a co-direction between the Lebanese University (LU) and IMT Mines Alès. The manuscript is transcribed into five chapters:

Chapter 1 presents a brief literature review of the main properties of PLA, PCL, PBAT, and GNP. The previous works that treated the development of PLA/PCL blends, PLA/PBAT blends, and their composites (manufactured by conventional methods and FFF) are presented. Then, some contributions related to the double electrical percolation phenomenon in carbon-based blend composites are mentioned. Afterwards, some research works that used the FFF technique to manufacture electrically conductive composites are presented.

In chapter 2, the influence of different GNP grades, differing mainly by their average particle size and surface area on the properties of pure PLA and PLA/PCL matrices is studied. The objective of this chapter is to evaluate which grade would have the best mechanical, electrical, and rheological performance in these matrices. Based on these results, this grade is implemented throughout the entire PhD work.

Chapter 3, which corresponds to a published research article contains all the experimental work that leads for the first time to manufacture electrically conductive PLA/PCL/GNP nanocomposites using FFF. In this study, the percentages of PLA and PCL are fixed and the concentration of GNP

is increased to explore the electrical percolation threshold in the 3D printed composites. For the aim of evaluating the effect of the process on the properties of the composites and mainly the electrical ones, injection moulded samples are also fabricated.

The purpose of chapter 4 which represents an accepted research article is the development of double electrical percolation in PLA/PCL/GNP composites prepared by FFF and compression moulding. After exploring the co-continuity range by theoretical and experimental methods, the effect of the processing techniques, parameters, and sequences on the co-continuous microstructure in PLA/PCL/GNP composites is studied. In this chapter, the percentages of PLA and PCL were varied and the concentration of graphene was kept constant (10 wt.%)

Finally, the fifth chapter is presented as an annex because it contains preliminary studies that need in the future to be further investigated. It explores the possibility to develop double electrical percolation in PLA/PBAT/GNP nanocomposites in samples manufactured by compression moulding and 3D printing.



## **Chapter I: State of Art**

This chapter which consists of five main parts is devoted to present a bibliographic review of the thesis. The first part concerns a presentation of the importance of bioplastics in which general features of three biodegradable polyesters: PLA, PCL, and PBAT are discussed. Graphene and graphene nanoplatelets as important polymeric nanofiller materials are discussed afterwards in a second part whereas the third one describes the biopolymer nanocomposites and especially PLA/PCL and PLA/PBAT pure and filled blends (whether manufactured by fused filament fabrication or by conventional injection and compression moulding methods). In the fourth part, the concept of double electrical percolation is explained including a lot of previous contributions concerning carbon-based melt blended composites in which this phenomenon was found. The last part gives some examples about electrically conductive carbon-based composites manufactured by fused filament fabrication.

# 1. Glossary

AFM: atomic force microscopy

BT: barium titanate

CB: carbon black

CF: carbon fibers

CNT: carbon nanotubes

DCM: dichloromethane

EFB: oil palm empty fruit bunch

EGMA: ethylene-methyl acrylate-glycidyl methacrylate terpolymer

EMA-GMA: ethylene-methyl acrylate-glycidyl methacrylate copolymer

Epoxy-POSS: epoxidized polyhedral oligomeric silsesquioxanes

ESO: epoxidized soybean oil

EVA: polyethylene-co-vinyl acetate

FFF: fused filament fabrication

GN: graphene nanosheets

GNP: graphene nanoplatelets

GO: graphene oxide

HA: hydroxyapatite

HDPE: high density polyethylene

HNT: halloysite nanotube

LDPE: low density polyethylene

MCC: microcrystalline cellulose

MWCNT: multiwalled carbon nanotubes

OMMT: organo-modified montmorillonite

PA: polyamide

PA6: polyamide 6

PA12: polyamide 12

PBS: polybutylene succinate

PBAT: polybutylene adipate terephthalate

PC: polycarbonate

PCL: poly caprolactone

PDLLA: poly-DL-lactide

PE: polyethylene

PEG: polyethylene glycol

PEI: polyetherimide

PET: polyethylene terephthalate

PHA: polyhydroxy alkanoate

phr: parts per hundred rubber

PLA: polylactic acid

PLA-g-GMA: glycidyl methacrylate grafted PLA

PLA-g-MA: maleic anhydride grafted PLA

PMMA: polymethyl methacrylate

PP: polypropylene

PS: polystyrene

PVA: polyvinyl alcohol

r-GO: reduced graphene oxide

SEM: scanning electron microscopy

Sic: silicon carbide

T<sub>g</sub>: glass transition temperature

T<sub>m</sub>: melting temperature

VP: volcanic particles

## 2. Bioplastics

Plastic industries have been developing very quickly worldwide to meet human needs in almost all life domains. For that, attractive plastic items, with better properties and low costs, have been massively produced after the 1950s. Although these materials caused great advance, yet their durability and poor end-of-life management led to an increase in the environmental issues.

Since 2000, waste generation was doubled worldwide to reach the estimated amount of 6300 million metric tons until 2015. But, only 9 % of this amount was recycled, 12% was incinerated, and 79% was accumulated in landfills or the natural environment [1]. In 2020, the global plastic production was estimated to be 367 million metric tons. This non-stop production has caused an increase in the waste accumulation in the environment. These wastes can spread in the environment through different ways and their lack of biodegradability results in their growing dissemination in the environment. For instance, around 268,940 tons of plastic products, that correspond to a minimum of 5.25 trillion particles, float on the surface of oceans [2]. These pollutants, whether sea or land originated, invaded all the widths and depths of oceans [3][4]. The main negative effects of plastic pollution on the marine biodiversity are: suffocation, toxicity, entanglement, starvation, and rafting of organisms [5]. Tourism, economy, and human health have been consequently endangered.

Plastic pollutants are dispersed in the ecosystem in different forms and sizes such as microplastics, mesoplastics, macroplastics, and megaplastics [4]. Macroplastics can decompose into microplastics (size less than 5 mm) under the effect of UV radiation and mechanical abrasion [6]. A study revealed that they are even present in snow and stream water of Mont Everest [7]. To help in reducing plastic pollution, improved waste management and posing strict policies to organize their production and disposal are required. However, replacing the traditional plastics by biodegradable bioplastics can contribute to reduce the accumulation of plastic waste across all major terrestrial and aquatic ecosystems.

Bioplastics were first introduced in 1980s and since then their market has grown rapidly. Currently, the biopolymer market has increased at an annual growth rate of 30 %, representing trillions of dollars in terms of global economic returns. Therefore, it is predictable that all the

materials used in the biomedical and agri-food applications would be replaced by bioplastics in the close future [8]. A plastic material can be bioplastic if it is biodegradable, biosourced, or both at the same time [9]. Biobased plastics are partially derived from biomass such as corn, sugarcane, and cellulose. Biodegradable plastics can totally degrade into carbon dioxide, compost, and water in the presence of oxygen under the effect of natural micro-organisms such as algae, bacteria, and fungi [10]. Based on ISO14855 EN 14046, biodegradability can be determined by estimating the metabolic conversion of compostable materials into carbon dioxide [11]. These reactions result in significant chemical microstructural changes if specific environmental conditions are satisfied. Since biodegradation depends on the polymer chemical structure rather than its origin, not all biodegradable polymers are biobased, meanwhile they can be also fossil-originated [12].

Examples of non-biodegradable biobased plastics are bio-PA, bio-PET, bio-PP, bio-PE, etc. Some of the biodegradable and biobased plastics are: PLA, PHA, PBS, and starch blends [13]. PCL and PBAT are examples of biodegradable and non-biobased polymers. Figure 1 presents the classification of biodegradability of common bioplastics [14].

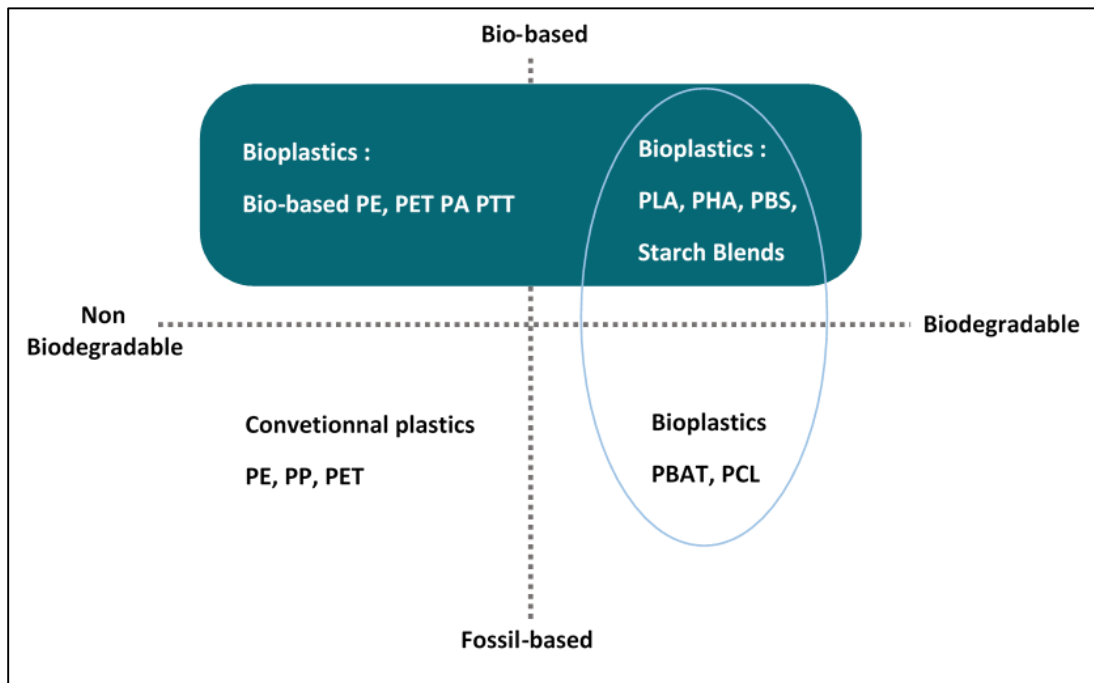


Figure 1: Classification of biodegradability of common bioplastics (readapted from reference [14])

## 2.1. Biopolyesters

Polyesters are polymers that contain ester functional groups attached to their chains. They are generally synthesized by polycondensation from combinations of diols and carboxylic acids [8]. Some polyesters are biodegradable and their biodegradation process starts from the hydrolysis of ester linkages. This results in chemical scissions and physical erosions under the biological action of enzymes or micro-organisms [15]. At present, these materials are used to manufacture bioabsorbable sutures, suture anchors, orthopaedic fixation devices, and various other products. These materials are also expected to be dominant in the world of tissue engineering in the future [16].

### 2.1.1. PLA

PLA is a compostable (figure 2), biodegradable, and biobased polymer. It is derived from renewable resources such as starch and other saccharides and belongs to the aliphatic polyester family. It is characterized with good processability, mechanical properties (high tensile strength and Young's modulus), and excellent biocompatibility [17]. Therefore, PLA can replace important petroleum based polymers such as PS, PET, HDPE, and PP in various applications (figure 3) [18][19]. Lactic acid ( $C_3H_6O_3$ ) is the building block of PLA. It is the most existing hydroxycarboxylic acid that can be synthesized by carbohydrate fermentation or chemical synthesis. Nowadays, fermentation is the most employed process for its production [20]. Microbial fermentation by lactic acid bacteria and genetic engineering bacteria is the industrial method to produce lactic acid. The latter has an asymmetric carbon atom and exists in two optically active configurations: L (+) and D (-) enantiomers. Optically pure D or L lactic acid can be synthesized via the microbial fermentation whereas a racemic mixture of L and D lactic acids can be produced through chemical routes. This mixture has limited applications on the contrary of pure lactic acids [21].

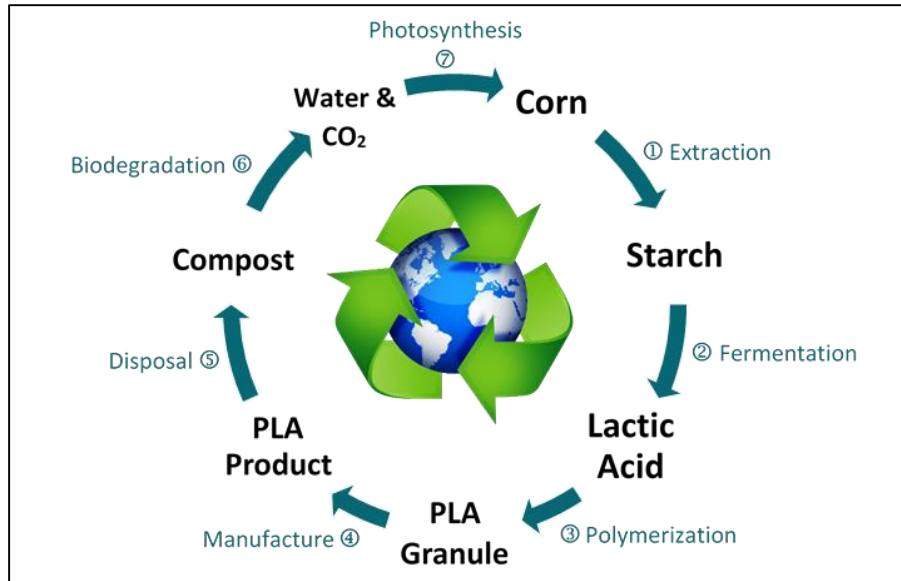


Figure 2: The life cycle of PLA (reproduced from reference [22])

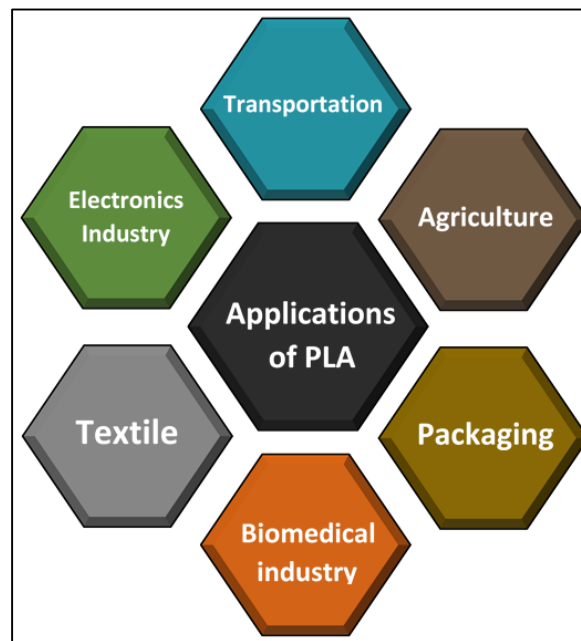


Figure 3: Various applications of PLA (readapted from reference [19])

The synthesis of high molecular weight PLA is driven via three routes such as azeotropic dehydrative condensation, direct condensation polymerization, and lactide formation followed by ring opening polymerization [23]. The ring opening polymerization of lactide is the most common technique to produce high molecular weight PLA. Lactide which is the cyclic lactic acid dimer is formed from L-lactic acid, D-lactic acid, or their mixtures. Therefore, three forms of lactide can be formed: L-lactide, D-lactide, and meso-lactide (figure 4). From these isomers, high

molecular weight PLA can be formed by catalytic ring opening polymerization. The ratio of D to L enantiomers is important for determining the degree of crystallinity of PLA and therefore its overall properties. For instance, the polymerization of a racemic mixture of L- and D-lactides usually leads to the production of PDLLA that is amorphous, whereas the use of stereospecific catalysts can lead to the formation of crystalline PLA [24]. PLLA produced from L-lactide is crystalline while PDLA synthesized from D-lactide is completely amorphous (if there is no mixture between the 2 forms). Higher crystallinity as in the case of PLLA leads to better mechanical properties, such as stiffness, as compared to less crystalline PDLLA and PDLA [25].

An efficient process to produce high molecular weight PLA was invented by Cargill Dow LLC. According to their process, both lactide and PLA are synthesized at the same time in the melt and not in solution. The first step of this technique is the condensation of aqueous lactic acid into low molecular weight PLA pre-polymer. Then, tin catalyst is used to convert the pre-polymer into a mixture of lactide stereoisomers that will be purified by vacuum distillation. Finally, ring opening polymerization of lactide into high molecular weight PLA takes place using the same catalyst. Due to the absence of solvents, this method is economic and widely applied [24].

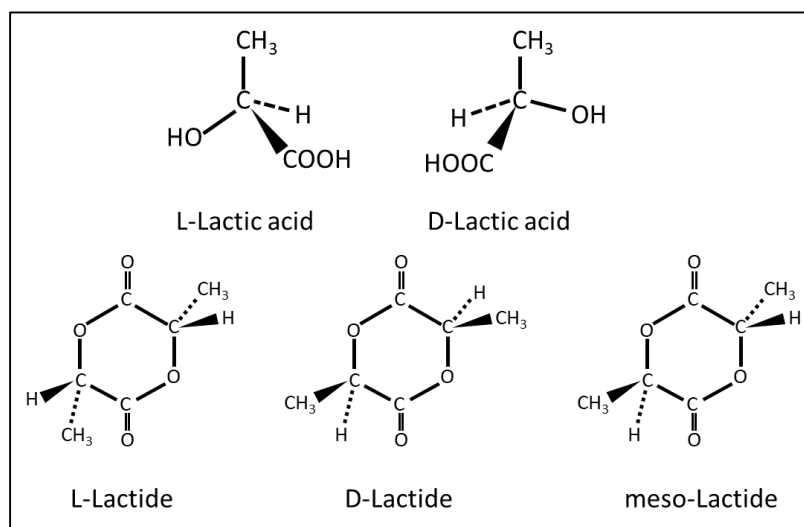


Figure 4: Stereoisomers of lactide [24]

PLA has different crystalline structures whose formation depends on the crystallization conditions. The most common form is the  $\alpha$  structure [26]. It is characterized by higher modulus and barrier properties and lower elongation at break as compared to the other crystalline forms

due to its ordered chain packing [27]. PLA has other crystalline forms such as the  $\gamma$  structure whose presence leads to greater thermal resistance [28][29]. The  $T_m$  of PLA is important for understanding its behaviour [30]. Several factors affect this temperature such as the molar mass, polymer purity, and the thermal history [31].

PLA is characterized by several interesting properties, but it has some drawbacks such as: hydrolytic and thermal degradation during melt blending, low toughness, and hydrophobicity [32][33]. Copolymerization, blending, and compositing could provide solutions for these problems.

### 2.1.2. PCL

PCL is known as a petroleum-derived synthetic aliphatic polyester having a biodegradable, semi-crystalline, and hydrophobic character while possessing high toughness and biocompatibility. It was first synthesized in the 1930s but was not used due its slow degradation and inability to bear heavy loads. It regained popularity after the emergence of tissue engineering in 1990s [34]. PCL is manufactured via the ring opening polymerization of  $\epsilon$ -caprolactone (figure 5) [35]. This reaction requires elevated temperature and a catalyst such as stannous octoate. Anionic, cationic, radical, and coordination mechanisms can influence this reaction by impacting the molecular weight, end-group composition, chemical structure, and molecular weight distribution of the copolymers [36].

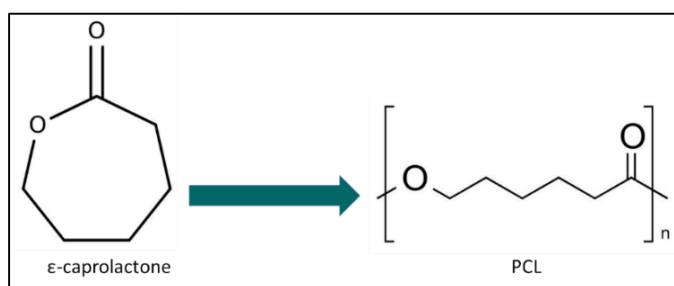


Figure 5: The chemical structures of  $\epsilon$ -caprolactone and PCL

Polycondensation of 6-hydroxycaproic acid can lead also to the production of PCL (figure 6). The disadvantage of this process is the difficulty of producing high molecular weights and high polymerization degrees. Bio-based route for the preparation of PCL was recently proposed in the literature. It seems that a two-steps process could be involved in its manufacturing. Saccharides

can be firstly fermented and converted into ethanol and acetic acid. Later, cyclohexanone can be generated from ethanol reaction with chromic acid, which can be transformed into caprolactone through a Bayer-Villiger oxidation reaction [37].

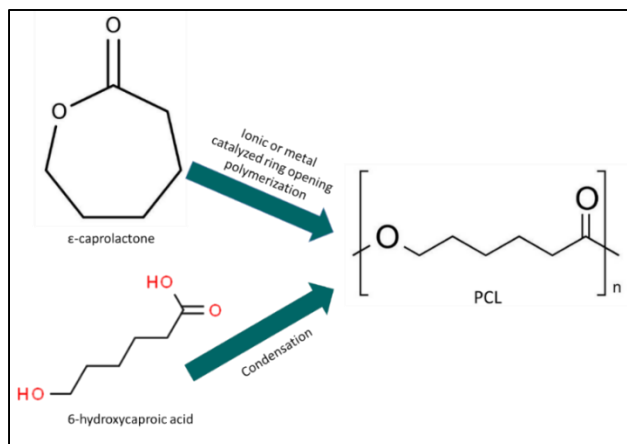


Figure 6: Synthesis of PCL from  $\epsilon$ -caprolactone and 6-hydroxyhexanoic (6-hydroxycaproic) acid [38]

PCL can be degraded by lipases and esterases enzymes that can both hydrolyse ester bonds [39]. Therefore, It is considered as one of the few fully biodegradable and biocompatible polymers [40]. With the increase of its molecular weight, its crystallinity decreases. The PCL degree of crystallinity and molecular weight affect its mechanical properties [38].

It has exceptional thermal, mechanical, chemical, and bioabsorbable properties [40]. For instance, it has low  $T_m$  (55-60 °C), low  $T_g$  (-60 °C), and low tensile strength (23 MPa). But its elongation at break is very high (700 %) [41]. In addition, it is characterized by good solubility in solvents such as chloroform, carbon tetrachloride, benzene, toluene, cyclohexanone, and 2-nitropropane at room temperature [41][42]. Some of the PCL properties are listed in table 1.

Table 1: Properties of PCL [43]

PCL properties	Value
Melting temperature (°C)	59-64
Glass transition temperature (°C)	-60
Density (g.ml <sup>-1</sup> )	1.1-1.15
Molecular weight (g.mol <sup>-1</sup> )	$3 \times 10^3$ - $8 \times 10^4$
Hydrophobicity	Highly hydrophobic
Biodegradation (years)	1-4
Young's modulus (GPa)	0.2-0.4

Regarding its applications, this polymer has been used as a biomaterial for the preparation of long-term implantable devices whether in bone tissue engineering [44] or in periodontal regeneration [44]. Moreover, various drugs have been encapsulated within PCL beads for controlled release and targeted drug delivery [45]. Figure 7 summarizes the main applications of PCL in the biomedical sector [46].

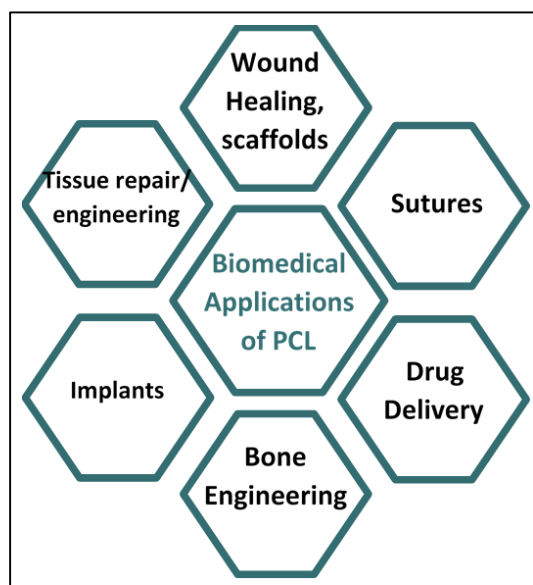


Figure 7: The main applications of PCL (reproduced from reference [46])

### 2.1.3. PBAT

Polybutylene adipate terephthalate (PBAT) is a petroleum-based biodegradable random copolymer, specifically a copolyester of adipic acid. PBAT, with both satisfactory mechanical properties and desirable biodegradability, can be produced via the poly-condensation reaction between butanediol (BDO), adipic acid (AA), and purified terephthalic acid (PTA) (figure 8). Organometallic compounds based on tin, titanium, and zinc can be used as catalysts to favour this reaction. The production of PBAT requires specific conditions such as temperature superior to 190 °C, long reaction time, and high vacuum. This synthesis is divided into three stages: pre-mixing, pre-polymerization, and final polymerization. In the final polymerization step, nucleating agents can be used to improve the PBAT crystallization behaviour [47].

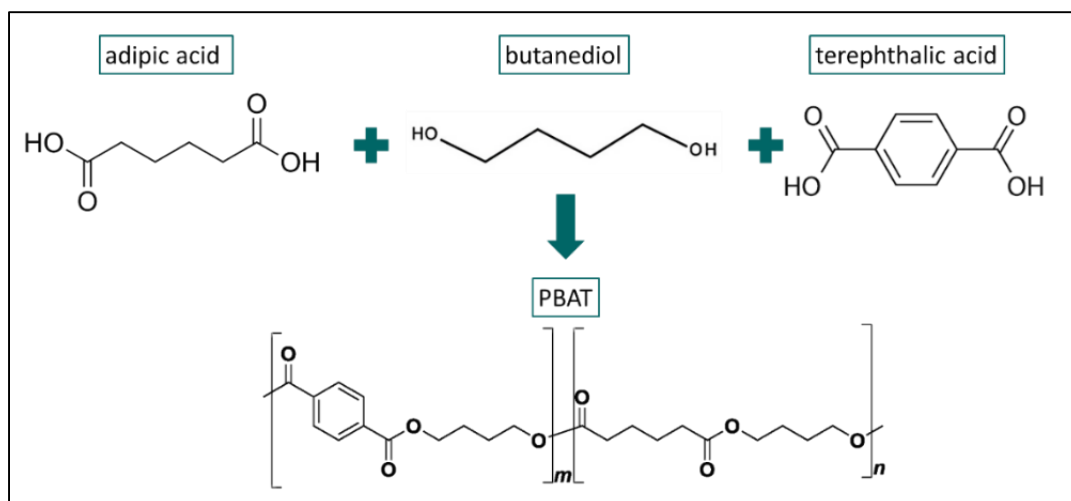


Figure 8: Synthesis of PBAT [47]

The biodegradation of this polymer is governed by the presence of aliphatic unit in the molecular chain which depends on its chemical structure and the environmental circumstances. This process occurs under the enzymatic action of micro-organisms [8]. Moreover, due to the existence of the aromatic unit, PBAT is characterized by good mechanical properties. It consists of two types of co-monomers: a rigid butylene terephthalate segment and a flexible butylene adipate section [47][48].

When compared to other biodegradable polymers such as PLA and PBS, PBAT is more flexible and comparable to LDPE. Molecular weight and proportions of different monomers affect the mechanical properties of PBAT. This means that it is possible to tailor the mechanical properties by controlling the process parameters such as the reactor temperature and pressure that have an impact on PBAT molecular weight. Some additional information related to PBAT (BASF Ecoflex® C1200 F Blend) properties are listed in table 2 [48-52]. This polymer has been used in several applications such as packaging materials (figure 9), hygiene products, biomedical domain, electronics, etc. [8][53][54].

Table 2: Properties of PBAT (BASF Ecoflex® C1200 F Blend) [48-52]

Properties	Test method	Results
Tensile strength (MPa)	ISO527	35-44
Elongation at break (%)	ISO527	560-710
Young's modulus (MPa)	ISO527	120
Flexural strength (MPa)	ASTM D790	8.44
Flexural modulus (MPa)	ASTM D790	127
Melting point (°C)	DSC	110-120
Maximal degradation temperature (°C)	TGA	398
Glass transition temperature (°C)	DSC	-33
Melt flow index (g/10 min)	ISO1133	2.7-4.9
Specific density (g.cm <sup>-3</sup> )	ISO1183	1.25-1.27

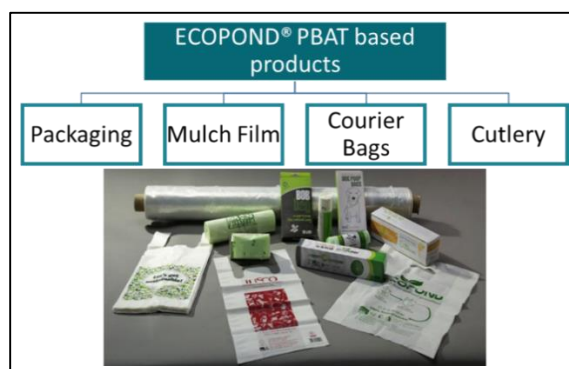


Figure 9: Some PBAT based products (reproduced from reference [54])

### 3. Graphene

Graphite is considered as one of the most important carbon allotropes. It is constituted of stacked layers of carbon atoms hybridizing  $sp^2$ . These layers relate to each other via Van der Waals bonds. However, the carbon atoms within each layer are linked by strong bonds. Graphene is just one layer of graphite. It is featured by interesting properties such as high specific surface area estimated as  $2600 \text{ m}^2.\text{g}^{-1}$ , thermal conductivity of  $4840\text{-}5300 \text{ W}.\text{(m.K)}^{-1}$ , density of  $2.25 \text{ g.cm}^{-3}$ , electrical conductivity of  $10^7 \text{ S.m}^{-1}$ , and Young's modulus of 1 TPa [55].

The first graphene synthesis was done via simple mechanical cleavage of graphite crystals. New synthesis methods were created later such as: epitaxial growth on SiC or metals, chemical

exfoliation of graphite oxide, liquid-phase ultrasonic graphite exfoliation, electrochemical graphite exfoliation, and chemical vapour deposition on metal substrates. Each of the mentioned methods has some advantages. For example, chemical vapour deposition and mechanical cleavage give the highest quality graphene. Large area of graphene can be produced by the epitaxial growth method. And mass production of graphene can be realized by chemical and liquid phase exfoliation methods [56].

Graphene can be considered as the name of a family of materials. The most popular graphene family members are pristine graphene, graphene oxide (GO), and reduced graphene oxide (r-GO) (figure 10). Pristine graphene possesses properties very similar to these of pure graphene. It is multi-layered and single layered graphene. The exfoliation of graphite via Hummer's method gives GO that has a great number of hydroxyl ions. r-GO can be produced by the elimination of most of the oxygen containing functional groups from GO [57].

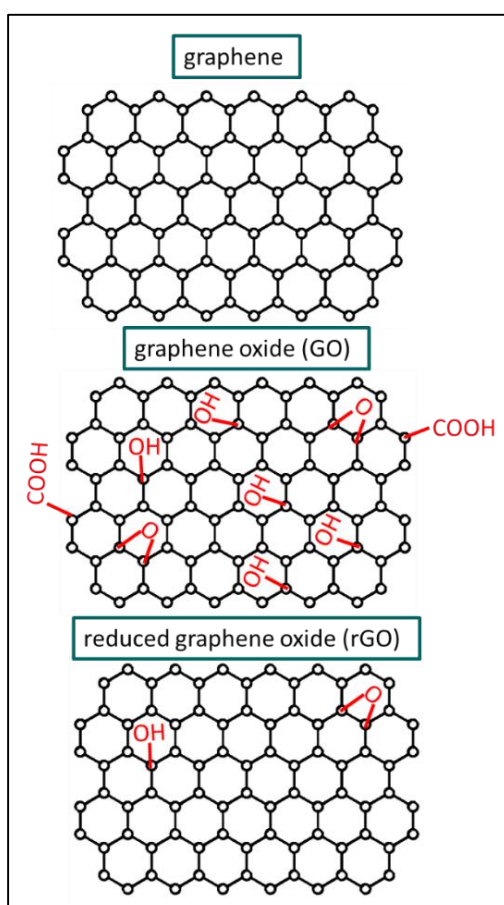


Figure 10: Graphene, GO, and r-GO chemical structures [57]

In addition to the different types of graphene already mentioned, other types also exist such as GN, which are single layer and high-quality graphene, and GNP. The latter have high aspect ratio and thickness ranging from 3 to 100 nm [58]. They are composed of more than 10 graphene layers [59] and their transversal size can be from several nanometers to a few microns. They are employed because of their lower cost and easier manufacturing as compared to pristine graphene and CNT [60].

The mass production of pure graphene with outstanding properties is still difficult due to the elevated costs and low fabrication rates, whereas GNP with interesting characteristics can be produced on the industrial scale. GNP preparation can be performed by liquid phase exfoliation, ball milling, microwave radiation of acid intercalated graphite, shear exfoliation, and wet jet milling. The differences between these manufacturing procedures cause variability at the level of the thickness, flakes lateral size, defect concentration, and aspect ratio. The produced GNP are composed of single and several graphene layers and nanostructured graphite (figure 11) [61].

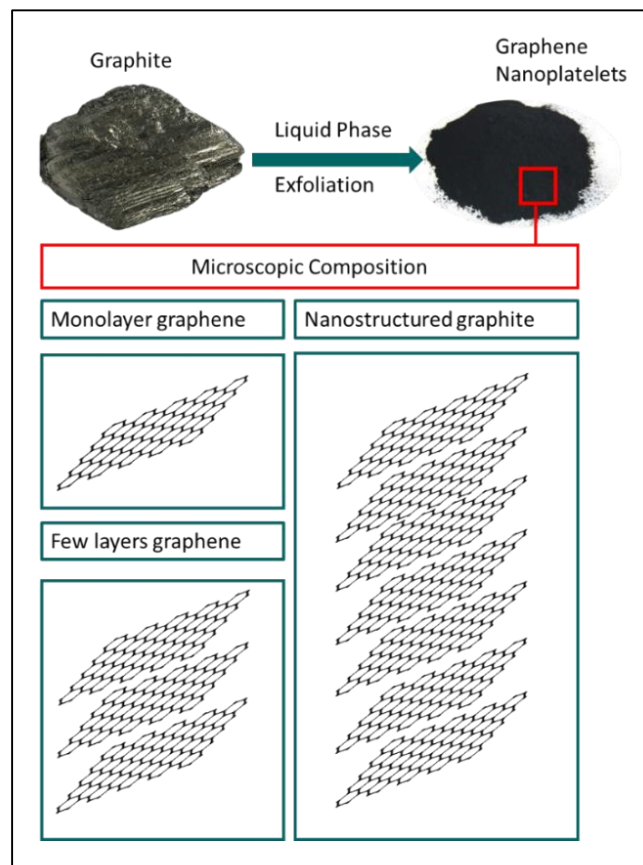


Figure 11: Liquid phase exfoliation of graphite to GNP [61]

GNP have good electrical and thermal conductivity, light weight, high aspect ratio, low cost (compared to pristine graphene), planar structure, and mechanical toughness. Thus, they can replace many nanostructured fillers such as CNT, CB, clay, and metallic nanoparticles. In addition, they can be integrated in the polymeric matrices by solvent or melt compounding methods. GNP based materials show good mechanical, flame retardant, thermal, biomedical, and gas barrier characteristics. In addition, they are capable of transforming an insulating polymer into an electrical conductor which can be used as a conformable material for electronics [61]. Some of the applications of GNP based composites are shown in figure 12.

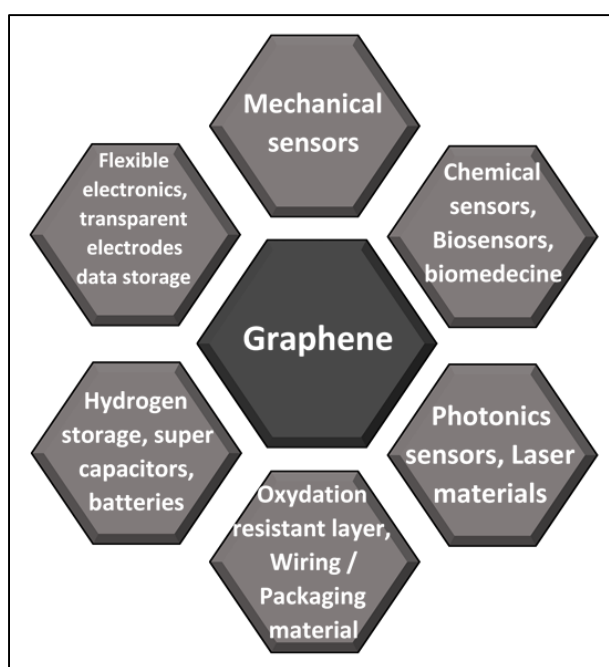


Figure 12: Some applications of GNP based composites (readapted from reference [62])

## 4. Biopolymer blend nanocomposites

Due to their eco-friendly and functional properties, biopolymers have been transformed into commercial products at the global level to replace the petroleum based plastic products. To match the desired applications, filling of the biopolymers is necessary for enhancing their mechanical, electrical, and thermal properties. The mixture of the filler and the biopolymer matrix is called a biopolymer composite. Three categories of these composites can be developed [63]: multiscale particle reinforced, structural/sandwich, and fiber reinforced composites [64].

## 4.1. Nanocomposites

Nanocomposites are multiphase materials that contain a filler having one of its dimensions in the nanoscale range [65]. Nanofillers exist in different sizes and shapes and can be classified into three main groups depending on their dimensions (figure 13) [66]:

- ❖ Plate-like nanofillers (1D) such as layered silicates, graphene sheets, and layered double hydroxides which are layered materials having a low thickness (1 nm) and high aspect ratio ( $\geq 25$ )
- ❖ Nanofibers (2D) such as CNT having diameter lower than 100 nm and an aspect ratio of at least 100
- ❖ Nanoparticles (3D) such as silica particles and metal oxides having 3D dimensions below 100 nm

There are four main methods for the preparation of polymeric nanocomposites. The first is the “solution method” in which the polymer is dissolved and mixed with the nanofiller in a convenient solvent followed by the solvent evaporation. The second is the melt blending of the polymer with nanofillers using an internal mixer, micro-compounder, or twin-screw extruder. The third one is the in-situ polymerization where nanofillers are first dispersed in a monomer solution and later polymerization takes place in the presence of the nanoscale particles. The fourth method is the template synthesis in which nanofillers are synthesized from precursor solution using polymers as templates [67].

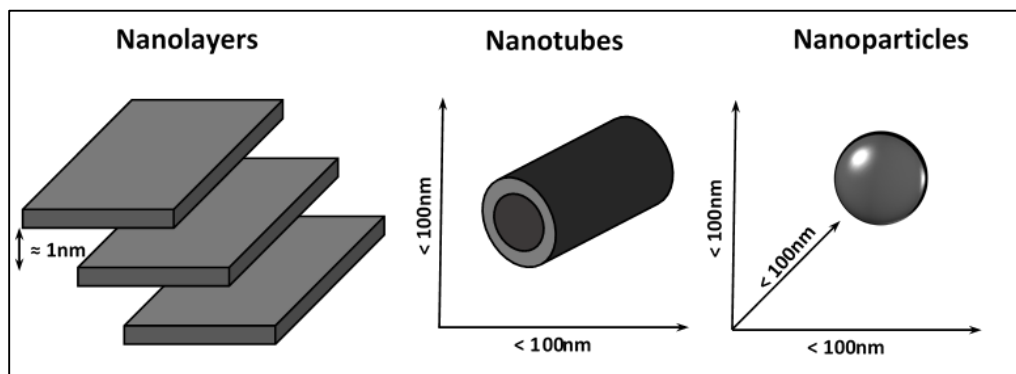


Figure 13: Various types of nanofillers [68]

## 4.2. Microstructure

The concept of combining two or more different polymers to obtain new material system with desirable features is not new. This technique offers the way to tailor the characteristics of polymeric materials. Different microstructures can exist for the polymer blends and each microstructure can yield an interesting functionality (figure 14) [69].

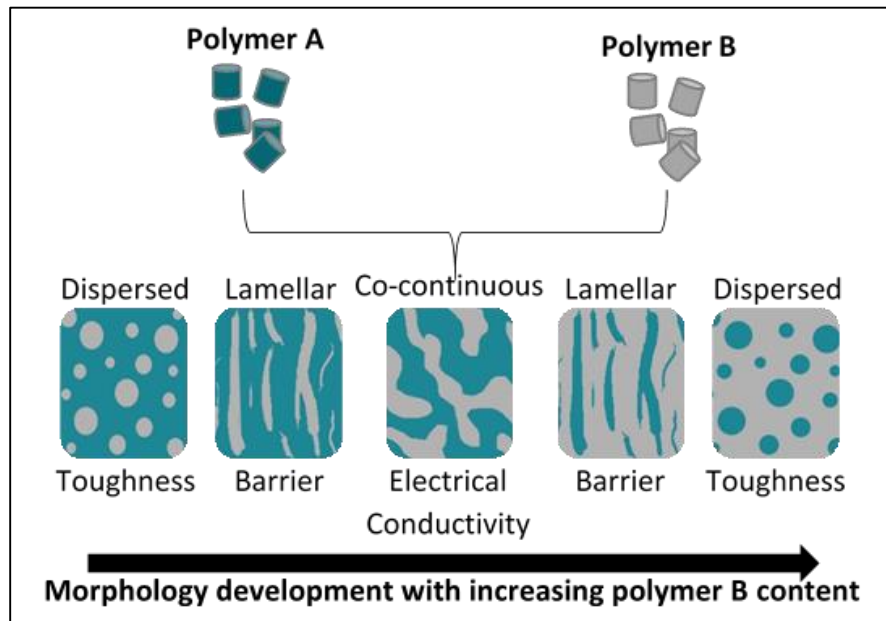


Figure 14: The various microstructures that can exist in the case of polymer blends (readapted from reference [69])

Using nanoparticles is an effective method for controlling the microstructure and the final performance of materials with phase-separated morphology, such as the immiscible polymer blends. Nano-sized fillers can induce morphology refinement or coarsening, or promote irregular polymer domains or co-continuous microstructures (figure 15) [70]. A post treatment process such as annealing can impact the microstructure by helping in increasing the co-continuity of the phases (carbon based blends for example) (figure 16) [71]. However, this is the opposite case in  $\text{TiO}_2$  filled blend systems.

The type of nanoparticles (spheres, plates, and tubes) and their preferential positioning (inside one of the phases or at the interface) are crucial in determining the resulting microstructure [70]. The aspect ratio is a key factor for the nanoparticle positioning at the blend interface during melt

mixing. The resulting microstructure influences the mechanical, barrier, thermal, electrical, and fire properties of the polymer blends [72].

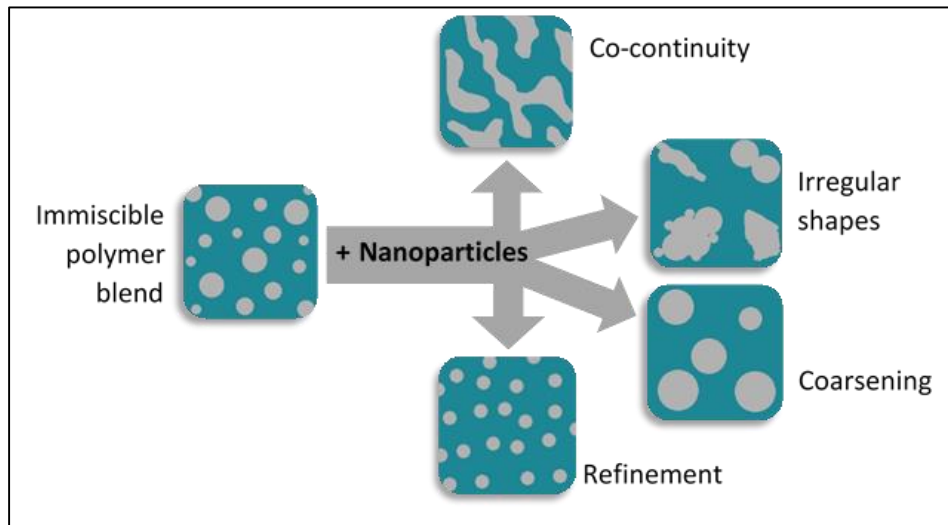


Figure 15: The various microstructures that can exist after mixing the polymer blend with nanoparticles (readapted from reference [70])

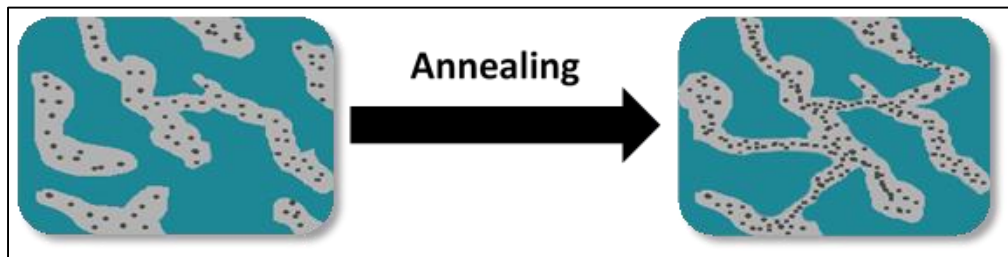


Figure 16: The impact of annealing on the microstructure of some filled immiscible polymer blends (readapted from reference [71])

### 4.3. Manufacturing methods-FFF

3D printing also known as additive manufacturing, rapid prototyping, and free form fabrication is a technique used for manufacturing light weight and complex objects. This process generates less waste and carbon emissions in comparison with more conventional polymer processing techniques due to lower energy consumption and using only the needed material when manufacturing an object. It is hugely applicable in various domains such as aerospace, medical, food, automotive, and robotics [73]. Although conventional techniques such as moulding, casting, and machining are still preferred for the large-scale production, yet most of them require

a special mould which limits designing and controlling complex and multi material objects on the contrary of the 3D printing technology [74].

3D printing is a layer-by-layer manufacturing process that can be divided into four steps as shown in figure 17. The first step is the design of a 3D model by using a special computer aided design (CAD) modelling software (step 1). The obtained file is transformed into a format suitable for a slicer software (step 2). This software allows to set all the parameters required for the manufacturing machine to properly print the object. All these conditions are then sent to the additive manufacturing machine (step 3). Subsequently, after optimizing the experimental printing conditions, the machine prints the object in a layer-by-layer pattern. Finally, the part is withdrawn from the plate (step 4) to be post-processed by surface finishing [75].

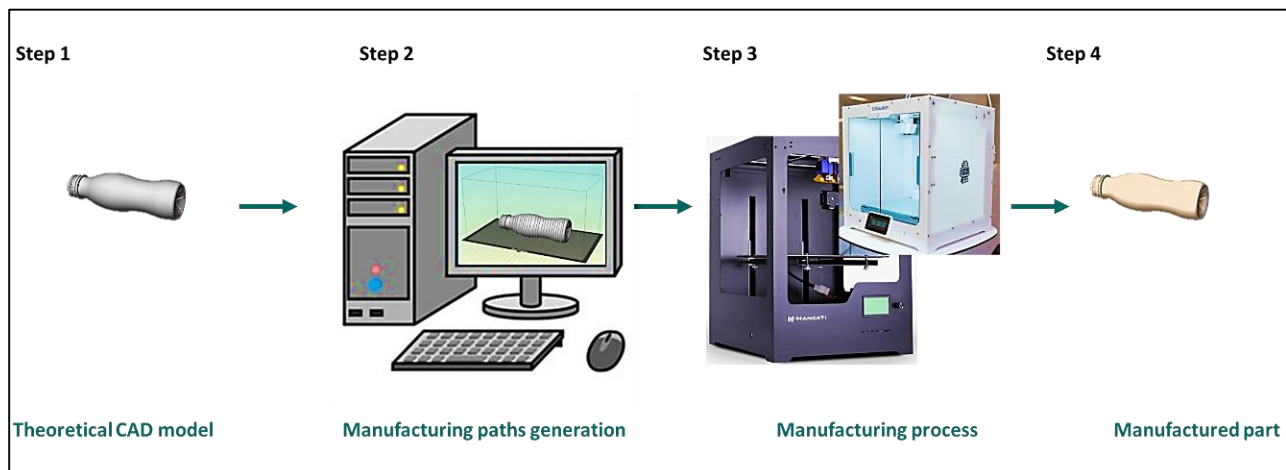


Figure 17: The main steps of 3D printing (reproduced from reference [75])

Thermoset and elastomeric materials have been employed in the additive manufacturing processes. However, most of the printable materials are the thermoplastics that can be printed by FFF which is the most used 3D printing technique. In this process, the material has big impact on the quality and function of the printed products [76]. In 1989, the co-founder of Stratasys, Scott Crump, has innovated a patent under the name of "fused deposition modelling (FDM)" [77]. The FDM is a cost effective and simple process that can be directly related to conventional extrusion-based polymer machines. The printer head is composed of the heating element, extruder, and nozzle. It operates at high temperatures to extrude and deposit the molten

material in a layer-by-layer pattern [78]. The FFF printed products meet applications in the aerospace, medicine, automobiles, construction, electronics, textiles, etc. [79].

Prior to FFF, using a single-screw extruder is mandatory to fabricate well calibrated filaments needed for achieving a successful extrusion during the FFF process. Temperature, screw speed, and pressure are the main parameters that affect the production of the filament [78].

The FFF process involves three main stages: The stage prior to deposition, the deposition stage, and the stage after the deposition. The prior to deposition and deposition stages are based on respectively 'filament in-feed' and 'molten material passage' through the melting reservoir. The parameters affecting this controlled flow are the geometry of the nozzle, the pressure gradient, the melt apparent viscosity, and the material stiffness. Some of the parameters that affect the 3D printed object properties are the infill style, infill percentage, number of contours, air gap, printing speed, printing temperature, layer thickness, raster angle, bed temperature, and number of solid laminates (top/bottom).

New materials are emerging such as ceramics, bio-glass, carbon (fibers and nanotubes), agricultural waste, animal residues, and others as a feedstock for the FFF [79]. However, thermoplastic polymers such as ABS and PLA remain the primary materials used for this process. In the second place, some other polymers are also implemented such as PC, PA, and PS. Figure 18 shows a schematic representation of the FFF technique [80].

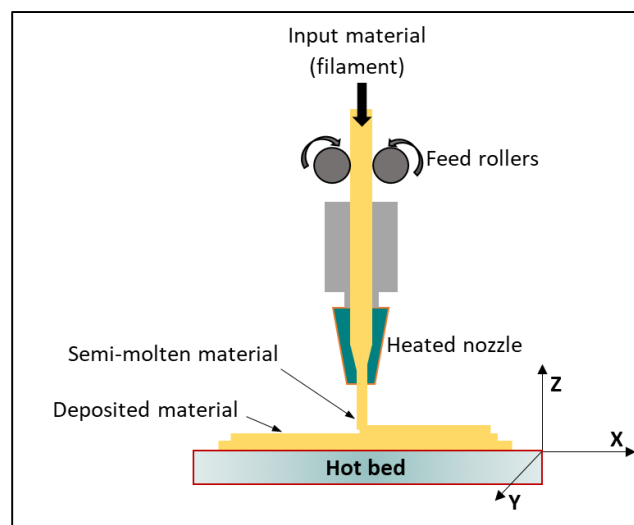


Figure 18: Schematic representation of the FFF technique (reproduced from reference [80])

## 4.4. PLA/PCL blends

Blending of polymers started before the 1970s. The emergence of biopolymers has led to new kinds of blends. Due to the diversity of biopolymers, a huge number of papers related to their blends was published [81]. As an example, PLA has been blended with several biopolymers including PCL because of its low toughness. PLA and PCL are immiscible but their blends can be characterized with increased ductility when compared to PLA alone and can possess high strength and processability when compared to pure PCL [82].

### 4.4.1. PLA/PCL blends- prepared by FFF

Regarding the fused filament fabrication of unfilled PLA/PCL blends, there are few published research works that were concerned with the mechanical properties of this type of blends. In this context, Jeantet et al. [83] used this technique to prepare PLA/PCL blends that are directed to the biomedical applications. Prior to FFF, twin-screw extrusion followed by single-screw extrusion was used. Different ratios of the polymers were manufactured (PLA content between 20 and 80 wt.%). They found that the ductility of the blends was strongly driven by the behaviour of its majority phase. Due to the low porosity and fibrillary shape of the polymeric phase of the 3D printed samples, their mechanical behaviour was determined to be quite like those made by injection moulding. Also, they mentioned that both polymer phases were continuous at PLA content between 40 and 60 wt.%. Figure 19 simulates the AFM image of the obtained co-continuous microstructure of PLA60/PCL40 calibrated filament.

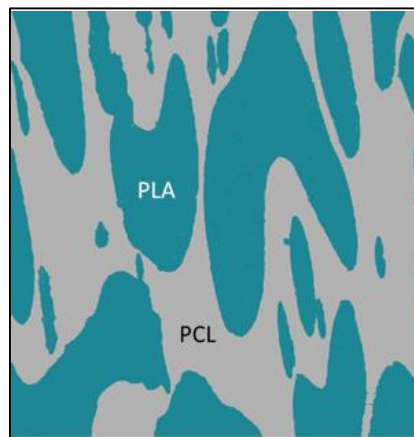


Figure 19: Schematic image simulating the AFM image of the co-continuous microstructure of PLA60/PCL40 calibrated filament (readapted from reference [83])

#### **4.4.2. PLA/PCL blends- prepared by injection and compression moulding**

Several previous contributions concerning PLA/PCL blends were published in which the test specimens were prepared by conventional methods such as injection and compression moulding. Ostafinska et al. [84] used an internal mixer followed by compression moulding to prepare PLA/PCL blends with optimal mechanical properties. According to their results, the viscosities of both polymers should be equal to have the best mechanical performance. In addition, compression moulding with fast cooling can lead to the optimal morphology required for the best mechanical properties (0.6  $\mu\text{m}$  average PCL particle diameter). These conditions can lead to good results in the case of PLA80/PCL20 which can be considered as the best composition. Matta et al. [85] reached the same conclusions after using the same experimental methods to prepare different PLA/PCL blends. PLA80/PCL20 blend exhibited the highest elongation at break and impact strength. The addition of PCL was found to accelerate the PLA crystallization rate but had little effect on its final degree of crystallinity.

Urquijo et al. [86] used twin-screw extrusion followed by injection moulding or compression moulding to prepare different compositions of PLA/PCL blends. Both polymers helped in increasing the crystallinity percentage of each other. The injection moulded samples showed smaller PCL particle size when compared to the compression moulded samples. That is why the ductility of the injection moulded samples was greater.

Luyt et al. [87] used an internal mixer followed by compression moulding to prepare PLA/PCL samples with the purpose of studying their thermal properties and crystallization behaviour. The presence of PCL in the blends had a strong influence on the PLA crystallization. Also, the presence of PLA in the blends had a strong effect on the PCL crystallinity which crystallized faster when compared to neat PCL.

Ostafinska et al. [88] used an internal mixer followed by compression moulding to prepare various PLA/PCL blends for the purpose of understanding the impact of PLA viscosity on the mechanical properties. The blend containing the most viscous PLA exhibited the smallest PCL particles (average diameter equal to 0.6  $\mu\text{m}$ ) and greatest improvement in toughness (greater by 16 times than pure PLA). This composition has the optimal morphology (figure 20) and properties.

The decrease in the matrix viscosity resulted in an increase in the average PCL particle size and dramatic decrease in the overall toughness. These materials can be used in the bone tissue engineering applications.

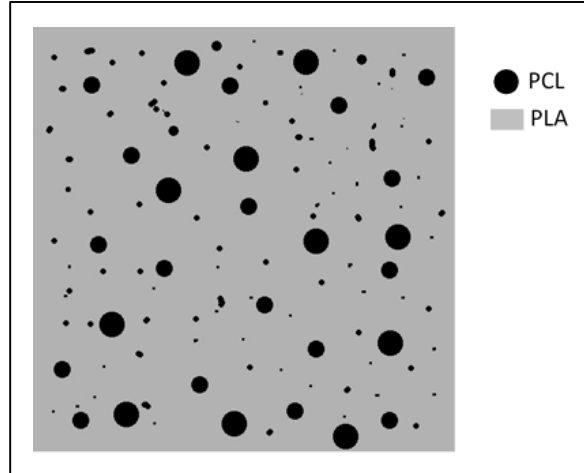


Figure 20: Schematic image simulating the SEM image of PLA80/PCL20 with the optimized morphology (readapted from reference [88])

#### 4.4.3. PLA/PCL blend composites- prepared by FFF

Not only pure PLA/PCL mixtures were studied, but also the filled ones for the purpose of improving their morphology dependent characteristics and functionality. PLA/PCL blends were reinforced by several fillers such as wood flour, CNT, OMMT, graphene, and GNP [89-93]. These different composites were manufactured via different methods and destined to various applications. In our previous work [94], the fabrication of electrically conductive PLA/PCL/GNP composites was accomplished, but this contribution is an integral part of the thesis and will be discussed in detail in Chapter 3.

In another work accomplished by Pitjmit et al. [95] and addressed to the biomedical field, PLA/PCL/HA composites were used to fabricate composite filaments for the FFF process. All the components were added to a single-screw extruder to manufacture a well-calibrated filament to be printed later using the FFF. The mixing ratio between PLA and PCL was fixed at 70 wt.%/30 wt.%. The weight percentage of the hydroxyapatite powder was up to 15 wt.%. At this percentage, the compressive strength was very high ( $82.72 \pm 1.76$  MPa). Moreover, the presence

of HA provided higher bone cell proliferation which made this composite with high potential to be used in the biomedical domain.

Akerlund et al. [96] also prepared PLA/PCL/HA composite filaments that were printed by a FFF machine. The HA percentage was fixed at 15 wt.% and the PLA and PCL percentages were varied (90/10, 80/20, and 70/30 wt.%/wt.%). Composite films were prepared by solvent casting where all the components were dissolved in DCM. After the solvent evaporation, the films were shredded into small pieces that fed later a single-screw extruder. The produced filaments were afterwards used to print the required samples for the characterizations. The results showed that all the 3D materials exhibited higher mechanical properties than a human bone. Thus, their study presented a material that could find application as potential bone implant.

Alam et al. [97] succeeded in manufacturing nanocomposite scaffolds comprised of PLA, PCL, and HNT. This composite can be used in the bone replacement and regeneration applications. The weight percentages of PLA and PCL were fixed at 50 wt.% for each polymer. However, the halloysite content was varied from 1 to 7 wt.% in the PLA/PCL blend. Using the solvent casting method, all the constituents were dissolved in DCM to form a film (after the DCM evaporation). All the films were chopped into small pieces that fed a micro-compounder. After micro-compounding, well-calibrated filaments were produced and used to print the test specimens via the FFF. The manufacturing process is illustrated in figure 21. The presence of PCL increased the elongation at break of PLA and decreased its tensile strength.

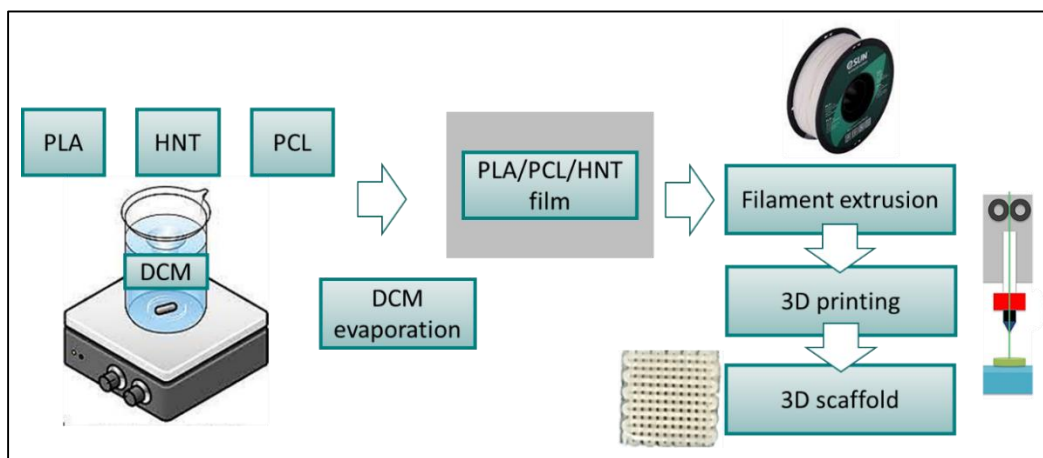


Figure 21: The manufacturing process of the PLA/PCL/HNT 3D printed scaffolds (Schematic representation readapted from reference [97])

Mystiridou et al. [98] used the solvent casting method to prepare PLA/PCL composite films containing two types of fillers (HA and/or BT). Their composite material is destined to the bone engineering field. The filler contents were chosen to be at 10 and 20 phr and DCM solvent was selected for the dissolution. After evaporating the solvent, the films were cut into small flakes to feed a single-screw extruder. The necessary test specimens were then manufactured using a FFF machine. Figure 22 shows all the steps of the process. They found that the PCL addition increased the elasticity of the filaments. The piezoelectric measurements performed in this study showed that these scaffolds have piezoelectric coefficients close to the human bone. These composites can be used as bone defect fillers in the human skeletal system.

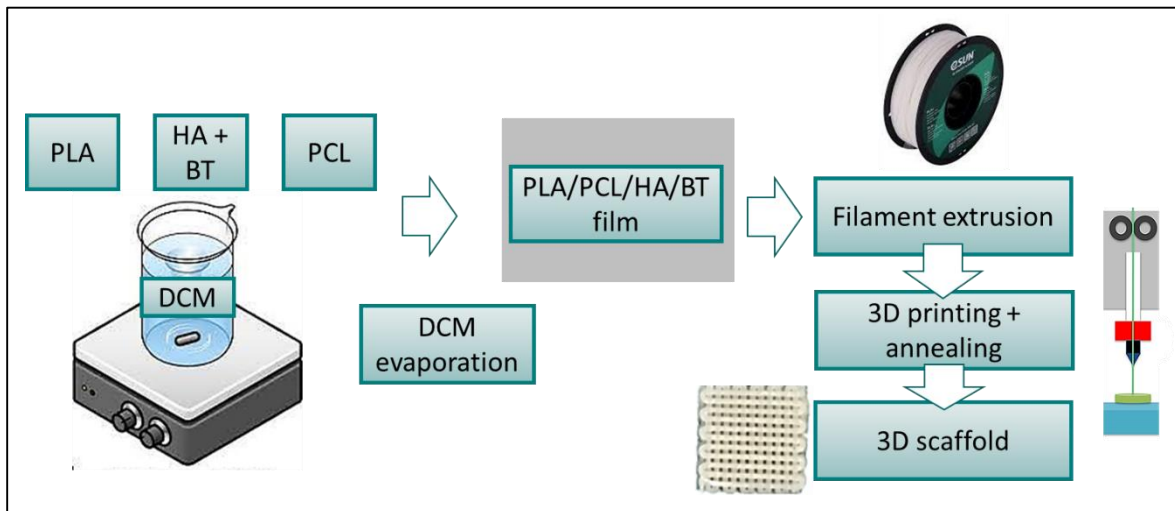


Figure 22: The manufacturing process of the PLA/PCL/HA/BT 3D printed scaffolds (Schematic representation readapted from reference [98])

#### 4.4.4. PLA/PCL blend composites- prepared by injection and compression moulding

Most of the papers in the literature that deal with PLA/PCL composites used the conventional methods to prepare the test samples. Ostafinska et al. [84] used an internal mixer followed by compression moulding to manufacture the test samples of PLA/PCL/TiO<sub>2</sub> composites. PLA80/PCL20 blends containing 10 wt.% of TiO<sub>2</sub> were prepared using different mixing methods. The addition of TiO<sub>2</sub> did not affect the morphology of the PLA/PCL blend and consequently there was no improvement in the mechanical properties because the nanofillers were aggregated (figure 23).

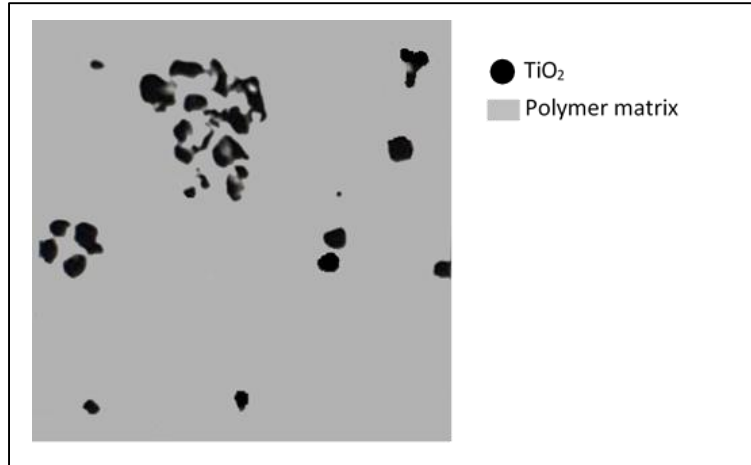


Figure 23: A simulation of the TEM image that shows the aggregations of  $\text{TiO}_2$  in the PLA/PCL matrix (reproduced from reference [84])

Rao et al. [92] prepared PLA80/PCL20 reinforced by OMMT using an internal mixer followed by compression moulding. The OMMT percentages in the composites were: 2, 4, and 6 wt.%. The added clay acted as a compatibilizer in the blend. As a result, tensile strength and storage modulus were enhanced. Highest tensile properties were obtained for nanocomposites with 4 wt.% of OMMT.

Wu et al. [93] used an internal mixer to blend PLA and PCL either with CNT or OMMT. They used later compression moulding for the preparation of the test samples. The PLA/PCL ratios were chosen to be 70/30 and 30/70. They found that the clay is selectively localized in the PLA phase and at the interface. This selective localization agrees with the thermodynamic prediction. For CNT, the high viscosity ratio between PLA and PCL is the driving force for their selective localization in PCL although based on the thermodynamics they should be in the PLA phase. Figure 24 shows the localization of the nanofillers. Regarding the crystallization of the polymer phases, the nanofiller localized in the PCL phase promotes a nucleating effect. Concerning PLA, the clay tactoids localized in this phase and at the interface enhanced its crystallinity.

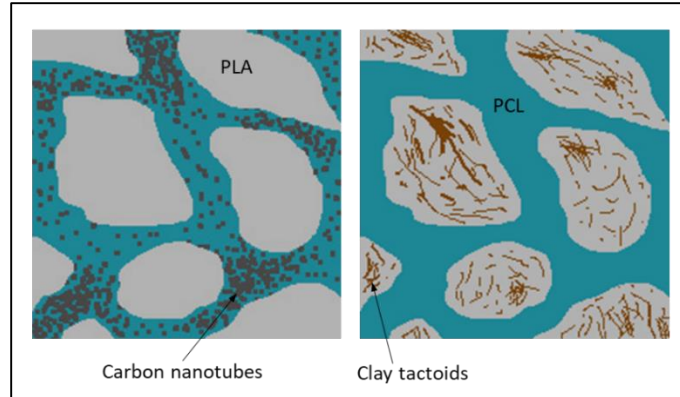


Figure 24: A schematic representation of the selective localization of the CNT and OMMT in the PLA/PCL blend (reproduced from reference [93])

Using an internal mixer followed by compression moulding, de Aguiar et al. [99] prepared PLA80/PCL20/carbon reinforced (0.5 wt.% of GNP or CNT) composites. In this work, different mixing procedures were used:

- a) Simultaneous mixing of the three components
- b) Simultaneous mixing of two components (polymer-polymer or polymer-nanoparticle) and addition of the third component later (polymer or nanoparticle)

But regardless to the mixing sequence, the nanoparticles had the tendency to migrate to the PCL phase because of the dominance of the rheological factor (PCL has lower viscosity as compared to PLA). The thermodynamic factors were negligible because of the small differences in interactions between CNT or GNP/PLA and CNT or GNP/PCL. There was increase in the PCL dispersed phase diameter in all the samples, more evidently for the ternary samples prepared with GNP than for the samples containing CNT.

Urquijo et al. [100] prepared PLA/PCL/CNT nanocomposites via a twin-screw extruder followed by compression moulding. A constant PLA80 wt.%/PCL20 wt.% was maintained for all the experiments. CNT whose content ranged between 0.8 and 5 wt.% was in the thermodynamically favoured PCL phase (figure 25). The result of this selective localization was the transformation of the “sea-island” morphology of the unfilled blend by a more continuous PCL dispersed phase in the ternary nanocomposites (figure 26). The PLA/PCL/CNT composites showed a ductile behaviour (elongation at break > 130 %) like that of the unfilled PLA/PCL. This behaviour was on

the contrary to the brittle behaviour of the binary PLA/CNT composites. The Young's modulus increased linearly upon the addition of CNT and the electrical conductivity was  $10^6$ - $10^7$  times higher than that of the unfilled blend.

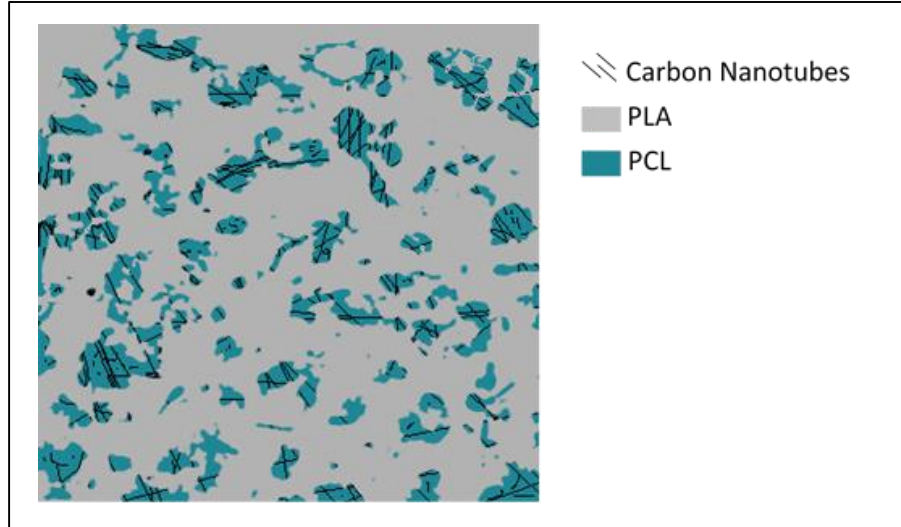


Figure 25: A simulation of the TEM image that shows the selective localization of the CNT in the PCL phase in the PLA/PCL blend (reproduced from reference [100])

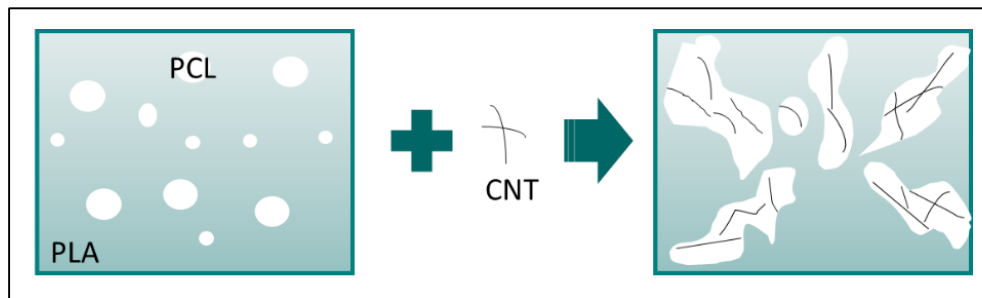


Figure 26: Effect of CNT localization on the blend morphology (image reproduced from reference [100])

Da Silva et al. [90] used a twin-screw extruder followed by injection moulding to prepare PLA/PCL/wood flour tensile specimens whose application is in disposable cups manufacturing (figure 27). Up to 30 wt.% of wood flour was added to the PLA/PCL blend. PLA and wood flour showed weak interfacial adhesion. Their results show that even though there is a reduction in the tensile strength and elastic modulus, these composites present satisfactory performance for their required application.

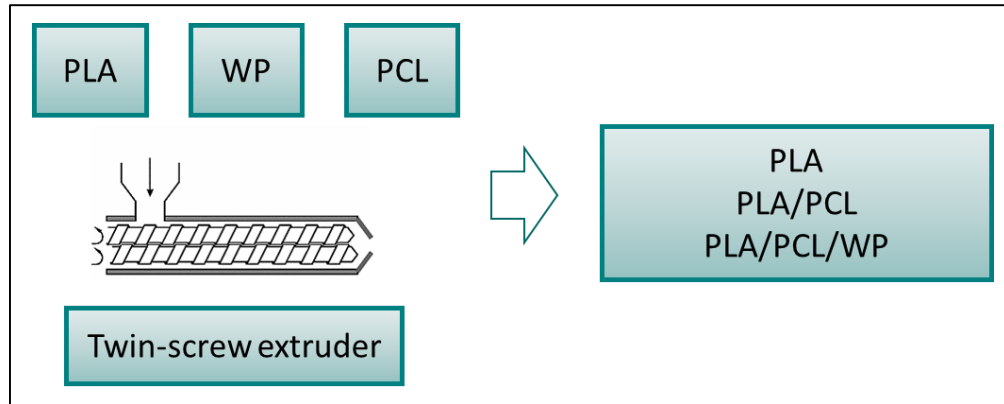


Figure 27: The manufacturing process of PLA/PCL/wood powder composites (image reproduced from reference [90])

## 4.5. PLA/PBAT blends

### 4.5.1. PLA/PBAT blends- prepared by FFF

Regarding the 3D printing of PLA/PBAT blends, there are few published works. Wang et al. [101] were interested in investigating the printing settings influence on the properties of PLA/PBAT blends. For this, PLA80/PBAT20 filament was fabricated via a single-screw extruder after using a twin-screw extruder. And later the effect of the nozzle diameter, printing speed, layer thickness, and processing temperature on the dimensional stability and the mechanical properties of the 3D printed PLA/PBAT samples were under study. They concluded that the sample performance was mainly affected by the diameter of the nozzle and the layer thickness whereas the printing speed and the processing temperature had lower influence. For the optimal tensile properties, the combination of low layer thickness, large nozzle size, high printing speed, and high temperature are recommended.

Lyu et al. [102] prepared samples of PLA/PBAT compatibilized by PLA-g-GMA using the FFF technique preceded by melt blending using the internal mixer. The mechanical properties of the compatibilized PLA/PBAT 3D printed composites were compared with these of the injection moulded samples. The results showed that the tensile strength and elongation at break of PLA70 wt.%/PBAT30 wt.% blend containing 10 wt.% of compatibilizer have reached 42.6 MPa and 200% respectively. These values are not only higher than these of the injection moulded samples, but also than the maximum values ever reported in the literature.

#### 4.5.2. PLA/PBAT blends- prepared by injection and compression moulding

Regarding the preparation of PLA/PBAT blends by conventional methods, several works were previously published. In most of the cases, a compatibilizer was used due to the strong immiscibility between PLA and PBAT. Wang et al. [103] reported the preparation of different ratios of PLA/PBAT blends using an internal mixer followed by compression moulding. Epoxy oligomers were used as compatibilizers that reacted with the PLA and PBAT chains to increase their melt elasticity, viscosity, and compatibility. The toughness of the blends as a result was improved. The effect of the compatibilizer on the blend microstructure and toughness is demonstrated in figure 28. Due to the improved interactions between the immiscible chains of PLA and PBAT thanks to the compatibilizer presence, these chains under the effect of stretching during the tensile tests were not easily broken which caused improvement in the elongation at break of the compatibilized samples.

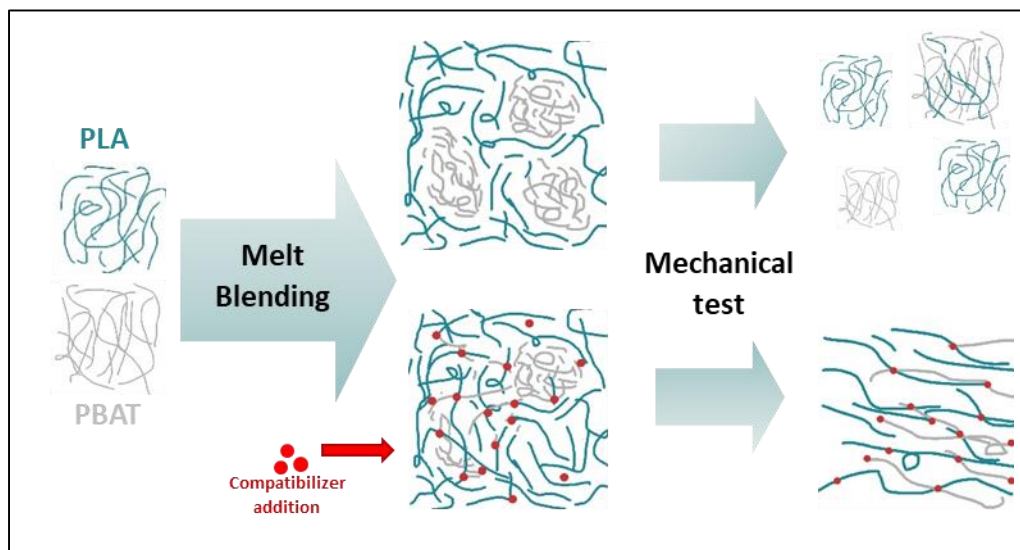


Figure 28: The effect of the compatibilizer on the microstructure of PLA/PBAT blends (image reproduced from reference [103])

Kilic et al. [104] used a micro-compounder followed by injection moulding to prepare PLA/PBAT blends compatibilized by Epoxy-POSS. The compatibilizer was found to be at the PLA/PBAT interface (figure 29). This compatibilization was evidenced by the decrease in the dispersed nodules size and the shift in the  $T_g$  of the phases. The mechanical properties were in general improved in the presence of the compatibilizer.

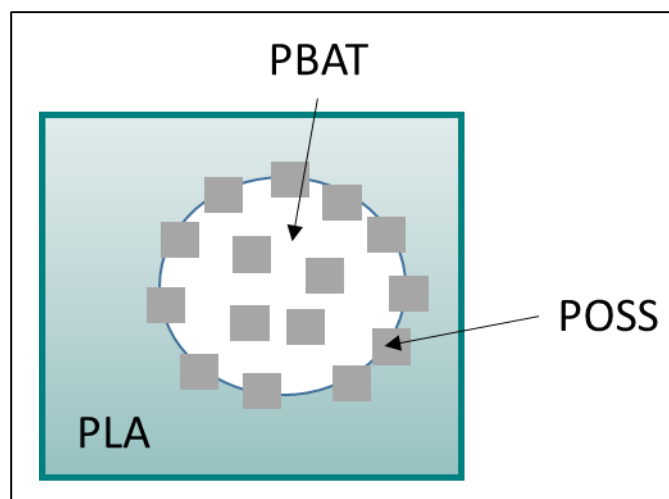


Figure 29: The location of the compatibilizer at the interface of PLA/PBAT blends (image reproduced from reference [104])

Ding et al. [105] used a twin-screw extruder followed by injection moulding to prepare PLA/PBAT blends compatibilized by PLA-PEG-PLA triblock copolymers. The compatibilizer presence caused an increase in the toughness (eight times greater than that of the uncompatibilized blends). Moreover, the sea-island microstructure was changed to a co-continuous one due to the improved interactions at the interface.

Al-Itry et al. [106] prepared PLA/PBAT blends (PLA80/PBAT20) using a twin-screw extruder with functionalized epoxy followed by injection moulding. The presence of this compatibilizer at the interface caused an improvement in the blend thermal stability. Moreover, the complex viscosity, storage modulus, tensile modulus, and elongation at break were enhanced because of the strong ester linkages at the interface.

Nofar et al. [107] prepared PLA75 wt./PBAT25 wt.% blends using two PLAs having different molecular weights. An internal mixer or a twin-screw extruder were used for the melt blending. PBAT droplets were much smaller when the twin-screw extruder was used for the blend preparation. The increasing shearing during melt blending favoured droplet coalescence in all the blends (figure 30). But coalescence and changes in the viscoelastic properties were more pronounced for PLA/PBAT blends based on low molecular weight PLA.

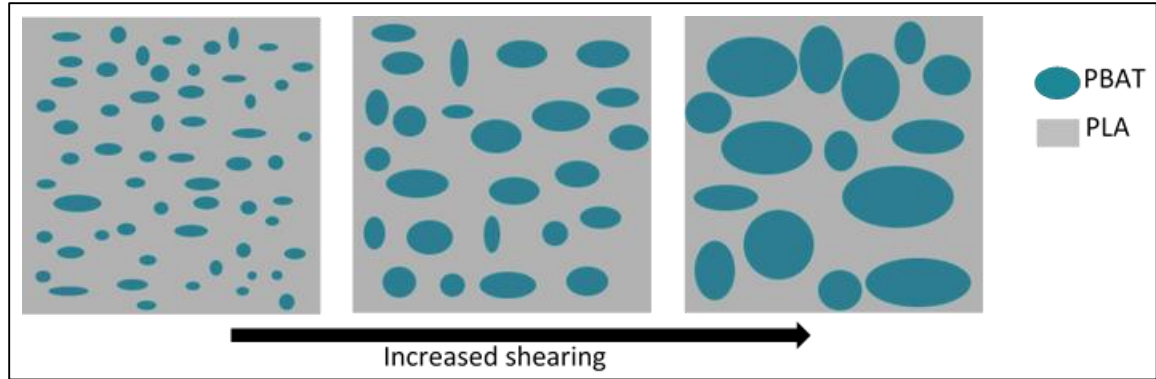


Figure 30: The impact of shearing on the microstructure of PLA/PBAT blends (image reproduced from reference [107])

Wu et al. [108] used an internal mixer followed by compression moulding to prepare PLA/PBAT blends containing EMA-GMA copolymer for the purpose of improving the blend toughness. The result was a super-tough PLA75 wt.%/PBAT10 wt.%/EMA-GMA15 wt.% that possessed improved notched impact strength, 13 times greater than that of PLA/10 wt.% PBAT binary blend. A special core-shell like dispersed phase microstructure involving PBAT particles and EMA-GMA phase at the surface of the PLA blends was obtained, thus producing strong interfacial adhesion and super toughening effect.

Chen et al. [109] used an internal mixer followed by injection moulding to prepare co-continuous PLA70/PBAT30 blends compatibilized by stereocomplex crystallites. They obtained an increase in the PLA crystallization rate. Also, the toughness, tensile strength, and impact strength of the blends were improved. Using the compatibilizer was also interesting because it acted as a rigid supporting layer between phases even above 200 °C, resulting in significantly enhanced morphology stability during melt blending.

#### 4.5.3. PLA/PBAT blend composites- prepared by FFF

There are few works regarding the FFF of PLA/PBAT composites. Wang et al. [110] used this technique preceded by twin-screw and single-screw extrusion to print samples based on PLA, PBAT, OMMT, and chain extender (figure 31). This combination led to high modulus, flexibility, toughness, and impact strength. These authors used annealing to increase the crystallinity and thus to improve the material properties.

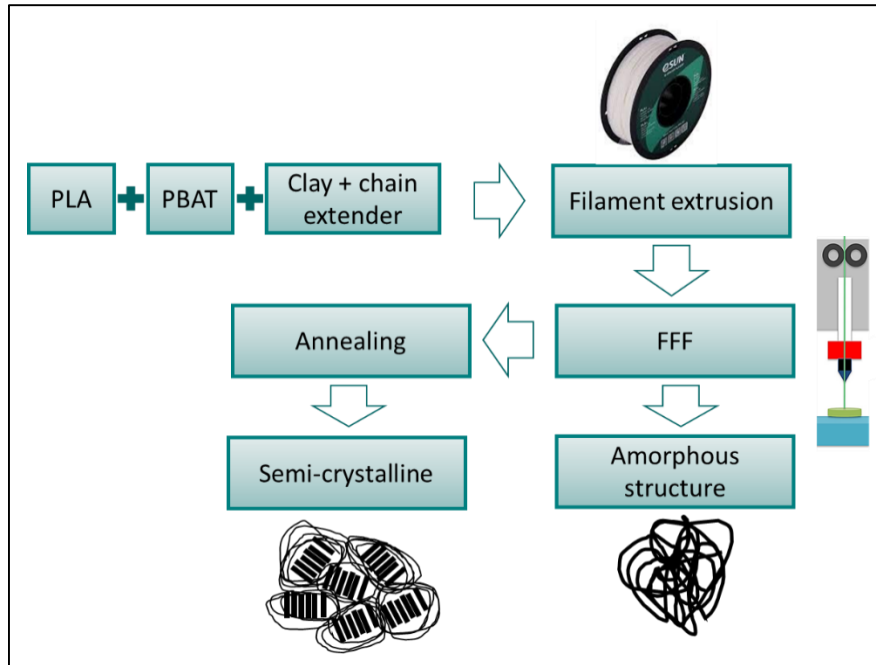


Figure 31: The manufacturing process of the PLA/PBAT compatibilized composites (image reproduced from reference [110])

Ayob et al. [111] prepared PLA80/PBAT20/EFB10 tensile specimens using the FFF technique. The tensile results indicated that the presence of PBAT decreased the tensile strength and tensile modulus of the 3D printed composite when compared to 3D printed PLA. However, the impact strength of the 3D printed composite is increased when compared to 3D printed PLA. The EFB particles were non-homogeneously distributed in the matrix and they were agglomerated.

#### 4.5.4. PLA/PBAT blend composites- prepared by injection and compression moulding

Few previous works were dealing with preparing PLA/PBAT composite specimens by the conventional methods. Coban et al. [112] manufactured PLA/PBAT blends reinforced by VP using micro-compounding followed by injection moulding. The optimal thermal properties of PLA/PBAT blends were found at 30 wt.% of PBAT. The mechanical properties were decreased with the PBAT incorporation. At 5 wt.% of VP in the PLA/PBAT blend, optimum thermal and mechanical properties were achieved.

Izzati et al. [113] used an internal mixer followed by compression moulding to prepare PLA/PBAT/MCC reinforced composites. After varying the proportions of PLA and PBAT, PLA80/PBAT20 showed the best properties and therefore it was chosen to be reinforced by MCC

(The maximal added MCC percentage was 5 wt.%). The added filler was aggregated in the matrix leading to a reduction in the impact strength. These authors emphasized the need to add a compatibilizer to improve the interfacial properties of the immiscible PLA/PBAT/MCC composites.

Teamsinsungvon et al. [114] used twin-screw extrusion followed by compression moulding to manufacture PLA/PBAT/CaCO<sub>3</sub> composites. PLA-g-MA was used as a compatibilizer. With the addition of PBAT into PLA, elongation at break and impact strength increased. The compatibilizer improved the mechanical properties of the blend.

Ludvik et al. [115] prepared composite specimens comprised from PLA, PBAT, cellulose fibers, and OMMT. This step was preceded by twin-screw extrusion. For PLA70/PBAT30 composite, the tensile strength and elongation at break were decreased when compared to the unfilled blend. Yet, Young's modulus was increased in the case of the composites when compared to the unfilled blends.

## **5. Electrical conductivity of polymer composites**

Electrically conductive polymer composites have applications in static charge dissipation, electromagnetic and radio frequency shielding, battery components, power cables, and membranes in fuel cells. But polymers in general are electrically insulating. Hence, mixing them with electrically conductive nanofillers such as carbon nanofillers results in the fabrication of electrically conductive nanocomposites. Recent studies have reported that various factors have an effect on the electrical conductivity of polymer composites such as the filler content, dispersion, orientation, shape, size, aspect ratio, conductivity, its interaction with the matrix, nature of the polymer matrix, wettability, surface energy, and processing method [116-128]. These factors influence the particles contact continuity that is necessary for the formation of continuous conductive filler path in the insulating matrix. So, based on these factors, different models were proposed to predict the electrical conductivity of the polymer composites. What is common among them is the use of the filler volume fraction as a base for the calculations.

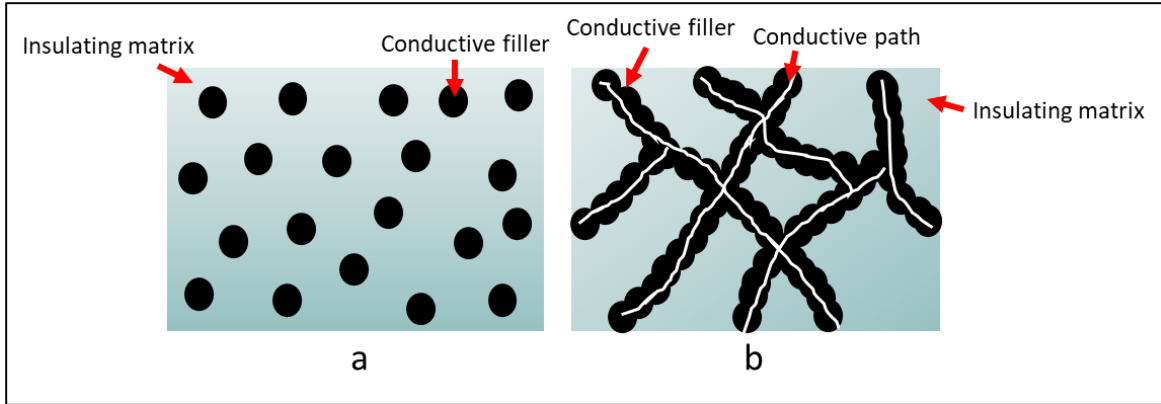


Figure 32: Schematic representation of conductive filler particles and insulating polymer in insulating (a) and conductive (b) composites

At a certain carbon filler percentage called the electrical percolation threshold  $\Phi_c$ , a continuous conductive pathway is constructed (figure 32) [129]. There exists a relationship between the electrical conductivity of the composites and the filler content. By referring to the classical percolation theory, this relationship is the scaling law which works in the 2D scale and it is as the following [130][131]:

$$\sigma = \sigma_0(\Phi - \Phi_c)^t$$

Where  $\sigma$  is the electrical conductivity of the composites,  $\sigma_0$  is the conductivity of the filler,  $\Phi$  is the volume fraction of the filler,  $\Phi_c$  is the electrical percolation threshold, and  $t$  is the critical exponent related to the dimensions of the conductive network. This relationship is exhibited in figure 33. At low filler content, the filler particles are not in contact with each other thus rendering the polymer matrix an insulator. But, when this content increases, these particles start to construct a conductive network within the polymer at the electrical threshold ( $\Phi_c$ ). Beyond this concentration, the electrical conductivity is boosted and the material starts to be conductive. This conductivity finally reaches a stable plateau due to the formation of a strong percolated conductive network.

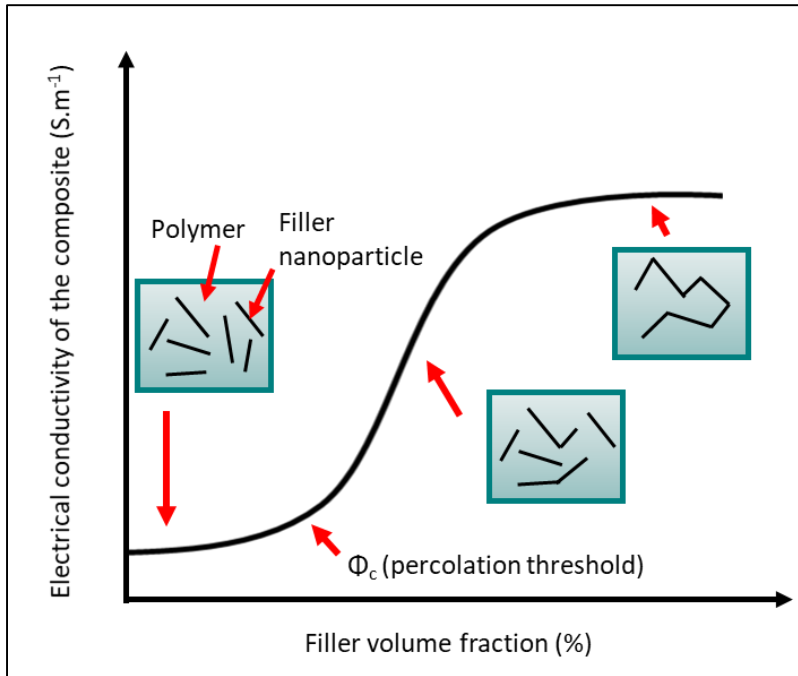


Figure 33: Electrical conductivity variation as function of the filler volume fraction (in this figure, the filler particles are fiber-shaped but other shapes also exist like the spherical (CB) and planar (graphene) forms)

The formation of the conductive network in polymer matrices results in the transport of electrons through two different mechanisms. The first is the direct contact between filler particles. The second is the “tunnelling” phenomenon in which electrons can tunnel from one particle to another if they are close enough. In this case, the electric charge transport depends on the temperature increase which reduces the tunnelling resistance. The electron tunnelling is the driving force in the conductive nanocomposites having very low filler contents. But it should be taken into consideration that enough conducting filler content is necessary to ensure that the gaps or distances between the neighbouring particles are small enough for this effect to exist. Figure 34 shows the difference between the direct contact and tunnelling effect in an electrically conductive nanocomposite [132].

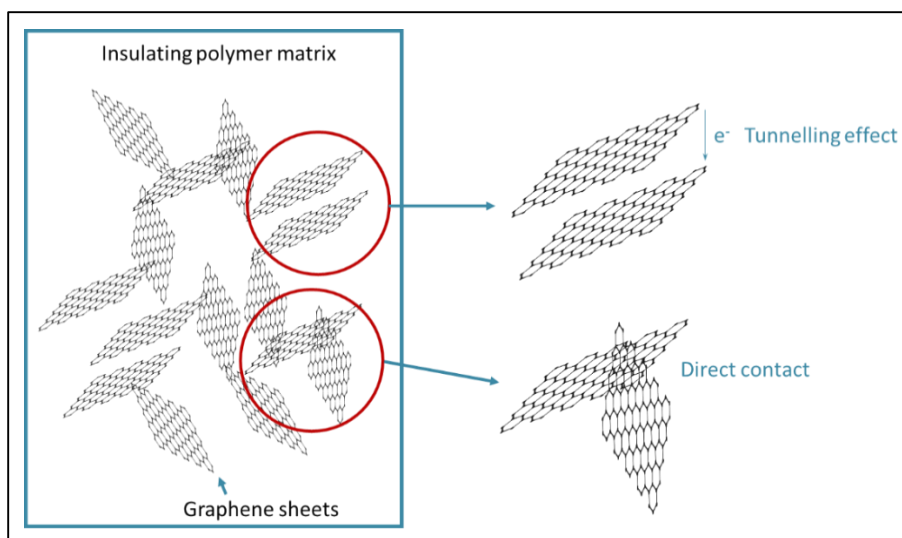


Figure 34: Schematic representation of the tunnelling and direct contact electrical conductivity mechanisms

As mentioned above, the aspect ratio of the nanofillers has an influence on the electrical percolation threshold and an exponential decrease of this threshold is found with the aspect ratio increase [133]. It can be defined as the ratio of the longest dimension of the object to its shortest dimension. For example, rod-like particles such as the carbon nanotubes have an aspect ratio that is equal to the ratio of the length to the diameter. However, for planar fillers such as graphene the aspect ratio is the ratio of the lateral dimension to the sheet thickness. High aspect ratio fillers percolate at lower percentages due to the fewer contacts required to construct more efficient conductive network [134]. In conductive polymer composites, it is recommended to choose high aspect ratio fillers in order to design conductive lightweight materials with reduced cost, lower filler amounts, and improved electrical properties [133].

Usually when studying the electrical properties of polymer nanocomposites, the filler dimensions and electrical conductivity are considered as homogeneous. However, there are large distributions in the filler length, diameter, and conductivity that affect the electrical percolation threshold. Under the influence of the shear forces that are present in the usual processing methods, the nanoparticles can be aligned along the shear flow direction [135]. Especially in the case of the anisotropic particles, the filler orientation has an important effect on the electrical conductivity. High alignment degree causes lower contact between the filler particles and therefore greater electrical percolation threshold if properties in one direction are desired [136].

To better explain this phenomenon, if an electron is travelling along highly aligned nanofiller network along the alignment direction, so it can travel the entire length without the need to tunnel. Whereas, if the electron travels transversely to the alignment direction, the electron needs to tunnel frequently to progress along the network. Therefore, as the alignment increases, an increasing number of tunnelling junctions are needed for the accomplishment of the complete journey [137].

## 5.1. Double electrical percolation

In order to fully understand the electrical response of the nanocomposites, it is crucial to introduce the concept of “double percolation” that was initially introduced by Sumita et al [138]. In this case, the conductive fillers should be selectively distributed in one phase or at the interface of a polymer blend. This confinement of the conducting particles in a heterogeneous polymer blend results in a conductive pathway formation at lower filler ratio due to the non-homogeneous filler dispersion in polymer blends. The hosting phase needs to be electrically conductive (first percolation), as well as continuous (second percolation) in a double percolation structure. Moreover, the lowest percolation threshold in a co-continuous blend is achieved when conductive fillers are restricted at the interface. The result of this phenomenon is creating versatile conductive composites. Figure 35 exhibits the schematic representation of the possible morphologies of the filler localization in co-continuous blend composites [132].

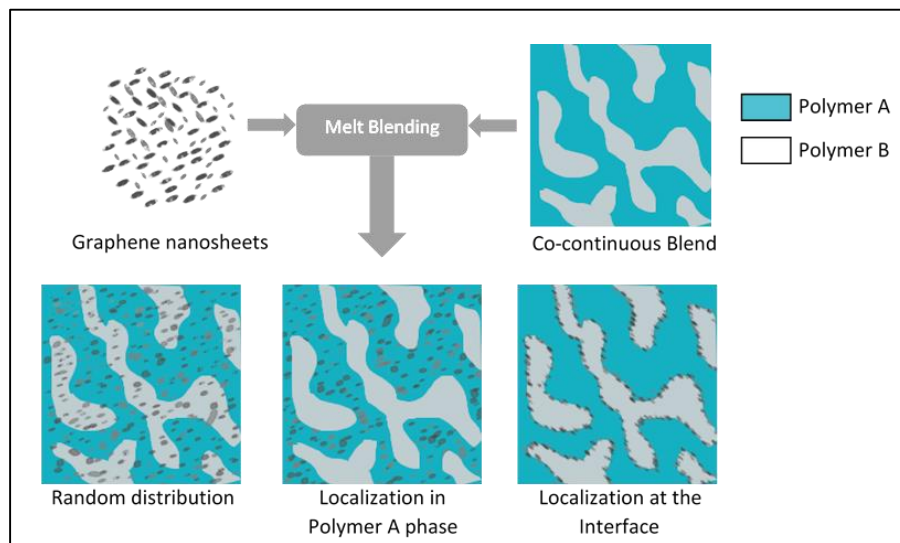


Figure 35: Possible morphologies of filler localization in co-continuous polymer blends [132]

### 5.1.1. Double electrical percolation in CNT melt blended nanocomposite blends

Carbon nanofillers and especially CNT are the most used nanofillers for the purpose of obtaining double electrical percolation threshold using the melt blending technique. In a matrix composed of PC and already melt blended ABS with MWCNT, electrically conductive materials with low electrical percolation threshold were manufactured by Maiti et al. [139]. The composites in this work were prepared by using an internal mixer followed by injection moulding. MWCNT were selectively localized in the ABS phase. Therefore, there was a sudden rise in the electrical conductivity ( $\sim 10^8$  orders of magnitude) of the nanocomposites at 0.328 vol.% of MWCNT due to the existence of the double percolation phenomenon (figure 36). The good dispersion of MWCNT in the ABS phase was responsible for the construction of the continuous MWCNT network structure that was also responsible for the increase in the storage modulus and thermal stability of the polymer blend.

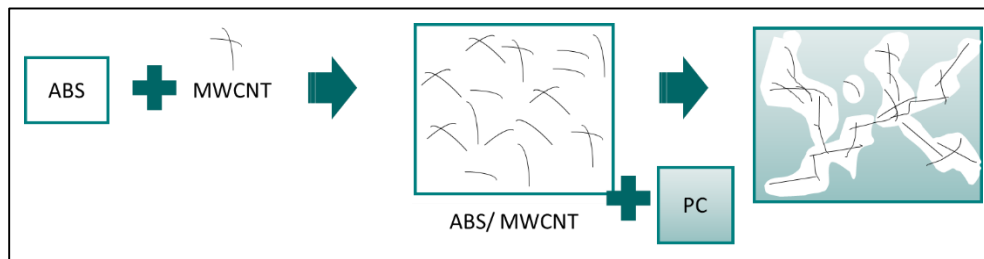


Figure 36: Double electrical percolation in ABS/PC/MWCNT composites (readapted from reference [139])

Huang et al. [140] used an internal mixer followed by compression moulding to fabricate PLA/PCL/MWCNT conductive composites. PLA and MWCNT were melt blended for few minutes before the addition of PCL. This mixing strategy caused the migration of the filler from the less favourable PLA phase to the more favourable PCL phase. The nanofiller was blocked at the interface which resulted in a very low electrical percolation threshold of 0.025 wt.% for the PLA50 wt.%/PCL50 wt.% composite.

Bose et al. [141] melt blended MWCNT with co-continuous PA50/ABS50 using a micro-compounder followed by injection moulding. They obtained an electrical percolation threshold at 3-4 wt.%. The produced double electrical percolation phenomenon was due to the selective localization of the MWCNT in the PA6 phase. They also observed refinement of the co-continuous morphology of the blends with the increase of the MWCNT content.

Chen et al. [142] used an internal mixer followed by compression moulding to prepare composite samples based on MWCNT, PS, and PMMA. MWCNT were selectively distributed at the interface of the polymer blend and therefore an electrical percolation threshold of 0.017 wt.% resulted. This localization was ascribed by the authors to the  $\pi$ - $\pi$  interactions between PS and MWCNT surface and the interactions between PMMA and the carboxyl groups on the MWCNT surface.

Strugova et al. [143] manufactured PP/PS/MWCNT systems via twin-screw extrusion and later compression moulding. With the additional thermal treatments, a very low electrical percolation threshold of 0.06 wt.% was established. The MWCNT were selectively localized at the interface in this work.

### ***5.1.2. Double electrical percolation in CB melt blended nanocomposite blends***

Regarding the research works where CB particles and melt blending technique were used, Chen et al. [144] declared the construction of a perfect double percolation structure in PS60 wt.%/PP40 wt.%/CB blend composites in the presence of a copolymer that acted as a compatibilizer (2 wt.%). The CB particles were selectively located in the PS phase and their composites showed good electrical and mechanical properties. The samples destined for the electrical conductivity measurements were prepared via melt compounding using an internal mixer followed by compression moulding. For improving the electrical conductivity of the composites, all the samples were thermally annealed inside an oven to increase the connections between the built conductive networks in the polymer matrix.

Gubbels et al. [145] studied the effect of CB on the morphology of filled PE/PS blends. The blend composites were prepared by melt blending using an internal mixer followed by compression moulding. The results showed that CB particles were located at the blend interface to yield a low electrical percolation threshold of 0.4 wt.%. They found that the annealing is an important post treatment to decrease the tortuosity of the polymer phases and consequently the interfacial area. In this case, the phase co-continuity was extended over much larger composition range and the phase morphology was stabilized.

Pan et al. [146] used an internal mixer and later the compression moulding technique to prepare PS/PMMA/CB composites possessing the double percolated structure. Moreover, the impact of

annealing on the electrical conductivity was examined. Annealing contributed to increase the electrical conductivity of the composites. The largest increase in electrical conductivity after annealing was found for PS70/PMMA30 blends filled with 1 vol.% of CB. With the PMMA content increase, this effect became less pronounced due to the decrease in the continuity of the CB filled PS phase induced by structure coarsening. The CB particles were selectively localized and percolated in the PS phase. PS30/PMMA70 blends exhibited the lowest electrical percolation threshold at 1.26 vol.% of CB.

Luo et al. [147] prepared PLA/HDPE/CB composites by melt mixing using an internal mixer followed by compression moulding. The CB particles were found to be selectively localized at the interface after the migration from the unfavourable PLA phase to the favourable HDPE phase. The electrical percolation threshold was therefore 2.42 wt.%. They obtained a co-continuous composite composed of PLA60 wt.%/HDPE40 wt.%.

Lu et al. [148] used a twin-screw extruder followed by injection moulding to prepare electrically conductive PLA/recycled HDPE/CB composites possessing a fine co-continuous microstructure. The CB particles were selectively localized in the HDPE phase. With the introduction of CB, the phase size of the PLA and HDPE components in the PLA/HDPE blends was reduced. The electrical percolation threshold of PLA70/HDPE30/CB composites was at around 5 wt.% of CB.

### ***5.1.3. Double electrical percolation in CF melt blended nanocomposite blends***

CF were also used to construct the double percolation threshold in polymer blends via the melt blending methods. The double electrical percolation threshold was established in a work carried out by Zhang et al [149]. These authors used the compression moulding to fabricate HDPE/PP/CF composite samples whose electrical percolation threshold was decreased thanks to the selective localization of the carbon fibers in the HDPE phase.

Zhang et al. [150] studied the morphology and electrical properties of short carbon fibers filled HDPE/PMMA polymer blend samples prepared by compression moulding. They obtained very low percolation threshold (1.25 phr) for HDPE50/PMMA50 blend composites because of the selective localization of the carbon fibers within the HDPE phase. With the increase of the filler

content, the HDPE domains were elongated from spherical into strip shape to finally develop a continuous structure.

#### **5.1.4. Double electrical percolation in graphene melt blended nanocomposite blends**

Graphene was added also to polymer blends for establishing the double electrical percolation threshold phenomenon. Bai et al. [151] worked on the preparation of electrically conductive composites by selectively localizing graphene at the interface of PLA/PS co-continuous polymer phases. The thermodynamic factors such as the surface energies of the filler and the polymers and the kinetic factors influenced the migration and localization of graphene in polymer blends during melt compounding. From a thermodynamic approach, GNP have preference to the PS phase, but the nanoparticles were trapped kinetically at the interface of the polymer blend. The premixing of GNP with the thermodynamically less favourable PLA phase led to their kinetic trapping at the interface during melt compounding. Shorter melt compounding time gave rise to greater GNP interfacial coverage and to more effective morphology stabilization effect. For instance, blends with as low as 0.5 wt.% of GNP prepared during 30 seconds of melt compounding possess an electrical conductivity of  $10^{-4} \text{ S.m}^{-1}$  that is larger than that of blends prepared during longer times.

Kou et al. [152] succeeded to localize GNP at the interface in a co-continuous polymer blend composed of PLA and EVA. According to the thermodynamics, GNP must be in the EVA phase. So, GNP migrated from the PLA phase in which they were initially mixed to the more favourable EVA phase to be kinetically trapped at the interface. Therefore, an ultralow percolation threshold of 0.048 wt.% of GNP was obtained as well as higher shear viscosity as compared to samples containing GNP entirely localized within the EVA phase. These robust GNP networks preserved their bulk electrical conductivity during melt processing and even after the application of non-linear deformations they remained at the interface.

## **5.2. FFF-printed carbon based electrically conductive composites**

Particularly in the energy applications, 3D printing technologies have been used to fabricate complex systems that cannot be accomplished by the conventional manufacturing techniques. Carbonaceous materials thanks to their excellent chemical stability, versatile nanostructure, and

high mechanical, electrochemical, thermal, and electrical properties, have been extensively used in 3D printing. For instance, polymers containing carbon fibers, carbon black, carbon nanotubes, graphene, and graphene oxide were already 3D printed and investigated. But, this process has to face several challenges such as: adjusting the carbon content in the polymer matrix prior to printing, studying the interactions between the carbon filler and the polymer matrix, optimizing the choice of the carbonaceous filler due to their diversity, and adjusting the properties of the printed materials and their porosity [153].

In this context, Vidakis et al. [154] prepared conductive polymer composites based on PLA and CB composite filaments for the FFF technique. The CB weight percentages were varied between 0.5 and 5 wt.%. Melt mixing was followed by a filament extrusion process to prepare the filaments for the FFF process (figure 37). The electrical percolation threshold was found at 2.5 wt.% of CB. The highest electrical conductivity was obtained at 5 wt.% of CB ( $0.9 \text{ S.m}^{-1}$ ). 10 wt.% CB conductive filaments were also produced but they were not processable towards continuous FFF 3D printing process.

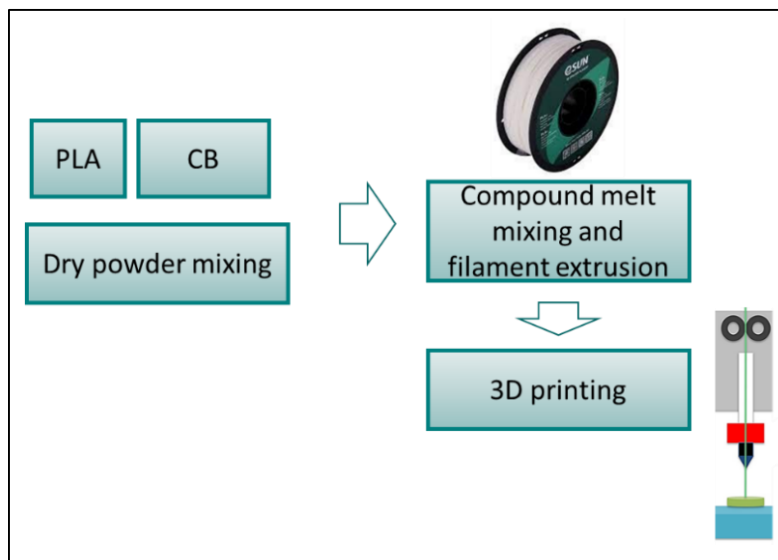


Figure 37: Schematic representation of the experimental procedure used to prepare 3D printed PLA/CB composites (readapted from reference [154])

Kanyan et al. [155] manufactured CNT-reinforced PEI filaments, whose CNT content varies between 0.1 and 7 wt.%, for the FFF technique. At 7 wt.% of CNT, the highest electrical conductivity of the composites was reported as  $2.57 \times 10^{-1} \text{ S.cm}^{-1}$ .

Vidakis et al. [156] prepared PA12 composites reinforced by MWCNT and CB at different loadings (varying between 2.5 and 10 wt.%) by melt mixing extrusion process followed by FFF. The highest electrical performance was obtained for PA12/10 wt.% CNT nanocomposite. These materials can find applications such as: 3D printed organic thermoelectric materials, resistors for flexible circuitry, and piezoresistive sensors for strain sensing.

Luo et al. [157] used the FFF technique to prepare PLA/MWCNT composites with different MWCNT contents for the aim of studying their printability and properties. The complete experimental procedure is shown in figure 38. Their experimental results showed that high conductivity ( $40 \pm 20 \text{ S.m}^{-1}$ ) could be realized in the 3D printed samples at 5 wt.% of MWCNT. These samples are also characterized by good tensile properties, flow rate, thermal properties, and printability.

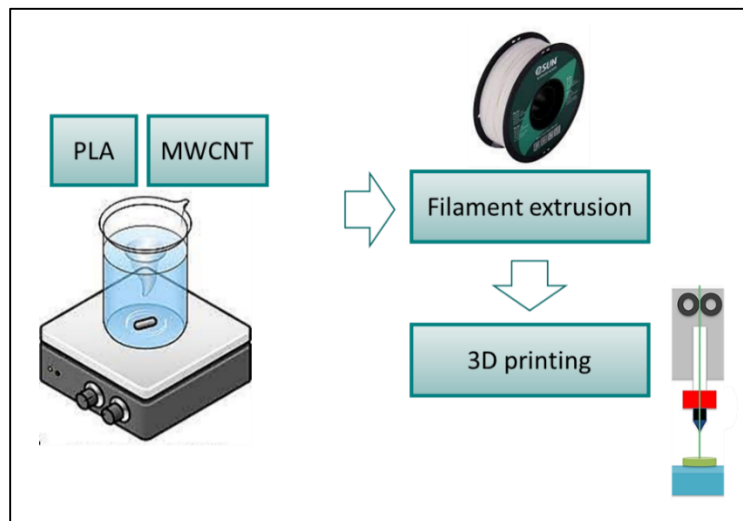


Figure 38: Schematic presentation of the experimental procedure used to prepare 3D printed PLA/MWCNT composites (readapted from reference [157])

Pei et al. [158] mixed GNP with PVA aqueous solution under ultrasonication after which glycerol was added as a plasticizer to enhance the thermal processability of the mixture. The electrical conductivity at 1 wt.% of GNP was  $2.4 \times 10^{-4} \text{ S.m}^{-1}$ . Therefore, the obtained functional nanocomposites were successfully used in the fabrication of various 3D printed functional parts with complex geometry/structure and good dimensional accuracy.

Podsiadly et al. [159] analysed the properties of nanocomposite filaments based on CNT and ABS for the FFF technique. Up to 9 wt.% of CNT was added into the polymer matrix to fabricate a

filament with 1.75 mm diameter. The measurements of the electrical properties of nanocomposites exhibited non-linear relation between the supplied voltage and the measured sample resistivity. This was explained by the semiconductor nature of the CNT functional phase and the occurrence of tunnelling effect in the percolation network. For 9 wt.% of CNT, the average resistivity of the printed samples is 0.15  $\Omega\cdot\text{m}$ . Their results showed that ABS/CNT composites are promising functional materials for the FFF fabrication of structural elements as well as structural electronics and sensors.

## **6. Conclusion**

The state of the art presented in this chapter makes it possible to place the thesis in its context through the various points addressed:

- The reason of the global trend to replace the traditional plastics with bioplastics
- Three examples on biopolyesters (PLA, PCL, and PBAT) with detailed description of their synthesis, properties, and applications
- Nanofillers definition and classification with graphene as an example
- The synthesis, characteristics, and applications of graphene nanoplatelets
- Biopolymer blends and their nanocomposites (examples on PLA/PCL and PLA/PBAT blends manufactured by fused filament fabrication and conventional methods (injection moulding and compression moulding))
- Definition of the electrically conductive polymer composites with the factors affecting their electrical properties
- Definition of the double electrical percolation phenomenon that exists in filled polymer blend composites (examples on carbon-based blends that possess this phenomenon)
- Some examples regarding electrically conductive carbon-based composites manufactured by fused filament fabrication technique

## 7. Bibliography

- [1] R. Geyer, J. R. Jambeck, and K. L. Law, "Production, use, and fate of all plastics ever made," *Sci. Adv.*, vol. 3, pp. 25–29, 2017, doi: 10.1126/sciadv.1700782.
- [2] M. Eriksen, L. C. M. Lebreton, H. S. Carson, M. Thiel, C. J. Moore, J. C. Borerro, F. Galgani, P. G. Ryan, and J. Reisser, "Plastic Pollution in the World's Oceans: More than 5 Trillion Plastic Pieces Weighing over 250,000 Tons Afloat at Sea," *PLoS One*, vol. 9, pp. 1–15, 2014, doi: 10.1371/journal.pone.0111913.
- [3] Z. Fadeeva and R. Van Berkel, "'Unlocking circular economy for prevention of marine plastic pollution: An exploration of G20 policy and initiatives,'" *J. Environ. Manage.*, vol. 277, p.111457, 2021, doi: 10.1016/j.jenvman.2020.111457.
- [4] G. G. N. Thushari and J. D. M. Senevirathna, "Plastic pollution in the marine environment," *Heliyon*, vol. 6, 2020, doi: 10.1016/j.heliyon.2020.e04709.
- [5] A. L. Andrady, "Microplastics in the marine environment," *Mar. Pollut. Bull.*, vol. 62, pp. 1596–1605, 2011, doi: 10.1016/j.marpolbul.2011.05.030.
- [6] P. L. Corcoran, M. C. Biesinger, and M. Grifi, "Plastics and beaches: A degrading relationship," *Mar. Pollut. Bull.*, vol. 58, pp. 80–84, 2009, doi: 10.1016/j.marpolbul.2008.08.022.
- [7] I. E. Napper, B. F. R. Davies, H. Clifford, S. Elvin, H. J. Koldewey, P. A. Mayewski, K. R. Miner, M. Potocki, A. C. Elmore, A. P. Gajurel, and R. C. Thompson, "Reaching New Heights in Plastic Pollution—Preliminary Findings of Microplastics on Mount Everest," *One Earth*, vol. 3, pp. 621–630, 2020, doi: 10.1016/j.oneear.2020.10.020.
- [8] F. V. Ferreira, L. S. Cividanes, R. F. Gouveia, and L. M. F. Lona, "An overview on properties and applications of poly(butylene adipate-co-terephthalate)–PBAT based composites," *Polym. Eng. Sci.*, vol. 59, pp. E7–E15, 2019, doi: 10.1002/pen.24770.
- [9] "https://www.activesustainability.com/environment/what-are-bioplastics/?\_adin=02021864894", accessed on November 21<sup>st</sup> 2022.
- [10] T. Iwata, "Biodegradable and Bio-Based Polymers: Future Prospects of Eco-Friendly Plastics," *Angew. Chemie Int. Ed.*, vol. 54, pp. 3210–3215, 2015, doi: https://doi.org/10.1002/anie.201410770.
- [11] D. Briassoulis, C. Dejean, and P. Picuno, "Critical review of norms and standards for biodegradable agricultural plastics Part II: Composting," *J. Polym. Environ.*, vol. 18, pp. 364–383, 2010, doi: 10.1007/s10924-010-0222-z.
- [12] S. RameshKumar, P. Shaiju, K. E. O'Connor, and R. B. P, "Bio-based and biodegradable polymers - State-of-the-art, challenges and emerging trends," *Curr. Opin. Green Sustain. Chem.*, vol. 21, pp. 75–81, 2020, doi: https://doi.org/10.1016/j.cogsc.2019.12.005.
- [13] "https://www.european-bioplastics.org/news/publications/#MarketData", accessed on November 22<sup>nd</sup> 2022.

- [14] C. Matthews, F. Moran, and A. Jaiswal, "A review on European Union's strategy for plastics in a circular economy and its impact on food safety," *J. Clean. Prod.*, vol. 283, p. 125263, 2021, doi: 10.1016/j.jclepro.2020.125263.
- [15] P. K. Samantaray, A. Little, A. M. Wemyss, E. Iacovidou, and C. Wan, "Design and Control of Compostability in Synthetic Biopolyesters," *ACS Sustain. Chem. Eng.*, vol. 9, pp. 9151–9164, 2021, doi: 10.1021/acssuschemeng.1c01424.
- [16] T. Freier, "Biopolyesters in Tissue Engineering Applications," C. Werner, Ed. Berlin, Heidelberg: Springer Berlin Heidelberg, pp. 1–61, 2006, [https://doi.org/10.1007/12\\_073](https://doi.org/10.1007/12_073).
- [17] D. Notta-Cuvier et al., "Tailoring polylactide (PLA) properties for automotive applications: Effect of addition of designed additives on main mechanical properties," *Polym. Test.*, vol. 36, pp. 1–9, 2014, doi: <https://doi.org/10.1016/j.polymertesting.2014.03.007>.
- [18] M. Nofar, D. Sacligil, P. J. Carreau, M. R. Kamal, and M. Heuzey, "Poly (lactic acid) blends : Processing , properties and applications," *Int. J. Biol. Macromol.*, vol. 125, pp. 307–360, 2019, doi: <https://doi.org/10.1016/j.ijbiomac.2018.12.002>.
- [19] E. Rezvani Ghomi, F. Khosravi, A. Saedi Adrahaei, Y. Dai, R. E. Neisiany, F. Foroughi, M. Wu, O. Das, and S. Ramakrishna, "The Life Cycle Assessment for Polylactic Acid (PLA) to Make It a Low-Carbon Material," *Polymers (Basel)*, vol. 13, p. 1854, 2021, doi: 10.3390/polym13111854.
- [20] R. Datta and M. Henry, "Lactic acid: recent advances in products, processes and technologies — a review," *J. Chem. Technol. Biotechnol.*, vol. 81, pp. 1119–1129, 2006, doi: <https://doi.org/10.1002/jctb.1486>.
- [21] S. Huang, Y. Xue, B. Yu, L. Wang, C. Zhou, and Y. Ma, "A Review of the Recent Developments in the Bioproduction of Polylactic Acid and Its Precursors Optically Pure Lactic Acids," *Molecules*, vol. 26, 2021, doi: 10.3390/molecules26216446.
- [22] T. Peng, "Energy Modelling for FDM 3D Printing from a Life Cycle Perspective," *Int. J. Manuf. Res.*, vol. 11, pp. 83-98, 2017, doi: 10.1504/IJMR.2017.10003722.
- [23] D. Garlotta, "A Literature Review of Poly (Lactic Acid)," *J. Polym. Environ.*, vol. 9, pp. 63–84, 2019, 10.1023/A:1020200822435.
- [24] K. Madhavan Nampoothiri, N. R. Nair, and R. P. John, "An overview of the recent developments in polylactide (PLA) research," *Bioresour. Technol.*, vol. 101, pp. 8493–8501, 2010, doi: 10.1016/j.biortech.2010.05.092.
- [25] G. Perego, G. D. Cella, and C. Bastioli, "Effect of molecular weight and crystallinity on poly(lactic acid) mechanical properties," *J. Appl. Polym. Sci.*, vol. 59, pp. 37–43, 1996, doi: 10.1002/(sici)1097-4628(19960103)59:1<37::aid-app6>3.0.co;2-n.
- [26] P. D. E. Santis and A. J. Kovacs, "Molecular Conformation of Poly (S-lactic Acid)," *Biopolymers*, vol. 6, pp. 299–306, 1968, doi:10.1002/bip.1968.360060305

- [27] J. Zhang, Y. Duan, H. Sato, H. Tsuji, I. Noda, S. Yan, and Y. Ozaki, "Crystal modifications and thermal behavior of poly(L-lactic acid) revealed by infrared spectroscopy," *Macromolecules*, vol. 38, pp. 8012–8021, 2005, doi: 10.1021/ma051232r.
- [28] W. Hoogsteen, A. R. Postema, A. J. Pennings, and G. ten Brink, "Crystal Structure, Conformation, and Morphology of Solution-Spun Poly ( L-lactide ) Fibers," *Macromolecules*, vol. 23, pp. 634–642, 1990, doi: 10.1021/ma00204a041.
- [29] B. Eling, S. Gogolewski, and A. J. Pennings, "Biodegradable materials of poly (L-lactic acid): Melt-spun and solution-spun fibres," *Polymer (Guildf)*, vol. 23, pp. 1587–1593, 1982, doi.org/10.1016/0032-3861(82)90176-8.
- [30] H. Tsuji and Y. Ikada, "Properties and morphology of poly(l-lactide). Effects of structural parameters on long-term hydrolysis of poly(l-lactide) in phosphate-buffered solution," *Polym. Degrad. Stab.*, vol. 67, pp. 179–189, 2000, doi: [https://doi.org/10.1016/S0141-3910\(99\)00111-1](https://doi.org/10.1016/S0141-3910(99)00111-1).
- [31] A. Södergård and M. Stolt, "Properties of lactic acid based polymers and their correlation with composition," *Prog. Polym. Sci.*, vol. 27, pp. 1123–1163, 2002, doi: [https://doi.org/10.1016/S0079-6700\(02\)00012-6](https://doi.org/10.1016/S0079-6700(02)00012-6).
- [32] K. Hamad, M. Kaseem, M. Ayyoob, J. Joo, and F. Deri, "Polylactic acid blends: The future of green, light and tough," *Prog. Polym. Sci.*, vol. 85, pp. 83–127, 2018, doi: <https://doi.org/10.1016/j.progpolymsci.2018.07.001>.
- [33] V. Taubner and R. Shishoo, "Influence of processing parameters on the degradation of poly(L-lactide) during extrusion," *J. Appl. Polym. Sci.*, vol. 79, pp. 2128–2135, 2001, [https://doi.org/10.1002/1097-4628\(20010321\)79:12<2128::AID-APP1020>3.0.CO;2-%23](https://doi.org/10.1002/1097-4628(20010321)79:12<2128::AID-APP1020>3.0.CO;2-%23).
- [34] O. S. Manoukian, N. Sardashti, T. Stedman, K. Gailunas, A. Ojha, A. Penalosa, C. Mancuso, M. Hobert, and S. G. Kumbar, "Biomaterials for Tissue Engineering and Regenerative Medicine," in *Encyclopedia of Biomedical Engineering*, pp. 462–482, 2019.
- [35] V. Guarino, G. Gentile, L. Sorrentino, and L. Ambrosio, "Polycaprolactone: Synthesis, Properties, and Applications," *J. Polym. Sci.*, pp. 1-36, 2017, doi.org/10.1002/0471440264.pst658.
- [36] M. Okada, "Chemical syntheses of biodegradable polymers," *Prog. Polym. Sci.*, vol. 27, pp. 87–133, 2002, doi: [https://doi.org/10.1016/S0079-6700\(01\)00039-9](https://doi.org/10.1016/S0079-6700(01)00039-9).
- [37] S. Sharma and G. U.Rani, "Biopolymers, Bioplastics and Biodegradability: An Introduction," *Encyclopedia of Materials: Plastics and Polymers*. pp. 474–486, 2022.
- [38] M. Bartnikowski, T. R. Dargaville, S. Ivanovski, and D. W. Hutmacher, "Degradation mechanisms of polycaprolactone in the context of chemistry, geometry and environment," *Prog. Polym. Sci.*, vol. 96, pp. 1–20, 2019, doi: <https://doi.org/10.1016/j.progpolymsci.2019.05.004>.
- [39] N. R. Nair, V. C. Sekhar, K. M. Nampoothiri, and A. Pandey, "32 - Biodegradation of Biopolymers," in *Current Developments in Biotechnology and Bioengineering*, Eds. Elsevier, pp. 739–755, 2017.

- [40] R. Reshmy, E. Philip, P.H. Vaisakh, R. Sindhu, P. Binod, A. Madhavan, A. Pandey, R. Sirohi, and A. Tarafdar, "Chapter 14 - Biodegradable polymer composites," in *Biomass, Biofuels, Biochemicals*, Eds. Elsevier, pp. 393–412, 2021.
- [41] L. S. Nair and C. T. Laurencin, "Biodegradable polymers as biomaterials," *Prog. Polym. Sci.*, vol. 32, pp. 762–798, 2007, doi: <https://doi.org/10.1016/j.progpolymsci.2007.05.017>.
- [42] O. Coulembier, P. Degée, J. L. Hedrick, and P. Dubois, "From controlled ring-opening polymerization to biodegradable aliphatic polyester: Especially poly( $\beta$ -malic acid) derivatives," *Prog. Polym. Sci.*, vol. 31, pp. 723–747, 2006, doi: <https://doi.org/10.1016/j.progpolymsci.2006.08.004>.
- [43] T. Borkar, V. Goenka, and A. K. Jaiswal, "Application of poly- $\epsilon$ -caprolactone in extrusion-based bioprinting," *Bioprinting*, vol. 21, p. e00111, 2021, doi: <https://doi.org/10.1016/j.bprint.2020.e00111>.
- [44] G. Manivasagam, A. Reddy, D. Sen, S. Nayak, M. T. Mathew, and A. Rajamanikam, "Dentistry: Restorative and Regenerative Approaches," in *Encyclopedia of Biomedical Engineering*, Oxford: Elsevier, pp. 332–347, 2019.
- [45] L. McKeen, "Chapter11 - The effect of heat aging on the properties of sustainable polymers," in *The Effect of Long Term Thermal Exposure on Plastics and Elastomers (Second Edition)*, Second Edition, L. McKeen, Ed. William Andrew Publishing, pp. 313–332, 2021.
- [46] M. Kurakula, G.S.N. Koteswara Rao, and K. S.Yadav, "Fabrication and characterization of polycaprolactone-based green materials for drug delivery," pp. 395–423, 2021, doi: [doi.org/10.1016/B978-0-12-820484-9.00016-7](https://doi.org/10.1016/B978-0-12-820484-9.00016-7).
- [47] J. Jian, Z. Xiangbin, and H. Xianbo, "An overview on synthesis, properties and applications of poly(butylene-adipate-co-terephthalate)–PBAT," *Adv. Ind. Eng. Polym. Res.*, vol. 3, pp. 19–26, 2020, doi: <https://doi.org/10.1016/j.aiepr.2020.01.001>.
- [48] L. C. Arruda, M. Magaton, R. E. S. Bretas, and M. M. Ueki, "Influence of chain extender on mechanical, thermal and morphological properties of blown films of PLA/PBAT blends," *Polym. Test.*, vol. 43, pp. 27–37, 2015, doi: <https://doi.org/10.1016/j.polymertesting.2015.02.005>.
- [49] "http://www.lookpolymers.com/polymer\_BASF-Ecoflex-C1200-F-Blend-Biodegradable-Polyester.php.", accessed on November 23<sup>rd</sup> 2022.
- [50] R. A. Garalde, R. Thipmanee, P. Jariyasakoolroj, and A. Sane, "The effects of blend ratio and storage time on thermoplastic starch/poly(butylene adipate-co-terephthalate) films," *Heliyon*, vol. 5, p. e01251, 2019, doi: <https://doi.org/10.1016/j.heliyon.2019.e01251>.
- [51] H. Kargarzadeh, A. Galeski, and A. Pawlak, "PBAT green composites: Effects of kraft lignin particles on the morphological, thermal, crystalline, macro and micromechanical properties," *Polymer (Guildf.)*, vol. 203, p. 122748, 2020, doi: <https://doi.org/10.1016/j.polymer.2020.122748>.

- [52] S. Dhandapani, S. K. Nayak, and S. Mohanty, "Analysis and evaluation of biobased polyester of PTT/PBAT blend: thermal, dynamic mechanical, interfacial bonding, and morphological properties," *Polym. Adv. Technol.*, vol. 27, pp. 938–945, 2016, doi: <https://doi.org/10.1002/pat.3752>.
- [53] K.-S. Kim, J. Yoo, J.-S. Shim, Y.-I. Ryu, S. Choi, J.-Y. Lee, H. M. Lee, J. Koo, and S.-K. Kang, "Biodegradable Molybdenum/Polybutylene Adipate Terephthalate Conductive Paste for Flexible and Stretchable Transient Electronics," *Adv. Mater. Technol.*, vol. 7, p. 2001297, 2022, doi: <https://doi.org/10.1002/admt.202001297>.
- [54] J. Jian, Z. Xiangbin, and H. Xianbo, "An Overview on Synthesis, Properties and Applications of Poly(butylene-adipate-co-terephthalate)-PBAT," *Adv. Ind. Eng. Polym. Res.*, vol. 3, 2020, doi: [10.1016/j.aiepr.2020.01.001](https://doi.org/10.1016/j.aiepr.2020.01.001).
- [55] Ö. Güler and N. Bağcı, "A short review on mechanical properties of graphene reinforced metal matrix composites," *J. Mater. Res. Technol.*, vol. 9, pp. 6808–6833, 2020, doi: <https://doi.org/10.1016/j.jmrt.2020.01.077>.
- [56] Z. Chen, L. Jin, W. Hao, W. Ren, and H.-M. Cheng, "Synthesis and applications of three-dimensional graphene network structures," *Mater. Today Nano*, vol. 5, p. 100027, 2019, doi: <https://doi.org/10.1016/j.mtnano.2019.01.002>.
- [57] C. Shen and S. O. Oyadiji, "The processing and analysis of graphene and the strength enhancement effect of graphene-based filler materials: A review," *Mater. Today Phys.*, vol. 15, p. 100257, 2020, doi: <https://doi.org/10.1016/j.mtphys.2020.100257>.
- [58] K. Chu, W. Li, and H. Dong, "Role of graphene waviness on the thermal conductivity of graphene composites," *Appl. Phys. A*, vol. 111, pp. 221–225, 2013, doi: [10.1007/s00339-012-7497-y](https://doi.org/10.1007/s00339-012-7497-y).
- [59] H. Yarmand, S. Gharekhani, G. Ahmadi, S. F. Seyed Shirazi, S. Baradaran, E. Montazer, M. N. Mohd Zubir, M. S. Alehashem, S. N. Kazi, and M. Dahari, "Graphene nanoplatelets–silver hybrid nanofluids for enhanced heat transfer," *Energy Convers. Manag.*, vol. 100, pp. 419–428, 2015, doi: <https://doi.org/10.1016/j.enconman.2015.05.023>.
- [60] M. Bahiraei and S. Heshmatian, "Graphene family nanofluids: A critical review and future research directions," *Energy Convers. Manag.*, vol. 196, pp. 1222–1256, 2019, doi: <https://doi.org/10.1016/j.enconman.2019.06.076>.
- [61] P. Cataldi, A. Athanassiou, and I. Bayer, "Graphene Nanoplatelets-Based Advanced Materials and Recent Progress in Sustainable Applications," *Appl. Sci.*, vol. 8, 2018, doi: [10.3390/app8091438](https://doi.org/10.3390/app8091438).
- [62] B. Aïssa, N. K. Memon, A. Ali, and M. K. Khraisheh, "Recent Progress in the Growth and Applications of Graphene as a Smart Material: A Review," *Front. Mater.*, vol. 2, 2015, doi: [10.3389/fmats.2015.00058](https://doi.org/10.3389/fmats.2015.00058).
- [63] S. K. Swain, A. J. Pattanayak, and A. P. Sahoo, "Functional Biopolymer Composites," in *Functional Biopolymers*, Springer International Publishing, pp. 159–182, 2018.

- [64] T. G. Yashas Gowda, M. R. Sanjay, K. Subrahmanya Bhat, P. Madhu, P. Senthamarai Kannan, and B. Yogesha, "Polymer matrix-natural fiber composites: An overview," *Cogent Eng.*, vol. 5, p. 1446667, 2018, doi: 10.1080/23311916.2018.1446667.
- [65] F. Hussain, M. Hojjati, M. Okamoto, and R. E. Gorga, "Review article: Polymer-matrix Nanocomposites, Processing, Manufacturing, and Application: An Overview," *J. Compos. Mater.*, vol. 40, pp. 1511–1575, 2006, doi: 10.1177/0021998306067321.
- [66] N. Herron and D. L. Thorn, "Nanoparticles: Uses and Relationships to Molecular Cluster Compounds," *Adv. Mater.*, vol. 10, pp. 1173–1184, 1998, [https://doi.org/10.1002/\(SICI\)1521-4095\(199810\)10:15<1173::AID-ADMA1173>3.0.CO;2-6](https://doi.org/10.1002/(SICI)1521-4095(199810)10:15<1173::AID-ADMA1173>3.0.CO;2-6).
- [67] A. P. Kumar, D. Depan, N. Singh Tomer, and R. P. Singh, "Nanoscale particles for polymer degradation and stabilization—Trends and future perspectives," *Prog. Polym. Sci.*, vol. 34, pp. 479–515, 2009, doi: <https://doi.org/10.1016/j.progpolymsci.2009.01.002>.
- [68] D. L. Francisco, L. B. Paiva, and A. Wagner, "Advances in polyamide nanocomposites: A review," *Polym. Compos.*, vol. 40, pp. 851–870, 2019, <https://doi.org/10.1002/pc.24837>.
- [69] I. Otero Navas, M. Kamkar, M. Arjmand, and U. Sundararaj, "Morphology Evolution, Molecular Simulation, Electrical Properties, and Rheology of Carbon Nanotube/Polypropylene/Polystyrene Blend Nanocomposites: Effect of Molecular Interaction between Styrene-Butadiene Block Copolymer and Carbon Nanotube," *Polymers (Basel)*, vol. 13, 2021, doi: 10.3390/polym13020230.
- [70] M. Salzano de Luna and G. Filippone, "Effects of nanoparticles on the morphology of immiscible polymer blends – Challenges and opportunities," *Eur. Polym. J.*, vol. 79, pp. 198–218, 2016, doi: <https://doi.org/10.1016/j.eurpolymj.2016.02.023>.
- [71] X. Cai, B. Li, Y. Pan, and G. Wu, "Morphology evolution of immiscible polymer blends as directed by nanoparticle self-agglomeration," *Polymer (Guildf)*, vol. 53, pp. 259–266, 2012, doi: <https://doi.org/10.1016/j.polymer.2011.11.032>.
- [72] A. Taguet, P. Cassagnau, and J.-M. Lopez-Cuesta, "Structuration, selective dispersion and compatibilizing effect of (nano)fillers in polymer blends," *Prog. Polym. Sci.*, vol. 39, pp. 1526–1563, 2014, doi: <https://doi.org/10.1016/j.progpolymsci.2014.04.002>.
- [73] M. N. Nadagouda, M. Ginn, and V. Rastogi, "A review of 3D printing techniques for environmental applications," *Curr. Opin. Chem. Eng.*, vol. 28, pp. 173–178, 2020, doi: <https://doi.org/10.1016/j.coche.2020.08.002>.
- [74] M. Falahati, P. Ahmadvand, S. Safaee, Y.-C. Chang, Z. Lyu, R. Chen, L. Li, and Y. Lin, "Smart polymers and nanocomposites for 3D and 4D printing," *Mater. Today*, vol. 40, pp. 215–245, 2020, doi: <https://doi.org/10.1016/j.mattod.2020.06.001>.
- [75] C. M. González-Henríquez, M. A. Sarabia-Vallejos, and J. Rodríguez-Hernández, "Polymers for additive manufacturing and 4D-printing: Materials, methodologies, and biomedical applications," *Prog. Polym. Sci.*, vol. 94, pp. 57–116, 2019, doi: <https://doi.org/10.1016/j.progpolymsci.2019.03.001>.

- [76] Y.-Q. Zhao, J.-H. Yang, X. Ding, X. Ding, S. Duan, and F.-J. Xu, "Polycaprolactone/polysaccharide functional composites for low-temperature fused deposition modelling," *Bioact. Mater.*, vol. 5, pp. 185–191, 2020, doi: <https://doi.org/10.1016/j.bioactmat.2020.02.006>.
- [77] S. Scott Crump, "Apparatus and method for creating three-dimensional objects," 1992.
- [78] S. C. Daminabo, S. Goel, S. A. Grammatikos, H. Y. Nezhad, and V. K. Thakur, "Fused deposition modeling-based additive manufacturing (3D printing): techniques for polymer material systems," *Mater. Today Chem.*, vol. 16, p. 100248, 2020, doi: <https://doi.org/10.1016/j.mtchem.2020.100248>.
- [79] S. Singh, G. Singh, C. Prakash, and S. Ramakrishna, "Current status and future directions of fused filament fabrication," *J. Manuf. Process.*, vol. 55, pp. 288–306, 2020, doi: <https://doi.org/10.1016/j.jmapro.2020.04.049>.
- [80] H. Bikas, P. Stavropoulos, and G. Chryssolouris, "Additive manufacturing methods and modeling approaches: A critical review," *Int. J. Adv. Manuf. Technol.*, vol. 83, pp. 389–405, 2016, doi: [10.1007/s00170-015-7576-2](https://doi.org/10.1007/s00170-015-7576-2).
- [81] B. Imre and B. Pukánszky, "Compatibilization in bio-based and biodegradable polymer blends," *Eur. Polym. J.*, vol. 49, pp. 1215–1233, 2013, doi: <https://doi.org/10.1016/j.eurpolymj.2013.01.019>.
- [82] K. Hamad, M. Kaseem, M. Ayyoob, J. Joo, and F. Deri, "Polylactic acid blends: The future of green, light and tough," *Prog. Polym. Sci.*, vol. 85, pp. 83–127, 2018, doi: [10.1016/j.progpolymsci.2018.07.001](https://doi.org/10.1016/j.progpolymsci.2018.07.001).
- [83] L. Jeantet, A. Regazzi, A. Taguet, M. Pucci, A.-S. Caro, and J.-C. Quantin, "Biopolymer blends for mechanical property gradient 3D printed parts," *Express Polym. Lett.*, vol. 15, pp. 137–152, 2021, doi: [10.3144/expresspolymlett.2021.13](https://doi.org/10.3144/expresspolymlett.2021.13).
- [84] A. Ostafinska, I. Fortelny, M. Nevoralova, J. Hodan, J. Kredatusova, and M. Slouf, "Synergistic effects in mechanical properties of PLA/PCL blends with optimized composition, processing, and morphology," *RSC Adv.*, vol. 5, pp. 98971–98982, 2015, doi: [10.1039/C5RA21178F](https://doi.org/10.1039/C5RA21178F).
- [85] A. K. Matta, R. U. Rao, K. N. S. Suman, and V. Rambabu, "Preparation and Characterization of Biodegradable PLA/PCL Polymeric Blends," *Procedia Mater. Sci.*, vol. 6, pp. 1266–1270, 2014, doi: <https://doi.org/10.1016/j.mspro.2014.07.201>.
- [86] J. Urquijo, G. Guerrica-Echevarría, and J. I. Eguiazábal, "Melt processed PLA/PCL blends: Effect of processing method on phase structure, morphology, and mechanical properties," *J. Appl. Polym. Sci.*, vol. 132, 2015, doi: <https://doi.org/10.1002/app.42641>.
- [87] A. S. Luyt and S. Gasmi, "Influence of blending and blend morphology on the thermal properties and crystallization behaviour of PLA and PCL in PLA/PCL blends," *J. Mater. Sci.*, vol. 51, pp. 4670–4681, 2016, doi: [10.1007/s10853-016-9784-z](https://doi.org/10.1007/s10853-016-9784-z).

- [88] A. Ostafinska, I. Fortelný, J. Hodan, S. Krejčíková, M. Nevoralová, J. Kredatusová, Z. Kruliš, J. Kotek, and M. Šlouf, "Strong synergistic effects in PLA/PCL blends: Impact of PLA matrix viscosity," *J. Mech. Behav. Biomed. Mater.*, vol. 69, pp. 229–241, 2017, doi: <https://doi.org/10.1016/j.jmbbm.2017.01.015>.
- [89] I. Kelnar, J. Kratochvíl, L. Kaprálková, A. Zhigunov, and M. Nevoralová, "Graphite nanoplatelets-modified PLA/PCL: Effect of blend ratio and nanofiller localization on structure and properties," *J. Mech. Behav. Biomed. Mater.*, vol. 71, pp. 271–278, 2017, doi: <https://doi.org/10.1016/j.jmbbm.2017.03.028>.
- [90] W. A. da Silva, C. B. B. Luna, J. B. da C. A. de Melo, E. M. Araújo, E. A. dos S. Filho, and R. N. C. Duarte, "Feasibility of Manufacturing Disposable Cups using PLA/PCL Composites Reinforced with Wood Powder," *J. Polym. Environ.*, vol. 29, pp. 2932–2951, 2021, doi: [10.1007/s10924-021-02076-8](https://doi.org/10.1007/s10924-021-02076-8).
- [91] B. Bouakaz, A. Habi, Y. Grohens, and I. Pillin, "Organomontmorillonite/graphene-PLA/PCL nanofilled blends: New strategy to enhance the functional properties of PLA/PCL blend," *Appl. Clay Sci.*, vol. 139, pp. 81–91, 2017, doi: [10.1016/j.clay.2017.01.014](https://doi.org/10.1016/j.clay.2017.01.014).
- [92] R. Umamaheswara Rao, B. Venkatanarayana, and K. N. S. Suman, "Enhancement of Mechanical Properties of PLA/PCL (80/20) Blend by Reinforcing with MMT Nanoclay," *Mater. Today Proc.*, vol. 18, pp. 85–97, 2019, doi: <https://doi.org/10.1016/j.matpr.2019.06.280>.
- [93] D. Wu, D. Lin, J. Zhang, W. Zhou, M. Zhang, Y. Zhang, D. Wang, and B. Lin, "Selective Localization of Nanofillers: Effect on Morphology and Crystallization of PLA/PCL Blends," *Macromol. Chem. Phys.*, vol. 212, pp. 613–626, 2011, doi: [10.1002/macp.201000579](https://doi.org/10.1002/macp.201000579).
- [94] N.-A. Masarra, M. Batistella, J.C. Quantin, A. Regazzi, M.F. Pucci, R. El Hage, J. M. Lopez-Cuesta, "Fabrication of PLA/PCL/Graphene Nanoplatelet (GNP) Electrically Conductive Circuit Using the Fused Filament Fabrication (FFF) 3D Printing Technique," *Materials (Basel)*, vol. 15, 2022, doi: [10.3390/ma15030762](https://doi.org/10.3390/ma15030762).
- [95] S. Pitjarnit, K. Thunsiri, W. Nakkiew, T. Wongwichai, P. Pothacharoen, and W. Wattanutchariya, "The Possibility of Interlocking Nail Fabrication from FFF 3D Printing PLA/PCL/HA Composites Coated by Local Silk Fibroin for Canine Bone Fracture Treatment," *Materials (Basel)*, vol. 13, 2020, doi: [10.3390/ma13071564](https://doi.org/10.3390/ma13071564).
- [96] E. Åkerlund, A. Diez-Escudero, A. Grzeszczak, and C. Persson, "The Effect of PCL Addition on 3D-Printable PLA/HA Composite Filaments for the Treatment of Bone Defects," *Polymers (Basel)*, vol. 14, 2022, doi: [10.3390/polym14163305](https://doi.org/10.3390/polym14163305).
- [97] F. Alam, P. Verma, W. Mohammad, J. Teo, K. M. Varadarajan, and S. Kumar, "Architected poly(lactic acid)/poly( $\epsilon$ -caprolactone)/halloysite nanotube composite scaffolds enabled by 3D printing for biomedical applications," *J. Mater. Sci.*, vol. 56, pp. 14070–14083, 2021, doi: [10.1007/s10853-021-06145-0](https://doi.org/10.1007/s10853-021-06145-0).

- [98] E. Mystiridou, A. C. Patsidis, and N. Bouropoulos, "Development and Characterization of 3D Printed Multifunctional Bioscaffolds Based on PLA/PCL/HAp/BaTiO<sub>3</sub> Composites," *Appl. Sci.*, vol. 11, 2021, doi: 10.3390/app11094253.
- [99] J. de Aguiar, M. Decol, W. M. Pachekoski, and D. Becker, "Mixing-sequence controlled selective localization of carbon nanoparticles in PLA/PCL blends," *Polym. Eng. & Sci.*, vol. 59, pp. 323–329, 2019, doi: <https://doi.org/10.1002/pen.24908>.
- [100] J. Urquijo, S. Dagr eou, G. Guerrica-Echevarr a, and J. I. Eguiaz abal, "Morphology and properties of electrically and rheologically percolated PLA/PCL/CNT nanocomposites," *J. Appl. Polym. Sci.*, vol. 134, p. 45265, 2017, doi: <https://doi.org/10.1002/app.45265>.
- [101] S. Wang, D. R. D'hooge, L. Daelemans, H. Xia, K. De Clerck, and L. Cardon, "The Transferability and Design of Commercial Printer Settings in PLA/PBAT Fused Filament Fabrication," *Polymers (Basel)*, vol. 12, 2020, doi: 10.3390/polym12112573.
- [102] Y. Lyu, Y. Chen, Z. Lin, J. Zhang, and X. Shi, "Manipulating phase structure of biodegradable PLA/PBAT system: Effects on dynamic rheological responses and 3D printing," *Compos. Sci. Technol.*, vol. 200, p. 108399, 2020, doi: <https://doi.org/10.1016/j.compscitech.2020.108399>.
- [103] X. Wang, S. Peng, H. Chen, X. Yu, and X. Zhao, "Mechanical properties, rheological behaviors, and phase morphologies of high-toughness PLA/PBAT blends by in-situ reactive compatibilization," *Compos. Part B Eng.*, vol. 173, p. 107028, 2019, doi: <https://doi.org/10.1016/j.compositesb.2019.107028>.
- [104] N. T. Kilic, B. N. Can, M. Kodal, and G. Ozkoc, "Compatibilization of PLA/PBAT blends by using Epoxy-POSS," *J. Appl. Polym. Sci.*, vol. 136, p. 47217, 2019, doi: <https://doi.org/10.1002/app.47217>.
- [105] Y. Ding, B. Lu, P. Wang, G. Wang, and J. Ji, "PLA-PBAT-PLA tri-block copolymers: Effective compatibilizers for promotion of the mechanical and rheological properties of PLA/PBAT blends," *Polym. Degrad. Stab.*, vol. 147, pp. 41–48, 2018, doi: <https://doi.org/10.1016/j.polymdegradstab.2017.11.012>.
- [106] R. Al-Itry, K. Lamnawar, and A. Maazouz, "Improvement of thermal stability, rheological and mechanical properties of PLA, PBAT and their blends by reactive extrusion with functionalized epoxy," *Polym. Degrad. Stab.*, vol. 97, pp. 1898–1914, 2012, doi: <https://doi.org/10.1016/j.polymdegradstab.2012.06.028>.
- [107] M. Nofar, M. C. Heuzey, P. J. Carreau, M. R. Kamal, and J. Randall, "Coalescence in PLA-PBAT blends under shear flow: Effects of blend preparation and PLA molecular weight," *J. Rheol. (N. Y. N. Y.)*, vol. 60, pp. 637–648, 2016, doi: 10.1122/1.4953446.
- [108] N. Wu and H. Zhang, "Mechanical properties and phase morphology of super-tough PLA/PBAT/EMA-GMA multicomponent blends," *Mater. Lett.*, vol. 192, pp. 17–20, 2017, doi: <https://doi.org/10.1016/j.matlet.2017.01.063>.
- [109] J. Chen, C. Rong, T. Lin, Y. Chen, J. Wu, J. You, H. Wang, and Y. Li, "Stable Co-Continuous PLA/PBAT Blends Compatibilized by Interfacial Stereocomplex Crystallites: Toward Full

Biodegradable Polymer Blends with Simultaneously Enhanced Mechanical Properties and Crystallization Rates,” *Macromolecules*, vol. 54, pp. 2852–2861, 2021, doi: 10.1021/acs.macromol.0c02861.

[110] S. Wang, L. Daelemans, D. R. D'hooge, L. Couck, W. Van Den Broeck, P. Cornillie, M. Gou, K. De Clerck, and L. Cardon, “Lifting the quality of fused filament fabrication of polylactic acid based composites,” *Compos. Part B Eng.*, vol. 210, p. 108613, 2021, doi: <https://doi.org/10.1016/j.compositesb.2021.108613>.

[111] N. A. I. Ayob, N. F. Mohammad Rawi, A. Abd Aziz, B. Azahari, and M. H. Mohamad Kassim, “The properties of 3D printed poly (lactic acid) (PLA)/poly (butylene-adipate-terephthalate) (PBAT) blend and oil palm empty fruit bunch (EFB) reinforced PLA/PBAT composites used in fused deposition modelling (FDM) 3D printing,” *Phys. Scien. Rev.*, 2022, doi:10.1515/psr-2022-0048.

[112] O. Çoban, M. Ö. Bora, T. Kutluk, and G. Özkoç, “Mechanical and thermal properties of volcanic particle filled PLA/PBAT composites,” *Polym. Compos.*, vol. 39, pp. E1500–E1511, 2018, doi: <https://doi.org/10.1002/pc.24393>.

[113] A. N. A. Izzati, W. C. John, M. R. N. Fazita, N. Najieha, A. A. Azniwati, and H. P. S. A. Khalil, “Effect of empty fruit bunches microcrystalline cellulose (MCC) on the thermal, mechanical and morphological properties of biodegradable poly (lactic acid) (PLA) and polybutylene adipate terephthalate (PBAT) composites,” *Mater. Res. Express*, vol. 7, p. 15336, 2020, doi: 10.1088/2053-1591/ab6889.

[114] A. Teamsinsungvon, Y. Ruksakulpiwat, and K. Jarukumjorn, “Preparation and Characterization of Poly(lactic acid)/Poly(butylene adipate-co-terephthalate) Blends and Their Composite,” *Polym. Plast. Technol. Eng.*, vol. 52, pp. 1362–1367, 2013, doi: 10.1080/03602559.2013.820746.

[115] C. N. Ludvik, G. M. Glenn, A. P. Klamczynski, and D. F. Wood, “Cellulose Fiber/Bentonite Clay/Biodegradable Thermoplastic Composites,” *J. Polym. Environ.*, vol. 15, pp. 251–257, 2007, doi: 10.1007/s10924-007-0072-5.

[116] W. Thongruang, R. J. Spontak, and C. M. Balik, “Bridged double percolation in conductive polymer composites: an electrical conductivity, morphology and mechanical property study,” *Polymer (Guildf.)*, vol. 43, pp. 3717–3725, 2002, doi: [https://doi.org/10.1016/S0032-3861\(02\)00180-5](https://doi.org/10.1016/S0032-3861(02)00180-5).

[117] R. Dweiri and J. Sahari, “RETRACTED: Microstructural image analysis and structure–electrical conductivity relationship of single- and multiple-filler conductive composites,” *Compos. Sci. Technol.*, vol. 68, pp. 1679–1687, 2008, doi: <https://doi.org/10.1016/j.compscitech.2008.02.006>.

[118] R. Taherian, M. J. Hadianfard, and A. N. Golikand, “A new equation for predicting electrical conductivity of carbon-filled polymer composites used for bipolar plates of fuel cells,” *J. Appl. Polym. Sci.*, vol. 128, pp. 1497–1509, 2013, doi: <https://doi.org/10.1002/app.38295>.

- [119] I. Balberg, "A comprehensive picture of the electrical phenomena in carbon black–polymer composites," *Carbon N. Y.*, vol. 40, pp. 139–143, 2002, doi: [https://doi.org/10.1016/S0008-6223\(01\)00164-6](https://doi.org/10.1016/S0008-6223(01)00164-6).
- [120] W.-Z. Cai, S.-T. Tu, and J.-M. Gong, "A Physically Based Percolation Model of the Effective Electrical Conductivity of Particle Filled Composites," *J. Compos. Mater.*, vol. 40, pp. 2131–2142, 2006, doi: [10.1177/0021998306062312](https://doi.org/10.1177/0021998306062312).
- [121] R. D. Chippendale and I. O. Golosnoy, "Percolation effects in electrical conductivity of Carbon Fibre Composites," in *IET 8th International Conference on Computation in Electromagnetics (CEM 2011)*, pp. 1–2, 2011, doi: [10.1049/cp.2011.0094](https://doi.org/10.1049/cp.2011.0094).
- [122] A. V Goncharenko and E. F. Venger, "Percolation threshold for Bruggeman composites," *Phys. Rev. E*, vol. 70, p. 57102, 2004, doi: [10.1103/PhysRevE.70.057102](https://doi.org/10.1103/PhysRevE.70.057102).
- [123] Y. R. Hernandez, A. Gryson, F. M., Blighe, M. Cadek, V. Nicolosi, W. J. Blau, Y. K. Gun'ko, and J. N. Coleman, "Comparison of carbon nanotubes and nanodisks as percolative fillers in electrically conductive composites," *Scr. Mater.*, vol. 58, pp. 69–72, 2008, doi: <https://doi.org/10.1016/j.scriptamat.2007.08.025>.
- [124] B. K. Kakati, V. K. Yamsani, K. S. Dhathathreyan, D. Sathiyamoorthy, and A. Verma, "The electrical conductivity of a composite bipolar plate for fuel cell applications," *Carbon N. Y.*, vol. 47, pp. 2413–2418, 2009, doi: <https://doi.org/10.1016/j.carbon.2009.04.034>.
- [125] J. M. Keith, J. A. King, and R. L. Barton, "Electrical conductivity modeling of carbon-filled liquid-crystalline polymer composites," *J. Appl. Polym. Sci.*, vol. 102, pp. 3293–3300, 2006, doi: <https://doi.org/10.1002/app.24748>.
- [126] F. Lux, "Models proposed to explain the electrical conductivity of mixtures made of conductive and insulating materials," *J. Mater. Sci.*, vol. 28, pp. 285–301, 1993, doi: [10.1007/BF00357799](https://doi.org/10.1007/BF00357799).
- [127] Y. P. Mamunya, V. V Davydenko, P. Pissis, and E. V Lebedev, "Electrical and thermal conductivity of polymers filled with metal powders," *Eur. Polym. J.*, vol. 38, pp. 1887–1897, 2002, doi: [https://doi.org/10.1016/S0014-3057\(02\)00064-2](https://doi.org/10.1016/S0014-3057(02)00064-2).
- [128] N. J. S. Sohi, S. Bhadra, and D. Khastgir, "The effect of different carbon fillers on the electrical conductivity of ethylene vinyl acetate copolymer-based composites and the applicability of different conductivity models," *Carbon N. Y.*, vol. 49, pp. 1349–1361, 2011, doi: <https://doi.org/10.1016/j.carbon.2010.12.001>.
- [129] K. Kalaitzidou, H. Fukushima, and L. T. Drzal, "A Route for Polymer Nanocomposites with Engineered Electrical Conductivity and Percolation Threshold," *Materials (Basel)*, vol. 3, pp. 1089–1103, 2010, doi: [10.3390/ma3021089](https://doi.org/10.3390/ma3021089).
- [130] C. Li, E. T. Thostenson, and T.-W. Chou, "Dominant role of tunneling resistance in the electrical conductivity of carbon nanotube–based composites," *Appl. Phys. Lett.*, vol. 91, p. 223114, 2007, doi: [10.1063/1.2819690](https://doi.org/10.1063/1.2819690).

- [131] S. M. Seyedi Ghezghapan and A. Javadi, "Effect of processing methods on electrical percolation and electromagnetic shielding of PC/MWCNTs nanocomposites," *Polym. Compos.*, vol. 38, pp. E269–E276, 2017, doi: <https://doi.org/10.1002/pc.24037>.
- [132] T. Khan, M. S. Irfan, M. Ali, Y. Dong, S. Ramakrishna, and R. Umer, "Insights to low electrical percolation thresholds of carbon-based polypropylene nanocomposites," *Carbon N. Y.*, vol. 176, pp. 602–631, 2021, doi: <https://doi.org/10.1016/j.carbon.2021.01.158>.
- [133] B. De Vivo, P. Lamberti, G. Spinelli, V. Tucci, L. Guadagno, and M. Raimondo, "The effect of filler aspect ratio on the electromagnetic properties of carbon-nanofibers reinforced composites," *J. Appl. Phys.*, vol. 118, 2015, doi: [10.1063/1.4928317](https://doi.org/10.1063/1.4928317).
- [134] R. M. Mutiso and K. I. Winey, "Electrical properties of polymer nanocomposites containing rod-like nanofillers," *Prog. Polym. Sci.*, vol. 40, pp. 63–84, 2015, doi: <https://doi.org/10.1016/j.progpolymsci.2014.06.002>.
- [135] J. Xu, W. Florkowski, R. Gerhardt, K. Moon, and C.-P. Wong, "Shear Modulated Percolation in Carbon Nanotube Composites," *J. Phys. Chem. B*, vol. 110, pp. 12289–12292, 2006, doi: [10.1021/jp061090i](https://doi.org/10.1021/jp061090i).
- [136] N. I. Lebovka, Y. Y. Tarasevich, N. V Vygornitskii, A. V Eserkepov, and R. K. Akhunzhanov, "Anisotropy in electrical conductivity of films of aligned intersecting conducting rods," *Phys. Rev. E*, vol. 98, p. 12104, 2018, doi: [10.1103/PhysRevE.98.012104](https://doi.org/10.1103/PhysRevE.98.012104).
- [137] T. N. Tallman and K. W. Wang, "The influence of nanofiller alignment on transverse percolation and conductivity," *Nanotechnology*, vol. 26, p. 25501, 2014, doi: [10.1088/0957-4484/26/2/025501](https://doi.org/10.1088/0957-4484/26/2/025501).
- [138] M. Sumita, K. Sakata, S. Asai, K. Miyasaka, and H. Nakagawa, "Dispersion of fillers and the electrical conductivity of polymer blends filled with carbon black," *Polym. Bull.*, vol. 25, pp. 265–271, 1991, doi: [10.1007/BF00310802](https://doi.org/10.1007/BF00310802).
- [139] S. Maiti, N. K. Shrivastava, and B. B. Khatua, "Reduction of percolation threshold through double percolation in melt-blended polycarbonate/acrylonitrile butadiene styrene/multiwall carbon nanotubes elastomer nanocomposites," *Polym. Compos.*, vol. 34, pp. 570–579, 2013, doi: <https://doi.org/10.1002/pc.22462>.
- [140] J. Huang, C. Mao, Y. Zhu, W. Jiang, and X. Yang, "Control of carbon nanotubes at the interface of a co-continuous immiscible polymer blend to fabricate conductive composites with ultralow percolation thresholds," *Carbon N. Y.*, vol. 73, pp. 267–274, 2014, doi: <https://doi.org/10.1016/j.carbon.2014.02.063>.
- [141] S. Bose, A. R. Bhattacharyya, A. P. Bondre, A. R. Kulkarni, and P. Pötschke, "Rheology, electrical conductivity, and the phase behavior of cocontinuous PA6/ABS blends with MWNT: Correlating the aspect ratio of MWNT with the percolation threshold," *J. Polym. Sci. Part B Polym. Phys.*, vol. 46, pp. 1619–1631, 2008, doi: <https://doi.org/10.1002/polb.21501>.
- [142] J. Chen, X. Cui, Y. Zhu, W. Jiang, and K. Sui, "Design of superior conductive polymer composite with precisely controlling carbon nanotubes at the interface of a co-continuous

polymer blend via a balance of  $\pi$ - $\pi$  interactions and dipole-dipole interactions,” *Carbon* N. Y., vol. 114, pp. 441–448, 2017, doi: <https://doi.org/10.1016/j.carbon.2016.12.048>.

[143] D. Strugova, J. C. Ferreira Junior, É. David, and N. R. Demarquette, “Ultra-Low Percolation Threshold Induced by Thermal Treatments in Co-Continuous Blend-Based PP/PS/MWCNTs Nanocomposites,” *Nanomaterials*, vol. 11, 2021, doi: 10.3390/nano11061620.

[144] J. Chen, X. Cui, K. Sui, Y. Zhu, and W. Jiang, “Balance the electrical properties and mechanical properties of carbon black filled immiscible polymer blends with a double percolation structure,” *Compos. Sci. Technol.*, vol. 140, pp. 99–105, 2017, doi: <https://doi.org/10.1016/j.compscitech.2016.12.029>.

[145] F. Gubbels, S. Blacher, E. Vanlathem, R. Jerome, R. Deltour, F. Brouers, and P. Teysse, “Design of Electrical Composites: Determining the Role of the Morphology on the Electrical Properties of Carbon Black Filled Polymer Blends,” *Macromolecules*, vol. 28, pp. 1559–1566, 1995, doi: 10.1021/ma00109a030.

[146] Y. Pan, X. Liu, X. Hao, Z. Starý, and D. W. Schubert, “Enhancing the electrical conductivity of carbon black-filled immiscible polymer blends by tuning the morphology,” *Eur. Polym. J.*, vol. 78, pp. 106–115, 2016, doi: <https://doi.org/10.1016/j.eurpolymj.2016.03.019>.

[147] Y. Luo, S.-Y. Xiong, F. Zhang, X.-X. He, X. Lu, and R.-T. Peng, “Preparation of conductive polylactic acid/high density polyethylene/carbon black composites with low percolation threshold by locating the carbon black at the Interface of co-continuous blends,” *J. Appl. Polym. Sci.*, vol. 138, p. 50291, 2021, doi: <https://doi.org/10.1002/app.50291>.

[148] X. Lu, B. Kang, and S. Shi, “Selective Localization of Carbon Black in Bio-Based Poly (Lactic Acid)/Recycled High-Density Polyethylene Co-Continuous Blends to Design Electrical Conductive Composites with a Low Percolation Threshold,” *Polymers (Basel)*, vol. 11, 2019, doi: 10.3390/polym111101583.

[149] C. Zhang, X. S. Yi, H. Yui, S. Asai, and M. Sumita, “Selective location and double percolation of short carbon fiber filled polymer blends: high-density polyethylene/isotactic polypropylene,” *Mater. Lett.*, vol. 36, pp. 186–190, 1998, doi: [https://doi.org/10.1016/S0167-577X\(98\)00023-8](https://doi.org/10.1016/S0167-577X(98)00023-8).

[150] C. Zhang, X.-S. Yi, H. Yui, S. Asai, and M. Sumita, “Morphology and electrical properties of short carbon fiber-filled polymer blends: High-density polyethylene/poly(methyl methacrylate),” *J. Appl. Polym. Sci.*, vol. 69, pp. 1813–1819, 1998, doi: [https://doi.org/10.1002/\(SICI\)1097-4628\(19980829\)69:9<1813::AID-APP16>3.0.CO;2-M](https://doi.org/10.1002/(SICI)1097-4628(19980829)69:9<1813::AID-APP16>3.0.CO;2-M).

[151] L. Bai, R. Sharma, X. Cheng, and C. W. Macosko, “Kinetic Control of Graphene Localization in Co-continuous Polymer Blends via Melt Compounding,” *Langmuir*, vol. 34, pp. 1073–1083, 2018, doi: 10.1021/acs.langmuir.7b03085.

[152] Y. Kou, A. T. Cote, J. Liu, X. Cheng, and C. W. Macosko, “Robust networks of interfacial localized graphene in cocontinuous polymer blends,” *J. Rheol. (N. Y. N. Y.)*, vol. 65, pp. 1139–1153, 2021, doi: 10.1122/8.0000294.

- [153] P. Blyweert, V. Nicolas, V. Fierro, and A. Celzard, "3D printing of carbon-based materials: A review," *Carbon* N. Y., vol. 183, pp. 449–485, 2021, doi: <https://doi.org/10.1016/j.carbon.2021.07.036>.
- [154] N. Vidakis, M. Petousis, E. Velidakis, N. Mountakis, P. E. Fischer-Griffiths, S. Grammatikos, and L. Tzounis, "Fused Filament Fabrication Three-Dimensional Printing Multi-Functional of Polylactic Acid/Carbon Black Nanocomposites," *C*, vol. 7, 2021, doi: 10.3390/c7030052.
- [155] O. Kaynan, A. Yıldız, Y. E. Bozkurt, E. Ozden Yenigun, and H. Cebeci, "Electrically conductive high-performance thermoplastic filaments for fused filament fabrication," *Compos. Struct.*, vol. 237, p. 111930, 2020, doi: <https://doi.org/10.1016/j.compstruct.2020.111930>.
- [156] N. Vidakis, M. Petousis, L. Tzounis, E. Velidakis, N. Mountakis, and S. A. Grammatikos, "Polyamide 12/Multiwalled Carbon Nanotube and Carbon Black Nanocomposites Manufactured by 3D Printing Fused Filament Fabrication: A Comparison of the Electrical, Thermoelectric, and Mechanical Properties," *C*, vol. 7, 2021, doi: 10.3390/c7020038.
- [157] J. Luo, H. Wang, D. Zuo, A. Ji, and Y. Liu, "Research on the Application of MWCNTs/PLA Composite Material in the Manufacturing of Conductive Composite Products in 3D Printing," *Micromachines*, vol. 9, 2018, doi: 10.3390/mi9120635.
- [158] H. Pei, L. Yang, Y. Xiong, Y. Chen, S. Shi, and J. Jing, "Fabrication, characterisation and properties of polyvinyl alcohol/graphene nanocomposite for fused filament fabrication processing," *Plast. Rubber Compos.*, vol. 50, pp. 263–275, 2021, doi: 10.1080/14658011.2020.1868668.
- [159] B. Podsiadły, P. Matuszewski, A. Skalski, and M. Słoma, "Carbon Nanotube-Based Composite Filaments for 3D Printing of Structural and Conductive Elements," *Appl. Sci.*, vol. 11, 2021, doi: 10.3390/app11031272.

# Chapter 2: Materials and methods implementation

## 1. Introduction

This chapter intends to introduce the various protocols that were used to select the relevant materials and the experimental procedures implemented in the following chapters. It consists of four sections and in each section, the following points are exposed:

- Objectives
- Materials and methods
- Results and their discussions

These optimization steps and the deduced information allowed us to clarify the orientation of the PhD work whose aim is to improve the electrical conductivity of PLA/PCL/GNP and PLA/PBAT/GNP nanocomposites implemented by additive manufacturing and especially the FFF process.

## 2. Properties of the different GNP grades

### 2.1. Objective

GNP which are composed of several layers of graphene are considered as attractive fillers to improve the properties of polymers owing to the abundance of naturally existing graphite as the source material for GNP [1-6]. The first part of this chapter aims to compare the properties of four GNP grades. The performance of these grades in the PLA matrix and PLA80/PCL20 matrix (whose choice will be justified) is analyzed in the following section.

### 2.2. Materials

Four grades of GNP (xGNP), namely M5, C300, C500, and C750 were purchased from XG Sciences (Lansing, Michigan) with increasing specific surface area, 120-150 m<sup>2</sup>.g<sup>-1</sup>,

300 m<sup>2</sup>.g<sup>-1</sup>, 500 m<sup>2</sup>.g<sup>-1</sup>, and 750 m<sup>2</sup>.g<sup>-1</sup> respectively. Information regarding the lateral dimension, thickness, and density of the different graphene grades are reported in table 3. In table 4 the characteristics of these grades are demonstrated.

Table 3 : The lateral dimension, thickness, and density of the different GNP grades

Samples	Lateral dimension (μm)	Thickness (nm)	Density (g.cm <sup>-3</sup> )
M5	5	6-8	2.2
C300	1-2	2	2-2.25
C500	1-2	2	2-2.25
C750	1-2	2	2-2.25

Table 4: The properties of the four GNP grades

GNP properties (all GNP grades)	Values
Carbon content (%)	>99.5
Thermal conductivity (W.m <sup>-1</sup> .K <sup>-1</sup> )	3000
Young's modulus (GPa)	1000
Tensile strength (GPa)	5
Electrical conductivity (S.m <sup>-1</sup> )	10 <sup>7</sup>

## 2.3. Characterizations

### 2.3.1. Scanning electron microscopy (SEM)

A scanning electron microscope (FEI Quanta 200 SEM, Fisher Thermo Scientific, Pittsburgh, US) equipment (figure 39), operating at 10 kV, was employed to analyse the microstructure of the different GNP grades. Using an OXFORD SDD 80 mm<sup>2</sup> (Silicon Drive Detector) instrument, Energy Dispersive X-Ray quantitative analysis (EDX) was carried out to measure the elemental composition of the C-GNP grades surfaces.



Figure 39: SEM FEI Quanta 200 FEG (Fisher Thermo Scientific) machine

### 2.3.2. X-ray diffraction (XRD)

The crystalline structure of the different GNP grades was analysed using an X-ray diffractometer BRUKER D8 Advance (figure 40). The XRD patterns were obtained at room temperature with an X-ray beam of known wavelength produced by a copper anode ( $\lambda$  (K $\alpha$ ) = 1.54 Å) and a scanning angle ( $2\theta$ ) which varies between 5 ° and 70 °.



Figure 40: X-ray BRUKER D8 Advance diffractometer

### 2.3.3. Thermogravimetric analysis (TGA)

The thermal stability of the different GNP powders was determined by a SETSYS evolution equipment (Setaram, France, figure 41). Samples weighing around 10 mg were heated in oxidative atmosphere (40 ml.min<sup>-1</sup>) in alumina ceramic crucible from 30 °C to 1000 °C at a heating rate of 10 °C.min<sup>-1</sup>. The samples weight loss was recorded as function of temperature.



Figure 41: SETSYS evolution equipment Setaram TGA equipment

## 2.4. Results and discussion

### 2.4.1. SEM, XRD, and TGA

Figure 42 shows the SEM images of the four GNP grades. The average particle diameter decreases from M5 GNP (a) to C750 GNP (g). M5 GNP has the largest aspect ratio and a platelet structure with sharp edges (a and b). The aspect ratios of M5 GNP and C GNP are 833 and 19 respectively [7]. Regarding the C grades, with the increase of the surface area, the particle geometry changes from a platelet or lamellar like (C300 and C500 GNP, images c-f) to a spherical like (C750 GNP, images g and h). In other words, the C-GNP, with high surface area resembles relatively to a low aspect ratio particulate rather than a platelet structure [7]. Small GNP tend to form aggregates (g and h) while large GNP reveal more individual flakes (a and b) [8].

Figure 43 demonstrates the EDX graphs of the three C grades. Carbon and oxygen are the main elements detected on the surface of these nanoplatelets. The oxygen content increase is directly proportional to the surface area of these grades. It increases from C300 GNP (a) to C750 GNP (c). This is in agreement with the XPS data provided by the manufacturer (figure 44) [9]. In this figure, the percentage of oxygen on the surface of M5 GNP is less than 1 %. The increase of the oxygen content seems to be inversely proportional to the average particle size. This can be due to the increase of the number of particles, with the decrease of their size, and consequently there will be more oxygen functional groups. The XPS spectra analysis of M5 GNP and C750 GNP was carried out by Wang et al. [10]. They used this technique to quantify and identify the different types of atoms present on the surface of the GNP and to identify the chemical bonds. Their results agreed with the manufacturer results where the C750 GNP had oxygen content at least two times greater than that present on the M5 GNP surface. Moreover, the oxygen functional groups existing on both GNP grades surfaces are: epoxide, carboxyl, and hydroxide. The higher concentration of oxygen on the C750 GNP surface can be due to the larger proportion of edges in this sample because of its smaller particle diameter or size. These authors also did Raman analysis of both grades and they concluded that M5 GNP possesses  $sp^2$  bonding between its carbon atoms, thus indicating non defective surface and well-ordered structure. However, this is not the case for the

C750 GNP which has greater degree of disorder caused by its smaller particles and the greater oxygen number containing functional groups on its surface and edges.

The XRD spectra of the different GNP grades measured in the range of  $2\theta$  from  $5^\circ$  to  $70^\circ$  are shown in figure 45. The hexagonal crystal structure of all GNP grades with no impurity or second-phase peaks is shown by the characteristic diffraction peaks indexed as (002), (111), and (004) planes [11][12]. Except C750, all the GNP grades possess intense carbon typical peak corresponding to planes matching the crystallographic plane of graphite at  $2\theta = 25^\circ$  [13-16]. Um et al. [17] calculated the number of graphene layers in the M5 GNP and C750 GNP and found that each M5 GNP has 58 graphene layers whereas each C750 GNP has 13 graphene layers. These authors concluded that the lower number of graphene layers is the reason behind its low and broad graphite peak at  $2\theta = 25^\circ$ . It has been mentioned that as the intensity of the carbon peak increases, the carbon nanofiller would have greater crystallinity and more ordered crystalline structure [18][19]. In this case, the graphite peak intensity decreases with the decrease of the graphene average particle size which indicates that the crystallinity of the GNP is higher for the larger aspect ratio GNP. Similar results were obtained by Gao et al. [8] who compared between the XRD spectra of XG Sciences M15 GNP grade (average particle diameter of  $15 \mu\text{m}$ ) and XG Sciences C750 GNP grade.

Table 5 and figure 46 exhibit the TGA data of the different GNP grades after tests performed in oxidative atmosphere. M5 GNP DTG curves shows two thermal degradation steps ( $450^\circ\text{C}$  and  $693^\circ\text{C}$ ) on the contrary of the C grades that possess only one degradation step.

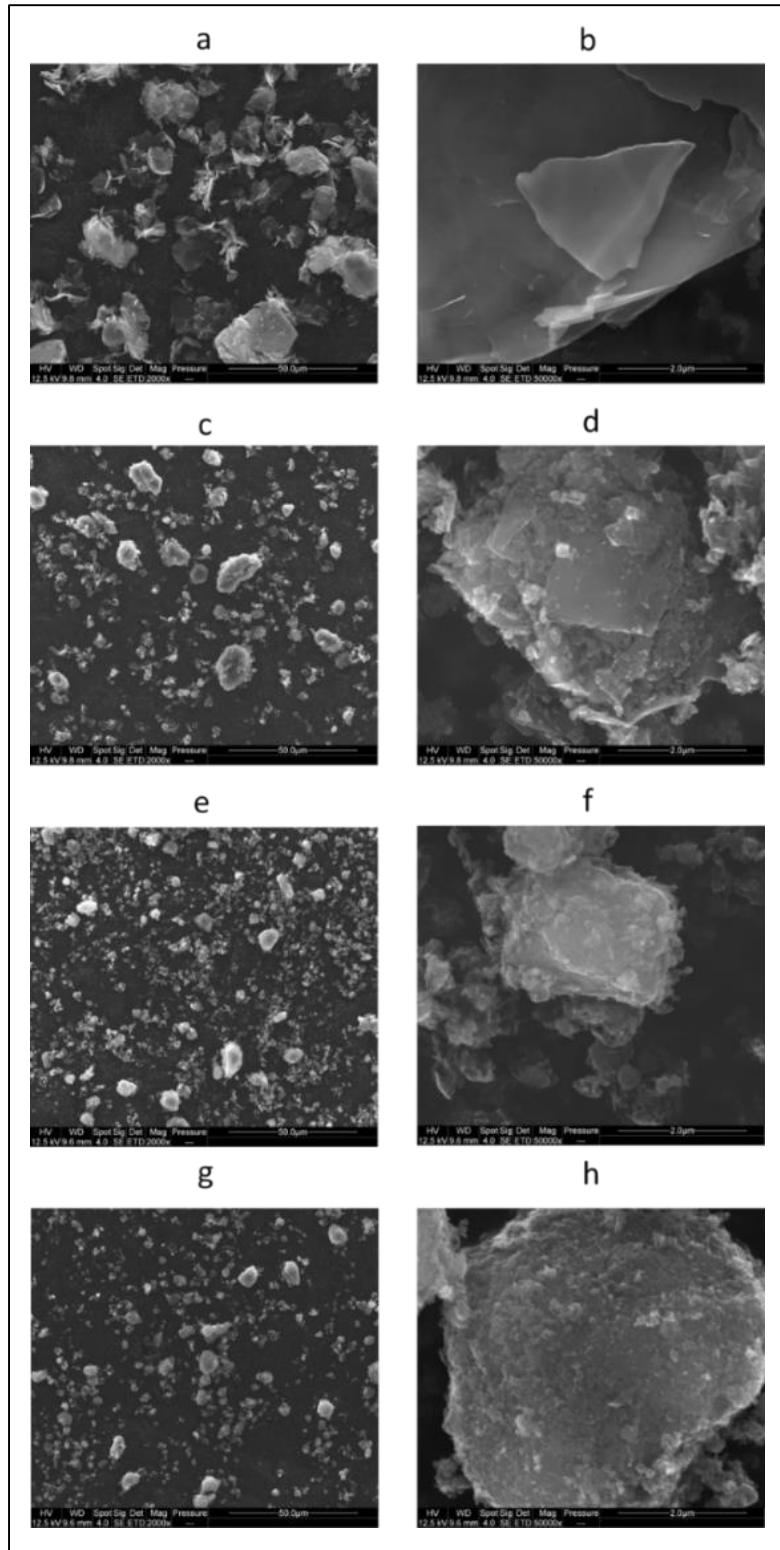


Figure 42: SEM images at two different magnifications of the different GNP grades, (a,b) M5 GNP, (c,d) C300 GNP, (e,f) C500 GNP, and (g,h) C750 GNP

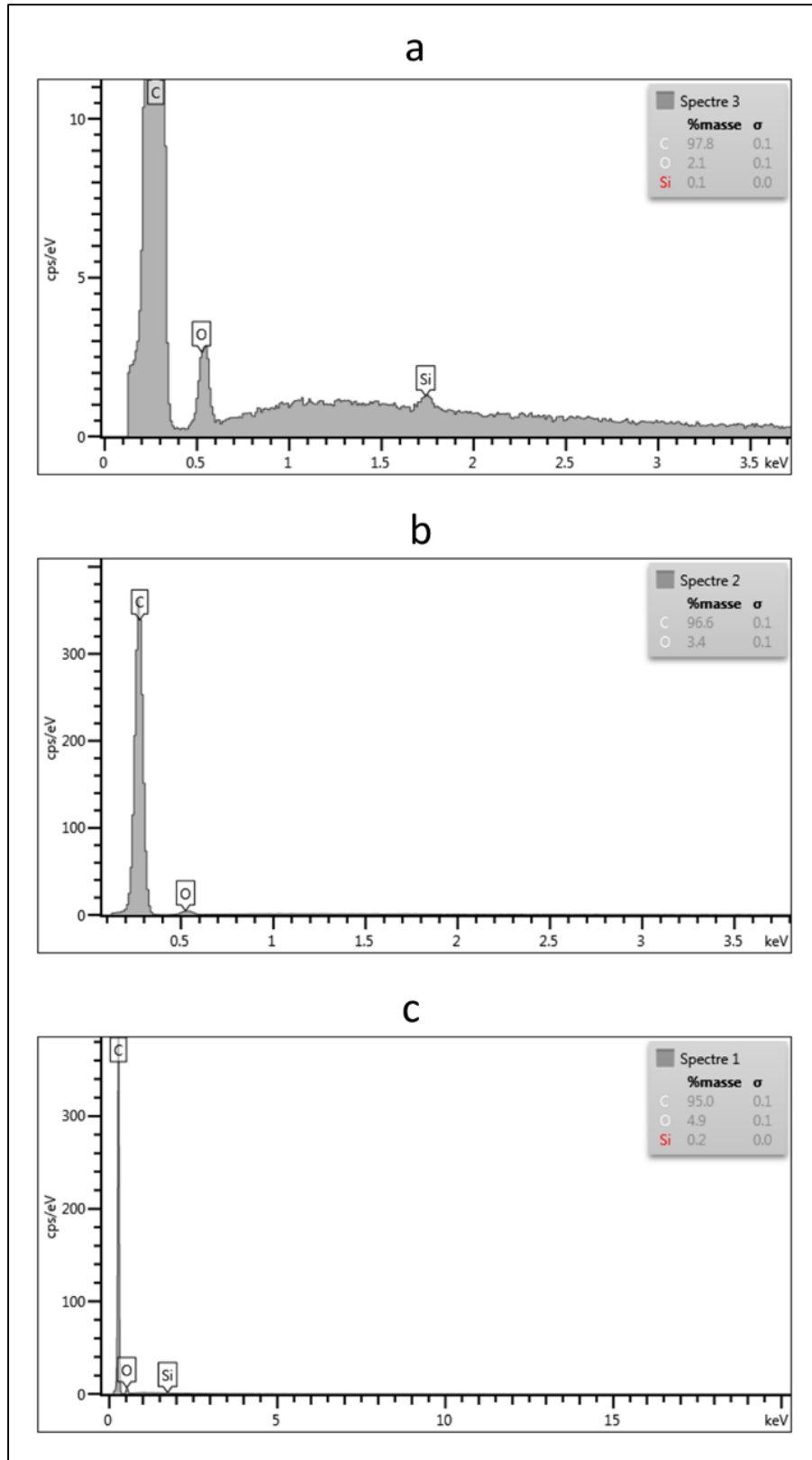


Figure 43: EDX graphs of the different C-GNP grades, (a) C300 GNP, (b) C500 GNP, and (c) C750 GNP

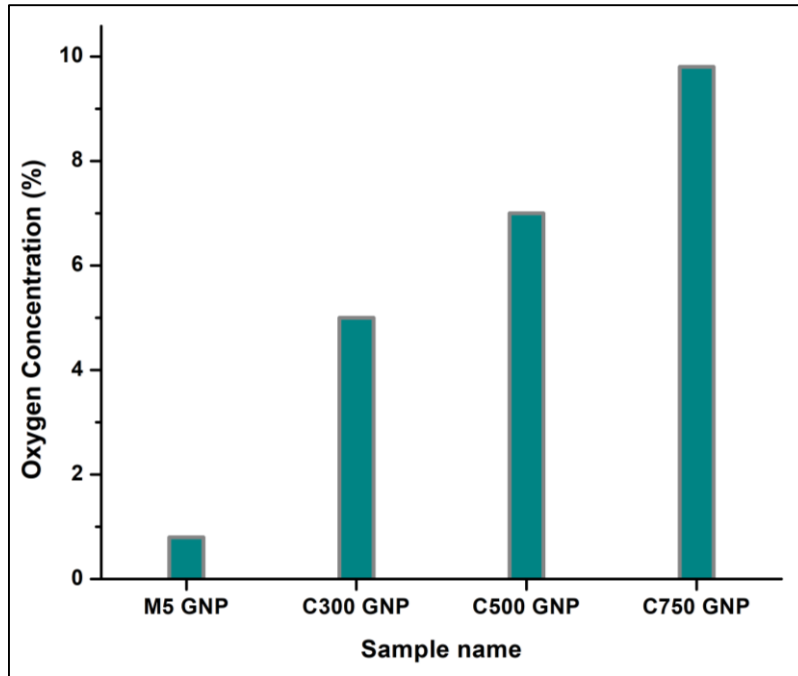


Figure 44: XPS data of the oxygen content of each GNP grade (readapted from the manufacturer data [9])

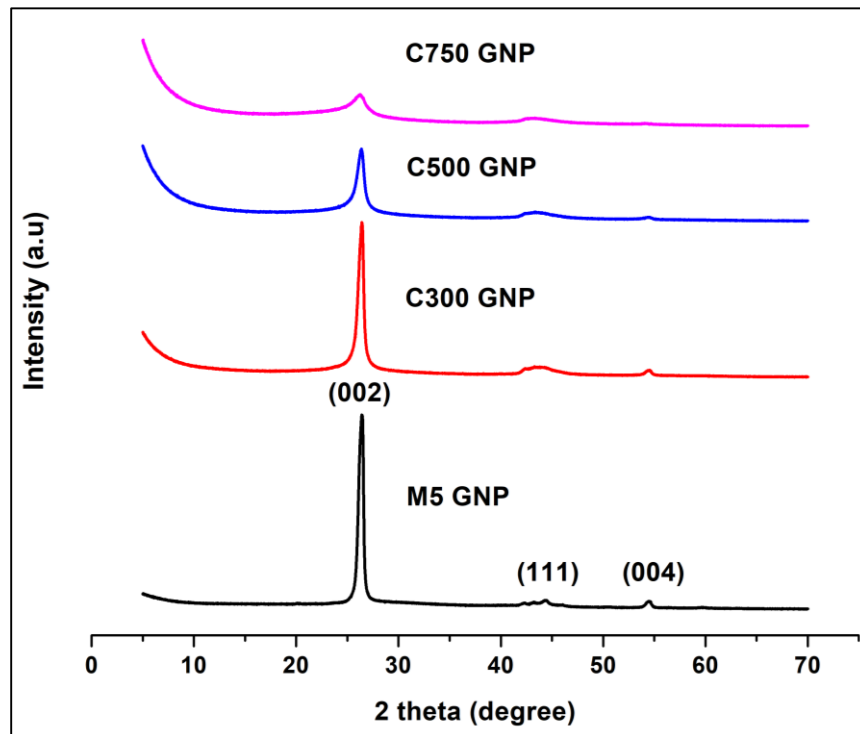
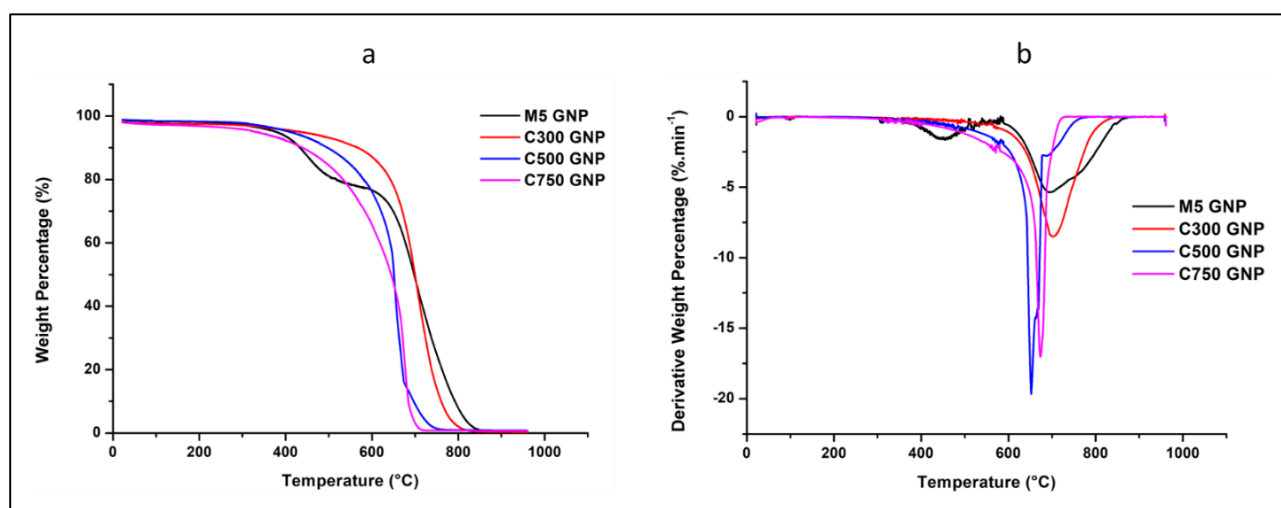


Figure 45: XRD curves of the four GNP grades

Table 5: TGA data of the different GNP grades (under O<sub>2</sub> atmosphere)

GNP Grade	Mass Loss (%)	Degradation Temperature (°C)	Onset Temperature (°C)
M5	98	450, 693	465
C300	97	701	616
C500	98	652	547
C750	97	673	495

Figure 46: TGA (a) and DTG (b) curves of the different GNP grades under O<sub>2</sub> atmosphere

### 3. GNP grades interaction with the PLA matrix

#### 3.1. Objective

This second section aims to evaluate the electrical and mechanical performance of the different GNP grades when melt blended with the PLA matrix. GNP were added at 1 wt.% and 3 wt.% for the twin-screw extruded blends. Moreover, the electrical percolation threshold of each GNP grade, where its content ranged between 3 wt.% and 20 wt.%, was determined for PLA composites prepared by solvent casting method.

## 3.2. Materials

The semi-crystalline PLA 2003D polymeric matrix used in this study is provided by NatureWorks (Minnetonka, USA). It is an extrusion grade [20] characterized by a density of  $1.24 \text{ g.cm}^{-3}$ , a glass transition temperature of  $60 \text{ }^\circ\text{C}$ , and a melting temperature of  $150 \text{ }^\circ\text{C}$ . Note that the twin-screw extrusion was used as the melt blending technique in all the PhD work.

## 3.3. Experimental procedure

### 3.3.1. Nanocomposites preparation

Each GNP grade (M5, C300, C500, and C750) was melt blended with the PLA matrix using a twin-screw extruder (BC21 Cleextral 900 mm length, Cleextral, Firminy, France) (figure 47) which possesses twelve heating zones ( $T_1= 50 \text{ }^\circ\text{C}$ ,  $T_{2,3,4}= 175 \text{ }^\circ\text{C}$ ,  $T_{\text{remaining zones}}= 180 \text{ }^\circ\text{C}$ ). For the preparation of 2 kg/formulation, a screw speed of 200 rpm and material flow rate of  $4 \text{ kg.h}^{-1}$  were used. The GNP were added at 1 wt.% and 3 wt.% in the PLA matrix (the addition of GNP and PLA, each using a feeder, was simultaneous during extrusion). The PLA pellets were vacuum dried at  $60 \text{ }^\circ\text{C}$  and the GNP grades were dried in a conventional oven at  $80 \text{ }^\circ\text{C}$  at least one night prior to the extrusion experiments.



Figure 47: BC21 Cleextral 900 mm twin-screw extruder

### 3.3.2. Solvent casting method

Solvent casting method [21] was used in this part to manufacture samples for the electrical measurements. Normally this preparation method leads to lower electrical percolation threshold

[22] as compared to the melt blending technique (used in all the PhD work) due to the higher degree of graphene dispersion [1][23]. This was already mentioned by Verdejo et al. [24] who collected the electrical percolation thresholds of graphene/polymer nanocomposites described in the literature to find that the processing strategy has a great influence on these threshold values. According to their results, the melt blending technique leads to greater threshold as compared to solvent mixing and in situ polymerization. Moreover, solvent casting was used since it enables to prepare a significant number of samples with small quantities while meeting the need to find the best GNP grade in terms of best electrical performance. The main steps of this method are shown in figure 48. At the end of this protocol, thin PLA/GNP films were obtained (thickness of 1 mm) from which rectangles of 25 mm × 5 mm were cut for the electrical resistance measurements. The percentage of each GNP grade was varied between 3 wt.% and 20 wt.% in the PLA matrix.

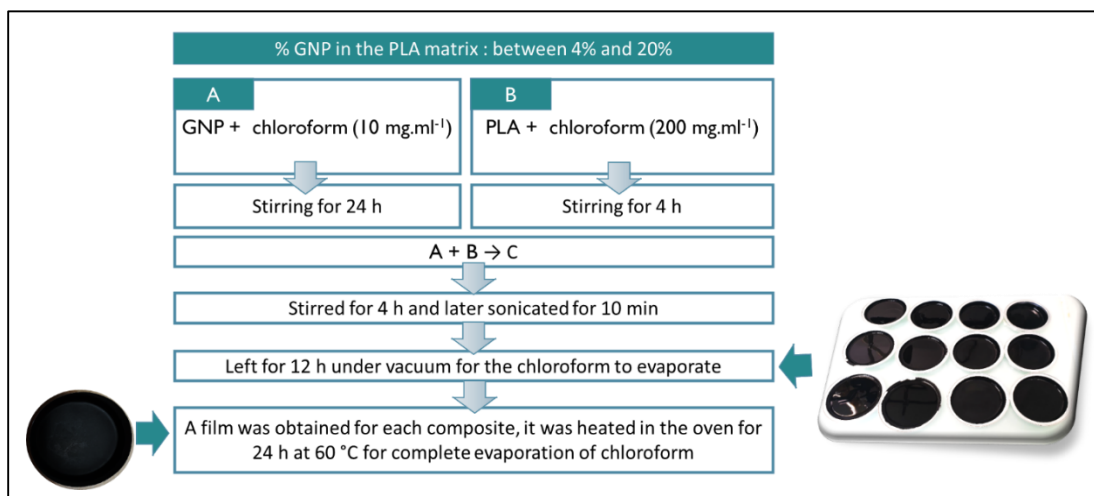


Figure 48: Scheme representing the different steps of solvent casting method

### 3.3.3. Injection moulding

Pure PLA and composite pellets were dried over night at 60 °C in compressed air Piovani dryers before injection moulding. A fraction of the twin-screw extruded pellets was injected with a 50 t KraussMaffei KM50-180CX injection moulding machine (Munich, Germany) (figure 49). The mould and barrel temperatures were set at 30 °C and 180 °C, respectively. The produced samples were ISO 527-2 standard (1A dumbbell samples) for tensile testing and 25 mm disks for the SEM and XRD investigations.



Figure 49: KraussMaffei injection moulding machine

### 3.3.4. Filament preparation for 3D Printing

Filaments of  $2.85 \pm 0.18$  mm calibrated diameter of dried pure PLA and composite pellets were produced using an Yvroud (Les Achards, France) line (figure 50) using the same processing temperature as that used during twin-screw extrusion. The production line consists of a single-screw extruder (H2528), a cooling bath (BAI-3000), a controlled pulling system (AR03-35), and a winding tool (CY600-1-SP).



Figure 50: Yvroud line

### 3.3.5. Fused filament fabrication (FFF)

The calibrated filaments of pure PLA and its composites previously produced were used to feed an A4v3 FFF printer (3ntr, Italy) (figure 51). For the aim of comparison, the printed samples were processed to meet the same geometry of the injection moulded ones using the following parameters:

- Nozzle diameter of 0.8 mm
- Infill percentage of 100 %
- Raster angle of +45 °/-45 °
- Printing speed of 40 mm.s<sup>-1</sup>
- Nozzle temperature of 185 °C
- Bed temperature of 60 °C



Figure 51: A4v3 FFF 3D printer

## 3.4. Characterizations

### 3.4.1. SEM

The SEM apparatus mentioned in section (I) was used to analyse the transversal section of the cryogenic fractured injection moulded composites. The objective of these observations is to evaluate the state of dispersion of each GNP grade in the PLA matrix. Before imaging, the surfaces were coated with a carbon layer in a vacuum chamber using 10 kV.

### 3.4.2. XRD

PLA pure polymer and PLA/3 wt.% GNP injection moulded disks were analysed by XRD (described in section (I)) to evaluate the exfoliation of GNP in each of these samples.

### 3.4.3. Porosity

The porosity ( $\phi$ ) of the 3D printed samples was evaluated by comparing their apparent and bulk densities. The apparent density of the samples ( $\rho_a$ ) was calculated from the ratio of their mass ( $m$ ) and their apparent volume ( $V_e$ ) measured by a digital calliper. The bulk density ( $\rho_b$ ) of each material was measured using an Ac-cuPyc 1330 (Micrometrics, Georgia, USA) helium pycnometer (figure 52). Specific printed samples, whose geometry perfectly fitted in the pycnometer sample chamber, were evaluated not to allow closed pores to be entrapped during manufacturing. Finally, the porosity was calculated using equation (1):

$$\phi = 1 - \frac{\rho_a}{\rho_b} = 1 - \frac{m}{\rho_b \times V_e} \quad (1)$$



Figure 52: Ac-cuPyc 1330 (Micrometrics) helium pycnometer

### 3.4.4. Tensile tests

Tensile tests of injected and 3D printed dumbbell samples were carried out using a ZwickRoell BZ2 (ZwickRoell, Ulm, Germany) device (figure 53) equipped with a 10 kN load cell. Young's modulus was determined at a crosshead speed of 1 mm.min<sup>-1</sup> using an extensometer. The tensile strength and elongation at break were determined at a cross-speed of 50 mm.min<sup>-1</sup>. At least five specimens of each formulation were tested to assess reproducibility.



Figure 53:Zwick Roell BZ2 machine

#### 3.4.5. Two-probes contact measurements of the solvent casted samples

The two-probes method was used to evaluate the resistance of the solvent casted samples. The two sample's extremities were painted with silver to improve the contact between the electrodes and the surface prior to measurements. The electrical percolation threshold was estimated to be the percentage of GNP at which the device starts to show values of resistance. When there were no values displayed, the sample was considered as insulator. Figure 54 shows the two-probes assembly.

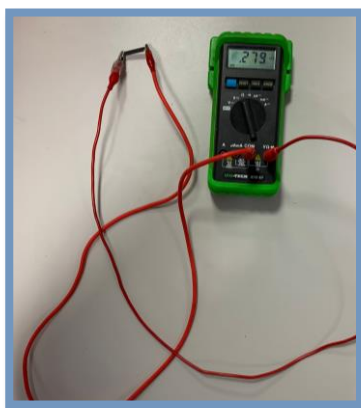


Figure 54: Two-probes electrical measurement assembly

## 4. Characterization of the selected materials

### 4.1. SEM

Carbon nanoparticles tend to form agglomerates and thus present dispersion challenges in the polymer matrices that mainly depend on the particle morphology, chemistry, size, and bulk density. In a work carried out by M. Santos et al. [25], a lower dispersion rate of GNP in the polypropylene matrix was observed for the GNP with larger surface area and higher bulk density. Wang et al. [10] obtained better dispersion of M5 GNP in the epoxy matrix when compared to the C750 GNP. They attributed this result to the greater surface area of the C750 GNP. But other research works reached to a contradictory conclusion regarding the effect of the GNP particle size on their dispersion state [17][26][27]. They found that the GNP size decrease leads to better dispersion in the polymer matrix. In a work performed by Muller et al., GNP with different morphologies (lamellar and compact) had almost the same dispersion state in the polycarbonate matrix after melt blending. In our work, at 1 wt.% of GNP (figure 55), we were not able to differentiate between the different GNP grades dispersion state in PLA. And all these GNP form some aggregates in the matrix (with greater C750 agglomerates size). At higher percentage of GNP (3 wt.%) (figure 56), the C750 GNP (18 c and d) seem to be more adhered with the matrix as compared to the larger GNP (M5 GNP) (18 a and b). This can be due to the greater oxygen content on the surface of C GNP (figure 44) that favoured better interactions with the matrix. In both figures (55 and 56), the M5 GNP were stacked on each other, whereas the C750 GNP were aggregated into ball like materials as it was also observed by Wang et al. [10]

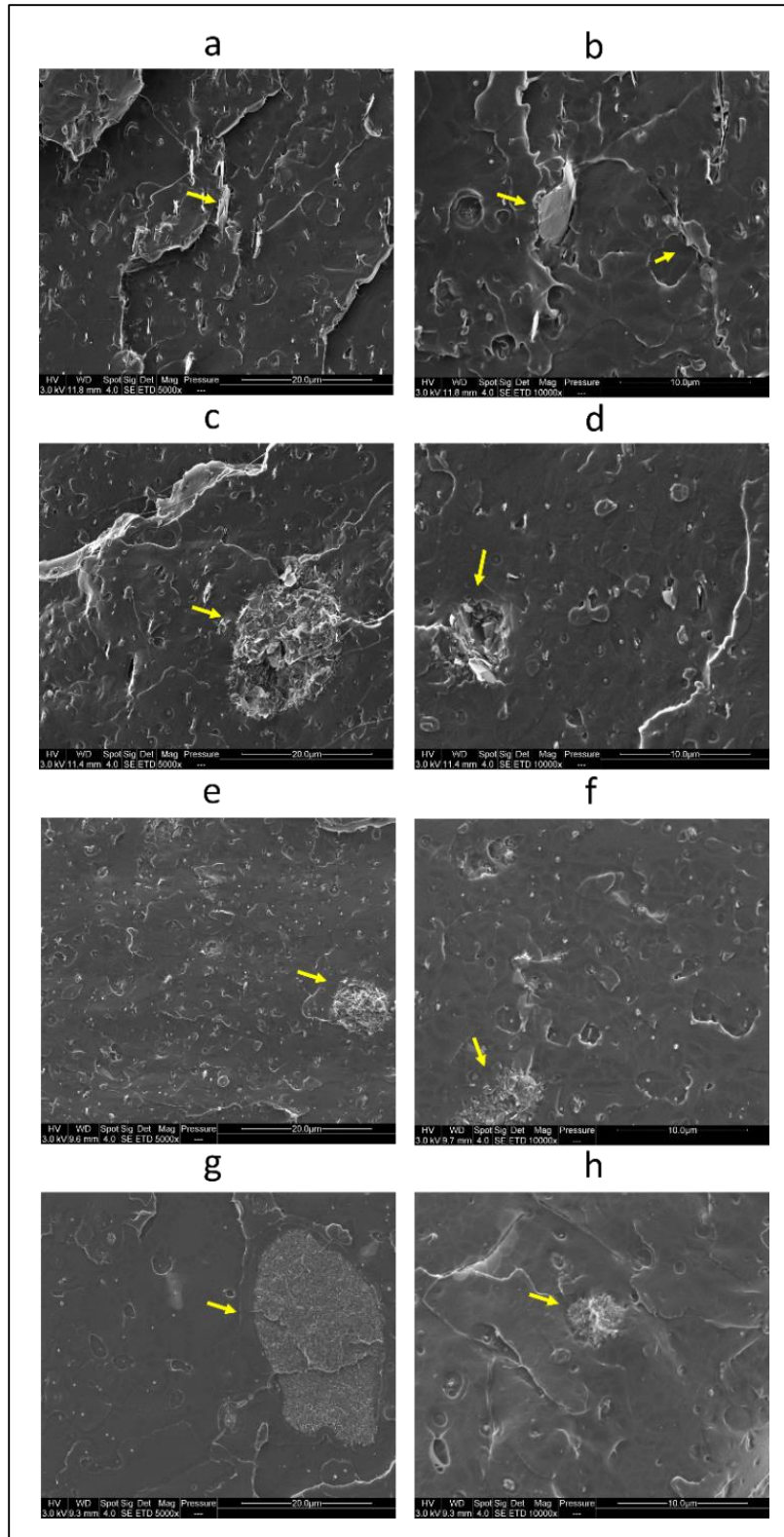


Figure 55: SEM images of PLA/1 wt.% GNP injection moulded composites at two different magnifications: (a,b) contain M5 GNP, (c,d) contain C300 GNP, (e,f) contain C500 GNP, and (g,h) contain C750 GNP (the yellow arrows indicate the GNP aggregates, all the shiny silver particles correspond to graphene)

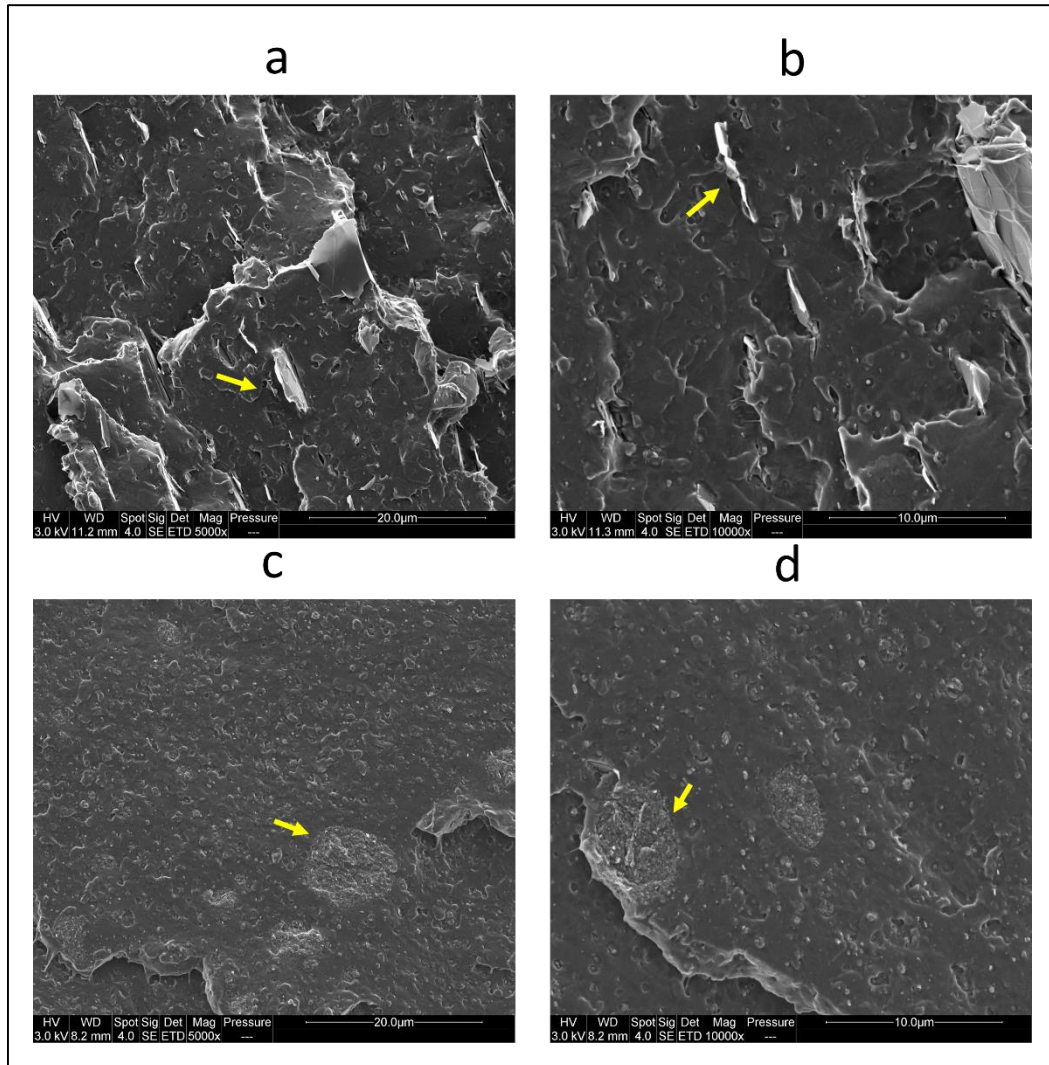


Figure 56: SEM images of PLA/3 wt.% GNP injection moulded composites at two different magnifications: (a,b) contain M5 GNP and (c,d) contain C750 GNP (the yellow arrows indicate the GNP aggregates or particles, all the shiny silver particles correspond to graphene)

## 4.2. XRD

Nanofillers are reported to act as nucleating agents in the nanocomposites [28] and only one nucleating site is required for the polymer to start its crystallization. The polymer chains align along the nanofiller surface and thus its crystallization behaviour is promoted [29]. The XRD spectra of pure PLA and PLA/3 wt.% GNP composites are presented in figure 57. The crystalline structure of pure PLA did not vary with the addition of GNP due to the lack of modification of its characteristic broad diffraction peak (110) at  $2\theta = 15^\circ$  [30]. The graphite peak at  $2\theta = 25^\circ$  is intense in all the PLA/GNP composites indicating the non-dispersion of the graphene nanoplatelets and

their presence in stacked form in the PLA matrix [19]. The PLA/C750 GNP composite is the only exception where this peak diminishes indicating the dispersion and the exfoliation of this GNP in the PLA matrix [30]. In the previous SEM images, there were some C750 GNP aggregates in the matrix, so the XRD and SEM results are not in total accordance. Ulm et al. [17] found similar XRD results that were justified by the better dispersion of this grade in a polyurethane (PU) matrix. This was due to the higher density of this grade and its fewer graphene layers as compared to other grades with lower density and greater average particle size.

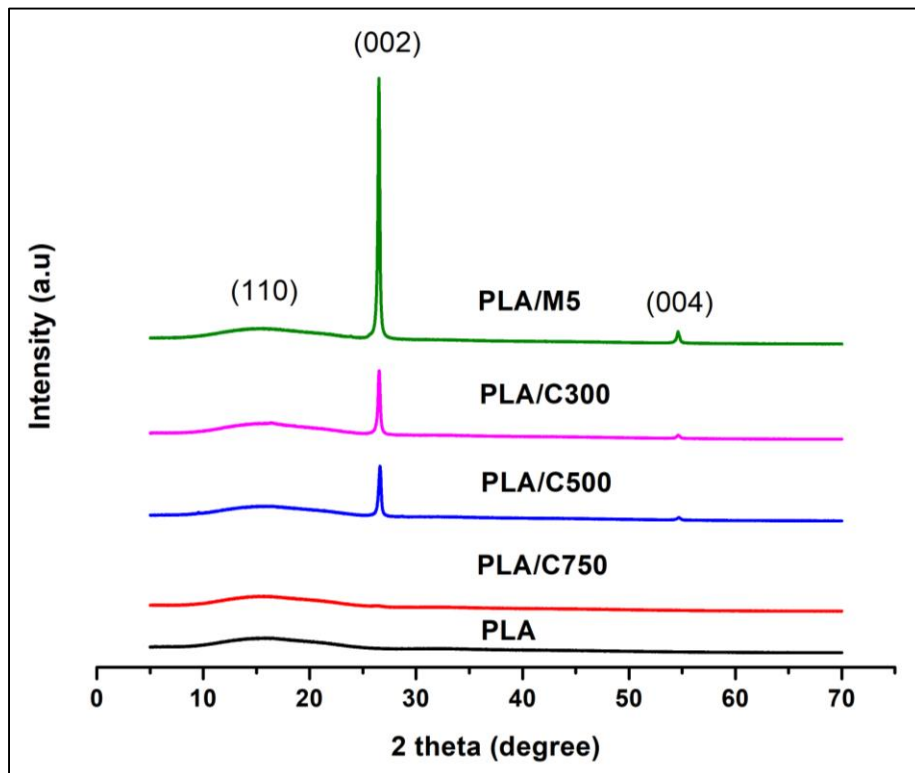


Figure 57: XRD graphs of PLA and PLA/3% GNP composites

### 4.3. Tensile properties of the injection moulded and 3D printed samples

The initial GNP characteristics have influence on the electrical, thermal, and mechanical properties of the composites and their applications. Tensile properties of injection moulded and 3D printed, pure PLA and their composites containing 1 wt.% and 3 wt.% of GNP, are presented in figures 58, 59 and 60. In table 6, the porosity values of the different 3D printed samples are presented and are lower than 10 %. Young's modulus results of the composites (figure 58) are comparable to these of pure PLA. PLA/3 wt.% M5 GNP sample is the only exception, where it has the greatest Young's modulus (greater by 900 MPa as compared to injection moulded pure PLA). The superior effect of larger particles (such as M5 GNP) in improving the modulus of the polymer matrix was observed by Chatterjee et al. [31]. According to them, larger aspect ratio of this grade is the reason behind this improvement. The aspect ratio importance is described by micromechanical models such as the Halpin-Tsai model [32], Mori-Tanaka model [33], and Shear Lag model [34][35]. These models illustrate that high aspect ratio fillers enable good load transfer from the matrix to the platelets, leading to higher modulus. Also based on the SEM images (figure 55), the C750 GNP agglomerations are larger when compared to M5 GNP and this contributed to lower modulus as it was also noticed by Wang et al. [10].

Table 6: The porosity values of 3D printed PLA polymer and its composites

3D printed samples	Porosity (%)
PLA	8.9 ± 2.3
PLA/1% M5	7.1 ± 0.3
PLA/3% M5	6.4 ± 1.1
PLA/1% C300	7.6 ± 0.5
PLA/3% C300	5.7 ± 0.3
PLA/1% C500	5.9 ± 0.3
PLA/3% C500	7.9 ± 1.3
PLA/1% C750	7.5 ± 0.6
PLA/3% C750	3.9 ± 2.2

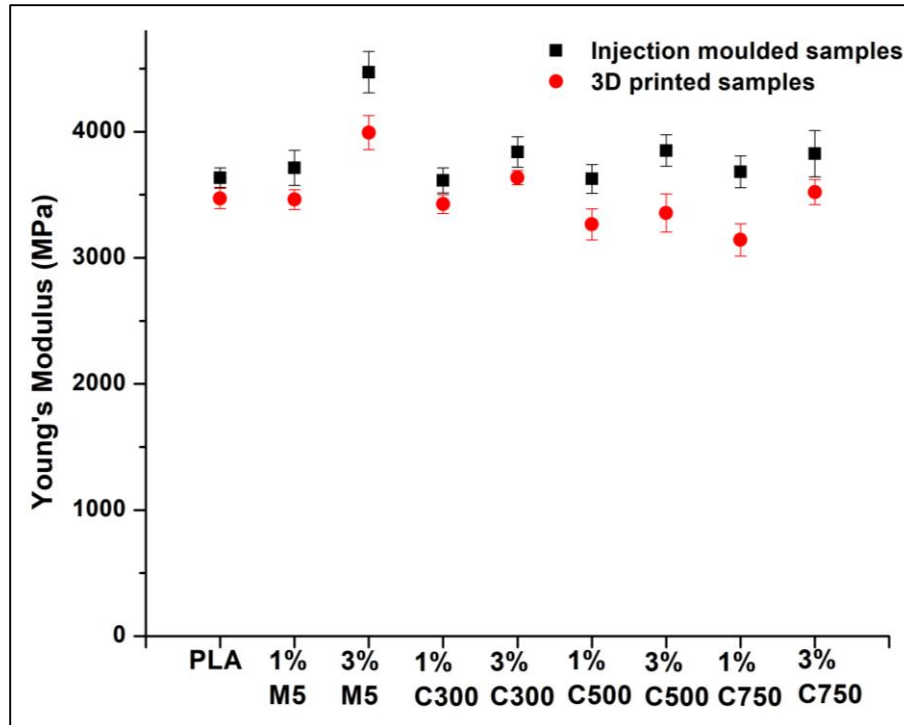


Figure 58: Young's modulus of injection moulded and 3D printed pure PLA and its composites

In figure 59, when comparing the composites with the pure polymer, there are no great differences between them. Yet, the C composites show slightly better tensile strength than the M5 GNP composites. According to Wang et al. [10], the incorporation of larger GNP reduced the tensile strength of the epoxy composites because of the weaker interfacial adhesion between the reinforcement and the polymer. Also, in our work the interfacial adhesion between M5 GNP and PLA seems to be worse than that between C GNP and PLA (figure 56). This might have resulted in stronger interfacial de-bonding between M5 GNP and PLA during the tensile tests. In other words, large M5 GNP flakes played the role of defects in the matrix and served as stress-concentration points. Thus, these composites failed earlier upon deformations to produce lower tensile strength. On the contrary to M5 GNP, the C grades have more oxygen-functional groups on their surface (figure 44) [10]. So, they will also aggregate through  $\pi$ - $\pi$  interactions but their agglomerates are more attached to the PLA matrix as compared to M5 GNP (figures 56) [36] [37][38].

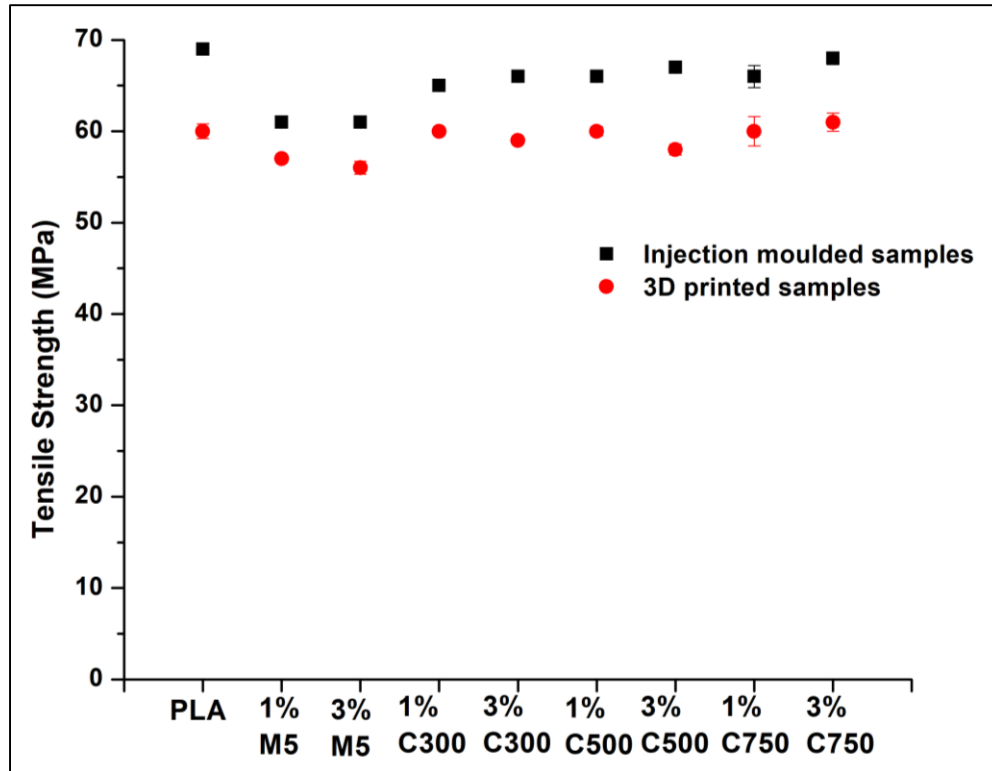


Figure 59: Tensile strength of injection moulded and 3D printed pure PLA and its composite

The ductility of GNP/polymer composites seems to be a more challenging task. So far, very little number of works succeeded to improve the ductility of these composites [39][40][41], and most of the works reported the deterioration of the ductility with the GNP addition [42-47]. In figure 60, the results of elongation at break are not improved in the case of the composites as compared to the pure PLA (whether injection moulded or 3D printed). Moreover, the injection moulded samples exhibited better tensile results in general as compared to the 3D printed ones (figures 58, 59, and 60) [48]. This can be due to the porosity and poor interlayer bonding between the deposited layers in the 3D printed samples that impacted their tensile properties [49][50].

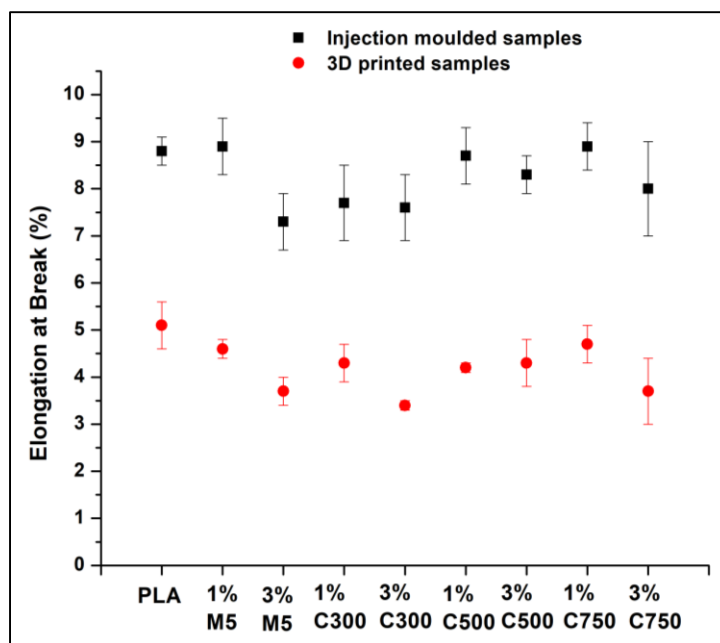


Figure 60: Elongation at break of injection moulded and 3D printed pure PLA and its composites

#### 4.4. Two-probes electrical resistance measurements and SEM observations

The applications of GNP in conductive polymer nanocomposites have received extensive attention. In this context, a great number of research works including GNP were published to improve the electrical properties of the polymer matrices [40][42][46][51-59]. The electrical performance of samples prepared by solvent casting (percentage of graphene up to 20 wt.% in the PLA matrix) was analysed. Hence, the electrical percolation thresholds of the different GNP grades are shown in table 7. M5 has the lowest percolation threshold that increases with the decrease of the aspect ratio of the GNP. The SEM images of some of these samples are demonstrated in figure 61. Figures a and b correspond to PLA/5 wt.% M5 GNP and PLA/10 wt.% M5 GNP solvent casted samples respectively. The comparison of these images with the ones of PLA/5wt.% C500 (c) and PLA/10 wt.% C500 (d) can explain the electrical results. The lower aspect ratio GNP like C500 GNP tend to agglomerate more in the PLA matrix at higher percentages and thus more GNP are needed to make the matrix electrically conductive. The aspect ratio is an important structural parameter of GNP that affects the formation of the conductive networks in the composites. And normally higher aspect ratio decreases the electrical percolation threshold [25][60-62].

Table 7: Electrical percolation thresholds of the PLA/GNP solvent casted samples (measured by two-probes method)

Sample	Electrical percolation threshold (wt.%)
PLA/M5	7
PLA/C300	14
PLA/C500	18
PLA/C750	>20

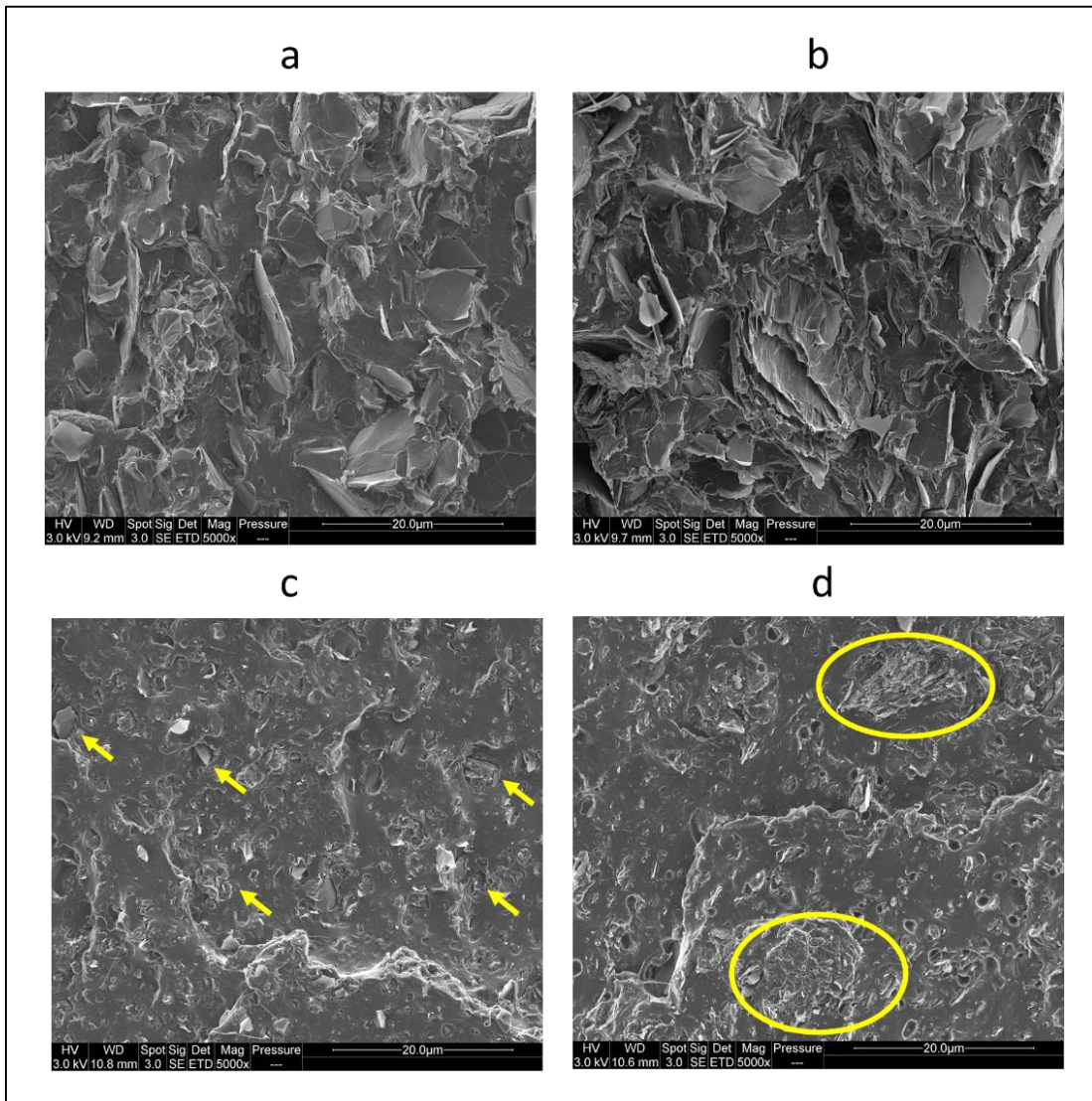


Figure 61: SEM images of PLA/5 wt.% M5 (a), PLA/10 wt.% M5 (b), PLA/5 wt.% C500 (c), and PLA/10 wt.% C500 (d) (the yellow indications show the GNP)

## 5. PLA/PCL ratio selection

### 5.1. Objective

In this section, samples containing different proportions of PLA and PCL were manufactured by injection moulding and 3D printing to select the more interesting blend composition that will be reinforced with the different GNP grades in the last section of this chapter. Moreover, in chapter 3 this proportion was taken into consideration.

### 5.2. Materials

The same PLA grade used in section II was used in this part. In addition to PLA, another polyester was used which is PCL (Capa™ 6800) purchased from Perstorp (Warrington, UK) and having the following characteristics: glass transition temperature of -60 °C, melting temperature of 60 °C, and MFR of 2.01-4.03 g/10 min (160 °C/5 kg).

### 5.3. Experimental procedure

#### 5.3.1. Nanocomposites preparation

After being vacuum dried at 60 °C and 40 °C respectively, PLA and PCL pellets were melt blended using a co-rotating Process 11 (Thermo Scientific, Massachusetts, USA) twin-screw extruder (figure 62). Different proportions of PLA (PLA content between 60 and 90 wt.%) and PCL were melt mixed to prepare pellets for the injection moulding and 3D printing experiments. The temperature profile of the twin-screw extruder was: 70 °C (feeder closest zone)-130 °C-190 °C (all the remaining zones) and the screw speed was 300 rpm. The total flow rate of the materials was 0.6 Kg.h<sup>-1</sup> and 250 g were prepared per formulation.



Figure 62: Process 11 twin-screw extruder

### 5.3.2. Injection moulding

Some of the extruded pellets were submitted to hot pressing in a mini-press Zamak Mercator (figure 63) to manufacture 25 mm disks for the SEM investigations. The parameters used were: oven temperature of 200 °C, mould temperature of 55 °C, pressure of 5 bars, and injection time of 5 s. The blends were dried at 50 °C in a vacuum oven before this step.

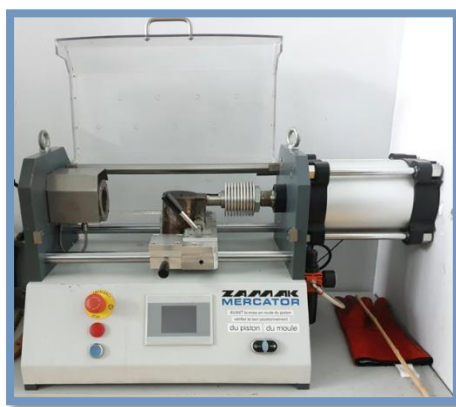


Figure 63: Mini-press Zamak Mercator

### 5.3.3. Filament preparation for 3D printing

Compounded blends were also used to feed a mini single-screw extruder (3devo, Utrecht, Netherlands) (figure 64) to obtain calibrated filaments (diameter of 2.85 mm). The parameters used in this step are: temperature increasing from 160 °C (first zone) to 190 °C (all the other zones) and screw speed of 5.2 rpm.



Figure 64: 3devo mini single-screw extruder

#### **5.3.4. FFF**

The same 3D printer as the one used in section (II) with the same printing parameters was implemented to prepare samples for the tensile tests (ISO 527 1BA) and the SEM investigations (disks of 25 mm diameter).

### **5.4. Characterizations**

#### **5.4.1. Porosity**

The porosity measurements and calculations for the 3D printed samples are described in section II.

#### **5.4.2. Tensile tests**

Tensile tests using the same equipment and parameters (as described in section II) were carried out on the 3D printed blends.

#### **5.4.3. SEM**

The same SEM equipment with the same conditions (as described in section II) was used to analyse the cryo-fractured surfaces of the 3D printed and injection moulded blends.

### **5.5. Blend selection and characterization**

#### **5.5.1. Porosity measurements, Tensile tests, and SEM**

As shown in table 8, 3D printed samples of the PLA/PCL blends containing PLA percentage up to 90 wt.% showed close porosity values which ranged between 4 and 7 %. The tensile properties of these samples are shown in figure 65. PLA80/PCL20 blend shows a compromise in terms of these properties as compared to the other blends. It has almost the same Young's modulus and tensile strength as compared to PLA90/PCL10 but its elongation at break is similar to that of PLA70/PCL30. Figures 66 and 67 show the SEM images of injection moulded and 3D printed PLA80/PCL20 and PLA70/PCL30 respectively. The 3D printed PLA80/PCL20 blend (figure 66 b) shows an orientation of the PCL nodules which is not the case in the 3D printed PLA70/PCL30 blend (figure 67 b) when both are compared to the injection moulded blends (figures 66 a and

67 a) respectively. Therefore, PLA80/PCL20 blend was chosen to be mixed with the different GNP grades in the following section.

Table 8: Porosity results of the 3D printed PLA/PCL blends

Sample name (3D printed samples)	Porosity (%)
PLA60/PCL40	5 ± 0.3
PLA70/PCL30	6 ± 0.7
PLA80/PCL20	4 ± 0.9
PLA90/PCL10	7 ± 1.2

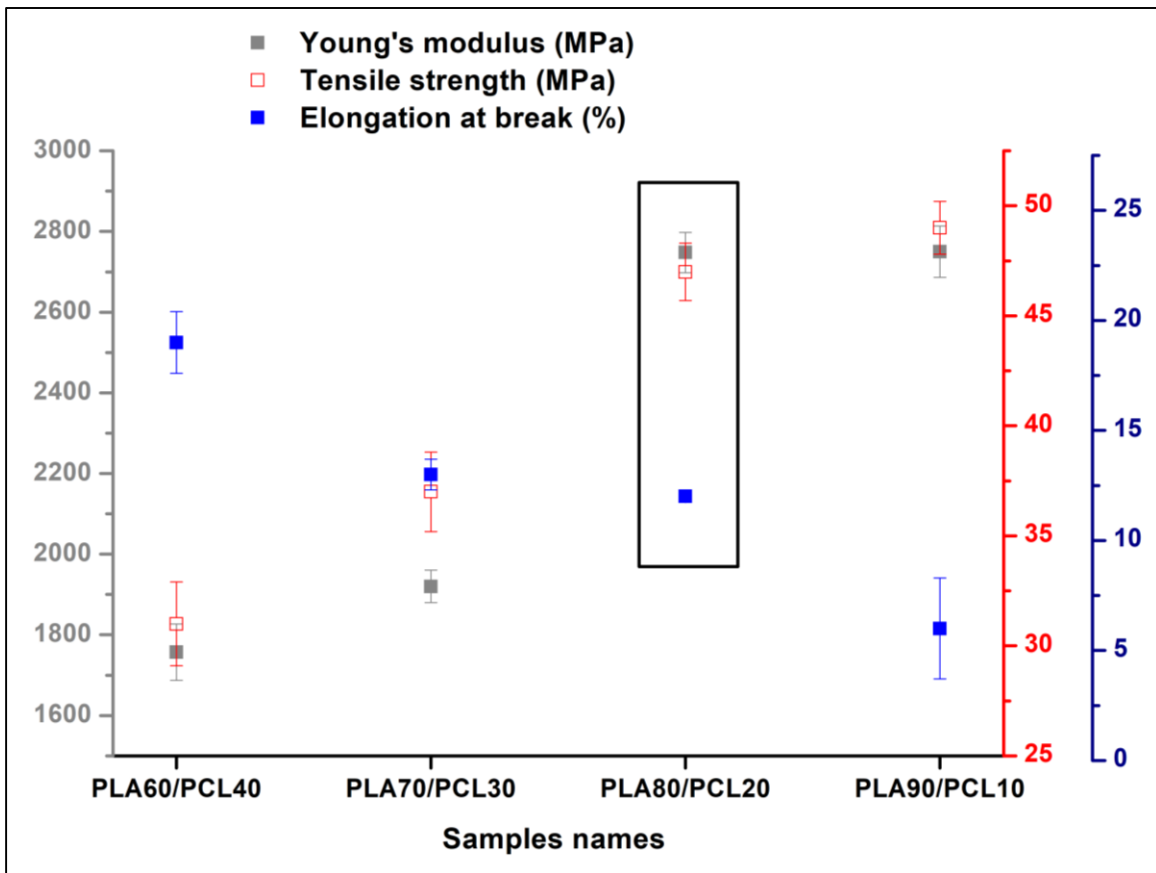


Figure 65: Tensile properties of 3D printed PLA/PCL blends

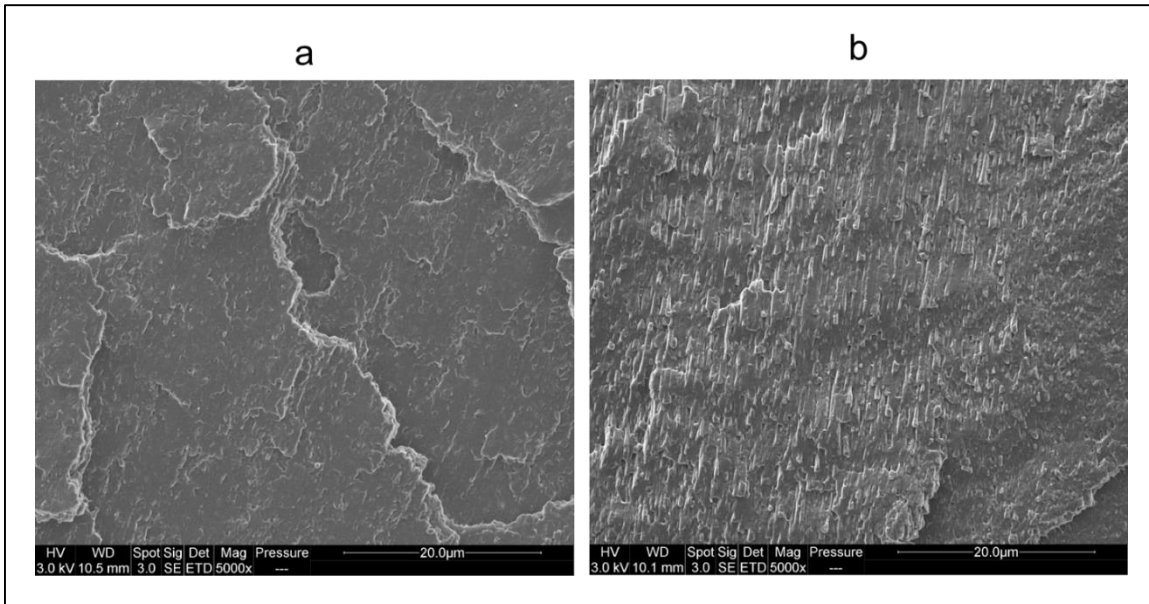


Figure 66: SEM images of injection moulded (a) and 3D printed (b) PLA80/PCL20 blends

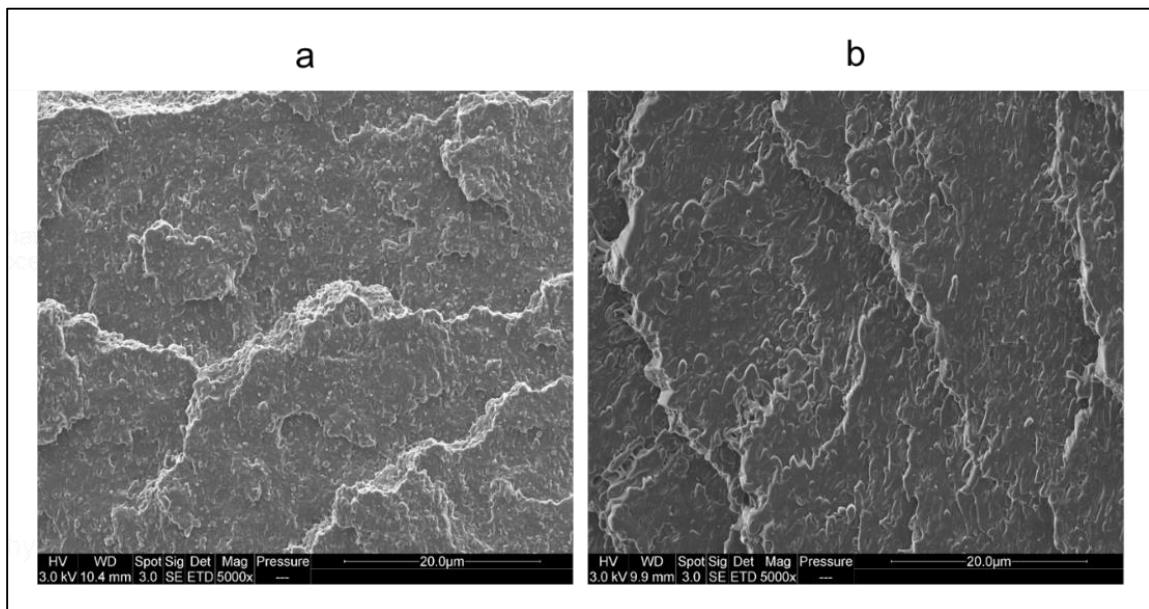


Figure 67: SEM images of injection moulded (a) and 3D printed (b) PLA70/PCL30 blends

## **6. Different GNP grades in PLA80/PCL20 blends**

### **6.1. Objective**

In the last section of this chapter, the different grades of GNP were added in the PLA80/PCL20 matrix. Injection moulded and 3D printed samples were characterized. At the end of this section, a conclusion will be stated regarding the GNP grade that gives the best mechanical, rheological, PLA percentage of crystallinity, and PCL thermal stability in PLA80/PCL20 blends. Therefore, this grade will be used throughout the whole PhD work.

### **6.2. Materials**

PLA, PCL, and the four GNP grades were used in this section (the detailed information related to them is discussed in sections I and II).

### **6.3. Experimental procedure**

#### ***6.3.1. Nanocomposites preparation***

The same extruder (section III) and the same parameters were applied to the blend and the composite components. Each GNP grade was added in the PLA80/PCL20 matrix at a fixed percentage of 10 wt.%.

#### ***6.3.2. Injection moulding***

Using the same machine and parameters (mentioned in section III), injection moulding experiments were carried out to obtain ISO 527 1BA dumbbell samples for the tensile tests.

#### ***6.3.3. Filament preparation***

Filaments for 3D printing were prepared using the same machine and parameters (section III).

#### ***6.3.4. FFF***

Using the same machine and parameters (sections II and III), ISO 5271BA tensile samples and disks (diameter of 25 mm) for the rheology tests were manufactured.

## 6.4. Characterizations

### 6.4.1. Differential scanning calorimetry (DSC)

Thermal analysis was performed by means of a PerkinElmer diamond (Massachusetts, USA) differential scanning calorimeter (DSC) (figure 68). The samples were sealed in aluminum pans (10 mg) and then heated from room temperature to 200 °C, held for 5 min to eliminate previous thermal history, cooled down to room temperature, and finally re-heated to 200 °C. A scanning rate of 10 °C.min<sup>-1</sup> was used in both heating steps and the cooling rate was chosen to be 1 °C.min<sup>-1</sup>. The crystallization temperature (T<sub>c</sub>) and melting temperature (T<sub>m</sub>) were determined. The degree of crystallinity of PLA in the samples (% X<sub>c</sub>) was determined based on Equation (2):

$$\%X_c = 100 \times \frac{\Delta H_m - \Delta H_c}{\Delta H_m^0 \cdot W} \quad (2)$$

Where,  $\Delta H_m^0$  is the enthalpy value of a pure crystalline PLA corresponding to 93.7 kJ.mol<sup>-1</sup> [63],  $\Delta H_m$  is the enthalpy of PLA related to the fusion process,  $\Delta H_c$  is the enthalpy of PLA related to the crystallization process, and W is the weight fraction of PLA in the blend and the composites.



Figure 68: Perkin-Elmer Diamond DSC device

### 6.4.2. PCFC

The thermal decomposition of samples at microscale of the different injection moulded and 3D printed nanocomposites was investigated using a Pyrolysis Combustion Flow Calorimeter (PCFC) (Fire Testing Technology, East Grinstead, UK) (figure 69). Samples (5 mg) were pyrolyzed at 1 °C.s<sup>-1</sup> under nitrogen flow from 90 to 750 °C (anaerobic pyrolysis – method A according to the standard ASTM D7309). Then, volatile thermal degradation products were swept from a pyrolysis chamber by an inert gas and combined with excess oxygen in a tubular furnace at flame temperatures to

force complete combustion. Heat release rate (HRR) which is the rate at which the fire releases energy was measured as function of temperature. This enabled the determination of the peak value of HRR as well as the Total Heat Release (THR, area below the HRR curve).



Figure 69: PCFC device

### 6.4.3. Rheology

The rheological measurements of the 3D printed disks were carried out with a rotational rheometer (MCR 702, Anton Paar, Graz, Austria) in oscillatory shear mode using a parallel-plate geometry (25 mm diameter) (figure 70) at 190 °C in the presence of nitrogen gas. First, thermal stability (time sweep) tests were performed and the results showed that all the samples were stable after 2 hours at 190 °C. Then, the upper limits of the viscoelastic range were determined by strain sweep tests at 200  $\text{rad}\cdot\text{s}^{-1}$ . Finally, frequency sweep tests were performed between 0.01 and 600  $\text{rad}\cdot\text{s}^{-1}$  at low strains (0.006- 10 %). Before these tests, the samples were vacuum dried at 50 °C during at least one night to avoid their degradation.



Figure 70: Rheometer (Anton Paar)

#### 6.4.4. Porosity

The porosity measurements and calculations concerning the 3D printed samples were previously described in sections II and III.

#### 6.4.5. Tensile tests

Tensile tests of injected and 3D printed samples were carried out using the same apparatus and parameters as described in sections II and III.

### 6.5. Results and discussion

#### 6.5.1. DSC

DSC was employed to measure the crystallinity of PLA in pure PLA, PLA/PCL blend, and PLA/PCL/10 wt.% GNP nanocomposites. The results obtained from the second heating step that was preceded by a cooling step ( $1\text{ }^{\circ}\text{C}\cdot\text{min}^{-1}$ ) of the injection moulded samples are shown in table 9 and figure 71. The degree of crystallinity of PLA was improved in the presence of both PCL and GNP which led to the appearance of the PLA crystallization peak due to their role as a nucleating agent for its crystallites [8][64-67]. Yet, the greatest improvement was in the presence of M5 GNP. The melting temperatures of both polymers were unaltered in the blend and the composites.

Table 9: DSC data of injection moulded pure polymers, their blend (PLA80/PCL20), and their composites (PLA80/PCL20/10 wt.% GNP)

Injection moulded samples	T <sub>m</sub> PLA (°C)	T <sub>m</sub> PCL (°C)	T <sub>c</sub> PLA (°C)	X <sub>c</sub> PLA (%)
PLA	151	-	-	0.3
PCL	-	59	-	-
PLA/PCL	151	59	129	1.9
PLA/PCL/M5	150	61	128	9.8
PLA/PCL/C300	153	59	129	4.5
PLA/PCL/C500	153	58	128	4.9
PLA/PCL/C750	152	56	128	3.4

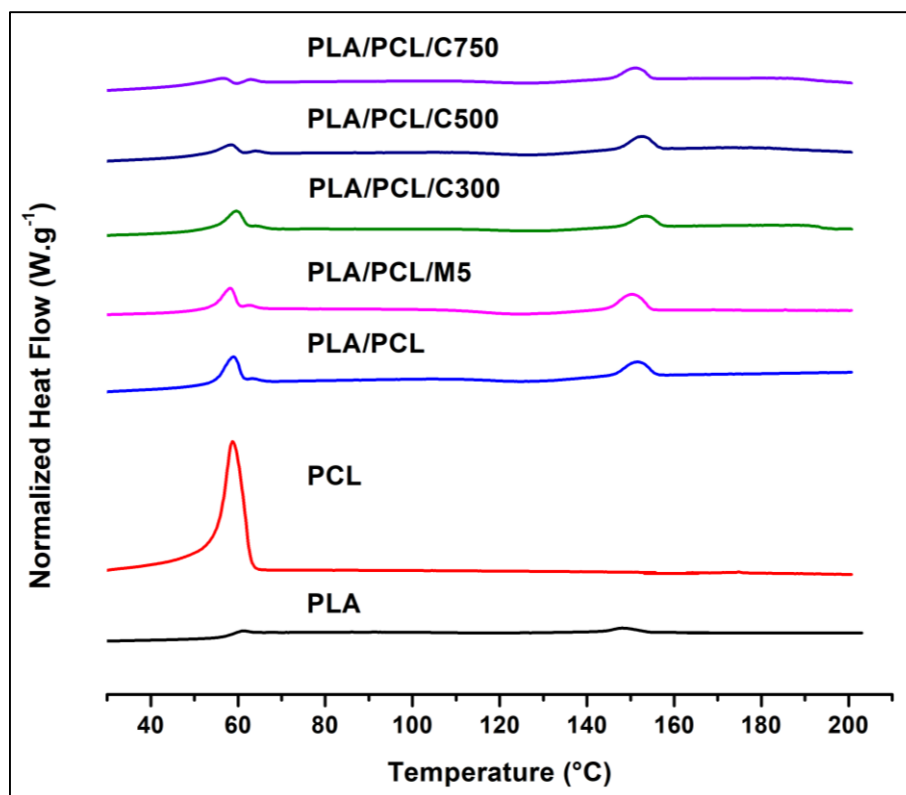


Figure 71: DSC curves of injection moulded pure polymers, their blend (PLA80/PCL20), and their composites (PLA80/PCL20/10 wt.% GNP)

Table 10 and figure 72 show the DSC features of the 3D printed samples that are close to the injection moulded ones (previously discussed). Also in this case, M5 GNP show the greatest enhancement in the degree of crystallinity of PLA.

Table 10: DSC data of 3D printed pure polymers, their blend, and their composites

3D printed samples	$T_m$ PLA (°C)	$T_m$ PCL (°C)	$T_c$ PLA (°C)	$X_c$ PLA (%)
PLA	149	-	-	0.8
PCL	-	60	-	-
PLA/PCL	151	58	125	1.4
PLA/PCL/M5	151	59	127	8.6
PLA/PCL/C300	152	60	130	3.8
PLA/PCL/C500	150	59	130	4.2
PLA/PCL/C750	150	59	129	3.5

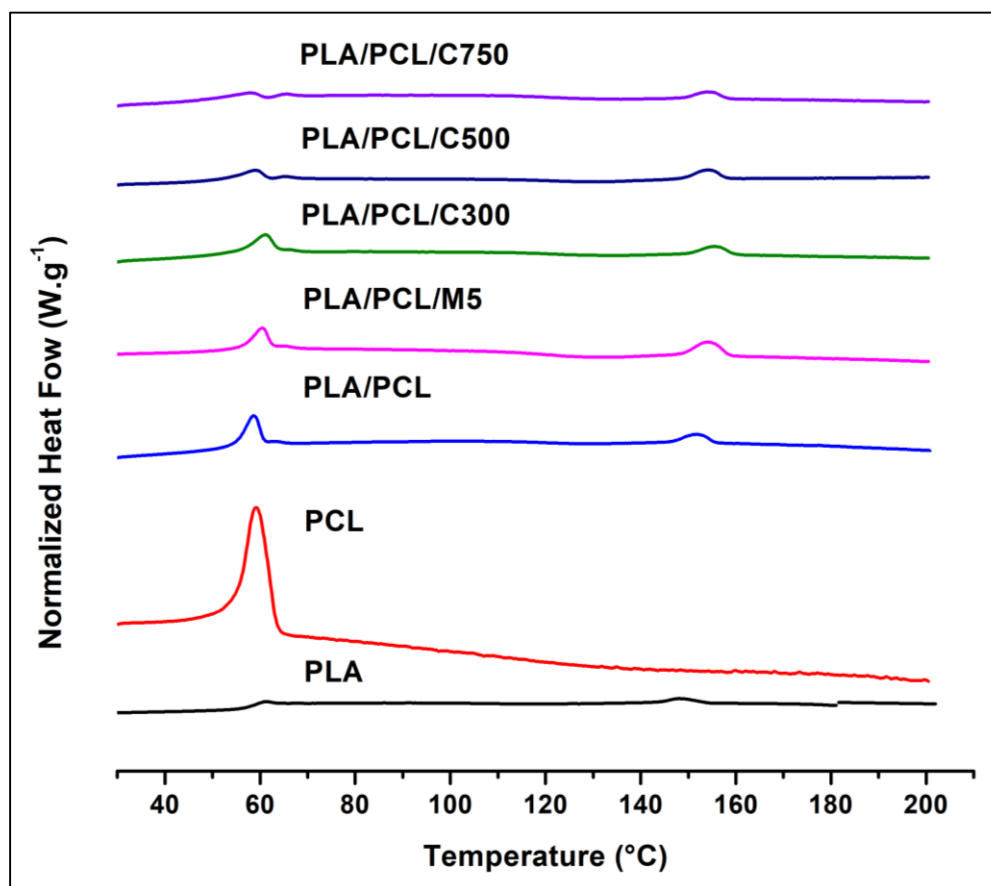


Figure 72: DSC curves of 3D printed pure polymers, their blend, and their composites

### 6.5.2. PCFC

The properties of nanofillers are critical for the improvement of the thermal stability. Several mechanisms have been proposed regarding the improvement of the thermal stability by GNP. First, the homogeneous dispersion of GNP enables them to act as efficient heat sinks. These sinks can extract more heat from the matrix and do not allow its oxidation at the early stages of the thermal degradation [57]. The second mechanism is summarized by the mass transfer barrier (shielding) effect against the volatile pyrolyzed polymer products caused by the homogeneous dispersion of GNP [47][68]. Finally, the interfacial polymer phases in the vicinity of graphene surfaces are restricted by the bonding with the GNP. This increases the energy needed for the decomposition and alters the ability of the degraded molecules to diffuse and evaporate [58][69].

In this context, the thermal stability of the composites was investigated by PCFC. The heat release rate curves of the injection moulded samples obtained from the PCFC tests are presented in table 11 and figure 73. The first peak between 370 °C and 390 °C corresponds to PLA. The other peak between 410 °C and 435 °C is relevant to PCL. PLA with C GNP nanoparticles exhibit lower HRR as compared to M5. However, this is the opposite case for C300 and C500 regarding HRR peaks corresponding to PCL. Normally, lower values of HRR and THR certify that graphene enhanced the flame retardancy of the composites. The reason suggested is the carbonisation reaction (charring) that could occur at the surface of the composites to hinder the heat transfer path and to reduce the concentration of the combustible gases [70]. The same thermal behaviour is observed for the 3D printed samples (table 12 and figure 74) to show that numerous processing steps did not modify the thermal degradation pathway of the PLA/PCL matrix.

*Table 11: PCFC data of injection moulded pure polymers, their blend (PLA80/PCL20), and their composites (PLA80/PCL20/10 wt.% GNP)*

Injection moulded samples	Total heat released (kJ.g <sup>-1</sup> )	PLA peak of HRR		PCL peak of HRR	
		W. g <sup>-1</sup>	°C	W. g <sup>-1</sup>	°C
PLA	17	458	387	-	-
PCL	26	-	-	580	434
PLA/PCL	19	377	390	125	432
PLA/PCL/M5	17	302	377	112	428
PLA/PCL/C300	17	260	376	149	416
PLA/PCL/C500	17	248	379	148	412
PLA/PCL/C750	17	284	384	127	417

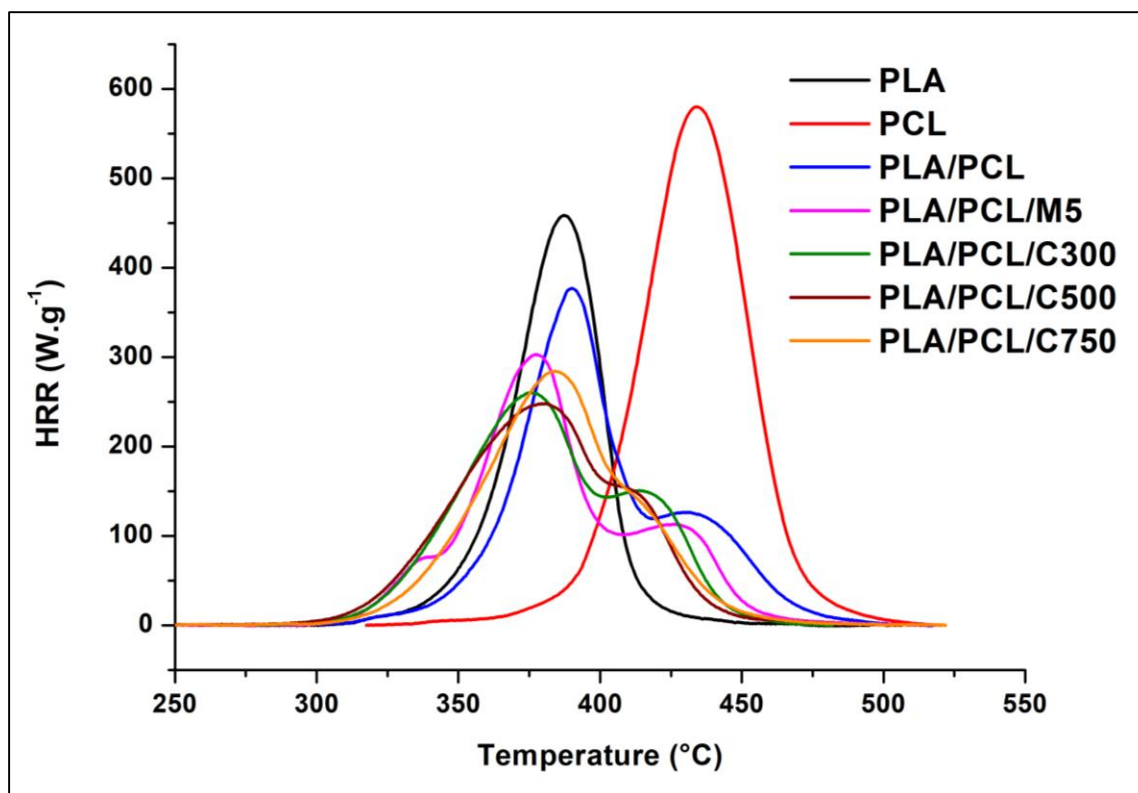


Figure 73: PCFC curves of injection moulded pure polymers, their blend (PLA80/PCL20), and their composites (PLA80/PCL20/10 wt.% GNP)

Table 12: PCFC data of 3D printed samples

3D printed samples	Total heat released ( $\text{kJ.g}^{-1}$ )	PLA peak of HRR		PCL peak of HRR	
		$\text{W.g}^{-1}$	$^{\circ}\text{C}$	$\text{W.g}^{-1}$	$^{\circ}\text{C}$
PLA	17	459	384	-	-
PCL	26	-	-	537	435
PLA/PCL	19	397	387	118	435
PLA/PCL/M5	17	313	377	100	428
PLA/PCL/C300	18	306	382	141	424
PLA/PCL/C500	17	280	382	133	419
PLA/PCL/C750	17	302	382	126	416

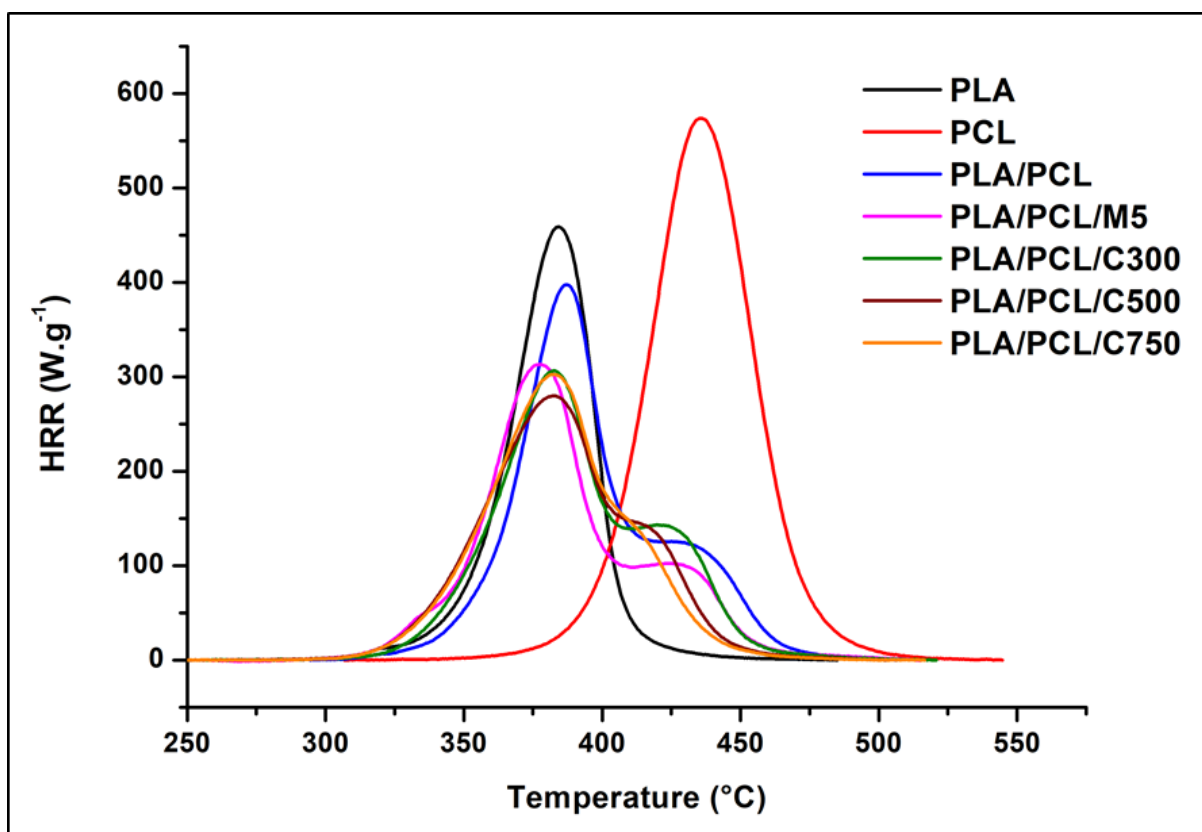


Figure 74: PCFC curves of 3D printed pure polymers, their blend, and their composites

### 6.5.3. Rheology

Rheological behaviour (complex viscosity and storage modulus) of polymer composites strongly depends on the formation and evolution of filler network structures in the polymer melt with the strain, time, and temperature. Normally, the increase of the GNP content leads to an increase in these parameters. For the pure polymers and their blend, the storage modulus is frequency dependent at low frequencies. As the loading of GNP increases, the GNP network will form step-by-step and the frequency dependent storage modulus at low frequency will finally diminish indicating a typical solid-like behaviour [71]. In this context, the liquid-solid transformation occurs at a certain GNP percentage called the rheological percolation threshold [71-74]. Simultaneously, the complex viscosity starts to show a shear thinning behaviour. This threshold depends on the aspect ratio of the fillers [3][71][75], their degree of dispersion, and their content. The rheological properties of the pure polymers, their blend, and 10 wt.% GNP composites are shown in figures 75 and 76. The complex viscosity was greater for all composites (and especially the M5 GNP composite) as compared to the pure polymers and the blend. The reason is the interactions

between GNP and PLA/PCL matrix that restricted the mobility of the chains close to or adsorbed on the GNP surface [76]. M5 GNP composite also possesses higher storage modulus (figure 76) when compared to the C GNP composites (in the low frequency region). In addition, the low frequency plateau is observed only for M5 GNP composite. This indicates that a strong graphene network is constructed only in this sample due to its greater aspect ratio [77-80].

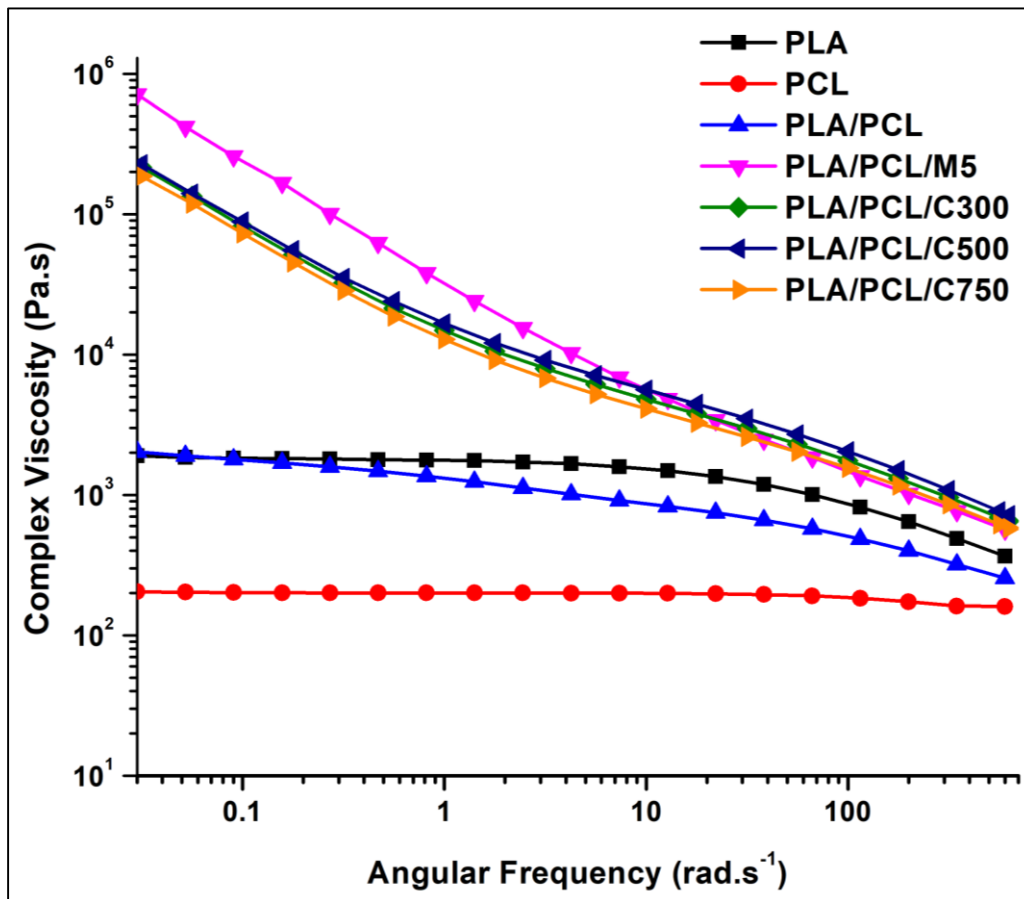


Figure 75: Complex viscosity curves of the pure polymers, their blend, and their composites

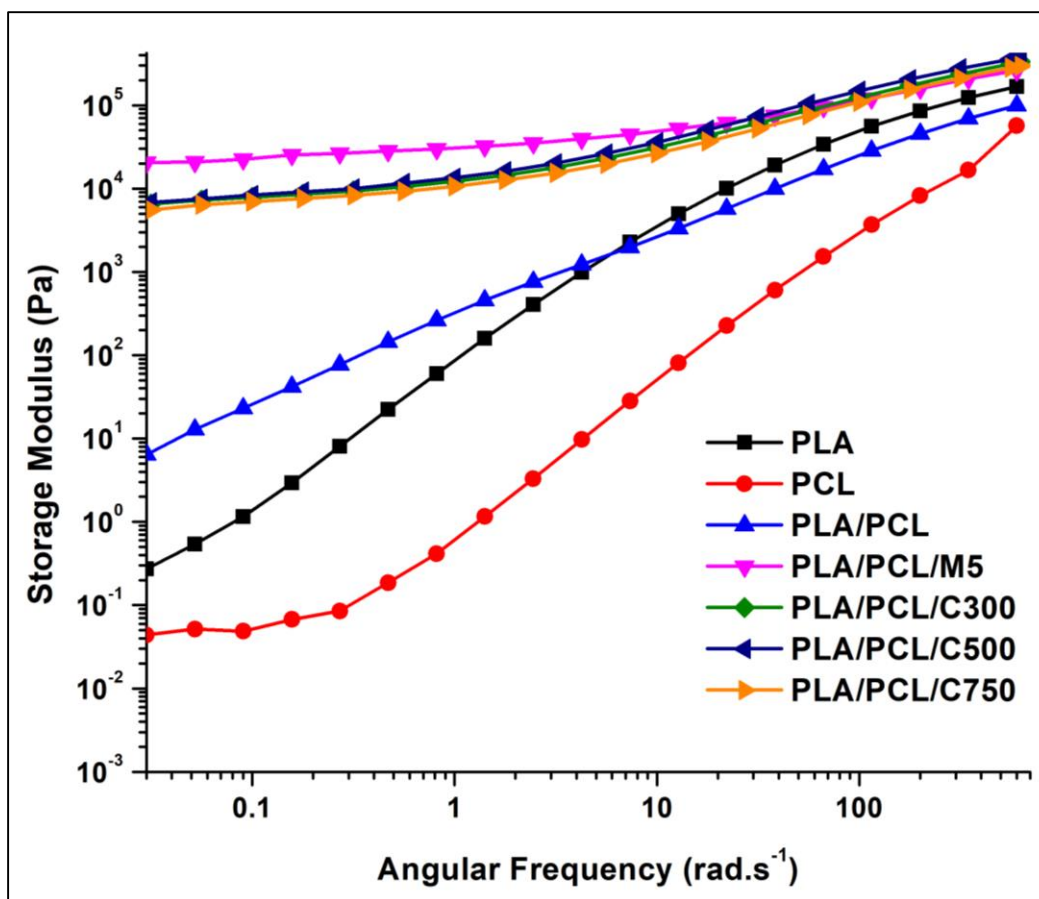


Figure 76: Storage modulus curves of the pure polymers, their blend, and their composites

#### 6.5.4. Porosity and tensile tests

The porosity results of the 3D printed blend and composites (table 13) exhibit close values that range between 4 and 8 %. The tensile properties of these samples and the injection moulded ones are shown in figures 77, 78, and 79. The Young's modulus results in figure 77 show superior results for the M5 GNP composite as compared to the pure blend which is not the case for the C grades blends. The reason is the higher aspect ratio of M5 GNP that caused an improvement in the stiffness of the composite [81]. The tensile strength (figure 78) and elongation at break (figure 79) are slightly better for the C GNP blends as compared to the M5 GNP sample. The reason can be the better adhesion of the C nanoplatelets with the PLA/PCL matrix due to the presence of more functional groups on their surface as already mentioned in this chapter. GNP can prevent the crack propagation throughout the matrix. But, a good dispersion of these nanoparticles in the polymer matrix along with strong interfacial adhesion between both are required for

increasing the energy dissipation and slowing down the crack propagation during the fracture process under tensile stresses [82].

Table 13: Porosity data of 3D printed blend and composites

3D printed samples	Porosity (%)
PLA/PCL	$8 \pm 3$
PLA/PCL/M5	$6 \pm 2$
PLA/PCL/C300	$5 \pm 1.5$
PLA/PCL/C500	$4.5 \pm 2$
PLA/PCL/C750	$5.2 \pm 1.9$

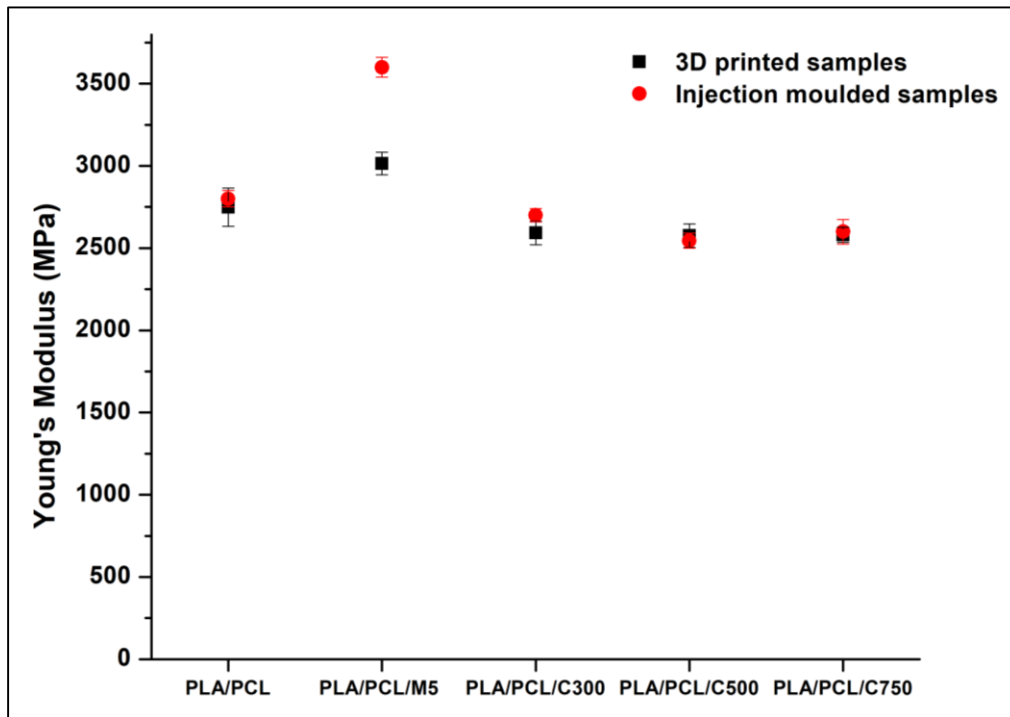


Figure 77: Young's modulus data of injection moulded and 3D printed blend and composites

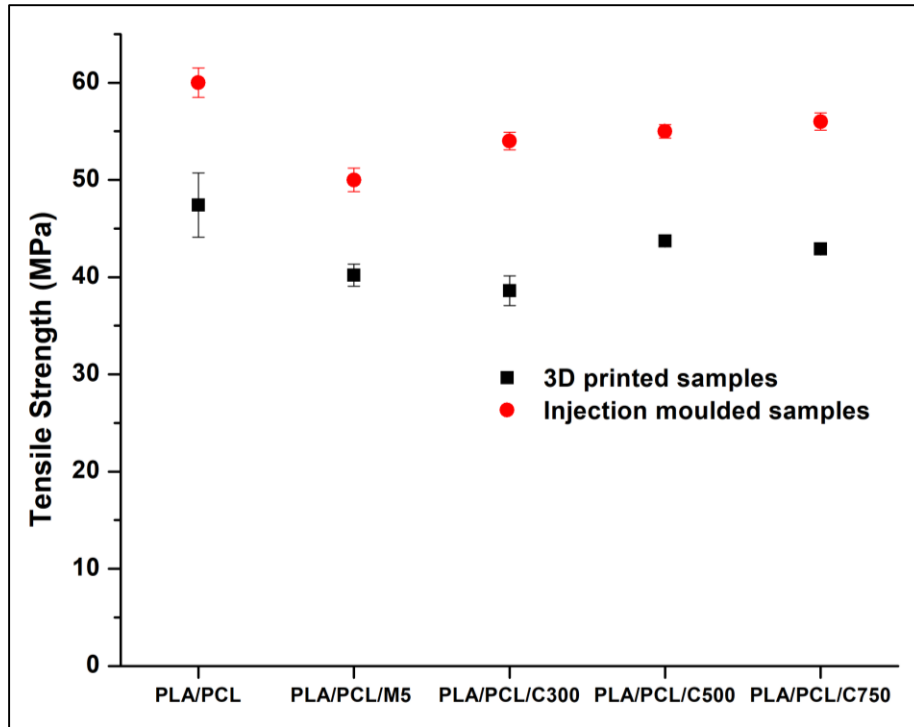


Figure 78: Tensile strength data of injection moulded and 3D printed blend and composites

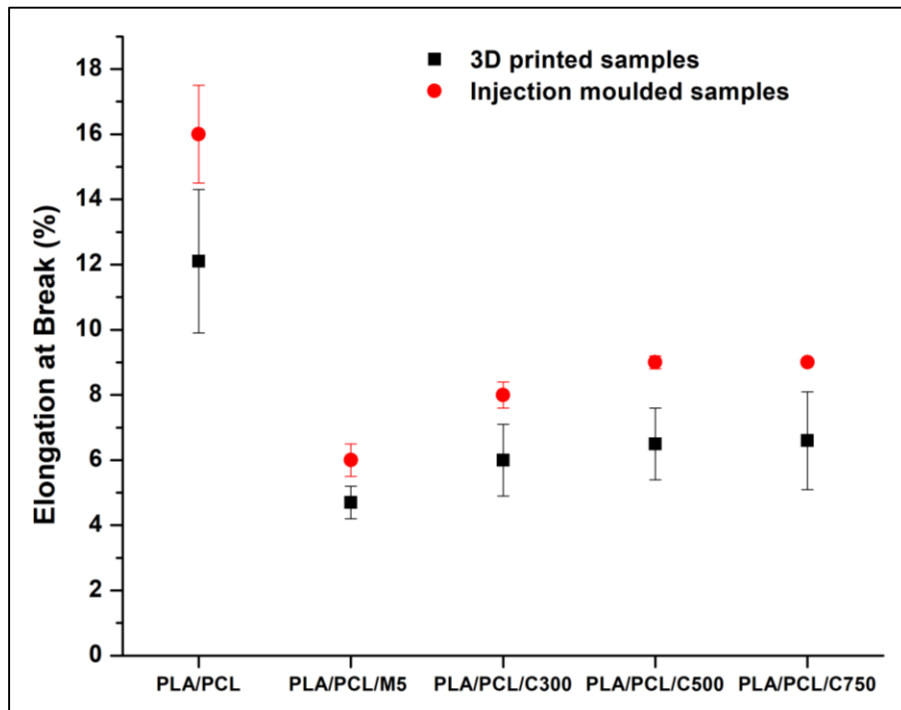


Figure 79: Elongation at break data of injection moulded and 3D printed blend and composites

## **7. Conclusion**

This chapter was focused on the selection of materials and the implementation of relevant methods that were necessary to select the most interesting GNP in the most relevant PLA/PCL blend. The first section showed that M5 GNP has the highest ordered crystalline structure and aspect ratio as compared to the C GNP grades. The second section indicated that mixing this GNP grade with the PLA matrix gave the greatest Young's modulus and lowest electrical percolation threshold but with the worse adhesion with the matrix. The third section showed that PLA80/PCL20 presents a compromise in the mechanical properties as compared to the other blends. And finally, the last section exhibited that M5 GNP caused better improvement in the PLA crystallinity, PCL thermal stability, PLA/PCL complex viscosity, storage modulus, and Young's modulus. Therefore, throughout the upcoming chapters, M5 GNP will be the only GNP that will be melt blended with the PLA/PCL blends. Also, this chapter showed that the 3D printing technique can give PLA composites with close thermal properties as compared to the injection moulding technique.

## 8. Bibliography

- [1] B. Li and W.-H. Zhong, "Review on polymer/graphite nanoplatelet nanocomposites," *J. Mater. Sci.*, vol. 46, no. 17, pp. 5595–5614, 2011, doi: 10.1007/s10853-011-5572-y.
- [2] Y. Zhan, Y. Lei, F. Meng, J. Zhong, R. Zhao, and X. Liu, "Electrical, thermal, and mechanical properties of polyarylene ether nitriles/graphite nanosheets nanocomposites prepared by masterbatch route," *J. Mater. Sci.*, vol. 46, no. 3, pp. 824–831, 2011, doi: 10.1007/s10853-010-4823-7.
- [3] X. Wu, S. Qi, J. He, and G. Duan, "High conductivity and low percolation threshold in polyaniline/graphite nanosheets composites," *J. Mater. Sci.*, vol. 45, no. 2, pp. 483–489, 2010, doi: 10.1007/s10853-009-3965-y.
- [4] J. J. George and A. K. Bhowmick, "Ethylene vinyl acetate/expanded graphite nanocomposites by solution intercalation: preparation, characterization and properties," *J. Mater. Sci.*, vol. 43, no. 2, pp. 702–708, 2008, doi: 10.1007/s10853-007-2193-6.
- [5] W. Lu, D. Wu, C. Wu, and G. Chen, "Nonlinear DC response in high-density polyethylene/graphite nanosheets composites," *J. Mater. Sci.*, vol. 41, no. 6, pp. 1785–1790, 2006, doi: 10.1007/s10853-006-3946-3.
- [6] B. Z. Jang and A. Zhamu, "Processing of nanographene platelets (NGPs) and NGP nanocomposites: a review," *J. Mater. Sci.*, vol. 43, no. 15, pp. 5092–5101, 2008, doi: 10.1007/s10853-008-2755-2.
- [7] H. M. Chong, S. Hinder, and A. Taylor, "Graphene nanoplatelet-modified epoxy: effect of aspect ratio and surface functionality on mechanical properties and toughening mechanisms," *J. Mater. Sci.*, vol. 51, pp. 8764–8790, 2016, doi: 10.1007/s10853-016-0160-9.
- [8] Y. Gao, O. T. Picot, E. Bilotti, and T. Peijs, "Influence of filler size on the properties of poly(lactic acid) (PLA)/graphene nanoplatelet (GNP) nanocomposites," *Eur. Polym. J.*, vol. 86, pp. 117–131, 2017, doi: 10.1016/j.eurpolymj.2016.10.045.
- [9] "www.xgsciences.com.", accessed on October 25<sup>th</sup> 2022.
- [10] F. Wang, L. T. Drzal, Y. Qin, and Z. Huang, "Mechanical properties and thermal conductivity of graphene nanoplatelet/epoxy composites," *J. Mater. Sci.*, vol. 50, no. 3, pp. 1082–1093, 2015, doi: 10.1007/s10853-014-8665-6.
- [11] Z. Q. Li, C. J. Lu, Z. Xia, Y. Zhou, and Z. Luo, "X-ray diffraction patterns of graphite and turbostratic carbon," *Carbon N. Y.*, vol. 45, pp. 1686–1695, 2007, doi.org/10.1016/j.carbon.2007.03.038.
- [12] H. Albetran, "Structural Characterization of Graphite Nanoplatelets Synthesized from Graphite Flakes.", Preprints, 2020, doi: 10.20944/preprints202008.0325.v1.

- [13] M. Sabzi, L. Jiang, F. Liu, I. Ghasemi, and M. Atai, "Graphene nanoplatelets as poly(lactic acid) modifier: Linear rheological behavior and electrical conductivity," *J. Mater. Chem. A*, vol. 1, no. 28, pp. 8253–8261, 2013, doi: 10.1039/c3ta11021d.
- [14] B. W. Chieng, N. Ibrahim, W. Yunus, M. Hussein, and V. S. G. Silverajah, "Graphene Nanoplatelets as Novel Reinforcement Filler in Poly(lactic acid)/Epoxidized Palm Oil Green Nanocomposites: Mechanical Properties," *Int. J. Mol. Sci.*, vol. 13, pp. 10920–10934, 2012, doi: 10.3390/ijms130910920.
- [15] C. Bao, L. Song, W. Xing, B. Yuan, C. A. Wilkie, J. Huang, Y. Guo, and Y. Hu, "Preparation of graphene by pressurized oxidation and multiplex reduction and its polymer nanocomposites by masterbatch-based melt blending," *J. Mater. Chem.*, vol. 22, no. 13, pp. 6088–6096, 2012, doi: 10.1039/C2JM16203B.
- [16] H. Kim and C. W. Macosko, "Morphology and Properties of Polyester/Exfoliated Graphite Nanocomposites," *Macromolecules*, vol. 41, no. 9, pp. 3317–3327, 2008, doi: 10.1021/ma702385h.
- [17] J. Um, Y.-S. Jun, H. Alhumade, H. Krithivasan, G. Lui, and A. Yu, "Investigation of the size effect of graphene nano-platelets (GnPs) on the anti-corrosion performance of polyurethane/GnP composites," *RSC Adv.*, vol. 8, pp. 17091–17100, 2018, doi: 10.1039/C8RA02087F.
- [18] T. Batakliiev, I. Petrova-Doycheva, V. Angelov, V. Georgiev, E. Ivanov, R. Kotsilkova, M. Casa, C. Cirillo, R. Adami, M. Sarno, and P. Ciambelli, "Effects of Graphene Nanoplatelets and Multiwall Carbon Nanotubes on the Structure and Mechanical Properties of Poly(lactic acid) Composites: A Comparative Study," *Appl. Sci.*, vol. 9, no. 3, p. 469, 2019, doi: 10.3390/app9030469.
- [19] L. Botta, R. Scaffaro, F. Sutera, and M. C. Mistretta, "Reprocessing of PLA/Graphene Nanoplatelets Nanocomposites," *Polymers (Basel)*, vol. 10, no. 1, p. 18, 2018, doi: 10.3390/polym10010018.
- [20] "[https://www.natureworksllc.com/~media/Technical\\_Resources/Technical\\_Data\\_Sheets/TechnicalDataSheet\\_2003D\\_FFP-FSW\\_pdf.pdf](https://www.natureworksllc.com/~media/Technical_Resources/Technical_Data_Sheets/TechnicalDataSheet_2003D_FFP-FSW_pdf.pdf)," accessed on October 25<sup>th</sup> 2022.
- [21] S. Lashgari, M. Karrabi, I. Ghasemi, H. Azizi, and M. Messori, "Graphene nanoplatelets dispersion in poly(l-lactic acid): preparation method and its influence on electrical, crystallinity and thermomechanical properties," *Iran. Polym. J.*, vol. 25, no. 2, pp. 193–202, 2016, doi: 10.1007/s13726-015-0413-5.
- [22] S. Azizi, E. David, M. F. Fréchet, P. Nguyen-Tri, and C. M. Ouellet-Plamondon, "Electrical and thermal phenomena in low-density polyethylene/carbon black composites near the percolation threshold," *J. Appl. Polym. Sci.*, vol. 136, no. 6, pp. 47043, 2019, doi: <https://doi.org/10.1002/app.47043>.

- [23] H. Kim, Y. Miura, and C. W. MacOsco, "Graphene/polyurethane nanocomposites for improved gas barrier and electrical conductivity," *Chem. Mater.*, vol. 22, no. 11, pp. 3441–3450, 2010, doi: 10.1021/cm100477v.
- [24] R. Verdejo, M. M. Bernal, L. J. Romasanta, and M. A. Lopez-Manchado, "Graphene filled polymer nanocomposites," *J. Mater. Chem.*, vol. 21, no. 10, pp. 3301–3310, 2011, doi: 10.1039/C0JM02708A.
- [25] R. M. Santos, S. T. Mould, P. Formánek, M. C. Paiva, and J. A. Covas, "Effects of Particle Size and Surface Chemistry on the Dispersion of Graphite Nanoplates in Polypropylene Composites," *Polymers (Basel)*, vol. 10, no. 2, p. 222, 2018, doi: 10.3390/polym10020222.
- [26] Y. J. Noh, H.-I. Joh, J. Yu, S. H. Huang, S. Lee, C. H. Lee, S. Y. Kim, and J. R. Youn, "Ultra-high dispersion of graphene in polymer composite via solvent free fabrication and functionalization," *Sci. Rep.*, vol. 5, no. 1, p. 9141, 2015, doi: 10.1038/srep09141.
- [27] Z. Qin, M. Taylor, M. Hwang, K. Bertoldi, and M. J. Buehler, "Effect of Wrinkles on the Surface Area of Graphene: Toward the Design of Nanoelectronics," *Nano Lett.*, vol. 14, no. 11, pp. 6520–6525, 2014, doi: 10.1021/nl503097u.
- [28] A. R. Bhattacharyya et al., "Crystallization and orientation studies in polypropylene/single wall carbon nanotube composite," *Polymer (Guildf)*, vol. 44, no. 8, pp. 2373–2377, 2003, doi: [https://doi.org/10.1016/S0032-3861\(03\)00073-9](https://doi.org/10.1016/S0032-3861(03)00073-9).
- [29] J.-Z. Xu, T. Chen, C.-L. Yang, Z.-M. Li, Y.-M. Mao, B.-Q. Zeng, and B. S. Hsiao, "Isothermal Crystallization of Poly(l-lactide) Induced by Graphene Nanosheets and Carbon Nanotubes: A Comparative Study," *Macromolecules*, vol. 43, no. 11, pp. 5000–5008, 2010, doi: 10.1021/ma100304n.
- [30] B. W. Chieng, N. A. Ibrahim, W. M. Z. W. Yunus, M. Z. Hussein, Y. Y. Then, and Y. Y. Loo, "Effects of Graphene Nanoplatelets and Reduced Graphene Oxide on Poly(lactic acid) and Plasticized Poly(lactic acid): A Comparative Study," *Polymers (Basel)*, vol. 6, no. 8, pp. 2232–2246, 2014, doi: 10.3390/polym6082232.
- [31] S. Chatterjee, F. Nafezarefi, N. H. Tai, L. Schlagenhauf, F. A. Nüesch, and B. T. T. Chu, "Size and synergy effects of nanofiller hybrids including graphene nanoplatelets and carbon nanotubes in mechanical properties of epoxy composites," *Carbon N. Y.*, vol. 50, no. 15, pp. 5380–5386, 2012, doi: <https://doi.org/10.1016/j.carbon.2012.07.021>.
- [32] J. C. Halpin, "Stiffness and Expansion Estimates for Oriented Short Fiber Composites," *J. Compos. Mater.*, vol. 3, no. 4, pp. 732–734, 1969, doi: 10.1177/002199836900300419.
- [33] T. Mori and K. Tanaka, "Average stress in matrix and average elastic energy of materials with misfitting inclusions," *Acta Metall.*, vol. 21, no. 5, pp. 571–574, 1973, doi: [https://doi.org/10.1016/0001-6160\(73\)90064-3](https://doi.org/10.1016/0001-6160(73)90064-3).
- [34] H L Cox, "The elasticity and strength of paper and other fibrous materials," *Br. J. Appl. Phys.*, vol. 3, no. 3, p. 72, 1952, doi: 10.1088/0508-3443/3/3/302.

- [35] X.-L. Gao and K. Li, "A shear-lag model for carbon nanotube-reinforced polymer composites," *Int. J. Solids Struct.*, vol. 42, no. 5, pp. 1649–1667, 2005, doi: <https://doi.org/10.1016/j.ijsolstr.2004.08.020>.
- [36] I. Zaman, B. Manshoor, A. Khalid, Q. Meng, and S. Araby, "Interface modification of clay and graphene platelets reinforced epoxy nanocomposites: a comparative study," *J. Mater. Sci.*, vol. 49, no. 17, pp. 5856–5865, 2014, doi: [10.1007/s10853-014-8296-y](https://doi.org/10.1007/s10853-014-8296-y).
- [37] I. Zaman, T. T. Phan, H.-C. Kuan, Q. Meng, L. T. B. La, L. Luong, O. Youssf, and J. Ma, "Epoxy/graphene platelets nanocomposites with two levels of interface strength," *Polymer (Guildf.)*, vol. 52, no. 7, pp. 1603–1611, 2011, doi: <https://doi.org/10.1016/j.polymer.2011.02.003>.
- [38] J. A. King, D. R. Klimek, I. Miskioglu, and G. M. Odegard, "Mechanical properties of graphene nanoplatelet/epoxy composites," *J. Appl. Polym. Sci.*, vol. 128, no. 6, pp. 4217–4223, 2013, doi: <https://doi.org/10.1002/app.38645>.
- [39] K. P. Pramoda, H. Hussain, H. M. Koh, H. R. Tan, and C. B. He, "Covalent bonded polymer–graphene nanocomposites," *J. Polym. Sci. Part A Polym. Chem.*, vol. 48, no. 19, pp. 4262–4267, 2010, doi: <https://doi.org/10.1002/pola.24212>.
- [40] L. Wang, J. Hong, and G. Chen, "Comparison study of graphite nanosheets and carbon black as fillers for high density polyethylene," *Polym. Eng. & Sci.*, vol. 50, no. 11, pp. 2176–2181, 2010, doi: <https://doi.org/10.1002/pen.21751>.
- [41] S. Gupta, P. Raju Mantena, and A. Al-Ostaz, "Dynamic Mechanical and Impact Property Correlation of Nanoclay and Graphite Platelet Reinforced Vinyl Ester Nanocomposites," *J. Reinf. Plast. Compos.*, vol. 29, no. 13, pp. 2037–2047, 2009, doi: [10.1177/0731684409341762](https://doi.org/10.1177/0731684409341762).
- [42] Y.-C. Li and G.-H. Chen, "HDPE/expanded graphite nanocomposites prepared via masterbatch process," *Polym. Eng. & Sci.*, vol. 47, no. 6, pp. 882–888, 2007, doi: <https://doi.org/10.1002/pen.20772>.
- [43] K. Wakabayashi, C. Pierre, D. A. Dikin, R. S. Ruoff, T. Ramanathan, L. C. Brinson, and J. M. Torkelson, "Polymer–graphite nanocomposites: effective dispersion and major property enhancement via solid-state shear pulverization," *Macromolecules*, vol. 41, no. 6, pp. 1905–1908, 2008, doi: [10.1021/ma071687b](https://doi.org/10.1021/ma071687b).
- [44] X. Jiang and L. T. Drzal, "Multifunctional high density polyethylene nanocomposites produced by incorporation of exfoliated graphite nanoplatelets 1: Morphology and mechanical properties," *Polym. Compos.*, vol. 31, no. 6, pp. 1091–1098, 2010, doi: <https://doi.org/10.1002/pc.20896>.
- [45] S. Kim, I. Do, and L. T. Drzal, "Multifunctional xGnP/LLDPE Nanocomposites Prepared by Solution Compounding Using Various Screw Rotating Systems," *Macromol. Mater. Eng.*, vol. 294, no. 3, pp. 196–205, 2009, doi: <https://doi.org/10.1002/mame.200800319>.
- [46] J. Yang, M. Tian, Q.-X. Jia, J.-H. Shi, L.-Q. Zhang, S.-H. Lim, Z.-Z. Yu, and Y.-W. Mai, "Improved mechanical and functional properties of elastomer/graphite nanocomposites

prepared by latex compounding,” *Acta Mater.*, vol. 55, no. 18, pp. 6372–6382, 2007, doi: <https://doi.org/10.1016/j.actamat.2007.07.043>.

[47] I.-H. Kim and Y. G. Jeong, “Polylactide/exfoliated graphite nanocomposites with enhanced thermal stability, mechanical modulus, and electrical conductivity,” *J. Polym. Sci. Part B Polym. Phys.*, vol. 48, no. 8, pp. 850–858, 2010, doi: <https://doi.org/10.1002/polb.21956>.

[48] W. Khan, “Comparison on Performance of Injection Moulding and 3D Printed Parts,” 2020.

[49] N. Narloğlu, “Comparison of Mechanical Properties of 3D-Printed and Compression-Molded Wood-Polylactic Acid (PLA) Composites,” *BioResources*, vol. 17, no. 2, pp. 3291–3302, 2022, doi: [10.15376/biores.17.2.3291-3302](https://doi.org/10.15376/biores.17.2.3291-3302).

[50] A. Golbang, M. Mokhtari, E. Harkin-Jones, E. Archer, and A. McIlhagger, “Additive Manufacturing and Injection Moulding of High-Performance IF-WS2/PEEK Nanocomposites: A Comparative Study,” *Front. Mater.*, vol. 8, p. 745088, 2021, doi: [10.3389/fmats.2021.745088](https://doi.org/10.3389/fmats.2021.745088).

[51] K. Kalaitzidou, H. Fukushima, and L. T. Drzal, “A new compounding method for exfoliated graphite–polypropylene nanocomposites with enhanced flexural properties and lower percolation threshold,” *Compos. Sci. Technol.*, vol. 67, no. 10, pp. 2045–2051, 2007, doi: <https://doi.org/10.1016/j.compscitech.2006.11.014>.

[52] Y. She, G. Chen, and D. Wu, “Fabrication of polyethylene/graphite nanocomposite from modified expanded graphite,” *Polym. Int.*, vol. 56, no. 5, pp. 679–685, 2007, doi: <https://doi.org/10.1002/pi.2191>.

[53] J. Li, J.-K. Kim, and M. Lung Sham, “Conductive graphite nanoplatelet/epoxy nanocomposites: Effects of exfoliation and UV/ozone treatment of graphite,” *Scr. Mater.*, vol. 53, no. 2, pp. 235–240, 2005, doi: <https://doi.org/10.1016/j.scriptamat.2005.03.034>.

[54] S.-E. Lee, O. Choi, and H. T. Hahn, “Microwave properties of graphite nanoplatelet/epoxy composites,” *J. Appl. Phys.*, vol. 104, no. 3, p. 33705, 2008, doi: [10.1063/1.2965195](https://doi.org/10.1063/1.2965195).

[55] J. Li, L. Vaisman, G. Marom, and J.-K. Kim, “Br treated graphite nanoplatelets for improved electrical conductivity of polymer composites,” *Carbon N. Y.*, vol. 45, no. 4, pp. 744–750, 2007, doi: <https://doi.org/10.1016/j.carbon.2006.11.031>.

[56] Y. C. Li, S. C. Tjong, and R. K. Y. Li, “Electrical conductivity and dielectric response of poly(vinylidene fluoride)–graphite nanoplatelet composites,” *Synth. Met.*, vol. 160, no. 17, pp. 1912–1919, 2010, doi: <https://doi.org/10.1016/j.synthmet.2010.07.009>.

[57] H. Hu and G. Chen, “Electrochemically modified graphite nanosheets and their nanocomposite films with poly(vinyl alcohol),” *Polym. Compos.*, vol. 31, no. 10, pp. 1770–1775, 2010, doi: <https://doi.org/10.1002/pc.20968>.

[58] T. Ramanathan, S. Stankovich, D. A. Dikin, H. Liu, H. Shen, S. T. Nguyen, and L. C. Brinson, “Graphitic nanofillers in PMMA nanocomposites—An investigation of particle size and dispersion

and their influence on nanocomposite properties,” *J. Polym. Sci. Part B Polym. Phys.*, vol. 45, no. 15, pp. 2097–2112, 2007, doi: <https://doi.org/10.1002/polb.21187>.

[59] G. Chen, X. Chen, H. Wang, and D. Wu, “Dispersion of graphite nanosheets in polymer resins via masterbatch technique,” *J. Appl. Polym. Sci.*, vol. 103, no. 6, pp. 3470–3475, 2007, doi: <https://doi.org/10.1002/app.24431>.

[60] C. Zheng, Z. Fan, T. Wei, and G. Luo, “Temperature dependence of the conductivity behavior of graphite nanoplatelet-filled epoxy resin composites,” *J. Appl. Polym. Sci.*, vol. 113, no. 3, pp. 1515–1519, 2009, doi: <https://doi.org/10.1002/app.30009>.

[61] M. T. Müller, K. Hilarius, M. Liebscher, D. Lellinger, I. Alig, and P. Pötschke, “Effect of Graphite Nanoplate Morphology on the Dispersion and Physical Properties of Polycarbonate Based Composites,” *Materials (Basel)*, vol. 10, no. 5, p. 545, 2017, doi: [10.3390/ma10050545](https://doi.org/10.3390/ma10050545).

[62] T. Evgin, A. Turgut, G. Hamaoui, Z. Spitalsky, N. Horny, M. Micusik, M. Chirtoc, M. Sarikanat, and M. Omastova, “Size effects of graphene nanoplatelets on the properties of high-density polyethylene nanocomposites: morphological, thermal, electrical, and mechanical characterization,” *Beilstein J. Nanotechnol.*, vol. 11, pp. 167–179, 2020, doi: [10.3762/bjnano.11.14](https://doi.org/10.3762/bjnano.11.14).

[63] R. Patwa, A. Kumar, and V. Katiyar, “Crystallization kinetics, morphology, and hydrolytic degradation of novel bio-based poly(lactic acid)/crystalline silk nano-discs nanobiocomposites,” *J. Appl. Polym. Sci.*, vol. 135, no. 33, p. 46590, 2018, doi: <https://doi.org/10.1002/app.46590>.

[64] J. Urquijo, G. Guerrica-Echevarría, and J. I. Eguiazábal, “Melt processed PLA/PCL blends: Effect of processing method on phase structure, morphology, and mechanical properties,” *J. Appl. Polym. Sci.*, vol. 132, no. 41, pp. 1–9, 2015, doi: [10.1002/app.42641](https://doi.org/10.1002/app.42641).

[65] Y. He, J. Yan, X. He, W. Weng, and K. Cheng, “PLLA/Graphene Nanocomposites Membranes with Improved Biocompatibility and Mechanical Properties,” *Coatings*, vol. 12, no. 6, p. 718, 2022, doi: [10.3390/coatings12060718](https://doi.org/10.3390/coatings12060718).

[66] D. Wu, Y. Cheng, S. Feng, Z. Yao, and M. Zhang, “Crystallization Behavior of Polylactide/Graphene Composites,” *Ind. Eng. Chem. Res.*, vol. 52, no. 20, pp. 6731–6739, 2013, doi: [10.1021/ie4004199](https://doi.org/10.1021/ie4004199).

[67] S. Karimi, I. Ghasemi, F. Abbassi-Sourki, M. Samara, and N. Demarquette, “PEG-Grafted Graphene/PLLA Nanocomposites: Effect of PEG Chain Length on Crystallization Kinetics of PLLA,” *ACS Omega*, vol. 7, no. 35, pp. 31197–31204, 2022, doi: [10.1021/acsomega.2c03397](https://doi.org/10.1021/acsomega.2c03397).

[68] S. Kim, I. Do, and L. T. Drzal, “Thermal stability and dynamic mechanical behavior of exfoliated graphite nanoplatelets-LLDPE nanocomposites,” *Polym. Compos.*, vol. 31, no. 5, pp. 755–761, 2010, doi: <https://doi.org/10.1002/pc.20781>.

[69] Z. Mo, H. Shi, H. Chen, G. Niu, Z. Zhao, and Y. Wu, “Synthesis of graphite nanosheets/polyaniline nanorods composites with ultrasonic and conductivity,” *J. Appl. Polym. Sci.*, vol. 112, no. 2, pp. 573–578, 2009, doi: <https://doi.org/10.1002/app.29411>.

- [70] F. Sun, T. Yu, C. Hu, and Y. Li, "Influence of functionalized graphene by grafted phosphorus containing flame retardant on the flammability of carbon fiber/epoxy resin (CF/ER) composite," *Compos. Sci. Technol.*, vol. 136, pp. 76–84, 2016, doi: <https://doi.org/10.1016/j.compscitech.2016.10.002>.
- [71] H. Kim and C. W. Macosko, "Processing-property relationships of polycarbonate/graphene composites," *Polymer (Guildf.)*, vol. 50, no. 15, pp. 3797–3809, 2009, doi: <https://doi.org/10.1016/j.polymer.2009.05.038>.
- [72] H. Kim, A. A. Abdala, and C. W. Macosko, "Graphene/Polymer Nanocomposites," *Macromolecules*, vol. 43, no. 16, pp. 6515–6530, 2010, doi: [10.1021/ma100572e](https://doi.org/10.1021/ma100572e).
- [73] A. A. Katbab, A. N. Hrymak, and K. Kasmadjian, "Preparation of interfacially compatibilized PP-EPDM thermoplastic vulcanizate/graphite nanocomposites: Effects of graphite microstructure upon morphology, electrical conductivity, and melt rheology," *J. Appl. Polym. Sci.*, vol. 107, no. 5, pp. 3425–3433, 2008, doi: <https://doi.org/10.1002/app.27454>.
- [74] K. Wakabayashi, P. J. Brunner, J. Masuda, S. A. Hewlett, and J. M. Torkelson, "Polypropylene-graphite nanocomposites made by solid-state shear pulverization: Effects of significantly exfoliated, unmodified graphite content on physical, mechanical and electrical properties," *Polymer (Guildf.)*, vol. 51, no. 23, pp. 5525–5531, 2010, doi: <https://doi.org/10.1016/j.polymer.2010.09.007>.
- [75] J. Vermant, S. Ceccia, M. K. Dolgovskij, P. L. Maffettone, and C. W. Macosko, "Quantifying dispersion of layered nanocomposites via melt rheology," *J. Rheol. (N. Y. N. Y.)*, vol. 51, no. 3, pp. 429–450, 2007, doi: [10.1122/1.2516399](https://doi.org/10.1122/1.2516399).
- [76] V. Sridhar, D. Xu, T. T. Pham, S. P. Mahapatra, and J. K. Kim, "Dielectric and dynamic mechanical relaxation behavior of exfoliated nano graphite reinforced flouroelastomer composites," *Polym. Compos.*, vol. 30, no. 3, pp. 334–342, 2009, doi: <https://doi.org/10.1002/pc.20559>.
- [77] L. Cui, L. Yi, Y. Wang, Y. Zhang, P. Polyák, X. Sui, and B. Pukánszky, "Rheology of PLA/regenerated cellulose nanocomposites prepared by the pickering emulsion process: Network formation and modeling," *Mater. Des.*, vol. 206, p. 109774, 2021, doi: <https://doi.org/10.1016/j.matdes.2021.109774>.
- [78] V. Solouki Bonab, O. Maxian, and I. Manas-Zloczower, "Carbon nanofiller networks- a comparative study of networks formed by branched versus linear carbon nanotubes in thermoplastic polyurethane," *Polymer (Guildf.)*, vol. 175, pp. 227–234, 2019, doi: <https://doi.org/10.1016/j.polymer.2019.05.031>.
- [79] S. P. Thomas, S. K. De, and I. A. Hussein, "Impact of Aspect Ratio of Carbon Nanotubes on Shear and Extensional Rheology of Polyethylene Nanocomposites," *Applied Rheology*, vol. 23, no. 2, p. 23635, 2013, doi: [10.3933/applrheol-23-23635](https://doi.org/10.3933/applrheol-23-23635).

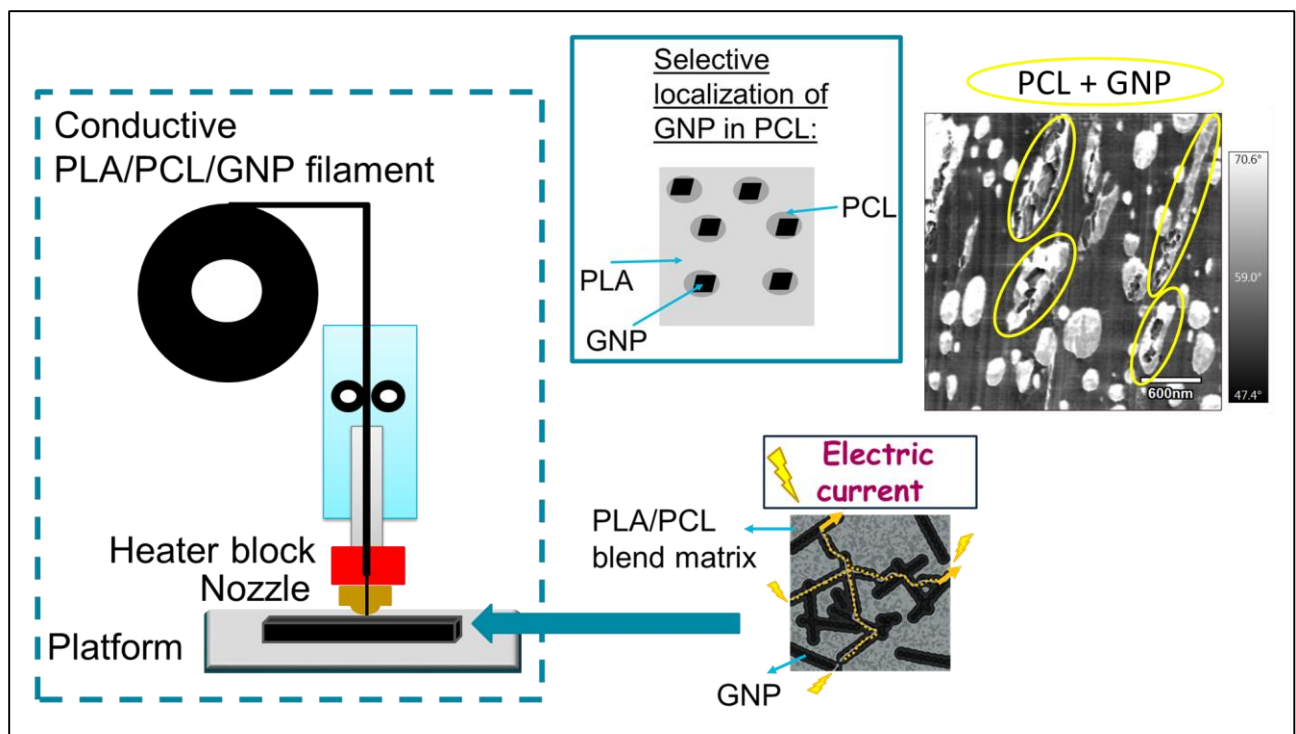
[80] M. Ajorloo, M. Fasihi, and H. Khoramishad, "The role of nanofiller size and polymer chain configuration on the properties of polypropylene/graphite nanoplates composites," *J. Taiwan Inst. Chem. Eng.*, vol. 108, pp. 82–91, 2020, doi: <https://doi.org/10.1016/j.jtice.2019.12.010>.

[81] S. Morimune-Moriya, T. Goto, and T. Nishino, "Effect of aspect ratio of graphene oxide on properties of poly (vinyl alcohol) nanocomposites," *Nanocomposites*, vol. 5, no. 3, pp. 84–93, 2019, doi: 10.1080/20550324.2019.1647688.

[82] S.-C. Her and K.-C. Zhang, "Mode II Fracture Analysis of GNP/Epoxy Nanocomposite Film on a Substrate," *Polymers (Basel)*., vol. 13, no. 16, p. 2823, 2021, doi: 10.3390/polym13162823.

# Chapter 3: Fabrication of PLA/PCL/Graphene Nanoplatelets (GNP) Electrically Conductive Circuit Using the Fused Filament Fabrication (FFF) 3D Printing Technique

## 1. Graphical Abstract



## 2. Abstract

For the purpose of fabricating electrically conductive composites via the fused filament fabrication (FFF) technique whose properties were compared with the injection moulded ones, Poly(lactic acid) (PLA) and Polycaprolactone (PCL) were mixed with different contents of graphene nanoplatelets (GNP). Wettability, morphological, rheological, thermal, mechanical, and electrical properties of the 3D printed samples were investigated. The microstructural images

showed the selective localization of the GNP in the PCL nodules that are dispersed in the PLA phase. The electrical resistivity results using the four probes method revealed that the injection moulded samples are insulators whereas the 3D printed samples having the same graphene contents are semiconductors. Varying the printing raster angles had an influence also on the electrical conductivity results. The electrical percolation threshold was found to be lower than 15 wt. %, whereas the rheological percolation threshold was found to be lower than 10 wt.%. Also, the 20 wt.% and 25 wt.% GNP composites were able to connect an electrical circuit. An increase in the Young's modulus was shown with the percentage of graphene. As a result, this work exhibited the potential of the FFF technique to fabricate biodegradable electrically conductive PLA-PCL-GNP composites which can be applicable in the electronic domain.

Keywords: electrical conductivity; fused filament fabrication; 3D printing, polymer bionanocomposites, PLA, PCL, GNP

### **3. Introduction**

The use of plastics is significantly increasing in all applications [1]. However, biopolymers have nowadays become of great interest due to the high demand on sustainable materials possessing eco-friendly characteristics. Among the reasons behind substituting the synthetic plastic materials is the dissemination of non-degradable plastic waste in oceans and aquatic systems and consequently the accompanied danger on the aquatic and human life which has become a major concern. Renewable natural resources are now able to replace the commonly used oil-based products to synthesize bioplastics that are often biodegradable through environmentally friendly bioprocesses [2].

Poly(lactic acid) or polylactide (PLA) is an aliphatic thermoplastic polyester that is biobased, biodegradable, biocompatible, and compostable. It is characterized by important mechanical properties such as Young's modulus in the 3-4 GPa range and tensile strength in the 60-70 MPa range [3]. Yet, PLA has some disadvantages such as lack of ductility (elongation at break < 10%) and blending it with other rubbery polymers such as polycaprolactone (PCL) can improve its toughness. PCL is a semi-crystalline aliphatic polyester that is biodegradable and biocompatible

but oil-derived. And due to the different mechanical and thermal properties of both polymers, their mixture can be a material with well-balanced properties [4].

PLA and PCL can be used as polymeric matrices to be mixed with micro and nano carbonaceous fillers of different geometries such as carbon black (CB) [5][6], single and multiwall carbon nanotubes (CNT) [7-10], graphite [11][12], and graphene [13][14] for improving their electrical, mechanical, and thermal properties [15]. Graphene or graphite nanoplatelets (GNP) are composed of stacked graphene sheets connected with each other by Van der Waals forces and are featured by important electrical properties (electron mobility:  $2.5 \times 10^5 \text{ cm}^2 \cdot \text{V}^{-1} \cdot \text{s}^{-1}$ ), outstanding thermal (thermal conductivity above  $3000 \text{ W} \cdot \text{m}^{-1} \cdot \text{K}^{-1}$ ) and mechanical properties (Young's modulus: 1 TPa and tensile strength: 130 GPa) [3]. These and other properties allow the GNP to be integrated into new generation of high speed and radio frequency logic devices, electronic circuits, sensors, and solar cells [16]. Moreover, when embedded in polymer matrices, they can improve their electrical conductivity and dielectric properties [17] as well as their mechanical properties, thermal stability, thermal conductivity, gas barrier properties, and dimensional stability [16].

The fused filament fabrication (FFF) technique is an interesting 3D printing technique due to its low cost, ease of use, small size, and the possibility to manufacture multi-functional parts [18]. PLA is the most adopted material by most of the FFF users [19]. And among the different technologies used for graphene-based products fabrication, FFF is promising and the development of new conductive polymer nanocomposites using this technique is highly desirable [20].

Few studies have been carried out to investigate the electrical properties of PLA/PCL composites, but none has used the 3D printing technique. Kim et al. [21] designed electrically conductive PLA/PCL/CB composites by induced CB particle aggregations in the PCL phase. PCL was added in small amount, therefore there was no deterioration of the mechanical performance of the composites. They therefore obtained an electrical conductivity of  $1 \text{ S} \cdot \text{m}^{-1}$  and they found the electrical percolation threshold below 4 wt.% of PCL. For preparing their composites, they pre-melted the PLA/PCL via an internal mixer and later they added the CB. Xu et al. studied the

influence of the acid-oxidized multi-wall carbon nanotubes (A-MWCNTs) on the phase morphology and the electrical conductivity of PLA/PCL/A-MWCNTs composites prepared by micro compounding and having PCL percentage ranging from 5 wt.% to 90 wt.%. They realized that the A-MWCNTs were homogeneously and selectively localized in the PCL phase [22]. Huang et al. could control the localization of MWCNTs at the continuous interface of immiscible PLA/PCL (50wt.%/50wt.%) blends through the migration of the MWCNTs from the unfavorable PLA phase to the favorable PCL phase. Because of the accumulation of MWCNTs at the interface, they obtained very low electrical percolation threshold of 0.025 wt.%. They prepared their composites by the internal mixer to compound the PLA and the MWCNTs together first and to mix the PCL with the PLA/MWCNTs later [23]. It is important to mention that in each of these works the compression moulding technique was used after the melt blending to fabricate the testing specimens.

To our knowledge, so far there are no contributions on the processing of PLA/PCL/GNP composites using the 3D printing technique and especially leading to good electrical conductivity. Therefore, this work reports for the first time the fabrication of electrically conductive PLA/PCL/GNP 3D printed materials that were able to connect an electrical circuit. Using the melt blending technique, PLA and PCL were mixed with GNP and later were extruded in the form of filaments. Finally, filaments were processed by 3D printing using the FFF technique. Later, the synthesized 3D printed materials have undergone contact angle measurement, rheological, thermal, mechanical, and electrical resistance tests in addition to the microstructural analysis. For comparison, samples manufactured by injection moulding were prepared to assess the potential of printing process on the microstructural and electrical properties of the composites.

## 4. Materials and Methods

### 4.1. Materials

PLA used in this work is a commercial grade Ingeo™ Biopolymer 2003D (MFR= 6 g/10 min (210 °C/2.16 kg) supplied by NatureWorks (Minnetonka, MN, USA). Its main properties are a density of 1.2 g.cm<sup>-3</sup>, a glass transition temperature of 60 °C, and a melting temperature of 150 °C.

PCL is a commercial grade Capa™ 6800 (MFR = 2.01-4.03 g/10 min (160 °C/5 kg) supplied by Perstorp UK Ltd. (Warrington, UK) in pellet form. PCL main thermal transitions are a glass transition temperature (T<sub>g</sub>) of -60 °C and a melting temperature (T<sub>m</sub>) in the 58-60 °C range.

Graphene nanoplatelets (GNP), trade name xGnP®, Grade M5 was supplied by XG Sciences Inc, Lansing, MI, USA. For this grade, the manufacturer reports an average lateral dimension of 5 μm, a thickness in the range of 6-8 nm, and a surface area of 120-150 m<sup>2</sup>.g<sup>-1</sup>. From the technical data sheet, some additional information regarding this material's characteristics are available such as: oxygen content less than 1% and residual acid content less than 0.5 wt.%. It has naturally occurring functional groups such as ether, carboxyl, or hydroxyl that can react with the atmospheric humidity to form acids or other compounds. Its density is 2.2 g.cm<sup>-3</sup>, thermal conductivity is 3000 W.m<sup>-1</sup>.K<sup>-1</sup>, thermal expansion of 4-6 × 10<sup>-6</sup> K<sup>-1</sup>, tensile modulus of 10<sup>3</sup> GPa, tensile strength of 5 GPa, and electrical conductivity of 10<sup>7</sup> S.m<sup>-1</sup>.

Diiodomethane (99 % purity) used in this study was purchased from Alfa Aesar and used as received.

### 4.2. Nanocomposites preparation

#### 4.2.1. Compounding

To prevent the hydrolytic degradation which is an undesirable reaction, PCL, PLA and GNP were dried at respectively 40, 60 and 80 °C overnight under vacuum before the melt mixing process. Melt blending using a co-rotating twin screw extruder Process 11 (Thermo Scientific, Massachusetts, United States) was carried out to produce the polymer blend and the composites. Before the processing step, PLA and PCL pellets were mixed manually and then placed in the

extruder's pellets feeder whereas the GNP were placed in the extruder's fillers feeder. Then during the extrusion process, all the materials were fed at the same time to produce a compounded wire that was immediately ground to form composite pellets. A PLA-PCL binary blend (80 wt.% of PLA and 20 wt.% of PCL) and PLA-PCL-GNP composites containing 10 wt.%, 15 wt.%, 20 wt.%, and 25 wt.% of M5 nanofillers were prepared. It is important to note that the weight percentages of PLA and PCL were fixed at 80 wt.% and 20 wt.% respectively with respect to the total polymer weight percentage in the polymer composites. The temperature profile of the twin-screw extruder was chosen as the following: 200 °C, 200 °C, 200 °C, 200 °C, 200 °C, 180 °C, 120 °C, and 70 °C set on the screw die zone and zones 8, 7, 6, 5, 4, 3, and 2 respectively. Note that zone 2 is the closest to the polymer feeder and zone 8 is the farthest. The rotor screw speed was 350 rpm, the total flow rate of the materials was 0.6 kg.h<sup>-1</sup>, and 300g of materials were produced per composition.

#### ***4.2.2. Injection moulding***

Following the twin-screw extrusion and after drying the composite pellets at 50 °C using a vacuum oven for at least one night, injection moulding was performed to manufacture samples for the electrical resistance characterizations. A mini-injection moulding machine IM15 (Zamak Mercator, Poland) was used and the parameters were: cylinder temperature of 180 °C, mould temperature of 60 °C, pressure of 5 bars, and the cycle duration was 3 min. The produced samples for the electrical resistance tests were the 1BA dumb-bell shaped samples (according to the standard EN ISO 527-2) whose middle part was cut to have bar-shaped samples of 30 mm length, 5 mm width, and 2 mm thickness.

#### ***4.2.3. Filament extrusion***

Compounded materials were also used to feed a mini single-screw extruder NEXT 1.0 (3devo, Netherlands) to obtain calibrated filaments. The processing temperature profile gradually increased from T1 = 165 °C to T2 = 190 °C, T3 = 200 °C and T4 = 195 °C. Note that T1 is the temperature of the zone that is closest to the feeder and the screw rotation speed was fixed at 5 rpm. The final diameter of the extruded filaments was approximately 2.85 mm.

#### 4.2.4. Fused filament fabrication

The 3D printed specimens were manufactured by an A4v3 FFF printer (3ntr, Italy), fed with the filaments extruded as described in the previous part. The 3D-printed samples were built in a horizontal configuration. All the specimens were 3D printed using the following printing parameters: nozzle diameter of 0.8 mm, layer height of 0.2 mm, infill percentage of 100 %, raster angle alternating between  $+45^\circ$  and  $-45^\circ$ , and infill speed of  $40 \text{ mm}\cdot\text{s}^{-1}$ . The 3D printed parts were built at a nozzle temperature of  $180^\circ\text{C}$  and at a bed temperature of  $60^\circ\text{C}$ .

The 3D printed geometries of the samples were 25 mm disks for the rheological and contact angle measurements, ISO 527-1BA samples for the mechanical tensile tests, and bar shaped samples for the electrical resistance measurements (30 mm long, 5 mm wide, and 2 mm thick). The bar-shaped 3D printed samples dimensions were chosen to be the same as the ones of the injection moulded samples to perform a comparative study. Moreover, for the purpose of studying the influence of the printing pattern on the electrical conductivity results, the raster angle was varied and three values were chosen:  $+45^\circ/-45^\circ$  (Figure 80.a),  $0^\circ$  (Figure 80.b), and  $90^\circ$  (Figure 80.c).

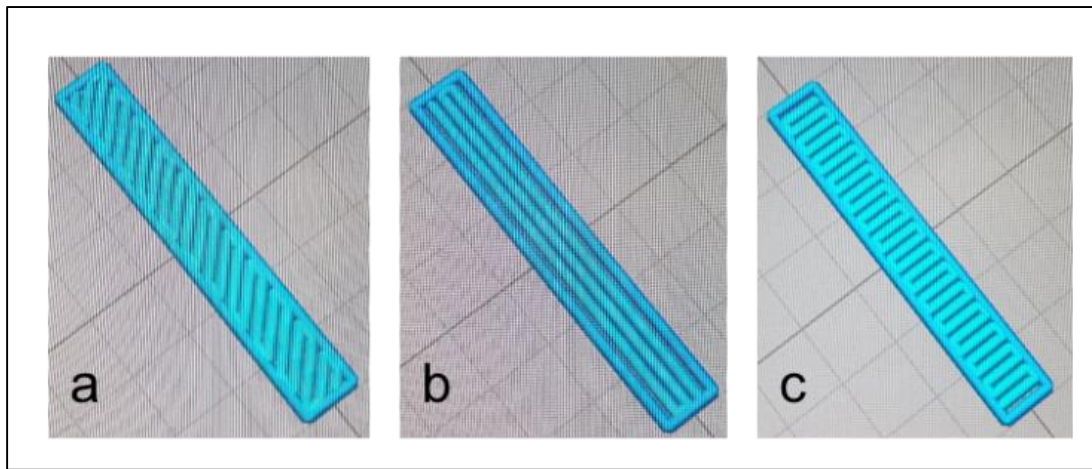


Figure 80: The different 3D printing patterns according to the three different raster angles: a)  $+45^\circ/-45^\circ$ , b)  $0^\circ$ , and c)  $90^\circ$

## 5. Characterization techniques

### 5.1. Contact angle measurements

The contact angle ( $\theta$ ) is the angle between the solid surface and the tangent drawn on the surface of a drop, passing through a triple intersection point between the atmosphere, liquid, and the solid. The  $\theta$  values of probe liquids on PLA, PCL, and M5 surfaces took place at room temperature using a Krüss DSA30 goniometer. Measurements were achieved using a sessile drop technique and a video-camera mounted on a microscope was used to record the drop images. Purified water (high polarity) and diiodomethane (completely dispersive) with known surface tension polar and dispersive components were used as liquid probes. A drop of the probe liquid (3  $\mu\text{l}$  for water and 1.5  $\mu\text{l}$  for diiodomethane) on the sample's surface was ejected and when the liquid drop settled, ten  $\theta$  values were taken consecutively and their average value was calculated.

The solid surface energy of a polymer is an important parameter that affects surface related processes such as wettability. Performing  $\theta$  measurements using probe liquids with well-known surface tension properties is the most practical way to determine the solid surface energy. The solid surface energy can be obtained from the contact angle using Young's equation (equation (1)) [24]:

$$\gamma_s = \gamma_l \cos \theta + \gamma_{sl} \quad (1)$$

Where,  $\gamma_s$  is the solid surface energy,  $\gamma_l$  is the liquid surface tension,  $\theta$  is the probe liquid contact angle, and  $\gamma_{sl}$  is the solid-liquid interfacial energy.  $\theta$  and  $\gamma_l$  are the only measurable quantities in Young's equation. To determine  $\gamma_s$ , its polar and dispersive components should be calculated first using Owens-Wendt model using contact angles with at least two probe liquids (equation (2)) [25]:

$$\frac{\gamma_l (1 + \cos \theta)}{2\sqrt{\gamma_l^d}} = \sqrt{\gamma_s^p} \times \frac{\sqrt{\gamma_l^p}}{\sqrt{\gamma_l^d}} + \sqrt{\gamma_s^d} \quad (2)$$

Where,  $\gamma_1^p$  is the liquid polar surface tension,  $\gamma_1^d$  is the liquid dispersive surface tension,  $\gamma_s^p$  is the solid polar surface energy, and  $\gamma_s^d$  is the solid dispersive surface energy. The total surface energy or tension is therefore the summation of the polar and dispersive surface energies or tensions.

The PLA and PCL samples for these tests were 3D printed 25 mm diameter disks, whose smooth side was tested, and the M5 samples was pressed into compact 25 mm disks. Six sessile drop tests were performed for each liquid and each sample, and two samples were tested per material. It is important to note that for the M5 GNP samples, the contact angles recorded in the first three seconds were taken into consideration as a first approximation of surface energy determination after each drop ejection, due to the absorptive capacity of the sample that is in a powdered form.

The liquid surface tensions and their polar and dispersive components of the test liquids are presented in Table 14 [26]. The solid surface energies of PLA, PCL, and M5 GNP can be used to calculate the interfacial energies between each two materials and finally to estimate the wetting coefficient that can be used to predict the selective localization of the fillers in the polymer blend composites. In this context, the formulas that can be used for these calculations are listed below [27]:

$$\gamma_{ij} = \gamma_i + \gamma_j - \frac{4\gamma_i^d \gamma_j^d}{\gamma_i^d + \gamma_j^d} - \frac{4\gamma_i^p \gamma_j^p}{\gamma_i^p + \gamma_j^p} \quad (3)$$

$$\gamma_{ij} = \gamma_i + \gamma_j - 2\sqrt{\gamma_i^d \gamma_j^d} - 2\sqrt{\gamma_i^p \gamma_j^p} \quad (4)$$

Equation (3) is the harmonic mean equation of Wu and is used to calculate the interfacial tension  $\gamma_{ij}$  between PLA and PCL using the polymers surface energies and their dispersive and polar components. For the calculation of the interfacial tension between the filler and the polymers, the geometric mean equation of Wu (equation (4)) can be used, where  $\gamma_i^d$  and  $\gamma_i^p$  are the dispersive and polar contributions to the total surface tension  $\gamma_i$ , respectively. The interfacial tensions between PLA and PCL ( $\gamma_{PLA/PCL}$ ) and between M5 and the polymers ( $\gamma_{M5/PLA}$  and  $\gamma_{M5/PCL}$ ) are therefore useful for the determination of the wetting coefficient ( $\omega_\alpha$ ) [27]:

$$\omega_{\alpha} = \cos \theta = \frac{\gamma_{M5/PCL} - \gamma_{M5/PLA}}{\gamma_{PLA/PCL}} \quad (5)$$

If the wetting coefficient ( $\omega_{\alpha}$ ) is greater than one, then M5 GNP should be in PLA. If it is smaller than -1, then M5 GNP should be localized in PCL. If ( $\omega_{\alpha}$ ) is between 1 and -1, then M5 should be located at the interface of the two polymers.

Table 14: The surface energy components of water and diiodomethane

Probe liquid	$\gamma_l$ (mJ.m <sup>-2</sup> )	$\gamma_l^p$ (mJ.m <sup>-2</sup> )	$\gamma_l^d$ (mJ.m <sup>-2</sup> )
Water	72.8	51.0	21.8
Diiodomethane	50.8	0.0	50.8

## 5.2. Scanning electron microscopy (SEM)

The morphology of the neat GNP as well as the injection moulded and 3D printed PLA/PCL/10 wt.% M5 and PLA/PCL/15 wt.% M5 samples were analysed at different levels of magnification by a scanning electron microscope (FEI Quanta 200 SEM) (Fisher Thermo Scientific) at an acceleration voltage of 10 kV. The analysis was preceded by cryofractures of cross sections using nitrogen. To assess the affinity of the GNP to the polymer phases, the cryofractured injection moulded and 3D printed PLA/PCL/10 wt.% M5 and PLA/PCL/15 wt.% M5 samples were immersed in toluene at room temperature for 3 hours in order to dissolve the PCL phase followed by washing to remove the dissolved fraction. Samples were then placed under the hood overnight for complete solvent evaporation prior to the SEM analysis. The observation of the bar-shaped samples, whether dissolved in toluene or not, took place along their transversal section.

## 5.3. Atomic force microscopy (AFM)

The morphology and microstructure of the injection moulded and 3D printed PLA/PCL/10 wt.% M5 composites were investigated by the atomic force microscopy (AFM) technique (MFP-3D infinity, Asylum Research AFM, Oxford instruments). The samples surfaces were cryogenically sectioned by diamond knives using an ultra-microtome (Leica EM UC7) to obtain flat and smooth surfaces. AFM characterisations were carried out along the transversal section of the bar-shaped

samples. In addition, AFM images were obtained in a tapping mode at ambient conditions using AC160TSR3 tip at a scan rate of 1 Hz. Images were made at different sizes, from 3x3 to 20x20  $\mu\text{m}^2$ . Both the topographic (height) and phase images were recorded and analysed.

#### 5.4. Rheological measurements

The rheological measurements were carried out in an oscillatory shear mode using parallel plate geometry (25 mm diameter) rheometer (Anton Paar, Austria) at 190 °C under nitrogen atmosphere to avoid the samples degradation. Frequency sweeps between 0.01 and 600  $\text{rad}\cdot\text{s}^{-1}$  were carried out at low strains (0.006-10 %) that were shown to be within the linear viscoelastic range of these materials. The upper limits of the viscoelastic range were determined by strain sweep tests at 200  $\text{rad}\cdot\text{s}^{-1}$ . Before testing, the PLA/PCL blends and the composites were vacuum dried overnight at 50 °C and the PLA and PCL pure samples were also vacuum dried at 60 °C and 40 °C respectively. The tests were repeated two times for each composition to assess reproducibility.

#### 5.5. Thermogravimetric analysis (TGA)

Thermogravimetric Analysis (TGA) was carried out on 10 mg samples using a TGA Perkin Elmer apparatus at 10  $^{\circ}\text{C}\cdot\text{min}^{-1}$  from 30 °C to 900 °C with nitrogen flow (40  $\text{ml}\cdot\text{min}^{-1}$ ). This step was preceded by an isothermal step for 30 min at room temperature. The weight loss was recorded as function of temperature. The experimental percentage of char yield at 600°C, the thermal onset degradation temperature at 5 % of mass loss ( $T_{\text{onset}}$ ), the maximum degradation temperature  $T_{\text{max}}$  (i.e. temperature of the mass loss rate peak), and the total mass loss over the entire temperature range were determined.

#### 5.6. Differential scanning calorimetry (DSC)

Thermal analysis was performed by means of a Perkin-Elmer Diamond differential scanning calorimeter (DSC). The samples were sealed in aluminium pans (10 mg) and then heated from room temperature to 200 °C, hold for 5 min to eliminate previous thermal histories, cooled down to room temperature, and finally re-heated to 200 °C. A scanning rate of 10  $^{\circ}\text{C}\cdot\text{min}^{-1}$  was used in both heating steps and the cooling rate was chosen to be 5  $^{\circ}\text{C}\cdot\text{min}^{-1}$ . The glass transition

temperature,  $T_g$ , was measured at the mid-point of the heat capacity inflexion point. The crystallization temperature,  $T_c$ , and melting temperature,  $T_m$ , were determined from the peak values of the respective exotherms and endotherms. The degree of crystallinity of PLA in the samples (%  $X_c$ ) was determined by means of equation (6):

$$\% X_c = 100 \cdot \frac{\Delta H_m - \Delta H_c}{\Delta H_m^0 \cdot W} \quad (6)$$

Where,  $\Delta H_m^0$  is the enthalpy value of a pure crystalline PLA and it corresponds to  $93.7 \text{ kJ.mol}^{-1}$  [28],  $\Delta H_m$  is the enthalpy of PLA related to the fusion process,  $\Delta H_c$  is the enthalpy of PLA related to the crystallization process, and  $W$  is the weight fraction of PLA in the blend and the composites.

## 5.7. Tensile tests

Tensile tests were carried out using a static materials testing machine ZwickRoell BZ010/TH2S (ZwickRoell, France) device equipped with a 2.5 kN load cell on dumbbell shaped specimens (geometry type 1BA, ISO 527). For the assessment of Young's modulus, the strain in the linear range was determined at a cross-head speed of  $1 \text{ mm.min}^{-1}$  by means of a clip-on extensometer. The yield stress and the elongation at break were determined at a crosshead speed of  $10 \text{ mm.min}^{-1}$ . Five 3D printed tensile specimens were tested for each formulation: PLA, PLA/PCL, and the composites.

## 5.8. Electrical resistance measurements

For moderately conductive materials (whose volume resistivity ranges between 1 and  $10^7 \Omega.\text{cm}$ ), volume resistivity was determined using four-probe contact configuration. The resistance measurement was performed on 6 bar-shaped samples for each formulation. Each specimen was tested at a voltage of 5 V by using a direct current (DC) power supply (Topward, TPS-4000). The current flow on the samples was measured between two external electrodes using a multimeter (ITT instruments, MX 579 Metrix) and the voltage was measured between the internal electrodes using a digital multimeter (HAMEG Instruments, HM 8011). One surface of each sample was in contact with the four identical copper electrodes whose dimensions were: length of 40 mm, width of 14 mm, and thickness of 1 mm. The electrodes were equidistant from each other with

3.7 mm. The resistance measurement setup is shown in Figure 81. The electrical volume resistivity ( $\rho$ ) was calculated according to the equation (7):

$$\rho = \frac{R \times S}{L} \quad (7)$$

Where, R is the electrical resistance ( $\Omega$ ), S is the cross-sectional area ( $m^2$ ) and it is equal to the width of the sample multiplied by its thickness, and L corresponds to the distance between the internal electrodes (3.7 mm).

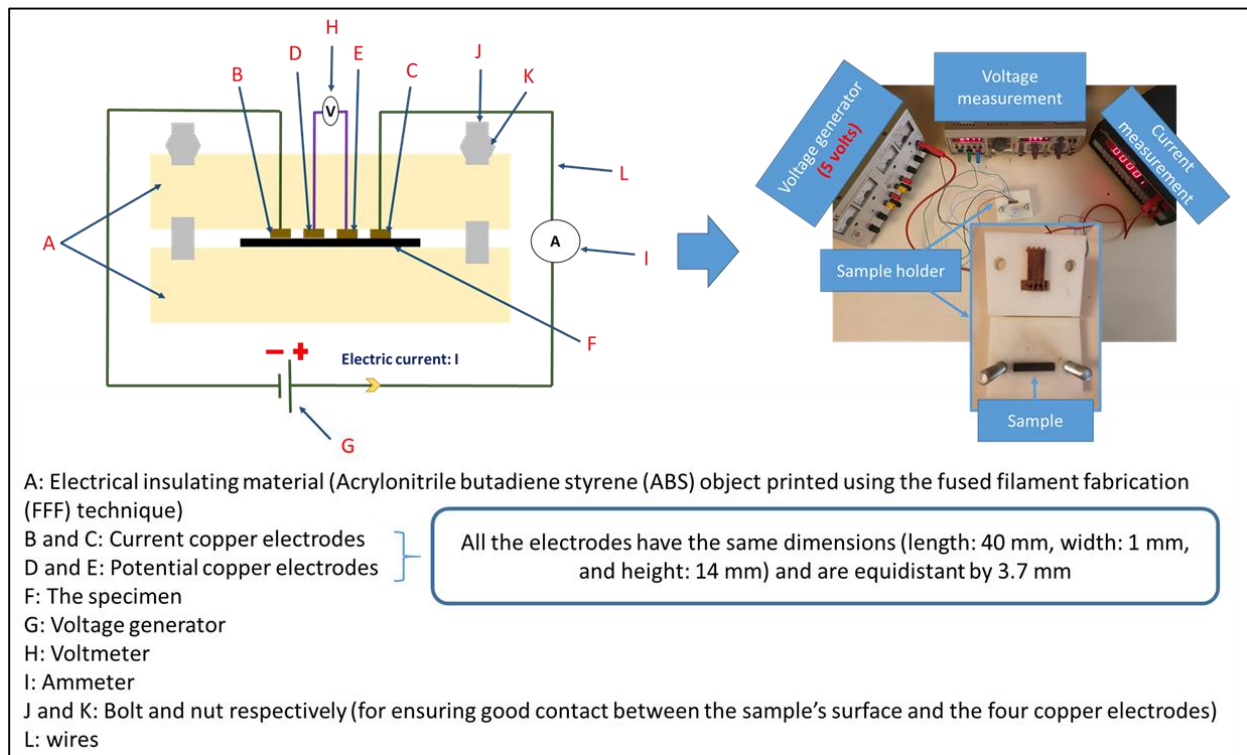


Figure 81: The setup of the electrical resistance measurement using the four probes method

## 6. Results and Discussion

### 6.1. Contact angle measurements

Based on the contact angle measurements performed in this study, the PLA and PCL possess solid surface energies equal to  $39.4 \pm 0.6 \text{ mJ.m}^{-2}$  and  $35.5 \pm 0.2 \text{ mJ.m}^{-2}$  respectively. These results are shown in table 15 and compared to results in the literature for the same materials. The values found in the literature are like ours for the three materials (polymers and graphene) although the experimentation conditions and/or the models used for calculating the surface energies are not the same. Furthermore, the results for M5 GNP are also presented and the solid surface energy value obtained by our measurements is  $58.9 \pm 0.1 \text{ mJ.m}^{-2}$ .

The calculations of the interfacial surface energies between PLA and PCL, PLA and M5, and PCL and M5 based on equations (3) and (4) in the characterizations section gave the following results respectively:  $\gamma_{\text{PLA/PCL}} = 0.424 \text{ mJ.m}^{-2}$ ,  $\gamma_{\text{M5/PLA}} = 8.835 \text{ mJ.m}^{-2}$ , and  $\gamma_{\text{M5/PCL}} = 11.468 \text{ mJ.m}^{-2}$ . Consequently, the wetting coefficient based on these results and calculated according to equation (5) in the characterizations section is 6.2 (greater than one) thus indicating that in principle M5 GNP should be localized in PLA. However, it is important to take into consideration that the thermodynamic factor is not the only factor that affects the localization of the fillers in the polymer blends. Some other factors such as the kinetic ones have an influence on the fillers localization phenomenon. For instance, the viscosity ratio between the polymers, the temperature, the time of mixing, the sequence of mixing of the components, and the shear rate are examples of these factors [39].

Table 15: The solid surface energy, its dispersive and polar components, the test liquids, and the models used for solid surface energy calculations of the PLA, PCL, and GNP

Material	Grade and/or company	Solid surface energy (mJ.m <sup>-2</sup> )	Dispersive component (mJ.m <sup>-2</sup> )	Polar component (mJ.m <sup>-2</sup> )	Test liquids	Model(s)	References
PLA	PLA2003D	39.4±0.6	34.9±1	4.5±0.4	Water, diiodomethane	Owens-Wendt	Present work
	PLA2002D	41.6	30.8	10.8	Water, formamide	Wu's method	[30]
	PLA4032D	40.6	36	4.6	Water, glycerol, diiodomethane	Good and Van Oss	[31]
	PLA3251D	35.5	26.4	9.1	Water, diiodomethane	Wu's method	[32]
	PLA3D850	43.9±0.7	36.8±0.2	7.1±0.5	Water, diiodomethane, ethylene glycol	Owens-Wendt	[26]
PCL	PCL 6800 Capa Perstorp	35.5±0.2	32.6±0.6	2.9±0.9	Water, diiodomethane	Owens-Wendt	Present work
	PCL6800 Capa Perstorp	42.9±0.5	39.8±0.3	3.1±0.2	Water, diiodomethane, ethylene glycol	Owens-Wendt	[26]
	Sigma Aldrich	40	25	15	Glycerol, water, diiodomethane	Owens-Wendt	[33]
GNP	M5 GNP XG sciences	58.9±0.1	33±0.1	25.9±0.05	Water, diiodomethane	Owens-Wendt	Present work
	Graphene expert Co.	54.8	41.6	13.2	-	-	[34]
	XG sciences	52.6	47.7	4.9	Water, formamide, ethylene glycol, diiodomethane	Owens-Wendt	[35]

## 6.2. Microscopy- SEM and AFM

Figure 82 corresponds to the scanning electron microscopy investigations carried out on the M5 GNP. Information about the morphology of M5 GNP was given by Figures 82.a and 3.b that show clearly the platelet form of graphene. Figure 82.c represents the energy-dispersive X-ray spectroscopy (EDX) analysis of the M5 GNP surface to figure out the elements composing the zone indicated by the square shown in Figure 82.d. These elements are mainly carbon (89.6 %) and oxygen (8.8 %). Other elements were also identified such as sulfur (1.6 %) and sodium (0.1 %). The M5 oxygen content can be attributed to the presence of carbonyl and ether/alcohol groups [36].

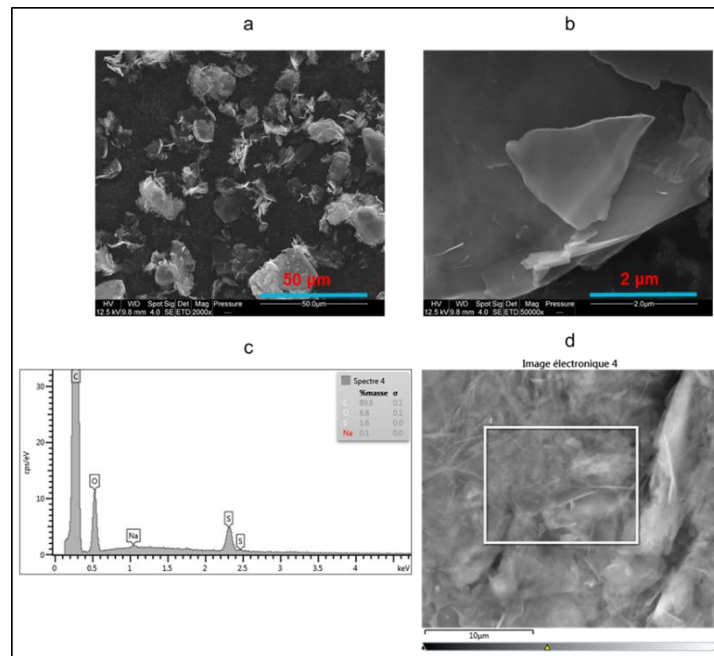


Figure 82: (a) and (b) SEM images of M5 GNP at different magnifications; (c) EDX graph; (d) the part of the surface that is surrounded by a rectangle and whose surface elements are shown in the EDX graph (c)

Atomic force microscopy (AFM) was performed on both injection moulded and 3D printed samples to investigate the influence of the process on the morphology of these composites. Figures 83.a and 83.b exhibit the topography and the phase of the injection moulded sample respectively. Topography (Figure 83.a) showed that roughness of the surface was quite low (<100 nm) with some rough (white) zones highlighting the presence of GNP. Phase contrasts (Figure 83.b) gave additional information: white nodules related to PCL (with the highest phase) are

clearly visible in a grey matrix (denoting the PLA). Graphene is also visible (in dark grey). To identify more precisely the elements of the composite, a profile was drawn on the images. Figure 83.c shows these profiles that correspond to the red line that is displayed in Figures 83.a and 83.b starting from the blue point (that is present in the images and the profiles). Along the drawn line, the three composite components were indicated by arrows whose colors match the color of the designations in the profiles. The components naming was achieved by considering that in the phase profile the greatest peak corresponds to the softest material such as the PCL and the lowest peak is relevant to the stiffest material such the graphene nanoplatelets. However, this is the inverse for the topography profile. The combination of the information from these figures confirms that the small white nodules are PCL, the grey matrix is PLA that is present in the greatest proportion, and the layered structured material, in dark grey corresponding to the lowest phase, is the graphene nanoplatelets.

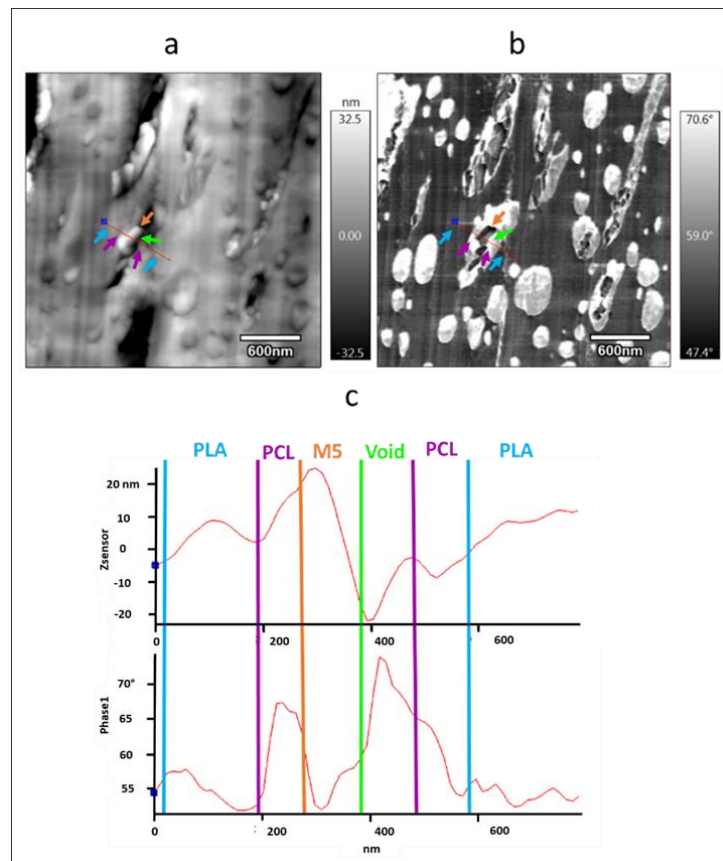


Figure 83: (a) AFM topography; (b) AFM phase images of the PLA/PCL/10 wt.% M5 injection moulded sample; (c) topography and phase profiles in a drawn red line that is traced in (a) and (b) (the arrows in the images point towards the different components of the components of the composite and their colors match the designation of the peaks in the profiles)

Figure 84 also corresponds to an injection moulded PLA/PCL/10 wt.% M5 composite. In both the topography (84.a, 84.c, and 84.e) and their corresponding phase images (84.b, 84.d, and 84.f), the yellow circles surround some graphene particles that seem to be localized in the PCL nodules. This selective localization of the graphene in the PCL phase rather than the PLA phase was achieved in a work carried out by De Aguiar et al. [37]. In their work they stated that the simultaneous melt blending of two polymers such as PLA and PCL, whose weight percentages were 80 wt.% and 20 wt.% respectively, characterized by different melting temperatures which are 155 °C and 60 °C respectively drives the nanoparticles to the PCL phase. The PLA's viscosity is greater than that of PCL for all the analyzed shear rates and this difference makes the preference of the nanoparticles to the lower viscosity polymer phase. Furthermore, due to the slight differences in terms of the interfacial tensions between PLA/GNP (0.82 mJ.m<sup>-2</sup>) and PCL/GNP (0.3 mJ.m<sup>-2</sup>), the viscosity effects dominate. In the present study and based on the contact angle measurements and the wettability calculations, the M5 GNP was expected to be localized in the PLA phase. But Figure 84 shows that it is not the case, and that M5 GNP prefers PCL and this can be explained by the dominance of the kinetic factors such as the viscosity over the thermodynamic ones. Moreover, it was highlighted by Kelnar et al. [38] that the addition of GNP to the PLA80/PCL20 blend showed a significant presence of the GNP in the PCL phase and a limited presence at the interface. These last authors explained this phenomenon by the initial dispersion of the nanoparticles in the first melting polymer phase which is PCL during the one-step melt mixing process. Furthermore, due to the similar interfacial energies of PLA and PCL with GNP, there is no sufficient driving force that can cause the transfer of graphene to PLA. It is important to also note the circular form of the PCL nodules indicated by blue circles in Figures 84.b, 84.d, and 84.f. When the M5 particles are situated in these nodules, their size becomes bigger and their form becomes more elongated (yellow circles in Figures 84.b, 84.d, and 84.f). This can be attributed to the aggregation of the nanoparticles and their alignment inside the PCL nodules and can be also the result of altering the polymers viscosity ratio by the nanoparticles present in one of the polymer phases [37].

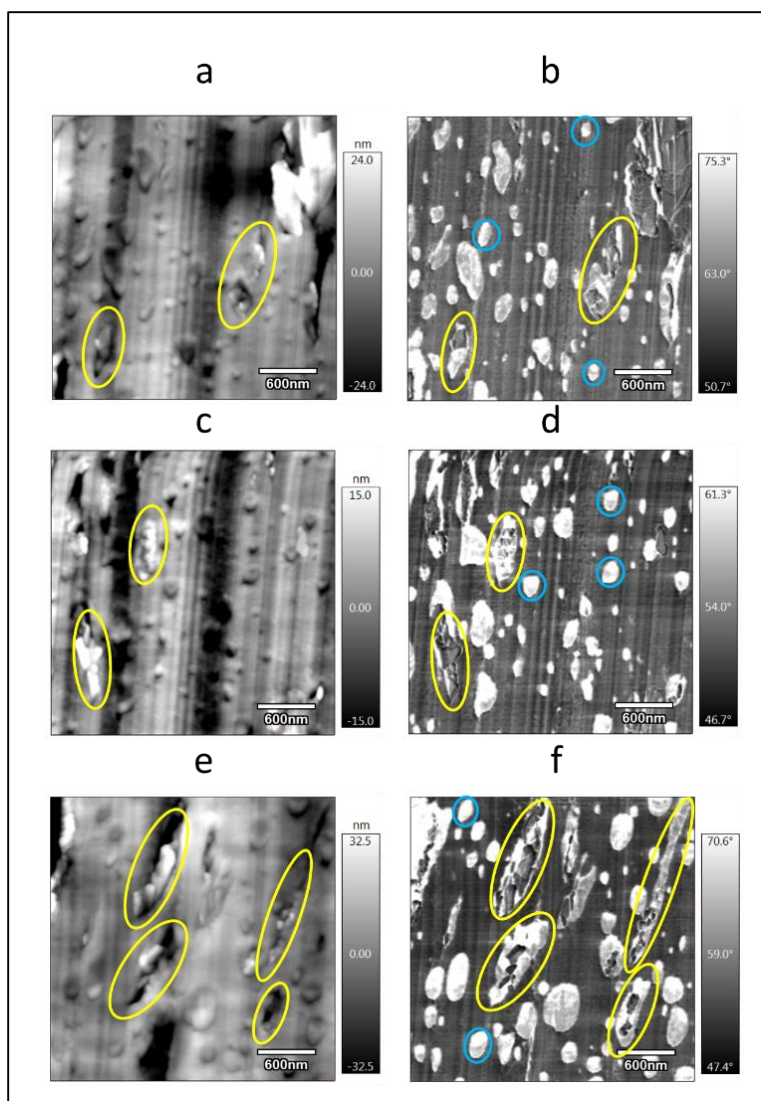


Figure 84: (a), (c), and (e) AFM topography; (b), (d), and (f) the corresponding phase images of (a), (c), and (e) respectively of the injection moulded PLA/PCL/10 wt.% M5 (the yellow circles surround the PCL particles containing GNPs and the blue circles surround the pure PCL nodules)

Figure 85 shows the AFM images of the 3D printed PLA/PCL/10 wt.% M5 composite where Figure 85.a and its zoomed image 85.c correspond to the topography images and Figure 85.b and its zoomed image 85.d are the relevant phase images. The yellow circles surround some graphene particles. The absence or the low presence of the graphene particles inside the PCL nodules is noticeable if compared to previous observations of the injection moulded samples. It might be due to the formation of more graphene aggregates in the 3D printed samples that hindered their positioning in the small PCL nodules and instead they were all distributed in the PLA matrix. Lower mixing and laminar flow during the fabrication of filaments prior to printing could cause

aggregations owing to the action of van der Waals interactions between the graphene particles. The zoomed images 85.c and 85.d show an example of these aggregates surrounded by a yellow circle.

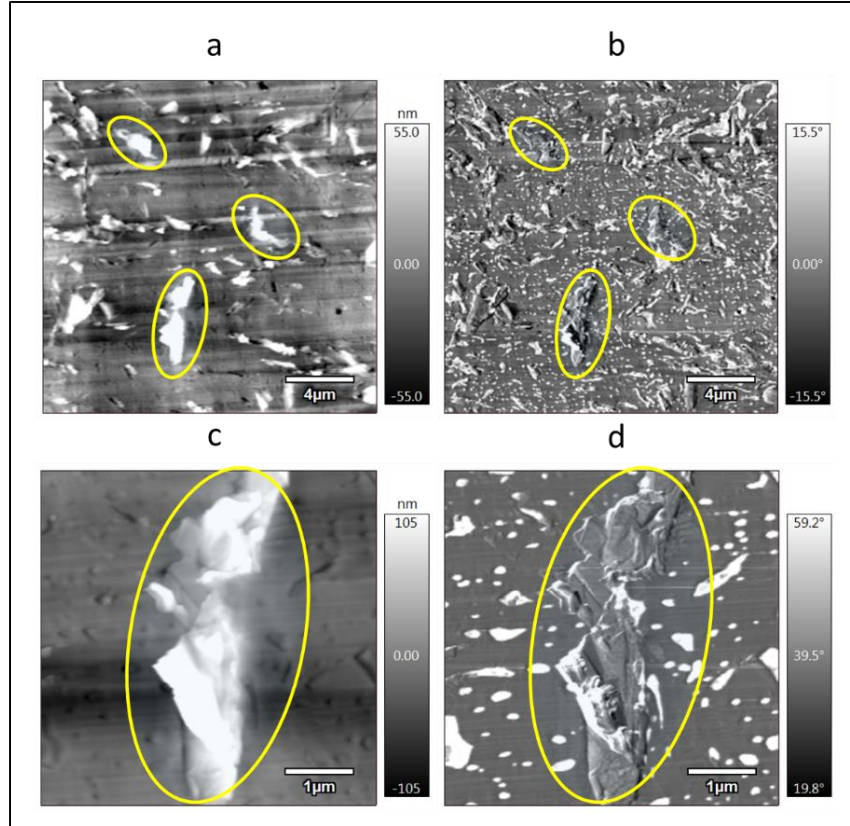


Figure 85: (a) AFM topography; (b) AFM phase, (c) zoomed image of (a); (d) zoomed image of (b), of 3D printed PLA/PCL/10 wt.% M5 (the yellow circles surround few GNPs)

The SEM images of the PLA/PCL/10 wt.% M5 injection moulded and 3D printed samples are exhibited in Figure 86. Prior to the SEM analysis, the surfaces of these samples were etched using toluene which can dissolve only the PCL phase at room temperature while it has no influence on the PLA phase. These images are in accordance with the AFM observations where in all of them the yellow arrows are pointed towards the pores where PCL were supposed to be present emphasizing the nodular structure of this polymer in the composites. In addition, the yellow circles surround some of the graphene flakes that are present in the PCL pores and thus confirming what has been indicated by the AFM technique regarding the preference of this nanofiller to the PCL phase.

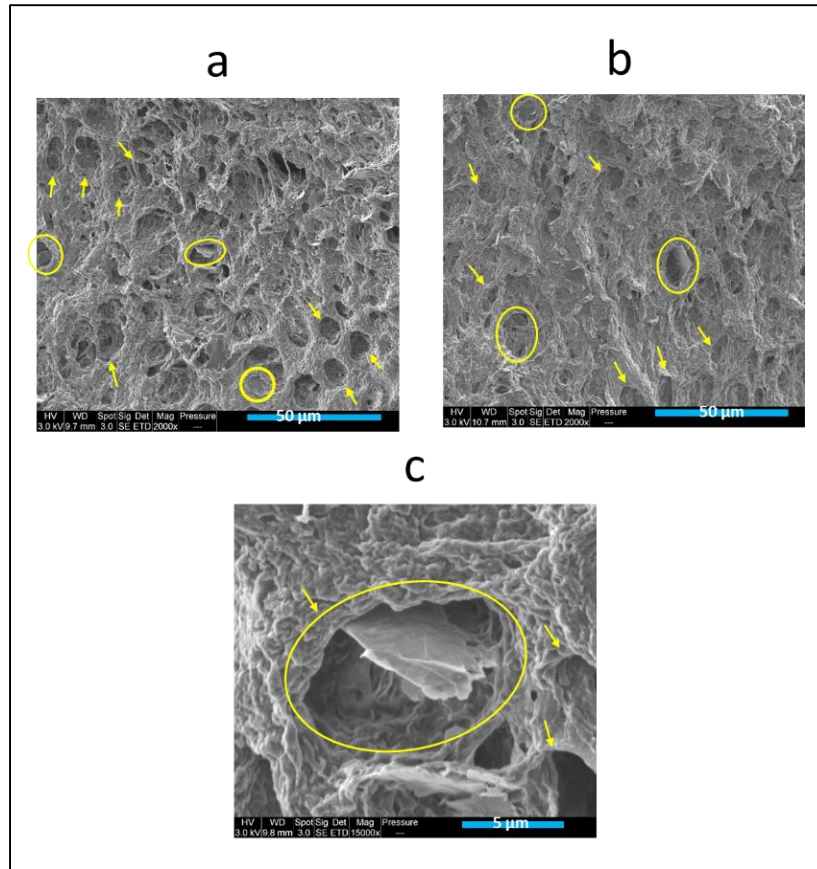


Figure 86: (a) and (c) SEM images of toluene etched injection moulded PLA/PCL/10 wt.% M5 composite; (b) SEM images of toluene etched 3D printed PLA/PCL/10 wt.% M5 composite (the yellow circles surround the GNPs positioned in the pores where the PCL nodules were supposed to be and the yellow arrows are pointed towards these pores)

In Figure 87, several SEM images of the injection moulded (b, c, d) and 3D printed PLA/PCL/15 wt.% M5 (a) composites are shown. The yellow ellipses in Figure 87.a surround some graphene platelets whose orientation is driven by the printing pattern. The extrusion induced orientation phenomenon of GNPs is due to the large shear rate between the molten composite and the inner wall of the nozzle [39]. In Figures 87.b, 87.c, and 87.d, the dotted blue lines show that most of the graphene nanoplatelets (surrounded by yellow circles) have similar orientation in these parts of the injected samples that is determined by the flow direction of the molten material during the injection process. Wu et Drzal compounded GNP and polyetherimide (PEI) by melt-extrusion followed by injection molding. They figured out that the GNP have unidirectional orientation in the injection moulded specimens [40].

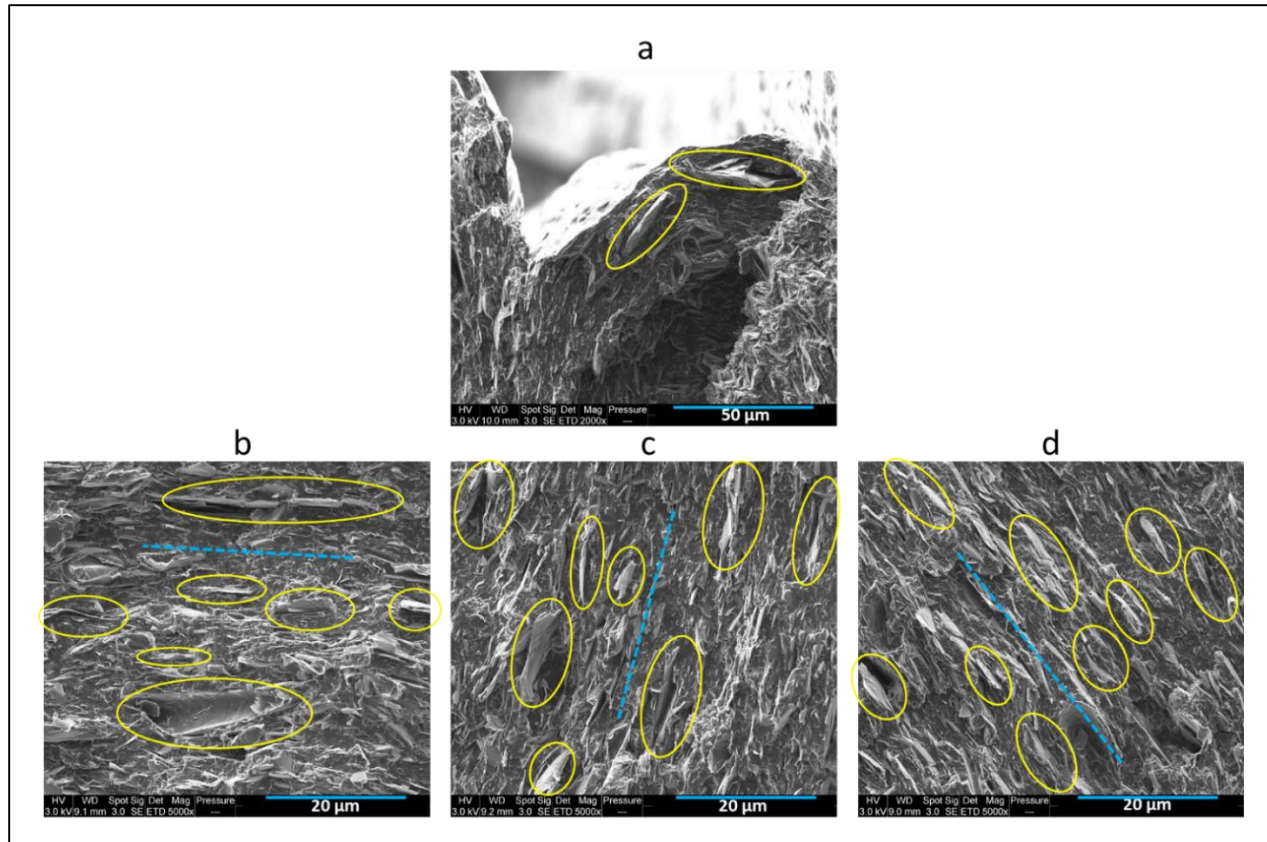


Figure 87: (a) SEM image of 3D printed PLA/PCL/15 wt% M5; (b), (c), and (d) SEM images of injection moulded PLA/PCL/15 wt.% M5 composite (the yellow ellipses surround some graphene flakes and the dotted lines indicate the similar orientation of the graphene platelets in the injection moulded samples)

Figures 88.a and 88.b correspond to the SEM pictures of the injection moulded and 3D printed PLA/PCL/15 wt.% M5 specimens respectively. These images are relevant to the parts close to the surface (small black circle in Figure 88.c). What is clear is the lower presence of graphene close to the surface of the injection moulded sample as compared to the 3D printed sample (graphene particles are surrounded by yellow circles) and this can be supported by the EDX spectra (Figures d and e). The EDX of the 3D printed sample shows greater carbon content (66.2%) as compared to the EDX of the injection moulded sample (60.2%) and this confirms the higher presence of GNP on the surface of the 3D printed sample.

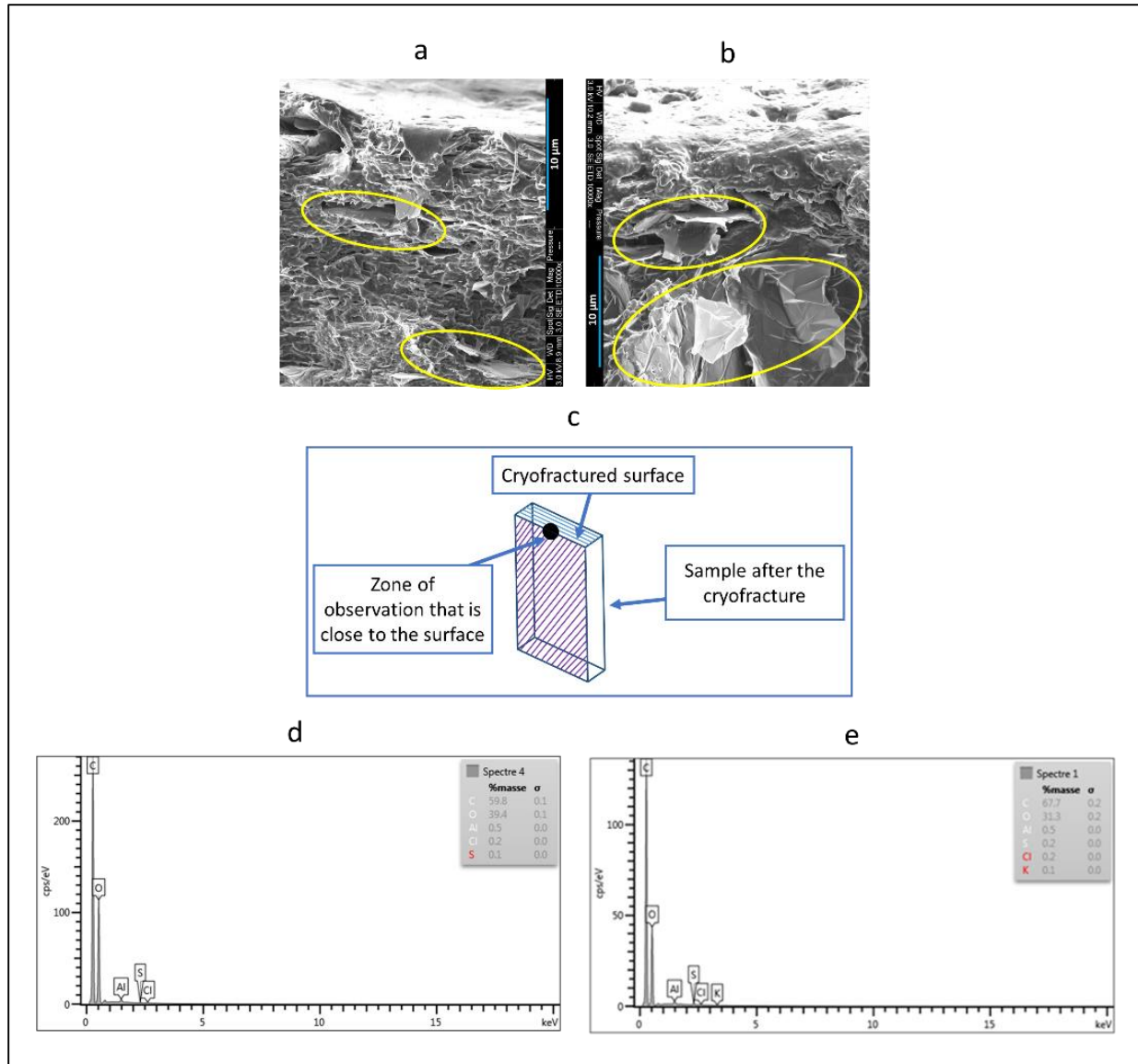


Figure 88: (a) SEM image of the injection moulded PLA/PCL/15 wt.% M5 composite and its EDX (d); (b) SEM image of 3D printed PLA/PCL/15 wt.% M5 composite and its EDX (e); (c) the zone of observation where (a) and (b) were taken and indicated by the small black circle (the yellow circles surround some graphene flakes)

Figure 89 shows the interface of two 3D printed filaments of non-etched (Figures 89.a and 89.b) and etched (Figures 89.c, 89.d, 89.e, and 89.f) surface samples. The yellow rectangles in Figures 89.a, 89.c, and 89.e are zoomed in Figures 89.b, 89.d, and 89.f respectively. In the zoomed images, the yellow arrows are pointed towards stacks of the graphene flakes present at the interface of two printed filaments in the final 3D printed part. During the printing process, the

material is deposited in the form of thin filaments and at this time the graphene flakes gather at the interface.

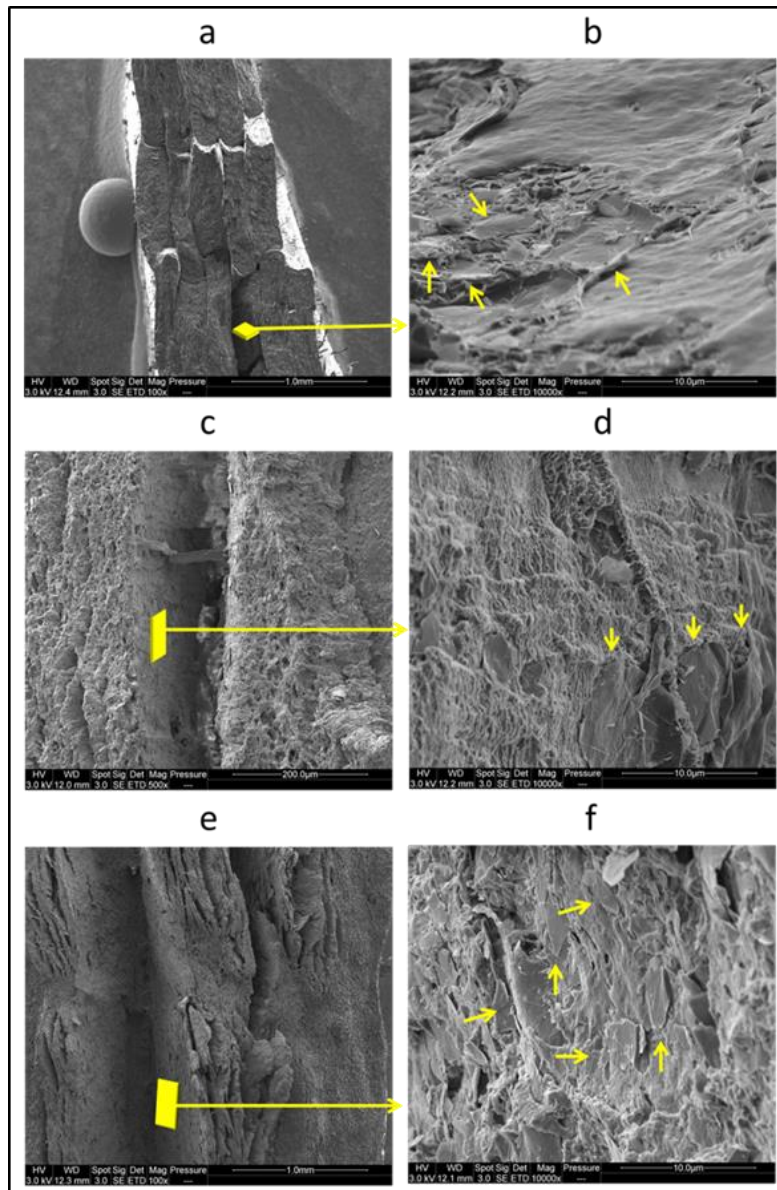


Figure 89: (a), (c), and (e) SEM images at the interface of two 3D printed filaments of PLA/PCL/15 wt.% M5 composites; (b), (d), and (f) the zoomed images of (a), (c), and (e) respectively (the yellow arrows are pointed towards some graphene nanoplatelets)

### 6.2.1. Rheology results of the 3D printed samples

The visco-elasticity measurements of the PLA/PCL/M5 nanocomposites were performed to study the influence of the GNP loading on the performance of the composites as well as to study the morphology and the formation of the internal graphene network within the manufactured

composite systems. The state of dispersion and interactions between polymer/nanoparticles are closely related to the rheological properties [41], therefore, the distribution of the nanoparticles in the polymer matrix was examined using this measurement technique.

Storage modulus ( $G'$ ) and complex viscosity dependence on the angular frequency in the linear viscoelastic region at 190 °C are presented in Figures 90 and 91 respectively. The pure polymers and the PLA/PCL blend exhibit a terminal liquid-like behaviour or a classical viscoelastic response in the storage modulus curve as shown in Figure 90. However, the composites exhibit an independence of the storage modulus on the angular frequency that is illustrated by a plateau in the terminal or low frequency region. This plateau indicates the formation of a non-terminal solid percolated network of the M5 GNP inside the polymer matrix. It is important to note that the storage modulus of the polymer composites increased with the increase of the percentage of graphene, and this is due to more filler-filler interactions as well as the reduction of the chain mobility of the polymers located near the graphene particles. Moreover, the length of the plateau is extended to higher frequencies with the increase of the percentage of graphene and this also emphasizes the fact of filler network formation and the entrapment of the polymeric chains in the filler network thus decreasing the flow of the polymers at low frequencies [42].

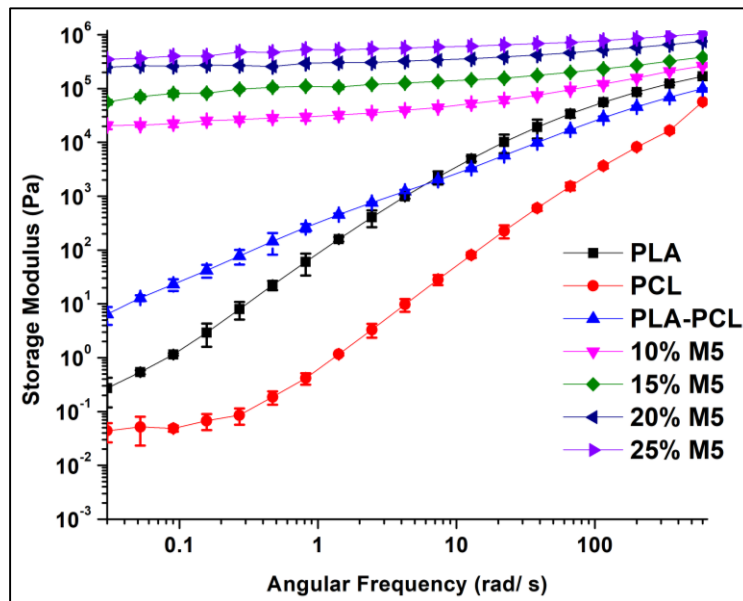


Figure 90: The storage modulus curves of PLA, PCL, PLA/PCL blend and its composites

In Figure 91, the complex viscosity increased with the increase of the graphene percentage in the matrix. This increase is more pronounced at lower frequency, and with the gradual increase of the frequency it is reduced due to the shear thinning behaviour [42]. The polymers and their blend exhibit a Newtonian behaviour followed by a shear-thinning behaviour which is considered as a common behaviour of the thermoplastics. For the composites this is not the case, there is no Newtonian behaviour and the increase in the viscosity at low frequency probably indicates a yield stress fluid behaviour.

Following the modulus and viscosity change in the low frequency region is important to determine the rheological percolation threshold of the filled polymer composites. The complex viscosity increases sharply at 10 wt.% of M5 indicating that there is a sudden change in the material structure and that the material has reached a rheological percolation at which the filler impedes the motion of the polymer matrix and forms a nanoscale network structure. In addition, the storage modulus is independent of the angular frequency in the low frequency region when the graphene percentage is 10 wt.%. This is an indication of the transition from a liquid-like to a solid-like viscoelastic behaviour thus declaring that this graphene percentage is above the rheological percolation threshold [43]

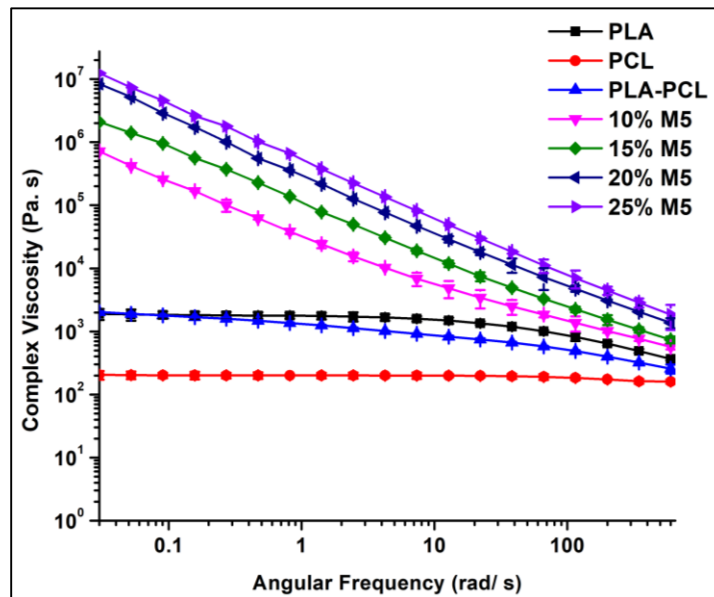


Figure 91: The complex viscosity curves of pure PLA and PCL polymers in addition to their blend and composites

### 6.2.2. Thermogravimetric analysis (TGA) of the 3D printed samples

The thermal stability of GNP, PLA, PCL, PLA/PCL blend and their composites are shown in Figure 92 and Table 16. These results show that PCL has better thermal stability as compared to PLA as indicated by the higher onset and maximal degradation temperatures. The mixture of the PLA and PCL gave a blend having close thermal properties to PLA rather than PCL due to the greater weight percentage of PLA in the polymer blend. In the blend and composites, there are two steps of degradation that correspond to the individual degradation of both non-miscible polymers. Also, the comparison between the theoretical and experimental percentage of char yield at 600 °C for all compositions, shows that both are close. This indicates that there is no improvement in the char formation and that there is a kind of dilution effect that could be attributed to the formation of graphene aggregates in the polymer matrix. Regarding the thermal stability of the composites, normally the GNP in these materials is prone to form a thermally stable network around the polymer matrix that could act as a protective layer. This layer is expected to lower the rate of heat transfer and the mass loss of polymers. In addition, GNP interfacial interaction with the polymer matrix could increase the energy required for the polymers decomposition leading to a greater thermal stability of the composites as compared to the polymers alone [44]. Also, the radical scavenging function of GNP could inhibit the degradation process of the organic polymers [45]. For instance, with respect to the PLA/Graphene and PCL/Graphene systems, normally graphene presence enhances the thermal stability of these polymers and this effect was obtained in several works [11][46-53]. Yet in our case, the addition of M5 GNP to the PLA/PCL blend did not cause any improvement in thermal stability whatever the percentage of GNP was. This may be attributed to the presence of aggregates of GNP and their poor interfacial adhesion with the polymer matrix.

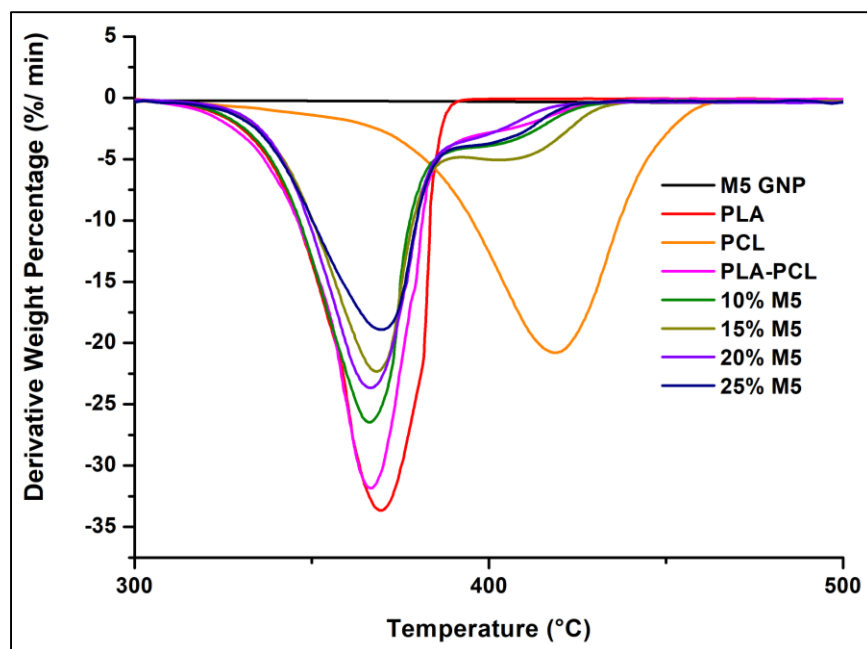


Figure 92: DTG curves ( $N_2$  atmosphere,  $10\text{ }^\circ\text{C}\cdot\text{min}^{-1}$ ) of GNP, PLA, PCL, PLA/PCL blends, and their composites

Table 16: The TGA results of PLA, PCL, their blend, and their composites

Sample name	Maximal Degradation Temperature ( $T_{\max}$ ) ( $^\circ\text{C}$ )	Total Mass Loss (%)	Experimental Percentage of Char Yield (at $600\text{ }^\circ\text{C}$ )	Theoretical Percentage of Char Yield (at $600\text{ }^\circ\text{C}$ )	Onset of Temperature ( $T_{\text{onset}}$ ) ( $^\circ\text{C}$ )
PLA	369	100	0	0	350
PCL	417	100	0	0	388
PLA/PCL	366	100	0	0	349
PLA/PCL/10 % M5	366	99	7	9	350
PLA/PCL/15 % M5	368	91	14	13	354
PLA/PCL/20 % M5	366	89	17	18	352
PLA/PCL/25 % M5	370	82	23	22	352

### 6.2.3. Differential scanning calorimetry (DSC) of the 3D printed samples

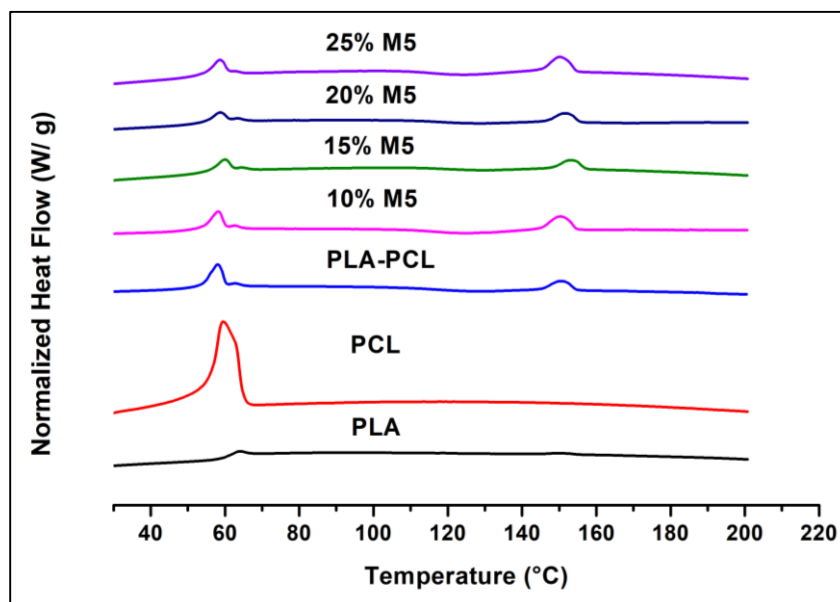


Figure 93: DSC curves of PLA, PCL, their blend, and their composites

Figure 93 shows the DSC curves of PLA, PCL, their blend, and their composites whose results are summarized in Table 17. The results were taken from the second heating step. The presence of PCL with PLA improved its crystallinity due to the appearance of the PLA crystallization peak in the PLA/PCL blend and the increase of the area of its melting peak. Similar nucleating effect of PCL in PLA was obtained in some other works [4][54-56] and the reason behind that is the recrystallization of the imperfect PLA crystals into more perfect  $\alpha$  crystals in the presence of PCL [57]. Other authors interpreted this improvement in the PLA crystallinity by the increase of the number of PLA nuclei that are generated at low temperatures and induced by the presence of PCL [58]. The degree of crystallinity of PLA was more enhanced in the case of composites with the increase of the percentage of graphene as compared to the pure blend. This indicates that graphene had a slight nucleating effect on the PLA crystallites in the PLA/PCL matrix. The melting temperatures of PLA and PCL were unchanged in the case of the blends and composites as compared to the pure polymers. Also, the PLA crystallization temperature was the same for the blend and the composites.

Table 17: The melting temperatures of PLA and PCL, crystallization temperature of PLA, and the degree of crystallinity of PLA in the PLA pure polymer, the blend, and the composites

Sample name	T <sub>m</sub> PLA (°C)	T <sub>m</sub> PCL (°C)	T <sub>c</sub> PLA (°C)	Degree of crystallinity of PLA (%)
PLA	149	-	-	0.7
PCL	-	59	-	-
PLA/PCL	150	58	126	1.5
PLA/PCL/10% M5	150	58	125	2.2
PLA/PCL/15% M5	153	59	128	2.4
PLA/PCL/20% M5	151	58	128	2.7
PLA/PCL/25% M5	150	58	123	4.5

#### 6.2.4. Tensile properties of the 3D printed samples

Mechanical properties in the polymer composites are governed by various factors such as the filler type and its structure and morphology, filler loading, filler quality, filler dispersion, filler orientation (random or aligned), filler-matrix adhesion, particles dimension, voids, filler surface modification, and the fabrication method [59]. What can lead to the improvement in the tensile properties of the GNP composites is the homogeneous dispersion of the nanoparticles, their orientation in the polymer matrix, and the strong interfacial interaction between graphene and the matrix [60]. In addition, when inorganic fillers such as GNP are loaded into the polymeric materials, they are capable to play the role of the skeleton in the matrix. Therefore, the movement of the macromolecular chains will be limited due to several physical cross-linking points between them and the polymer chains and thus improving the composites stiffness. The stiffness could be improved also by the heterogeneous nucleation performed by the filler that causes an increase in the degree of crystallinity of the matrix or change its crystal type structure [61].

Table 18 shows the tensile properties of 3D printed PLA, PLA/PCL blend, and PLA/PCL/M5 composites (raster angle: +45°/-45°). The Young's modulus was enhanced in the composites as

compared to the pure blend. This increase shows that GNP has a stiffening effect on the PLA/PCL matrix.

When a polymer composite filled with inorganic thin sheet shaped particles is under tensile load, the matrix will generate relative deformation whereas the particles will not deform [61]. The tensile strength could be decreased due to the geometry of the GNP that possess a flaky shaped structure and stack over each other to form agglomerations. As well as due to their sharp edges that initiate the cracks within the matrix [59]. In our case, the maximal tensile strength decreased with the addition of graphene. Moreover, referring to the SEM images of the 3D printed PLA/PCL/15 wt.% M5 composites (Figures 87.a and 88.b), the limited adhesion between the graphene particles and the matrix is obvious. This can explain the decrease in the tensile strength of the composites. This decrease could also be due to the location of the GNP at the surface of the filaments (Figure 89) which can enhance the delamination of the 3D printed adjacent layers. In a work addressed for understanding the influence of the filler size on the properties of PLA/GNP nanocomposites, the tensile strength was increased for the composites containing 7 wt.% of filler but beyond this value of weight percentage the tensile strength was decreased due to the presence of aggregates [3].

Tensile elongation at break is an important parameter for characterizing the ductility or the tensile fracture toughness of the materials. The elongation at break was enhanced just in the case of PLA/PCL blend as compared to PLA alone. The increase of graphene percentage led to the further decrease of this parameter. This result was also obtained by Gao et al. [3] who explained it by the fact that large GNP platelets exhibit large interfacial surface area that could make them more efficient in transferring stresses and thus acting as stiffening fillers but at the expense of the composite's ductility. This can be due to the larger interfacial surface area (per plate) that causes higher local stress concentrations in the matrix and therefore resulting in the embrittlement of the composite. Apart from this, composites ductility is affected by the state of dispersion of the GNP and more aggregations lead to lower toughness.

Table 18: The tensile properties of the 3D printed PLA, PLA/PCL blend, and its composites

Sample name	Young's Modulus (MPa)	Maximal Tensile Strength (MPa)	Elongation at Break (%)
PLA	3472 ± 151	60.9 ± 1.8	5.1 ± 0.5
PLA/PCL	2748 ± 117	47.4 ± 3.3	12.1 ± 2.2
PLA/PCL/10 % M5	3014 ± 67	40.2 ± 1.1	4.7 ± 0.5
PLA/PCL/15 % M5	3866 ± 173	39.9 ± 3.4	3 ± 0.2
PLA/PCL/20 % M5	3744 ± 211	40 ± 2	3.2 ± 0.1
PLA/PCL/25 % M5	3997 ± 126	34.7 ± 0.8	2.2

### 6.2.5. Electrical volume resistivity

Table 19: Electrical volume resistivity of 3D printed composites having graphene percentages starting from 10 wt.% to 25 wt.% (The raster angle of these samples is +45°/-45°, Figure 80.a)

Sample name	Electrical volume resistivity ( $\Omega$ .cm)
PLA/PCL/10% M5	No results
PLA/PCL/15% M5	660.2 ± 62.3 (9.4%)
PLA/PCL/20% M5	171.8 ± 15.8 (9.2 %)
PLA/PCL/25% M5	18.9 ± 1.5 (7.9 %)

The conductive nanofillers provide many conductive pathways in an insulating matrix resulting in the increase of its electrical conductivity. For the composites to be electrically conductive, the incorporated conductive fillers should make contact with one another and construct interconnected pathways for electrons to travel. Using fillers with large-sized sheets makes it

possible for the pathways to be formed with low concentration [62]. For instance, there are many types of contact between the GNP particles in the polymer matrix such as the plane to plane, edge to edge, and edge to plane [63].

When the electrical resistance measurements were performed using the four probes contact method on the injection moulded and 3D printed composites, there were no results for the injection moulded samples. This was also reached by Wu et Drzal who found much better electrical conductivity for the compression moulded GNP/Polyetherimide (PEI) composites as compared to the injection moulded ones (two times greater). The reason according to them was the aligned orientation of the GNP particles in the injection moulded samples that prevented them from connecting with each other [40]. This could be also explained by the presence of more PLA and PCL polymers at the surface of the injection moulded samples as it was exhibited by the SEM analysis in the present study (Figure 88.a). Through the electrical conductivity measurements using the four probes method, the electrons are transferred from one external copper probe to the other external probe in a 2D radial pattern [64]. During their trajectory, the electrons cross through the sample's surface. Then, if the surface is insulating as in the case of the injection moulded sample, these electrons will not be able to accomplish their journey. Conversely, the presence of more graphene close to the surface of the 3D printed samples was highlighted in Figure 88.b. In addition, the 3D printed samples showed stacking of the graphene platelets at the interface of the layers (Figure 89) and consequently this explains the electrical conductivity results for these samples on the contrary to the injection moulded ones which do not possess a similar layered structure.

The electrical percolation threshold is defined as the minimal percentage of conductive filler required to be added to transform a polymer from an insulating material to a semi-conductive one. For the 3D printed samples, the 10 wt.% of M5 is under the electrical percolation threshold. However, since the 15 wt.% M5 composite showed an electrical resistance value using the four probes measurement method, then it is considered beyond the electrical percolation threshold. The electrical volume resistivity clearly decreased as the percentage of graphene increased to 20 wt.%. However, a significant decrease of the resistivity is observed when the percentage of graphene reached 25 wt.%. Table 19 and Figure 94 show this decrease in the electrical volume

resistivity of the composites with the increase of percentage of graphene. It has been mentioned that the 10wt.% of graphene is considered as beyond the rheological percolation threshold but according to the electrical conductivity results this composite is electrically insulating. This indicates that the rheological percolated network can be formed at lower percentage of graphene as compared to the electrical percolated network due to the difference in the percolation mechanisms. The rheological percolation requires larger inter-particle distance (tens of nanometers), whereas the electrical percolation needs around 5 nm to establish electron hopping. Add to this, there are three kinds of networks in the graphene-polymer composites: a temporary entangled polymer network, a combined graphene-polymer-graphene network, and interconnected graphene network. At low graphene concentrations, graphene sheets exist as individual units because the average distance between them is greater than their own size range. Then, when the graphene concentration reaches the rheological percolation threshold, a polymer-bridged graphene network is constructed in the composites. In this case, the polymer chains attach on the surface of the graphene nanoplatelets and act as bridges to connect the graphene sheets thus restricting the motion of the polymer chains through a pseudo-solid-like behaviour. When the graphene concentration is high enough for these sheets to be in direct contact, a 3D graphene network is constructed to establish the onset of the electrical percolation threshold. Within this network, the free rotation of graphene nanoplatelets is hindered by the adjacent ones and the polymer chains are confined to form high density interfacial region in the vicinity of these nanoplatelets [65]. Several works dealing with the graphene composites have also obtained inferior rheological percolation threshold as compared to the electrical percolation one [41][66-68].

In a work conducted to study the effect of GNP on the physical properties of acrylonitrile-butadiene-styrene nanocomposites, M5 GNP was used. According to their results, for compression moulded samples containing 15 wt.%, 20 wt.%, and 25 wt.% of M5, the volume electrical resistivity values were approximately  $10^6$ ,  $10^4$  and  $10^3$   $\Omega$ .cm respectively [69]. Whereas in our case for the same weight percentages of M5 GNP, the obtained resistivity values were 660.2, 171.8, and 18.9  $\Omega$ .cm respectively. In another work directed for studying the effect of the graphene nanoplatelets morphology on the dispersion and physical properties of polycarbonate

composites, and by using M5 GNP, the authors obtained for compression moulded samples an electrical volume conductivity of  $10^{-10}$  S.cm<sup>-1</sup> for 15 wt.% of filler whereas in our case the electrical volume conductivity is  $1.5 \times 10^{-3}$  S.cm<sup>-1</sup> [70]. For 20 wt.% of M5, their obtained volume conductivity was  $10^{-6}$  S.cm<sup>-1</sup> whereas  $5.8 \times 10^{-3}$  S.cm<sup>-1</sup> was achieved in the present study. This indicates that although our printed samples have some porosity due to the process that is absent in the compression moulded samples, we obtained higher values of conductivity for the same weight percentages of M5 GNP.

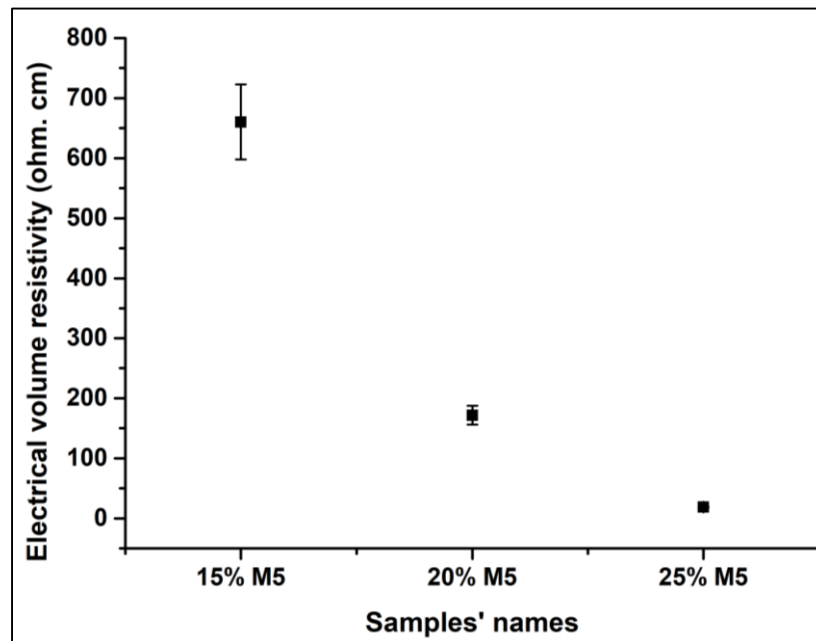


Figure 94: The variation of the electrical volume resistivity of the composites as function of the percentage of M5 GNP

To test the applicability of these semi-conductive 3D printed composites, an electrical circuit was constructed using a voltage generator (voltage of 5 V), a LED, and the 3D printed sample. When the 3D printed PLA/PCL/15 wt.% M5 was connected in the circuit, there was no lightening of the LED. However, when the PLA/PCL/20 wt.% M5 and PLA/PCL/25 wt.% M5 were connected instead, the LED was lightened up. By keeping the same voltage (5 V), the 25 wt.% sample led to more light intensity of the LED due to its lower electrical volume resistivity. The circuit connected using the PLA/PCL/25 wt.% M5 3D printed composite is shown in Figure 95.

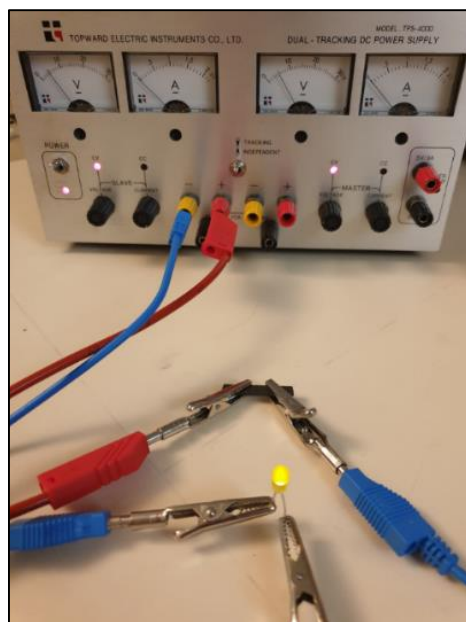


Figure 95: The electrical circuit connected using the 3D printed PLA/PCL/25 wt.% M5 composite

The electrical volume resistivity results of the PLA/PCL/20 wt.% M5 composites printed according to the diagonal pattern (alternating raster angle of  $+45^\circ/-45^\circ$ ) (Figure 80.a), the longitudinal pattern (raster angle of  $0^\circ$ ) (Figure 80.b), and transversal pattern (raster angle of  $90^\circ$ ) (Figure 80.c) are shown in Table 20.

Table 20: The electrical volume resistivity results of the PLA/PCL/20 wt.% M5 composites according to three different patterns by changing the printing raster angles

Raster angle	Electrical volume resistivity ( $\Omega\cdot\text{cm}$ )
$+45^\circ/-45^\circ$	$171.8 \pm 15.8$ (9.2%)
$0^\circ$	$106 \pm 10.1$ (9.5%)
$90^\circ$	$138.4 \pm 7.5$ (5.4%)

The electrical volume resistivity of the transversal pattern composite was lower than that of the one printed according to the  $+45^\circ/-45^\circ$  raster angle. The composite printed in the longitudinal pattern showed the lowest electrical resistivity. It was reported that the best reinforcement efficiency of GNPs within PA12 matrix was for samples printed according to  $0^\circ$  raster angle and this was explained by the fact that in this case the GNPs were aligned along the stretching direction [39]. It seems that the oriented fillers can build conductive pathways more easily thus

leading to lower resistivity. The GNPs will be oriented in the direction of stretching; therefore, the raster angle is an important criterion to be taken into consideration when dealing with the electrical conductivity of the material.

## **7. Conclusion**

This study shows for the first time the fabrication of semi-conductive PLA/PCL/GNP composites using FFF technique. The microstructural analysis showed that M5 GNP was selectively localized in PCL rather than PLA and this has been ascribed to the lower viscosity and lower melting temperature of PCL that favoured the localization of the graphene in this polymer during extrusion. This is not in accordance with the wettability prediction, thus revealing that in this case the kinetic factors defeated the thermodynamic ones. The GNP/PCL nodules have greater size as compared to the pure PCL nodules. Moreover, the thermal tests exhibited that no thermal stability improvement was accomplished in the presence of graphene and this may be ascribed to the aggregation of these nanoparticles in the polymer matrix. The DSC tests revealed that the percentage of crystallinity of PLA increased slightly in the presence of PCL and with the increase of the percentage of graphene. The electrical resistance measurement using the four-probe method indicated that the injection moulded composites containing 15 wt.%, 20 wt.%, and 25 wt.% are electrically insulators whereas the 3D printed composites containing the same percentages of graphene are semi-conductors. In particular, the 20 wt.% and 25 wt.% 3D printed samples were able to connect an electrical circuit. The reason behind these differences lies in the microstructural differences between both types of samples that are caused by the process, where the injection moulded samples lack enough conductive fillers on their surface whereas the 3D printed samples have graphene platelets on the surface of the printed filaments (during printing on the building platform) whose direction fits to the direction of printing. The presence of a plateau in the storage modulus curves in the low frequency region suggested the formation of a rheological percolated network that needs lower graphene percentage as compared to the electrical percolated network. The Young's modulus results are in agreement with the electrical results and the increase in the graphene percentage leads to increasing this property, but a

levelling off appears starting from 15 wt.% of GNP. However, probably due to the localization of the graphene sheets on the surface of the printed filaments which weakens the interfacial adhesion between the layers, the tensile strength decreased with the increase of the graphene percentage whose aggregations caused the decrease in the elongation at break of the composites. It is important to notice also that the raster angle has also an impact on the electrical resistance results where the samples printed in the longitudinal direction showed the best electrical conductivity results.

## 8. Bibliography

- [1] T. A. Hottle, M. M. Bilec, and A. E. Landis, "Sustainability assessments of bio-based polymers," *Polym. Degrad. Stab.*, vol. 98, no. 9, pp. 1898–1907, 2013, doi: <https://doi.org/10.1016/j.polymdegradstab.2013.06.016>.
- [2] K. Fukushima and Y. Kimura, "Stereocomplexed polylactides (Neo-PLA) as high-performance bio-based polymers: their formation, properties, and application," *Polym. Inter.*, vol. 55, no. 6, pp. 626–642, 2006.
- [3] Y. Gao, O. T. Picot, E. Bilotti, and T. Peijs, "Influence of filler size on the properties of poly(lactic acid) (PLA)/graphene nanoplatelet (GNP) nanocomposites," *Eur. Polym. J.*, vol. 86, pp. 117–131, 2017, doi: [10.1016/j.eurpolymj.2016.10.045](https://doi.org/10.1016/j.eurpolymj.2016.10.045).
- [4] J. Urquijo, G. Guerrica-Echevarría, and J. I. Eguiazábal, "Melt processed PLA/PCL blends: Effect of processing method on phase structure, morphology, and mechanical properties," *J. Appl. Polym. Sci.*, vol. 132, no. 41, pp. 1–9, 2015, doi: [10.1002/app.42641](https://doi.org/10.1002/app.42641).
- [5] Z. Su, K. Huang, and M. Lin, "Thermal and Mechanical Properties of Poly(lactic acid)/Modified Carbon Black Composite," *J. Macromol. Sci. Part B*, vol. 51, no. 8, pp. 1475–1484, Aug. 2012, doi: [10.1080/00222348.2011.632741](https://doi.org/10.1080/00222348.2011.632741).
- [6] N. Al Habis, A. El Moumen, M. Tarfaoui, and K. Lafdi, "Mechanical properties of carbon black/poly ( $\epsilon$ -caprolactone)-based tissue scaffolds," *Arab. J. Chem.*, vol. 13, no. 1, pp. 3210–3217, 2020, doi: <https://doi.org/10.1016/j.arabjc.2018.10.005>.
- [7] W. M. Chiu, H. Y. Kuo, P. A. Tsai, and J. H. Wu, "Preparation and Properties of Poly (Lactic Acid) Nanocomposites Filled with Functionalized Single-Walled Carbon Nanotubes," *J. Polym. Environ.*, vol. 21, no. 2, pp. 350–358, 2013, doi: [10.1007/s10924-012-0514-6](https://doi.org/10.1007/s10924-012-0514-6).
- [8] H. Tohidlou, S. S. Shafiei, S. Abbasi, M. Asadi-Eydivand, and M. Fathi-Roudsari, "Amine-functionalized Single-walled Carbon Nanotube/Polycaprolactone Electrospun Scaffold for Bone Tissue Engineering: in vitro Study," *Fibers Polym.*, vol. 20, no. 9, pp. 1869–1882, 2019, doi: [10.1007/s12221-019-1262-1](https://doi.org/10.1007/s12221-019-1262-1).
- [9] G. Wang, L. Wang, L. H. Mark, V. Shaayegan, G. Wang, H. Li, G. Zhao, and C. B. Park, "Ultralow-Threshold and Lightweight Biodegradable Porous PLA/MWCNT with Segregated Conductive Networks for High-Performance Thermal Insulation and Electromagnetic Interference Shielding Applications," *ACS Appl. Mater. Interfaces*, vol. 10, no. 1, pp. 1195–1203, Jan. 2018, doi: [10.1021/acsami.7b14111](https://doi.org/10.1021/acsami.7b14111).
- [10] P. Pötschke, T. Villmow, and B. Krause, "Melt mixed PCL/MWCNT composites prepared at different rotation speeds: Characterization of rheological, thermal, and electrical properties, molecular weight, MWCNT macrodispersion, and MWCNT length distribution," *Polymer (Guildf.)*, vol. 54, no. 12, pp. 3071–3078, 2013, doi: <https://doi.org/10.1016/j.polymer.2013.04.012>.
- [11] M. Murariu, A.-L. Dechief, L. Bonnaud, Y. Paint, A. Gallos, G. Fontaine, S. Bourbigot, and P. Dubois, "The production and properties of polylactide composites filled with expanded

graphite,” *Polym. Degrad. Stab.*, vol. 95, no. 5, pp. 889–900, 2010, doi: <https://doi.org/10.1016/j.polymdegradstab.2009.12.019>.

[12] M. Forouharshad, L. Gardella, D. Furfaro, M. Galimberti, and O. Monticelli, “A low-environmental-impact approach for novel bio-composites based on PLLA/PCL blends and high surface area graphite,” *Eur. Polym. J.*, vol. 70, pp. 28–36, 2015, doi: <https://doi.org/10.1016/j.eurpolymj.2015.06.016>.

[13] D. Wu, Y. Cheng, S. Feng, Z. Yao, and M. Zhang, “Crystallization Behavior of Polylactide/Graphene Composites,” *Ind. Eng. Chem. Res.*, vol. 52, no. 20, pp. 6731–6739, May 2013, doi: 10.1021/ie4004199.

[14] W. Wang et al., “Enhancing the Hydrophilicity and Cell Attachment of 3D Printed PCL/Graphene Scaffolds for Bone Tissue Engineering,” *Materials (Basel)*, vol. 9, no. 12, 2016, doi: 10.3390/ma9120992.

[15] E. Chiesa, R. Dorati, S. Pisani, G. Bruni, L. G. Rizzi, B. Conti, T. Modena, and I. Genta, “Graphene Nanoplatelets for the Development of Reinforced PLA–PCL Electrospun Fibers as the Next-Generation of Biomedical Mats,” *Polymers (Basel)*, vol. 12, no. 6, 2020, doi: 10.3390/polym12061390.

[16] S. Kashi, R. K. Gupta, T. Baum, N. Kao, and S. N. Bhattacharya, “Phase transition and anomalous rheological behaviour of polylactide/graphene nanocomposites,” *Compos. Part B Eng.*, vol. 135, pp. 25–34, 2018, doi: <https://doi.org/10.1016/j.compositesb.2017.10.002>.

[17] S. Kashi, R. K. Gupta, N. Kao, S. A. Hadigheh, and S. N. Bhattacharya, “Influence of graphene nanoplatelet incorporation and dispersion state on thermal, mechanical and electrical properties of biodegradable matrices,” *J. Mater. Sci. Technol.*, vol. 34, no. 6, pp. 1026–1034, 2018, doi: <https://doi.org/10.1016/j.jmst.2017.10.013>.

[18] Z. Liu, Y. Wang, B. Wu, C. Cui, Y. Guo, and C. Yan, “A critical review of fused deposition modeling 3D printing technology in manufacturing polylactic acid parts,” *Int. J. Adv. Manuf. Technol.*, vol. 102, no. 9, pp. 2877–2889, 2019, doi: 10.1007/s00170-019-03332-x.

[19] M. Fredrick Madaraka and E. T. Akinlabi, “Basics of Fused Deposition Modelling ( FDM ),” *Nat. Public Heal. Emerg. Collect.*, vol. 30, pp. 1–15, 2020, doi: 10.1007/978-3-030-48259-6.

[20] E. Ivanov, R. Kotsilkova, H. Xia, Y. Chen, R. K. Donato, A. P. Godoy, R. Di Maio, C. Silvestre, S. Cimmino, and V. Angelov, “PLA/Graphene/MWCNT Composites with Improved Electrical and Thermal Properties Suitable for FDM 3D Printing Applications,” *Appl. Sci.*, vol. 9, no. 6, 2019, doi: 10.3390/app9061209.

[21] J. H. Kim, J. S. Hong, and K. H. Ahn, “Design of electrical conductive poly(lactic acid)/carbon black composites by induced particle aggregation,” *J. Appl. Polym. Sci.*, vol. 137, no. 42, p. 49295, 2020, doi: <https://doi.org/10.1002/app.49295>.

[22] Z. Xu, Y. Zhang, Z. Wang, N. Sun, and H. Li, “Enhancement of Electrical Conductivity by Changing phase Morphology for Composites Consisting of Polylactide and Poly( $\epsilon$ -caprolactone)

Filled with Acid-Oxidized Multiwalled Carbon Nanotubes,” *ACS Appl. Mater. Interfaces*, vol. 3, no. 12, pp. 4858–4864, Dec. 2011, doi: 10.1021/am201355j.

[23] J. Huang, C. Mao, Y. Zhu, W. Jiang, and X. Yang, “Control of carbon nanotubes at the interface of a co-continuous immiscible polymer blend to fabricate conductive composites with ultralow percolation thresholds,” *Carbon N. Y.*, vol. 73, pp. 267–274, 2014, doi: <https://doi.org/10.1016/j.carbon.2014.02.063>.

[24] E. D. Yildirim, H. Ayan, V. N. Vasilets, A. Fridman, S. Guceri, and W. Sun, “Effect of Dielectric Barrier Discharge Plasma on the Attachment and Proliferation of Osteoblasts Cultured over Poly( $\epsilon$ -caprolactone) Scaffolds,” *Plasma Process. Polym.*, vol. 5, no. 1, pp. 58–66, 2008, doi: <https://doi.org/10.1002/ppap.200700041>.

[25] D. K. Owens and R. C. Wendt, “Estimation of the surface free energy of polymers,” *J. Appl. Polym. Sci.*, vol. 13, no. 8, pp. 1741–1747, 1969, doi: <https://doi.org/10.1002/app.1969.070130815>.

[26] L. Jeantet, A. Regazzi, A. Taguet, M. Pucci, A.-S. Caro, and J.-C. Quantin, “Biopolymer blends for mechanical property gradient 3D printed parts,” *Express Polym. Lett.*, vol. 15, pp. 137–152, 2021, doi: 10.3144/expresspolymlett.2021.13.

[27] S. Steinmann, W. Gronski, and C. Friedrich, “Influence of selective filling on rheological properties and phase inversion of two-phase polymer blends,” *Polymer (Guildf.)*, vol. 43, no. 16, pp. 4467–4477, 2002, doi: [https://doi.org/10.1016/S0032-3861\(02\)00271-9](https://doi.org/10.1016/S0032-3861(02)00271-9).

[28] R. Patwa, A. Kumar, and V. Katiyar, “Crystallization kinetics, morphology, and hydrolytic degradation of novel bio-based poly(lactic acid)/crystalline silk nano-discs nanobiocomposites,” *J. Appl. Polym. Sci.*, vol. 135, no. 33, pp. 1–18, 2018, doi: 10.1002/app.46590.

[29] A. Taguet, P. Cassagnau, and J.-M. Lopez-Cuesta, “Structuration, selective dispersion and compatibilizing effect of (nano)fillers in polymer blends,” *Prog. Polym. Sci.*, vol. 39, no. 8, pp. 1526–1563, 2014, doi: <https://doi.org/10.1016/j.progpolymsci.2014.04.002>.

[30] O. Yousefzade, J. Jeddi, E. Vazirinasab, and H. Garmabi, “Poly(lactic acid) phase transitions in the presence of nano calcium carbonate: Opposing effect of nanofiller on static and dynamic measurements,” *J. Thermoplast. Compos. Mater.*, vol. 32, p. 089270571875938, 2018, doi: 10.1177/0892705718759386.

[31] A. Mirzadeh, H. Ghasemi, F. Mahrous, and M. R. Kamal, “Reactive extrusion effects on rheological and mechanical properties of poly(lactic acid)/poly[(butylene succinate)-co-adipate]/epoxy chain extender blends and clay nanocomposites,” *J. Appl. Polym. Sci.*, vol. 132, no. 48, 2015, doi: <https://doi.org/10.1002/app.42664>.

[32] M. Mehrabi Mazidi, A. Edalat, R. Berahman, and F. S. Hosseini, “Highly-Toughened Polylactide- (PLA-) Based Ternary Blends with Significantly Enhanced Glass Transition and Melt Strength: Tailoring the Interfacial Interactions, Phase Morphology, and Performance,” *Macromolecules*, vol. 51, no. 11, pp. 4298–4314, Jun. 2018, doi: 10.1021/acs.macromol.8b00557.

- [33] E. Yildirim-Ayan, S. Güçeri, and W. Sun, "Effect of Oxygen-Radio Frequency Plasma Treatment on Three Dimensional Poly( $\epsilon$ -Caprolactone) Scaffolds," 2007, doi: 10.1115/MSEC2007-31169.
- [34] A. Paydayesh, A. Arefazar, and A. Jalaliarani, "A morphological study on the migration and selective localization of graphene in the PLA/PMMA blends," *J. Appl. Polym. Sci.*, vol. 133, no. 34, 2016, doi: <https://doi.org/10.1002/app.43799>.
- [35] J.-M. Park, G.-Y. Gu, Z.-J. Wang, D.-J. Kwon, and K. L. DeVries, "Interfacial durability and acoustical properties of transparent graphene nano platelets/poly (vinylidene fluoride) composite actuators," *Thin Solid Films*, vol. 539, pp. 350–355, 2013, doi: <https://doi.org/10.1016/j.tsf.2013.05.078>.
- [36] S. Dul, L. Fambri, C. Merlini, G. M. O. Barra, M. Bersani, L. Vanzetti, and A. Pegoretti, "Effect of graphene nanoplatelets structure on the properties of acrylonitrile–butadiene–styrene composites," *Polym. Compos.*, vol. 40, pp. E285–E300, 2019, doi: 10.1002/pc.24645.
- [37] J. de Aguiar, M. Decol, W. M. Pachekoski, and D. Becker, "Mixing-sequence controlled selective localization of carbon nanoparticles in PLA/PCL blends," *Polym. Eng. Sci.*, vol. 59, no. 2, pp. 323–329, 2019, doi: 10.1002/pen.24908.
- [38] I. Kelnar, J. Kratochvíl, L. Kaprálková, A. Zhigunov, and M. Nevoralová, "Graphite nanoplatelets-modified PLA/PCL: Effect of blend ratio and nanofiller localization on structure and properties," *J. Mech. Behav. Biomed. Mater.*, vol. 71, pp. 271–278, 2017, doi: <https://doi.org/10.1016/j.jmbbm.2017.03.028>.
- [39] D. Zhu, Y. Ren, G. Liao, S. Jiang, F. Liu, J. Guo, and G. Xu, "Thermal and mechanical properties of polyamide 12/graphene nanoplatelets nanocomposites and parts fabricated by fused deposition modeling," *J. Appl. Polym. Sci.*, vol. 134, no. 39, pp. 1–13, 2017, doi: 10.1002/app.45332.
- [40] H. Wu and L. T. Drzal, "Graphene nanoplatelet-polyetherimide composites: Revealed morphology and relation to properties," *J. Appl. Polym. Sci.*, vol. 130, no. 6, pp. 4081–4089, 2013, doi: 10.1002/app.39678.
- [41] A. Alipour, T. Giffney, R. Lin, and K. Jayaraman, "Effects of matrix viscosity on morphological and rheological properties and the electrical percolation threshold in graphene/epoxy nanocomposites," *Express Polym. Lett.*, vol. 15, no. 6, pp. 541–553, 2021, doi: 10.3144/expresspolymlett.2021.46.
- [42] S. E. Zakiyan, H. Azizi, and I. Ghasemi, "Influence of chain mobility on rheological, dielectric and electromagnetic interference shielding properties of poly methyl-methacrylate composites filled with graphene and carbon nanotube," *Compos. Sci. Technol.*, vol. 142, pp. 10–19, 2017, doi: <https://doi.org/10.1016/j.compscitech.2017.01.025>.
- [43] Q. Zhang, S. Rastogi, D. Chen, D. Lippits, and P. J. Lemstra, "Low percolation threshold in single-walled carbon nanotube/high density polyethylene composites prepared by melt

processing technique,” *Carbon* N. Y., vol. 44, no. 4, pp. 778–785, 2006, doi: <https://doi.org/10.1016/j.carbon.2005.09.039>.

[44] M. Ajorloo, M. Fasihi, M. Ohshima, and K. Taki, “How are the thermal properties of polypropylene/graphene nanoplatelet composites affected by polymer chain configuration and size of nanofiller?,” *Mater. Des.*, vol. 181, p. 108068, 2019, doi: <https://doi.org/10.1016/j.matdes.2019.108068>.

[45] K. Behera, M. Yadav, F.-C. Chiu, and K. Y. Rhee, “Graphene Nanoplatelet-Reinforced Poly(vinylidene fluoride)/High Density Polyethylene Blend-Based Nanocomposites with Enhanced Thermal and Electrical Properties,” *Nanomaterials*, vol. 9, no. 3, 2019, doi: [10.3390/nano9030361](https://doi.org/10.3390/nano9030361).

[46] P. Manafi, I. Ghasemi, M. Karrabi, H. Azizi, M. R. Manafi, and P. Ehsaninamin, “Thermal stability and thermal degradation kinetics (model-free kinetics) of nanocomposites based on poly(lactic acid)/graphene: the influence of functionalization,” *Polym. Bull.*, vol. 72, no. 5, pp. 1095–1112, 2015, doi: [10.1007/s00289-015-1325-4](https://doi.org/10.1007/s00289-015-1325-4).

[47] X. Li, Y. Xiao, A. Bergeret, M. Longerey, and J. Che, “Preparation of polylactide/graphene composites from liquid-phase exfoliated graphite sheets,” *Polym. Compos.*, vol. 35, no. 2, pp. 396–403, 2014, doi: <https://doi.org/10.1002/pc.22673>.

[48] R. Scaffaro and F. Lopresti, “Properties-morphology relationships in electrospun mats based on polylactic acid and graphene nanoplatelets,” *Compos. Part A Appl. Sci. Manuf.*, vol. 108, pp. 23–29, 2018, doi: <https://doi.org/10.1016/j.compositesa.2018.02.026>.

[49] R. B. Valapa, G. Pugazhenthii, and V. Katiyar, “Effect of graphene content on the properties of poly(lactic acid) nanocomposites,” *RSC Adv.*, vol. 5, no. 36, pp. 28410–28423, 2015, doi: [10.1039/C4RA15669B](https://doi.org/10.1039/C4RA15669B).

[50] M. Bagheri and A. Mahmoodzadeh, “Polycaprolactone/Graphene Nanocomposites: Synthesis, Characterization and Mechanical Properties of Electrospun Nanofibers,” *J. Inorg. Organomet. Polym. Mater.*, vol. 30, no. 5, pp. 1566–1577, 2020, doi: [10.1007/s10904-019-01340-8](https://doi.org/10.1007/s10904-019-01340-8).

[51] P. X. Thinh, C. Basavajara, J. K. Kim, and D. S. Huh, “Characterization and electrical properties of honeycomb-patterned poly( $\epsilon$ -caprolactone)/reduced graphene oxide composite film,” *Polym. Compos.*, vol. 33, no. 12, pp. 2159–2168, 2012, doi: <https://doi.org/10.1002/pc.22357>.

[52] R. Wang, X. Wang, S. Chen, and G. Jiang, “In Situ Polymerization Approach to Poly( $\epsilon$ -caprolactone)-Graphene Oxide Composites,” *Des. Monomers Polym.*, vol. 15, no. 3, pp. 303–310, 2012, doi: [10.1163/156855511X615696](https://doi.org/10.1163/156855511X615696).

[53] E. Murray, S. Sayyar, B. C. Thompson, R. Gorkin III, D. L. Officer, and G. G. Wallace, “A bio-friendly, green route to processable, biocompatible graphene/polymer composites,” *RSC Adv.*, vol. 5, no. 56, pp. 45284–45290, 2015, doi: [10.1039/C5RA07210G](https://doi.org/10.1039/C5RA07210G).

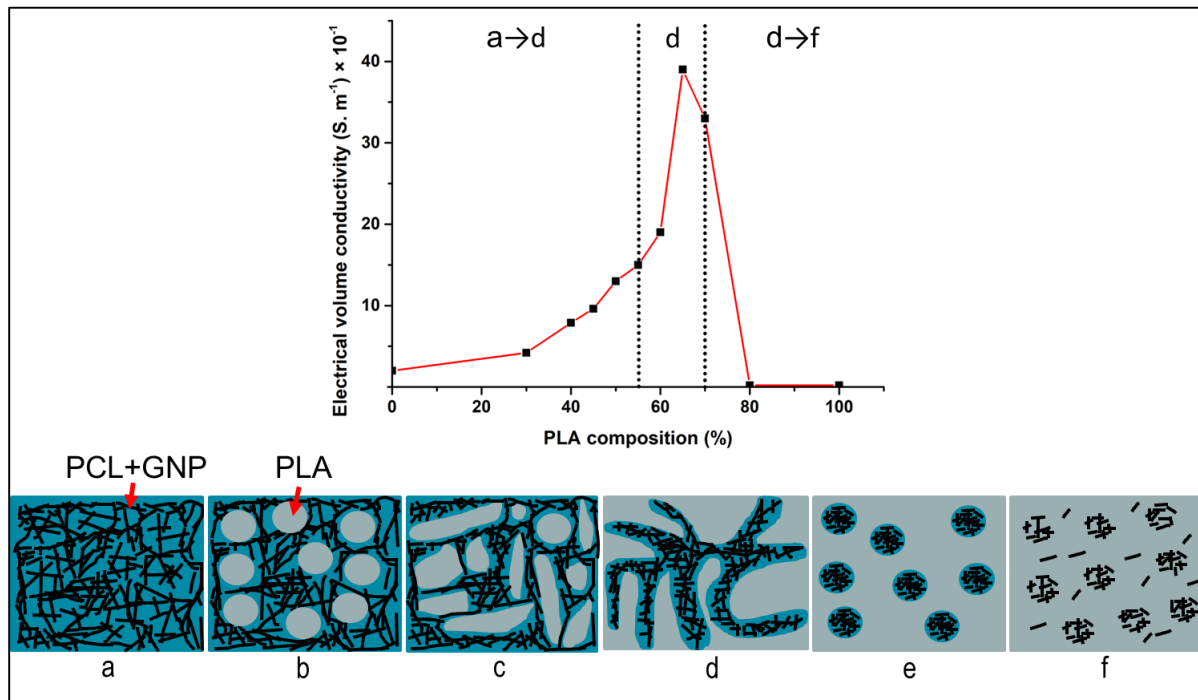
- [54] C. L. Simões, J. C. Viana, and A. M. Cunha, "Mechanical properties of poly( $\epsilon$ -caprolactone) and poly(lactic acid) blends," *J. Appl. Polym. Sci.*, vol. 112, no. 1, pp. 345–352, 2009, doi: <https://doi.org/10.1002/app.29425>.
- [55] M. Harada, K. Lida, K. Okamoto, H. Hayashi, and K. Hirano, "Reactive compatibilization of biodegradable poly(lactic acid)/poly( $\epsilon$ -caprolactone) blends with reactive processing agents," *Polym. Eng. Sci.*, vol. 48, no. 7, pp. 1359–1368, 2008, doi: [10.1002/pen](https://doi.org/10.1002/pen).
- [56] F. Tuba, L. Oláh, and P. Nagy, "Characterization of reactively compatibilized poly(d,l-lactide)/poly( $\epsilon$ -caprolactone) biodegradable blends by essential work of fracture method," *Eng. Fract. Mech.*, vol. 78, no. 17, pp. 3123–3133, 2011, doi: <https://doi.org/10.1016/j.engfracmech.2011.09.010>.
- [57] N. López-Rodríguez, A. López-Arraiza, E. Meaurio, and J. R. Sarasua, "Crystallization, morphology, and mechanical behavior of polylactide/poly( $\epsilon$ -caprolactone) blends," *Polym. Engineering Sci.*, vol. 46, no. 9, pp. 1299–1308, 2006, doi: <https://doi.org/10.1002/pen.20609>.
- [58] F. Sakai, K. Nishikawa, Y. Inoue, and K. Yazawa, "Nucleation Enhancement Effect in Poly(l-lactide) (PLLA)/Poly( $\epsilon$ -caprolactone) (PCL) Blend Induced by Locally Activated Chain Mobility Resulting from Limited Miscibility," *Macromolecules*, vol. 42, no. 21, pp. 8335–8342, Nov. 2009, doi: [10.1021/ma901547a](https://doi.org/10.1021/ma901547a).
- [59] J. Ervina, M. Jaafar, and S. Hamdan, "Effect of Filler Loading on the Tensile Properties of Multi-walled Carbon Nanotube and Graphene Nanopowder filled Epoxy Composites," *Procedia Chem.*, vol. 19, pp. 897–905, Dec. 2016, doi: [10.1016/j.proche.2016.03.132](https://doi.org/10.1016/j.proche.2016.03.132).
- [60] B. W. Chieng, N. A. Ibrahim, W. M. Z. W. Yunus, and M. Z. Hussein, "Poly(lactic acid)/Poly(ethylene glycol) Polymer Nanocomposites: Effects of Graphene Nanoplatelets," *Polymers (Basel)*, vol. 6, no. 1, pp. 93–104, 2014, doi: [10.3390/polym6010093](https://doi.org/10.3390/polym6010093).
- [61] J.-Z. Liang, Q. Du, G. C.-P. Tsui, and C.-Y. Tang, "Tensile properties of graphene nanoplatelets reinforced polypropylene composites," *Compos. Part B Eng.*, vol. 95, pp. 166–171, 2016, doi: <https://doi.org/10.1016/j.compositesb.2016.04.011>.
- [62] Y. Jun, J. G. Um, G. Jiang, and A. Yu, "A study on the effects of graphene nano-platelets (GnPs) sheet sizes from a few to hundred microns on the thermal, mechanical, and electrical properties of polypropylene (PP)/GnPs composites," *Express Polym. Lett.*, vol. 12, pp. 885–897, 2018.
- [63] D. Xiang, L. Wang, Y. Tang, C. Zhao, E. Harkin-Jones, and Y. Li, "Effect of phase transitions on the electrical properties of polymer/carbon nanotube and polymer/graphene nanoplatelet composites with different conductive network structures," *Polym. Int.*, vol. 67, no. 2, pp. 227–235, 2018, doi: <https://doi.org/10.1002/pi.5502>.
- [64] I. Miccoli, F. Edler, H. Pfnür, and C. Tegenkamp, "The 100th anniversary of the four-point probe technique: The role of probe geometries in isotropic and anisotropic systems," *J. Phys. Condens. Matter*, vol. 27, no. 22, 2015, doi: [10.1088/0953-8984/27/22/223201](https://doi.org/10.1088/0953-8984/27/22/223201).

- [65] C. He, X. She, Z. Peng, J. Zhong, S. Liao, W. Gong, J. Liao, and L. Kong, "Graphene networks and their influence on free-volume properties of graphene-epoxidized natural rubber composites with a segregated structure: Rheological and positron annihilation studies," *Phys. Chem. Chem. Phys.*, vol. 17, pp. 12175–12184, Apr. 2015, doi: 10.1039/c5cp00465a.
- [66] C. Gao, P. Liu, Y. Ding, T. Li, F. Wang, J. Chen, S. Zhang, Z. Li, and M. Yang, "Non-contact percolation of unstable graphene networks in poly(styrene-co-acrylonitrile) nanocomposites: Electrical and rheological properties," *Compos. Sci. Technol.*, vol. 155, pp. 41–49, 2018, doi: 10.1016/j.compscitech.2017.11.023.
- [67] S. Sadeghi, M. Arjmand, I. Otero Navas, A. Zehtab Yazdi, and U. Sundararaj, "Effect of Nanofiller Geometry on Network Formation in Polymeric Nanocomposites: Comparison of Rheological and Electrical Properties of Multiwalled Carbon Nanotube and Graphene Nanoribbon," *Macromolecules*, vol. 50, no. 10, pp. 3954–3967, May 2017, doi: 10.1021/acs.macromol.7b00702.
- [68] N. L. Batista, E. Helal, R. S. Kurusu, N. Moghimian, E. David, N.R. Demarquette, and P. Hubert, "Mass-produced graphene—HDPE nanocomposites: Thermal, rheological, electrical, and mechanical properties," *Polym. Eng. Sci.*, vol. 59, no. 4, pp. 675–682, 2019, doi: 10.1002/pen.24981.
- [69] S. Dul, A. Pegoretti, and L. Fambri, "Effects of the Nanofillers on Physical Properties of Acrylonitrile-Butadiene-Styrene Nanocomposites: Comparison of Graphene Nanoplatelets and Multiwall Carbon Nanotubes," *Nanomaterials*, vol. 8, no. 9, 2018, doi: 10.3390/nano8090674.
- [70] M. T. Müller, K. Hilarius, M. Liebscher, D. Lellinger, I. Alig, and P. Pötschke, "Effect of Graphite Nanoplate Morphology on the Dispersion and Physical Properties of Polycarbonate Based Composites," *Materials (Basel)*, vol. 10, no. 5, 2017, doi: 10.3390/ma10050545.



# Chapter 4: Influence of polymer processing on the double electrical percolation threshold in PLA/PCL/GNP nanocomposites

## 1. Graphical abstract



## 2. Abstract

For the first time, the double electrical percolation threshold was obtained in polylactide (PLA)/polycaprolactone (PCL)/graphene nanoplatelets (GNP) composite systems prepared by compression moulding and fused filament fabrication (FFF). Using scanning electron microscopy (SEM) and atomic force microscopy (AFM), the localization of GNP as well as the morphology of PLA and PCL phases were evaluated and correlated with the electrical conductivity results estimated by the four-point probe method electrical measurements. Solvent extraction method was used to confirm and quantify the co-continuity in these samples. At 10 wt.% of GNP,

compression moulded samples possessed a wide co-continuity range varying from PLA55/PCL45 to PLA70/PCL30. The best electrical conductivity results were found for compression moulded and 3D printed PLA65/PCL35/GNP that have the full co-continuous structure based on the experimental and theoretical findings. This composite owns the highest storage modulus and complex viscosity at low angular frequency range according to the melt shear rheology. Moreover, it exhibited the highest char formation and polymers degrees of crystallinity after the thermal investigation by thermogravimetric analysis (TGA) and differential scanning calorimetry (DSC) respectively. The effect of GNP content, compression moulding time, and multiple twin-screw extrusion blending steps on the co-continuity were also evaluated. Results showed that increasing the GNP content decreased the continuity of the polymer phases. Therefore, this work concluded that polymer processing methods impact the electrical percolation threshold and that the 3D printing of polymer composites entails higher electrical resistance as compared to compression moulding.

### **3. Introduction**

Nowadays, conductive polymer composites (CPCs) are required in various applications such as anti-static materials, electromagnetic interference shielding (EMI), sensors, and conductors [1-5] because they are light, cost-effective, and easily processed. But, it is important to manufacture these composites with low content of conductive fillers to avoid problems such as low mechanical properties, high costs, and high melt viscosities [6]. One of the most effective methods to reduce the electrical percolation threshold is to add the conductive fillers to an immiscible polymer blend that possesses a co-continuous structure. In this method, conductive fillers are selectively located in one polymer phase or at the interface [7] and can therefore yield what is known as “double percolation”. The latter refers to the percolation of the filler within one phase of the polymer blend (first percolation) that itself percolates in the blend (double percolation) [8].

Due to their tendency to be selectively distributed in polymer blends, carbon fillers have been extensively used to create the double electrical percolation in the polymer composites. In this context, the most implemented carbon fillers are carbon nanotubes [7][9-12] and carbon black

[13-17]. Graphene was also used for this purpose in two previously published contributions. Kou et al. [18] succeeded to interfacially localize GNP in a co-continuous polymer blend constituted of PLA and poly (ethylene-co-vinyl acetate) (EVA). They prepared a ternary composite by a two-step compounding sequence where PLA/GNP masterbatch was first prepared via solution blending and then melt compounded with EVA. In the second step, GNP are transferred to the thermodynamically favoured phase (EVA) to be trapped at the interface. This resulted in an ultralow percolation threshold of 0.048 wt.% and an electrical conductivity of  $10^{-3} \text{ S.m}^{-1}$  at 0.5 wt.% of GNP. Using the same experimental protocol, Bai et al. [19] introduced GNP into a blend made of co-continuous PLA and polystyrene (PS). These authors were also able to trap graphene at the interface of the blend although it has preference to PS. The double electrical percolation obtained led to an electrical conductivity of  $10^{-6} \text{ S.cm}^{-1}$  at 0.5 wt.% of GNP.

There are different methods to manufacture test samples of conductive carbon-based polymer nanocomposites. Conventional processing techniques such as compression moulding and more recent ones such as fused filament fabrication (FFF) can be used for this purpose. There is only one published work regarding the impact of the two mentioned processes on the double electrical percolation. In this regard, Bertolini et al. [20] manufactured co-continuous poly(vinylidene fluoride) (PVDF)/thermoplastic polyurethane (TPU) (50 vol.%/50 vol.%) filled with CB-polypyrrole. The filler was preferably localized in the PVDF phase. Their results demonstrated that at the same filler content, the samples possessing a co-continuous structure have higher conductivities as compared to the ones with dispersed morphologies. Thus, the 3D printing of the co-continuous composites gave a material that can be used for electrically conductive applications. For example, 3D printed co-continuous composite containing 6.77 vol.% of filler presented an electrical conductivity of  $4.14 \text{ S.m}^{-1}$ .

This work is a pioneer in studying the influence of compression moulding and FFF on the double electrical percolation threshold in graphene-based polymer blend composites. PLA/PCL/GNP nanocomposites were prepared using twin-screw extrusion for this objective. The range of blend ratios in which the existence of the co-continuous morphology, accompanied by the double electrical percolation threshold, was determined for compression moulded samples. Rheological and thermal tests were performed to evaluate if the co-continuous microstructure can entail

superior viscoelastic and thermal stability characteristics. After combining the information from the microstructural and the electrical properties, the most interesting co-continuous composition was revealed. Moreover, the impact of the variation of graphene percentage as well as some processing parameters on the microstructure were investigated. Finally, the possibility of manufacturing electrically conductive graphene co-continuous nanocomposites using the FFF technique was verified for the first time. Hence, this work aims to represent the first attempt of creating electrically conductive graphene biodegradable nanocomposites having double electrical percolation.

## **4. Materials and methods**

### **4.1. Materials**

PLA Ingeo™ Biopolymer 2003D was provided from NatureWorks (Minnetonka, MN, USA). It has a melt flow rate of 6 g/10 min (210 °C/2.16 kg), a glass transition temperature of 60 °C, melting temperature of 150 °C, and a density of 1.24 g.cm<sup>-3</sup>. PCL grade Capa™ 6800 was purchased from Perstorp UK Ltd. (Warrington, UK). This grade has a melt flow rate in the range of 2.01-4.03 g/10 min (160 °C/5 kg), a melting temperature in the 58-60 °C range, and a glass transition temperature of -60 °C.

M5 grade graphene nanoplatelets purchased from XG Sciences Inc., Lansing, MI, USA is characterized by: an average lateral dimension of 5 μm, a thickness in the range of 6-8 nm, a specific surface area of 120-150 m<sup>2</sup>.g<sup>-1</sup>, a high electrical conductivity of 10<sup>7</sup> S.m<sup>-1</sup>, and a density of 2.2 g.cm<sup>-3</sup>.

### **4.2. Nanocomposite blends preparation**

Twin-screw extrusion (Process 11, Thermo Scientific, MA, USA) was used to mix PLA, PCL, and GNP together. The parameters set in this process are demonstrated in figure 96. The materials were dried overnight prior to the extrusion experiments (PLA and PCL were vacuum dried at 60 °C and 40 °C respectively whereas GNP powder was dried in a conventional oven at 80 °C). Table

21 summarises the three main compositions of the extruded nanocomposites and the reason behind preparing each.

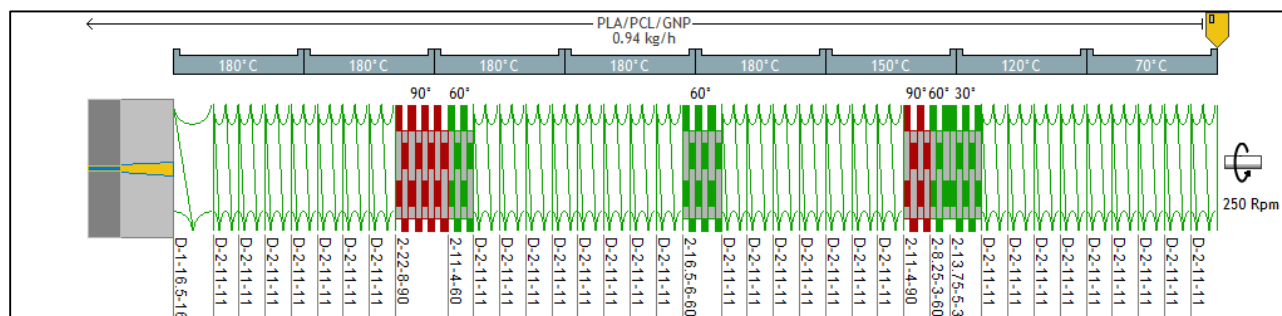


Figure 96: Screw profile and conditions set during PLA/PCL/GNP nanocomposites processing (picture from Ludovic® software)

Table 21: The three main series of extruded composites and the objective behind preparing each composition

Extruded bionanocomposites	Graphene percentage	PLA and PCL percentages	Objective
PLAx/PCLy/10 wt.% GNP	10 wt.% GNP	x and y range between 0 and 100 wt.% (with respect to the total weight fraction of 90 wt.% of polymers)	Exploring the co-continuity range in the compression moulded samples at 10 wt.% of GNP
PLA65/PCL35/x wt.% GNP	x varies between 5 and 20 wt.%	Fixed at 65 wt.% and 35 wt.% for PLA and PCL respectively (with respect to the total weight fraction of 90 wt.% of polymers)	Exploring the influence of the graphene percentage on the co-continuous microstructure in the compression moulded samples
PLA65/PCL35/10 wt.% GNP (2 extrusion steps)	10 wt.%	PLA and 10 wt.% of GNP (with respect to the PLA/PCL/GNP composite) were blended and subsequently the resulting composite was melt blended with PCL (PLA and PCL proportions were 65 and 35 wt.% with respect to the total weight of the 90 wt.% of polymers).	Studying if mixing GNP with the less favourable PLA phase would cause its migration to the more favourable PCL phase and the consequences of this migration on the co-continuous microstructure

For the purpose of using several storage modulus and complex viscosity based models that help in the theoretical prediction of the co-continuity, twin-screw extrusion of PCL/GNP composites containing graphene percentage varying between 10 wt.% and 20 wt.% was carried out. The parameters set in these experiments are: a flow rate of  $0.94 \text{ kg}\cdot\text{h}^{-1}$ , a screw speed of 200 rpm, and a temperature profile of  $60 \text{ }^\circ\text{C}$  (feeding zone)-  $70 \text{ }^\circ\text{C}$ -  $75 \text{ }^\circ\text{C}$ -  $80 \text{ }^\circ\text{C}$ -  $80 \text{ }^\circ\text{C}$ -  $85 \text{ }^\circ\text{C}$  (all the remaining screw zones until the die zone).

### 4.3. Compression moulding

The vacuum dried nanocomposites and pure PLA pellets were compression moulded using a laboratory hot press (LAB 800 PA, PINETTE PEI, France) by maintaining them for 10 minutes at  $180 \text{ }^\circ\text{C}$ , a rate of  $30 \text{ }^\circ\text{C}\cdot\text{min}^{-1}$ , and a load of 500 kN. Samples demoulding was achieved after cooling down to  $80 \text{ }^\circ\text{C}$  at a rate of  $30 \text{ }^\circ\text{C}\cdot\text{min}^{-1}$  using a water-cooling system. The prepared samples were disks of  $25\times 3 \text{ mm}$  intended for melt-shear rheological tests, scanning electron microscopy (SEM), and atomic force microscopy (AFM). Moreover, square plates of  $100\times 100\times 3 \text{ mm}$ , from which bars of  $30\times 5\times 3 \text{ mm}$  were cut for the electrical resistance tests, were also manufactured. For the viscosity-based models, PCL/GNP disks were prepared by applying a load of 200 kN at  $120 \text{ }^\circ\text{C}$  for 10 minutes. Afterwards, the cooling step took place by decreasing the temperature to  $50 \text{ }^\circ\text{C}$  at a rate of  $20 \text{ }^\circ\text{C}\cdot\text{min}^{-1}$  before samples demoulding. The overall time of compression moulding of all the samples was 35 minutes. Yet, several PLA65/PCL35/10 wt.% GNP samples were prepared during 10, 20, and 35 minutes to study the impact of the annealing time increase on the co-continuity.

### 4.4. Filament preparation

The nanocomposite pellets were used to feed a mini single-screw extruder (3devo, Utrecht, Netherlands) to prepare calibrated filaments with a diameter of 2.83 mm. The obtained filament was used as an input material in the 3D printing process. The filament extrusion parameters are: a speed of 5 rpm and a temperature profile of  $165 \text{ }^\circ\text{C}$  (feeding zone)-  $190 \text{ }^\circ\text{C}$ -  $200 \text{ }^\circ\text{C}$ -  $195 \text{ }^\circ\text{C}$ .

## 4.5. Fused filament fabrication (FFF)

An A4v3 FFF printer (3ntr, 28047 Oleggio NO, Italy) was used to print the manufactured filaments into bars and disks for the electrical resistance measurements and the microscopy investigations respectively. For the aim of comparison, the manufactured samples have the same dimensions as the compression moulded ones and the applied processing parameters are: a nozzle diameter of 0.8 mm, a printing speed of 40 mm.s<sup>-1</sup>, a primary layer height of 0.2 mm, a raster angle of +45°/-45°, a nozzle temperature of 180 °C, and a heated platform temperature of 60 °C. The 3D printed samples are: PLAx/PCLy/ 10 wt.% GNP (x varies between 80 and 30 wt.% with respect to the total weight fraction of 90 wt.% of polymers).

# 5. Characterization techniques

## 5.1. Scanning electron microscopy (SEM)

The morphologies of the compression moulded and 3D printed samples were analysed along their transversal section using a scanning electron microscope (SEM) (FEI Quanta 200) at an acceleration voltage of 10 kV. A cryo-ultramicrotome (Leica EM UC7, Nanterre, France) was used to smooth the surface for obtaining a better contrast and quality of observations with SEM. The obtained images were produced via back scattered mode (BSE) and secondary electron (SE) beam modes. A particular preparation was made before SEM observation of 3D printed PLA65/PCL35/10% GNP composite. Each sample was immersed in toluene at room temperature for 3 h to dissolve the PCL phase followed by washing to remove the dissolved fraction. Solvent etching technique was used especially for this sample due to the difficulty to differentiate between both phases when the observations took place directly. The reason is the high roughness of the surface and the high content of PLA. This problem did not exist for 3D printed samples containing dispersed PLA phase in the continuous PCL matrix.

## 5.2. Atomic force microscopy (AFM)

An atomic force microscope (AFM, MFP-3D infinity, Asylum Research, Oxford instruments, Abingdon, UK) was used to confirm the complete localization of GNP in the PCL phase. The

investigations were carried out on the cryo-fractured smooth transversal sections of each sample. The images were obtained in a bimodal tapping mode (also known as Amplitude Modulation-Frequency Modulation mode (AM-FM) mode [21]) under ambient conditions using AC160TSR3 tip at a scan rate of 1 Hz. The topography (height), phase (phase angle), and elastic modulus images were recorded and analysed to have full understanding of the results.

### 5.3. Solvent extraction method

Several methods have been extensively used to determine the co-continuity range including rheology [22-25], microscopy [22][26-29], and solvent extraction [30-42]. Solvent extraction experiments are the simplest and most popular technique to detect the co-continuity and they require at least one of the polymer phases to be selectively removed from the sample. In this work, PCL was chosen to be extracted and not the PLA phase since the latter is more solvent resistant and cannot be removed without damaging the PCL phase. Therefore, the PCL containing graphene phase was extracted (the complete selective localization of graphene in the PCL phase is proved in the first section of the results and discussion). Compression moulded bar shaped samples (length: 3 cm, width: 6 mm, thickness: 3 mm) with various compositions were selected for these experiments. Each sample was immersed in 5 ml of toluene in a closed test tube during 5 h and 30 min at 60 °C (the toluene was renewed each two hours) to selectively extract the completely dissolved PCL phase. The complete extraction of the graphene filled PCL phase was verified by the darkness of the extracted solution. Before weighing, the samples were dried in an oven at 40 °C for the complete evaporation of the solvent. After the complete dissolution of the graphene containing PCL phase, there exist two cases [43]:

- 1) The extraction left the sample compact (no fragmentation into small pieces): PLA is 100% continuous and the PCL continuity is quantified by the weight fraction of PCL that is extracted according to equation (1):

$$PCL \text{ continuous fraction } (\%) = \frac{m_2}{m_1} \times 100 \quad (1)$$

$m_1$  is the mass of graphene filled PCL phase before the solvent dissolution (mg)

$$(m_1 = m_{total \text{ before the solvent extraction}} \times (wt. \%_{(PCL+GNP)}))$$

$m_2$  is the mass of graphene filled PCL phase after the solvent dissolution (mg)

$$(m_2 = m_{total \text{ (before the solvent extraction)}} - m_{total \text{ (after the solvent extraction)}})$$

This is the case of samples containing high PLA percentage.

2) The sample fell apart:

PCL is 100% continuous and the PLA continuity is represented by the biggest compact PLA piece released at the end of the extraction. The percentage of continuity of PLA in this case is calculated according to equation (2):

$$PLA \text{ continuous fraction (\%)} = \frac{m'}{m''} \times 100 \quad (2)$$

$m'$  is the mass of the biggest part of PLA (mg)

$m''$  is the mass of PLA in the sample before the solvent dissolution (mg)

$$(m'' = m_{total \text{ before the solvent dissolution}} \times (wt. \%_{(PLA)}))$$

This is the case of the co-continuous samples and samples containing dispersed PLA nodules in the PCL phase. The samples possessing a fully dispersed PLA structure showed complete disintegration after the dissolution of the PCL phase where the mass of the biggest PLA part is too low to yield a negligible percentage of continuity of PLA.

## 5.4. Electrical resistance measurements

As described by our previous work [44], a four point probe measurement technique was used to measure the resistance of both the compression moulded and 3D printed bars. Measurements took place on 10 bar-shaped samples that were conditioned for at least 48 hours under controlled temperature (25 °C) and humidity (50 %) conditions. Each test specimen was tested at a voltage of 5 V by using a direct current (DC) power supply (Topward, TPS-4000). The voltage was measured between the two internal copper electrodes using a digital multimeter (HM 8011, HAMEG Instruments, Mainhausen, Germany) and the current flow was measured between the two external copper electrodes using a multimeter (MX 579 Metrix, ITT instruments, New York, USA). These four copper electrodes were identical and equidistant. Only one surface of each sample was in contact with the electrodes. After knowing the voltage and the current, the electrical volume resistivity  $\rho$  of each sample was calculated according to equation (3):

$$\rho = \frac{R \times S}{L} \quad (3)$$

Where R is the electrical resistance ( $\Omega$ ) (calculated using Ohm's law), S is the cross-sectional area ( $m^2$ ) (equal to the width of the sample multiplied by its thickness), and L corresponds to the distance between the internal electrodes and is equal to 3.7 mm.

## 5.5. Rheological measurements

The complex viscosity and the storage modulus of the PLA, PLA/GNP, PCL/GNP, and PLA/PCL/GNP composites were evaluated using a rotational rheometer (MCR 702, Anton Paar, Graz, Austria) by performing oscillatory shear mode measurements using parallel plates geometry (25 mm diameter). At least one night prior to testing, the samples were dried in a vacuum oven at 50 °C. After verifying the thermal stability of all the samples at 180 °C and under constant flow of nitrogen gas to prevent the degradation of the samples, the strain sweep tests were performed at 628  $rad.s^{-1}$  in order to determine the upper limit of the linear viscoelastic domain. Finally, frequency sweep tests between 0.01 and 628  $rad.s^{-1}$  were carried out at a shear strain percentage of 1% for PLA, 0.001%-0.06% for PCL/GNP, and 0.006% for PLA/PCL/GNP.

## 5.6. Differential Scanning Calorimetry (DSC)

A Perkin-Elmer Diamond differential scanning calorimeter (DSC) was used mainly to estimate the percentage of crystallinity of both PLA and PCL in the pure polymers and the composites. First, the samples were weighed and sealed in aluminium pans (10 mg). Then, they were heated from -70 °C to 200 °C, held for 5 min to eliminate the previous thermal histories, cooled down to -70 °C, and finally reheated to 200 °C. The heating rate was chosen to be 10 °C.min<sup>-1</sup> and the cooling rate was 5 °C.min<sup>-1</sup>. The glass transition temperature,  $T_g$ , of PLA was measured at the inflection point of the heat capacity curve (in the PLA and PLA-GNP samples) and was considered to be located at an equivalent position to the melting temperature of PCL in the PLA-PCL-GNP composites due to the overlapping of both peaks. The crystallization temperature,  $T_c$ , of PLA and the melting temperatures,  $T_m$ , of both polymers were determined from the peak values of the respective exotherms and endotherms. The degree of crystallinity of PLA and PCL in the samples ( $X_c$ ) was determined by using equation (4):

$$X_c = 100 \times \frac{\Delta H_m - \Delta H_c}{\Delta H_m^0 \cdot W} \quad (4)$$

Where  $\Delta H_m$  is the enthalpy of fusion of each polymer,  $\Delta H_c$  is the enthalpy of crystallization of PLA,  $\Delta H_m^\circ$  is the enthalpy of 100% crystalline polymer ( $\Delta H_m^\circ(PLA) = 93.6 \text{ J.g}^{-1}$  and  $\Delta H_m^\circ(PCL) = 135.4 \text{ J.g}^{-1}$ ) [45][46], and  $W$  is the weight fraction of each polymer in the blend and the composites.

## 5.7. Thermogravimetric analysis (TGA)

To correlate the sample microstructure to the thermal stability of the composites, thermogravimetric analysis (TGA) tests were accomplished. For these tests, 10 mg of each sample were subjected to heating from room temperature to 900 °C at a rate of 10 °C.min<sup>-1</sup> in the presence of nitrogen gas (40 ml.min<sup>-1</sup>). This step followed an isothermal step for 30 min at room temperature. After recording the weight loss as function of temperature, the following parameters were determined: the experimental percentage of char yield at 600 °C, the thermal onset degradation temperature at 15 wt.% of mass loss ( $T_{\text{onset}}$ ), the maximum degradation temperatures ( $T_{\text{max}}$ ) of PLA and/or PCL peaks, and the total mass loss over the entire temperature range.

# 6. Results and discussion

## 6.1. Selective localization of graphene in the PCL phase in compression moulded samples

Studying the evolution of the microstructure in the compression moulded samples is of great interest. This is related to its strong influence on the electrical conductivity of the composites that can be boosted when the co-continuous structure exists thanks to the double electrical percolation phenomenon. Since the selective localization of the nano-fillers in one polymer phase is an indispensable condition for the occurrence of the double electrical percolation, it is necessary to verify it in the PLA/PCL/GNP compositions. This selective localization in polymer blends prepared by melt mixing is affected by various physical and processing parameters such as the absolute viscosity, the viscosity ratio of the polymers, the elasticity of the polymers, the interfacial tension among the constituents, and the mixing parameters [47]. However, the

complex viscosity ratio can be considered as one of the main factors that affects the phase morphology and the location of the fillers in the polymer blend composites [48].

Before observing the filler localization in the PLA/PCL/GNP composites, the morphology of the PLA/GNP and PCL/GNP composites was investigated using SEM. In figure 97, PCL/10 wt.% GNP (figures 97.a, 97.b) shows different orientation of the graphene aggregates (indicated by yellow arrows) as compared to PLA/10 wt.% GNP composite (figures 97.c and 97.d). The graphene orientations in each of these samples seem to be perpendicular to each other.

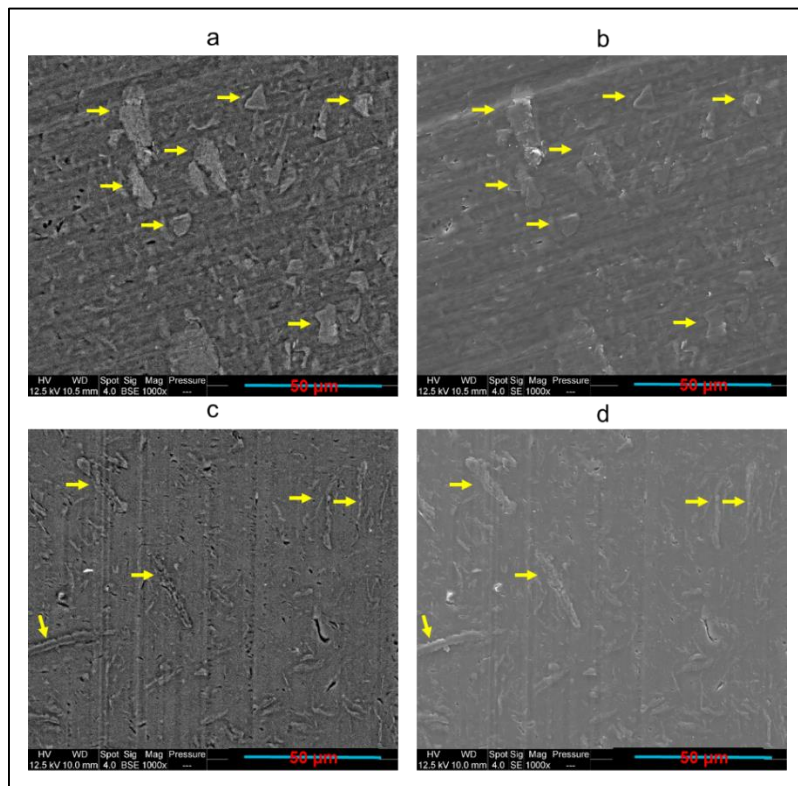


Figure 97: SEM BSE and SE images of PCL/10 wt.% GNP (a,b) and PLA/10 wt.% GNP (c,d) compression moulded composites (the yellow arrows indicate the presence of GNP)

Figure 98.b shows the different components along an AFM profile (indicated by a red line) drawn in figure 98.a for mapping the elastic modulus. Due to the differences in stiffness of the different composite components, it was possible to identify the polymer phases and the preferential localization of GNP in PLA60/PCL40/10 wt.% GNP composite. But first, for the interpretation of this profile, elastic modulus of each of the three composite constituents should be known. In this case, Young's modulus of PLA is 3500 GPa [49], that of PCL is  $560 \pm 50$  MPa [50], and that of graphene fluctuates between 0.98 and 1.04 TPa [51]. Then, starting from the blue point in figures

98.a and 98.b, the highest modulus peak is ascribed to GNP particle (surrounded by a yellow ellipse in figure 98.a). Subsequently, the red triangle in both figures 98.a and 98.b indicates the presence of PCL filled with 10 wt.% GNP particles. Fluctuations of stiffness are observed indicating the presence of particles in the PCL phase. Finally, the blue star denotes the PLA phase having an intermediate modulus between the GNP and PCL. The stability of modulus profile (figure 98.b) of the PLA phase emphasizes its purity and emptiness from any GNP particles.

Further AFM images were taken on another zone of the sample's surface. Observations are shown in figures 98.c (topography), 98.d (phase), and 98.e (elastic modulus). Considering the latter, the brighter zone which possesses the greatest elastic modulus indicates the GNP (surrounded by yellow ellipses), the darkest zone which has the lowest elastic modulus (indicated by the red triangle) shows the PCL phase, and the grey zone with intermediate elastic modulus between GNP and PCL indicates the PLA presence (indicated by the blue star). The topography (98.c) and the phase (98.d) images give the same information where in the topography image the greatest roughness (brightest colour) is due to the GNP presence and in the phase image the highest angle (brightest colour) indicates generally the softest material which is PCL.

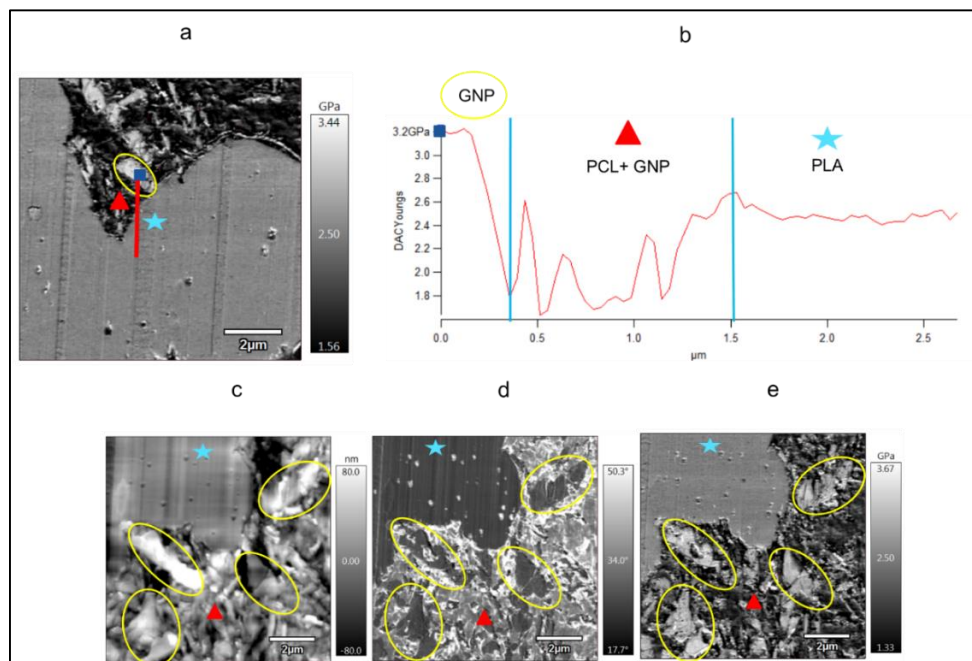


Figure 98: AFM images of PLA60/PCL40/GNP, where (b) shows the components of the profile drawn on (a) and (c), (d), and (e) represent the topography, phase, and elastic modulus images of another observed zone on the same surface (the yellow ellipses surround the GNP, the blue stars denote the PLA phase, and the red triangles indicate the graphene containing PCL phase)

Other PLA/PCL/GNP compositions show also selective localization of GNP in the PCL phase. Figure 99 shows a series of samples containing 10 wt.% of GNP and PLA content ranging between 65 wt.% (99.c) to 30 wt.% (99.g). In these images, GNP are totally localised in the PCL phase (indicated by yellow arrows) with total absence in the PLA phase (indicated by blue arrows). The phases were identified in these secondary electron images by comparing a BSE image (99.a) with a SE image (99.b) of PLA60/PCL40/GNP. The brighter phase in the BSE image is the oxygen content richer polymer phase (PLA phase) as indicated by blue arrows whereas it is the opposite for the SE image (brighter phase is the PCL phase as indicated by yellow arrows).

The selective localisation of nanofillers in a specific phase or at the interface of immiscible polymer blends is mainly controlled by the combined action of the thermodynamics and the kinetics. To reduce the free energy of the system, nanoparticles tend to selectively locate in the more thermodynamically favourable phase during the melt mixing process. The thermodynamic preference of nanoparticles could be determined by the wetting coefficient which measures the tendency of a liquid phase to spread [8]. It can be calculated from the ratio of the interfacial tensions (the subtraction of the interfacial tensions between the polymer/filler systems over the interfacial tension of the polymer/polymer system). In this framework, based on the contact angle measurements and the wetting coefficient calculations that were carried out in our previous work [44], GNP should have preference to the PLA phase. Anyway, these observations do not consider the process temperature and what happens during high shear melt blending at 180 °C.

From a kinetic point of view, nanoparticles tend to localise in the phase with lower viscosity during melt mixing since the less viscous polymer wets nanoparticles more easily in the early stages of melt mixing [8]. In this work, the complex viscosity of PLA ( $819.47 \pm 114.06$  Pa.s at  $115$  rad.s<sup>-1</sup>) is greater than that of PCL ( $183.67 \pm 15.94$  Pa.s at  $115$  rad.s<sup>-1</sup>), so the nanoparticles can easily migrate into the PCL phase during melt-mixing. Several previous works highlighted the same observation of GNP preferential positioning in the PCL phase rather than the PLA phase [44][52][53].

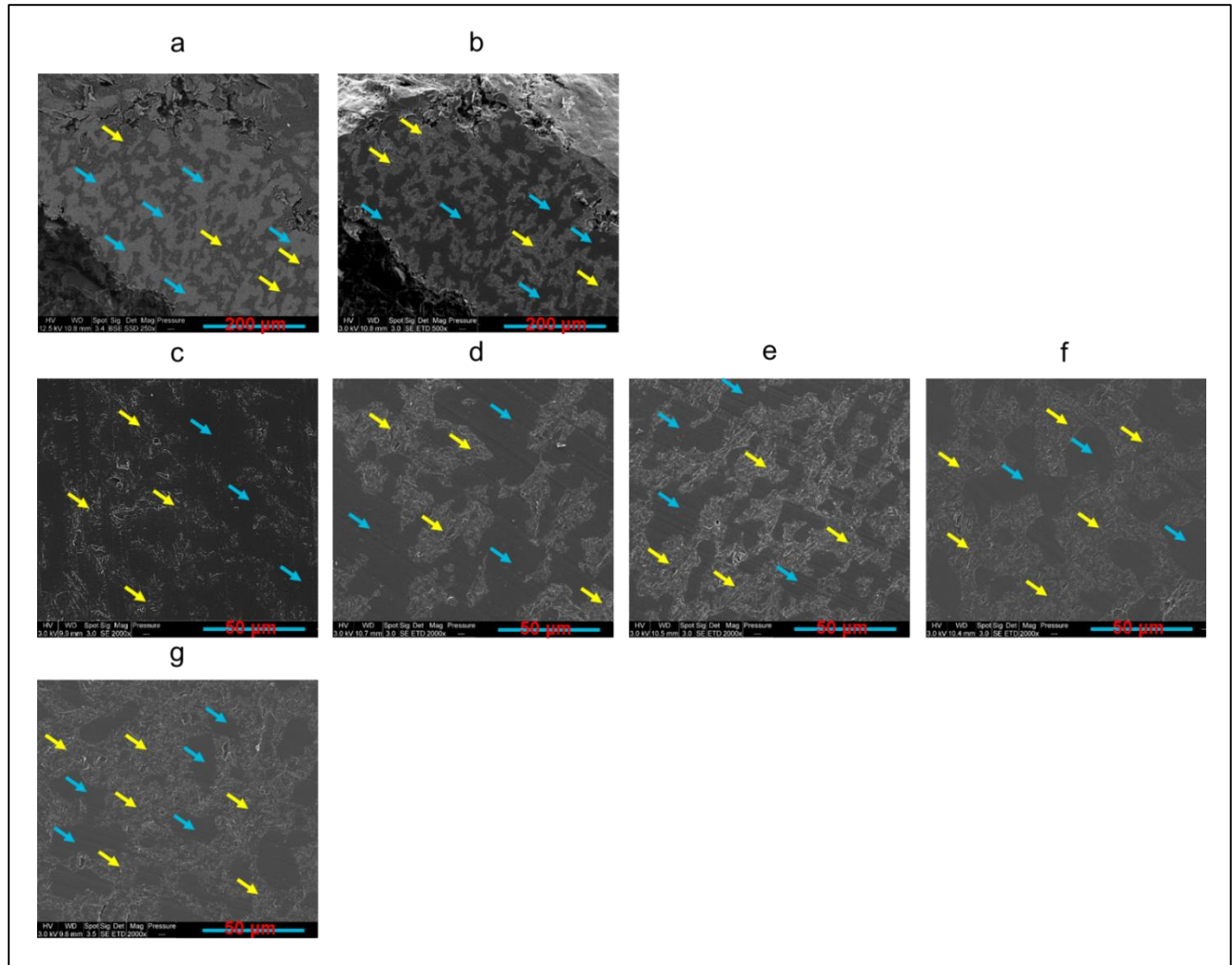


Figure 99: SEM images of PLA60/PCL40/GNP, BSE (a) and SE (b) and SE images at lower magnification of PLA65/PCL35/GNP (c), PLA60/PCL40/GNP (d), PLA50/PCL50/GNP (e), PLA40/PCL60/GNP (f), and PLA30/PCL70/GNP (g) compression moulded composites (the yellow arrows indicate the GNP rich PCL phase and the blue ones indicate the PLA phase)

## 6.2. Theoretical prediction of the co-continuity

The continuous phase depends mainly on the composition and the viscosity ratio of the components. For instance, by starting with polymer A and consequently adding to it polymer B, the dispersion of polymer B in A is obtained. If the volume fraction of polymer B still increases, the phase inversion point is reached after which polymer B becomes the continuous phase and polymer A is the dispersed phase [54]. In other words, increasing the dispersed volume fraction at constant melt blending speed may result first in a co-continuous system and eventually a phase inversion point beyond which the reversed system is obtained.

Several empirical and semi-empirical models have been developed over the last three decades to estimate the phase inversion composition in terms of processing conditions and material properties. Paul and Barlow proposed one of the simplest models that uses the viscosity ratio of the two polymer phases to estimate the phase inversion point. According to these authors, the less viscous phase will have the greater ability to be the continuous phase [55]. In addition, Ho et al. [56], Kitayama et al. [57] and Everaert et al. [58] have modified the general equation by introducing a prefactor and/or an exponent to better fit the experimental results. Instead of using the viscoelastic parameters, Metelkin and Blekht [59] were the first to introduce the empirical relationship to predict the phase inversion using the concept of capillary instabilities of individual layers. Utracki [60] developed another approach based on the suspension theory using the intrinsic viscosities  $[\eta]$  and maximum packing volume fraction  $\varphi_m$ . Steinmann et al. [27] proposed an approach based on the assumption that the shape relaxation times of blend components meet a maximum at the phase inversion point. Bourry and Favis [22] have developed a different approach using the storage modulus instead of the viscosity ratios by considering the elastic contribution of the blend components.

In most of the above mentioned models, the volume percentages of PLA and PCL at the phase inversion point can be calculated by using the complex viscosities of both polymers owing to the influence of the viscosity ratio on the morphology of the polymer blends [6]. As mentioned before, graphene is completely localized in the PCL phase. Thus, the rheological parameters of pure PLA and PCL/GNP composites have been used in the different equations (table 23). But, only the values at  $120 \text{ rad.s}^{-1}$  and  $628 \text{ rad.s}^{-1}$  were taken into consideration (table 22) due to the fitting of only these values with the various models. The results at both shear rates of each model are similar (table 23) indicating that the inversion point was not affected by the shear rate variation. In the following sections, the combination of various results will indicate the sample which has the best co-continuity and therefore it will be considered as the experimental phase inversion point and will be compared with the results of the different models in this section.

Table 22: Complex viscosity and storage modulus results of PLA and PCL/GNP composites at 180 °C and 120 rad. s<sup>-1</sup> and 628 rad. s<sup>-1</sup>

Sample name	Complex viscosity (Pa.s) (120 rad.s <sup>-1</sup> )	Complex viscosity (Pa.s) (628 rad.s <sup>-1</sup> )	Storage modulus (Pa) (120 rad.s <sup>-1</sup> )	Storage modulus (Pa) (628 rad.s <sup>-1</sup> )
PLA	1409	545.16	117630	287750
PCL/10% GNP	197	144.07	10168	36269
PCL/15% GNP	672	280.76	67115	127125
PCL/20% GNP	1971	623.83	222643	329913

Table 23: Different phase inversion models and their results in PLA/PCL/10wt.% GNP composites at 180 °C and 120 rad. s<sup>-1</sup> and 628 rad. s<sup>-1</sup>

Authors	Equation	Results (628 rad.s <sup>-1</sup> )	Results (120 rad.s <sup>-1</sup> )	Ref.
Paul et Barlow	$\frac{\phi_{PCL+M5}}{\phi_{PLA}} = \frac{\eta_{PCL+M5}}{\eta_{PLA}}$	PLA52/PCL48/ 10 wt.% GNP	PLA45/PCL55/ 10 wt.% GNP	[55]
Kitayama et al.	$\frac{\phi_{PCL+M5}}{\phi_{PLA}} = 0.887 \left( \frac{\eta_{PCL+M5}}{\eta_{PLA}} \right)^{0.29}$	PLA58/PCL42/ 10 wt.% GNP	PLA55/PCL45/ 10 wt.% GNP	[57]
Steinmann et al.	$\phi_{PLA} = -0.12 \log \left( \frac{\eta_{PCL+M5}}{\eta_{PLA}} \right) + 0.48$	PLA52/PCL48/ 10 wt.% GNP	PLA51/PCL49/ 10 wt.% GNP	[27]
Ho et al.	$\frac{\phi_{PCL+M5}}{\phi_{PLA}} = 1.22 \left( \frac{\eta_{PCL+M5}}{\eta_{PLA}} \right)^{0.29}$	PLA49/PCL51/ 10 wt.% GNP	PLA47/PCL53/ 10 wt.% GNP	[56]
Everaert et al.	$\frac{\phi_{PCL+M5}}{\phi_{PLA}} = \left( \frac{\eta_{PCL+M5}}{\eta_{PLA}} \right)^{0.3}$	PLA54/PCL46/ 10 wt.% GNP	PLA53/PCL47/ 10 wt.% GNP	[58]

Matelkin- Blekht	$\Phi_{PLA} = \left[ 1 + \frac{\eta_{PCL+M5}}{\eta_{PLA}} \left[ 1 + 2.25 \log \left( \frac{\eta_{PCL+M5}}{\eta_{PLA}} \right) + 1.81 \left( \log \left( \frac{\eta_{PCL+M5}}{\eta_{PLA}} \right) \right)^2 \right] \right]^{-1}$	PLA47/PCL53/ 10 wt.% GNP	-	[59]
Utracki	$\Phi_{PLA} = \frac{\left( 1 - \log \left( \frac{\eta_{PCL+M5}}{\eta_{PLA}} \right) / [\eta] \right)}{2}$ <p><math>[\eta] \cdot \phi_m = 1.9</math> [35][61][62]</p>	PLA53/PCL47/ 10 wt.% GNP	PLA51/PCL49/ 10 wt.% GNP	[60]
Bourry- Favis	$\frac{\Phi_{PLA}}{\Phi_{PCL+M5}} = \frac{G'_{PCL+M5}}{G'_{PLA}}$	PLA60/PCL40/ 10 wt.% GNP	-	[22]

### 6.3. Experimental prediction of the co-continuity range in the compression moulded samples

#### 6.3.1. SEM results

As the composites with co-continuous morphology may offer more interesting combination of properties such as the electrical ones as compared to blends with dispersed structure, there has been a growing interest in this type of materials. In this work, samples having PLA content between 70 wt.% and 55 wt.% (figures 100.a-100.d) were found to be co-continuous. This co-continuity was lost at lower PLA percentage (50 wt.%-30 wt.%) (figures 100.e-100.h) where the nodules of PLA are dispersed in the continuous GNP rich PCL phase. It was long ago believed that the co-continuous morphologies exist only close to the phase inversion point, but recently several researchers showed that a range of co-continuity can exist rather than a single point. The co-continuous morphologies can be formed at the initial, intermediate, and final stages of melt

blending depending on several factors such as the mixing conditions, the type of extruders, and so on [63].

There is a debate in the literature regarding the mechanism of formation of co-continuity in polymer blends whether it starts by droplet deformation/breakup or by sheet forming mechanism [35]. In unfilled polymer blends, the thermodynamic stability of the elongated domains depends on the polymer-polymer interfacial tension that causes the retraction of the minor phase to a spherical shape or its fragmentation into small droplets. The addition of nanoparticles affects the interfacial tension and the rheological behaviour and consequently the co-continuity equilibrium [64-66]. Indeed, there is no clear understanding of the mechanisms that lead to the formation of the co-continuity in presence of nano-fillers, even if it has been reported that the rheology contributes greatly to this aspect. When the nanoparticles are selectively located in one polymer phase, the increase of the elasticity and viscosity of the host slows down its shape relaxation and breakdown processes to stabilise the irregularly shaped domains. This may eventually result in stable co-continuous morphologies [47].

Several authors have obtained co-continuous blends with the selective localization of the nanoparticles in one polymer phase. For example, Filippone et al. [34] found that PA6/PP/clay systems, in which the clay is selectively localised in the PA6 minor phase, exhibited co-continuous microstructure. For explaining their results, they proposed a gelation mechanism where the PA6 chains coat the organoclay network. Li et al. [67] also suggested a mechanism for the formation of a co-continuous structure in clay filled PA6/(poly(phenylene oxide)) (PPO) blends. They indicated that the filler presence in the PA6 phase refines the domain size and increases the effective filling volume of the minor phase. The enhanced droplet/droplet interactions finally lead to the formation of the co-continuous structure. Cui et al. [68] have obtained the double electrical percolation in immiscible PP/Novolac blends filled with CB particles that were selectively localised in the thermosetting Novolac phase. At the processing temperature of 190 °C, Novolac has lower melt viscosity than PP and this favours the CB incorporation into the Novolac resin. This preferential localization increased the Novolac viscosity until it became equivalent to PP and thus facilitating the co-continuity formation. According to these authors, it is indispensable for a co-continuous morphology formation that the shear forces applied on a

system are greater than the interfacial forces within the given system to favour the phase elongation. The greater interfacial stress between the blend polymers results in smaller dispersive mixing and thus instability of the elongated particles.

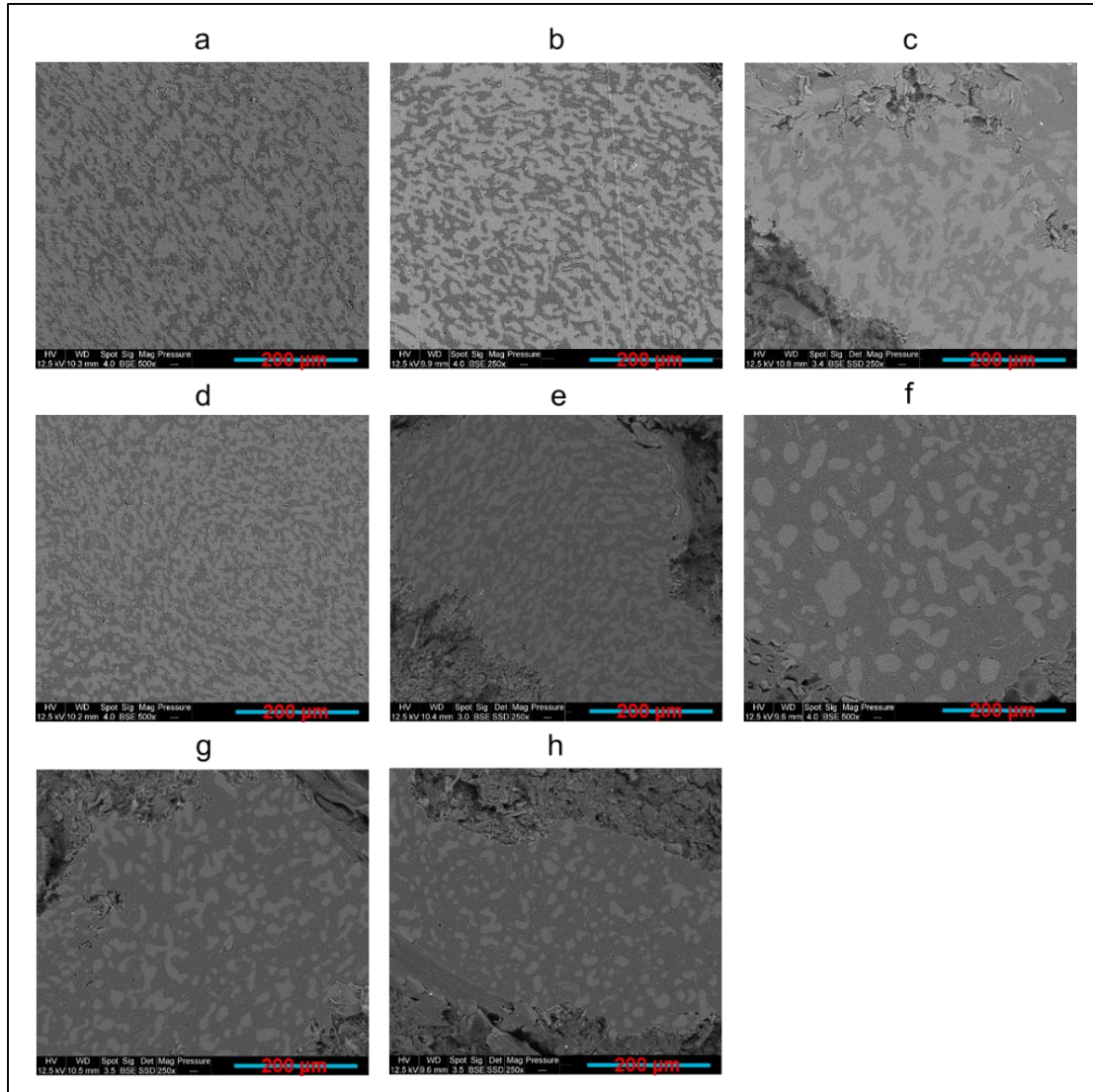


Figure 100: SEM BSE images of PLA70/PCL30/GNP (a), PLA65/PCL35/GNP (b), PCL60/PCL40/GNP (c), PLA55/PCL45/GNP (d), PLA50/PCL50/GNP (e), PLA45/PCL55/GNP (f), PLA40/PCL60/GNP (g), PLA30/PCL70/GNP (h) (PLA is the white phase and PCL is the grey phase)

### 6.3.2. Electrical resistivity and solvent extraction method results

The composites electrical conductivity is very sensitive to their microstructure. Moreover, in order to obtain electrically conductive composites the electrons tunnelling (filler particles are close but not in contact) and/or direct contact effects should exist [48]. In this context, composite

nanomaterials containing 10 wt.% of GNP and PLA concentration varying between 0 and 100 wt.% were fabricated and tested. The electrical volume resistivity results, the electric current at 5 V, and the LED photographs at 5 V are presented in table 24. The LED photographs were taken after the assembly of a circuit consisting of a LED, a voltage generator (5 V), and the sample in series. The lowest electrical resistivity results are for samples containing PLA content varying between 55 and 70 wt.% (greater electric current and LED luminosity as compared to the other samples). This can be attributed to the double electrical percolation phenomenon that exists in these samples as will be proved by the full continuity of the phases using the solvent extraction method.

Both the microstructural and electrical resistivity results led to the same conclusion regarding the composites co-continuity range which is between 55 wt.% and 70 wt.% of PLA. The solvent extraction method was implemented to quantify the 3D co-continuity by extracting the PCL phase using toluene solvent. Figure 101 exhibits the plot of the continuous fraction percentage of each polymer as function of the PLA weight percentage in the 10 wt.% GNP compression moulded composites. The PLA curve has a classical sigmoid shape. At low percentage of PLA ( $\leq 45$  wt.%), its continuity is zero. This means that the PLA phase is dispersed as droplets in the PCL phase (as observed in figures 100.f and 100.h). At 50 wt.% of PLA, the beginning of the coalescence of PLA droplets starts (also obvious in figure 100.e) and continues until 55 wt.% that corresponds to the onset of the co-continuity. Starting from this value, the PLA phase becomes almost fully continuous. The co-continuity interval extends from 55 wt.% to 70 wt.% of PLA (the last PLA percentage at which both polymers are fully continuous) (exhibited in figures 100.a and 100.d). This range is between the dotted lines shown in figure 101 and was determined in the same way as reference [69]. The PCL curve has the same shape but it has broader full continuity range (0-70 wt.% of PLA) as compared to PLA due to its lower complex viscosity. The dispersed PCL structure in the PLA phase is observed only beyond 70 wt.% of PLA (almost zero continuity of the PCL phase). These results emphasise the co-continuity range already observed by the microstructural and electrical analyses.

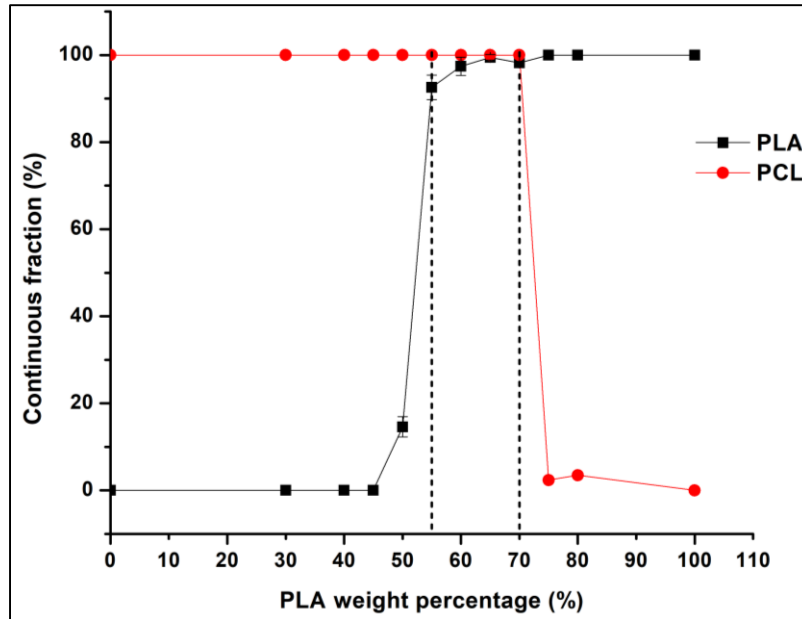


Figure 101: Continuous fraction percentage plot of PLA and PCL phases of each compression moulded composite containing 10 wt.% of GNP versus the PLA weight percentage (these results were obtained from the solvent extraction method)

What can be also realised in table 24 is that as the percentage of PCL increases from 35 wt.% to 100 wt.% the electrical resistivity increases because of the lower GNP confinement and their greater dispersion in the larger PCL phase. Meanwhile, PLA80/PCL20/GNP has high electrical volume resistivity ( $4900 \pm 90 \Omega \cdot \text{cm}$ ) although the lowest PCL content in this sample. The morphology of this sample demonstrated in our previous work [44] can explain this result. The scarcity of the graphene filled PCL content that exists in a nodular form in the continuous PLA matrix causes the separation of the graphene clusters by the insulating PLA chains. In addition, comparing the PLA/GNP results ( $4866 \pm 65 \Omega \cdot \text{cm}$ ) with the PCL/GNP ones ( $500 \pm 30 \Omega \cdot \text{cm}$ ) shows a large difference among them (ratio of 9.7). This is due to the different GNP orientation in the PCL phase in comparison with the PLA matrix (figure 97). In the PCL/GNP composite, graphene flakes are along the direction of the copper electrodes (of the electrical resistance measurement setup sample holder) (97.a and 97.b) which makes the transfer of the electrons easier as compared to the orientation of the GNP perpendicular to the copper electrodes direction in the PLA matrix (in PLA/GNP composite, 97.c and 97.d). The four-probes electrical resistance measurement setup is demonstrated in our previous work [44].

Table 24: Electrical volume resistivity and electric current results with the accompanied LED photos at 5 V of the compression moulded samples containing 10 wt.% of GNP and PLA content between 0 wt.% to 100 wt.%

Sample	Electrical volume resistivity ( $\Omega \cdot \text{cm}$ )	Electric current (mA) (5 V)	LED (5 V)
PLA/GNP	$4866 \pm 65$	$0.000001 \pm 0.0007$	No light
PLA80/PCL20/GNP	$4900 \pm 90$	$0.000001 \pm 0.004$	No light
PLA70/PCL30/GNP	$30 \pm 1$	$9 \pm 0.06$	
PLA65/PCL35/GNP	$26 \pm 5$	$9 \pm 0.04$	
PLA60/PCL40/GNP	$54 \pm 12$	$6 \pm 0.08$	
PLA55/PCL45/GNP	$67 \pm 10$	$5 \pm 0.09$	
PLA50/PCL50/GNP	$76 \pm 15$	$3 \pm 0.05$	
PLA45/PCL55/GNP	$104 \pm 12$	$2 \pm 0.01$	
PLA40/PCL60/GNP	$126 \pm 21$	$1 \pm 0.02$	
PLA30/PCL70/GNP	$237 \pm 25$	$1 \pm 0.01$	
PCL/GNP	$500 \pm 30$	$0.01 \pm 0.05$	

### 6.3.3. Melt shear rheology results

The rheological properties of the polymer nanocomposites are sensitive to their inner microstructures. Thus, the storage modulus and complex viscosity curves, obtained after performing melt shear rheology tests at 180 °C, are depicted in figures 102.a and 102.b respectively. Conversely to PLA/GNP, the complex viscosity and storage modulus curve shape of PCL/GNP is similar to that of the ternary composites. This confirms that all the nanocomposites except the PLA/GNP exhibit a yield stress behaviour that is not exclusive for the co-continuous composites [47][70].

In the low frequency region, the comparison between the storage modulus curves gives the following order: PLA65/PCL35/GNP > PLA50/PCL50/GNP > PLA30/PCL70/GNP > PLA80/PCL20/GNP. For all these systems, the storage modulus at low frequency follows the same trend as that of the electrical volume conductivity for the same structural reasons. This result was obtained in a previous work performed by Hadaeghnia et al. [70] who explained the increase of low frequency storage modulus by the formation of a strong percolated structure of graphene particles and the presence of a co-continuous structure in PA6/PEO blends. Lyu et al. [71] found superior storage modulus of the co-continuous poly vinyl chloride (PVC)/PLA blends as compared to the composites with dispersed morphology because of the better interaction stresses between the two polymer phases that hindered the chain relaxation and enhanced the elasticity.

Concerning the composites of this study, PLA and PCL contents are not constant. Thus in principle, the sample that contains more PLA content should exhibit higher storage modulus because of the greater storage modulus of pure PLA ( $55,861 \pm 1121 \text{ Pa}$  at  $115 \text{ rad}\cdot\text{s}^{-1}$ ) as compared to pure PCL ( $3678 \pm 398 \text{ Pa}$  at  $115 \text{ rad}\cdot\text{s}^{-1}$ ) [44]. Yet, PLA80/PCL20/GNP, although it contains the greatest PLA content, shows the lowest storage modulus as compared to the other ternary composites. The reason might be the absence of the strong interconnected graphene network in this sample as indicated by the high electrical volume resistivity ( $4900 \pm 90 \text{ }\Omega\cdot\text{cm}$ ).

Moreover, the formation of a plateau in the low frequency region is a clue regarding the presence of strong particulate network [72-75]. And because PLA65/PCL35/GNP composite demonstrates this plateau, this emphasises the fact that graphene is more concentrated in the PCL phase in this

sample [48]. The continuous graphene network restricted the movement of the PCL chains and the PLA chains at the interface [76] which caused the increase of the complex viscosity of the co-continuous sample at elevated temperature (figure 102.b). In conclusion, the selective localization of the nanofiller along with the co-continuous structure are the reasons behind the superior viscous and elastic properties of PLA65/PCL35/GNP composite [77].

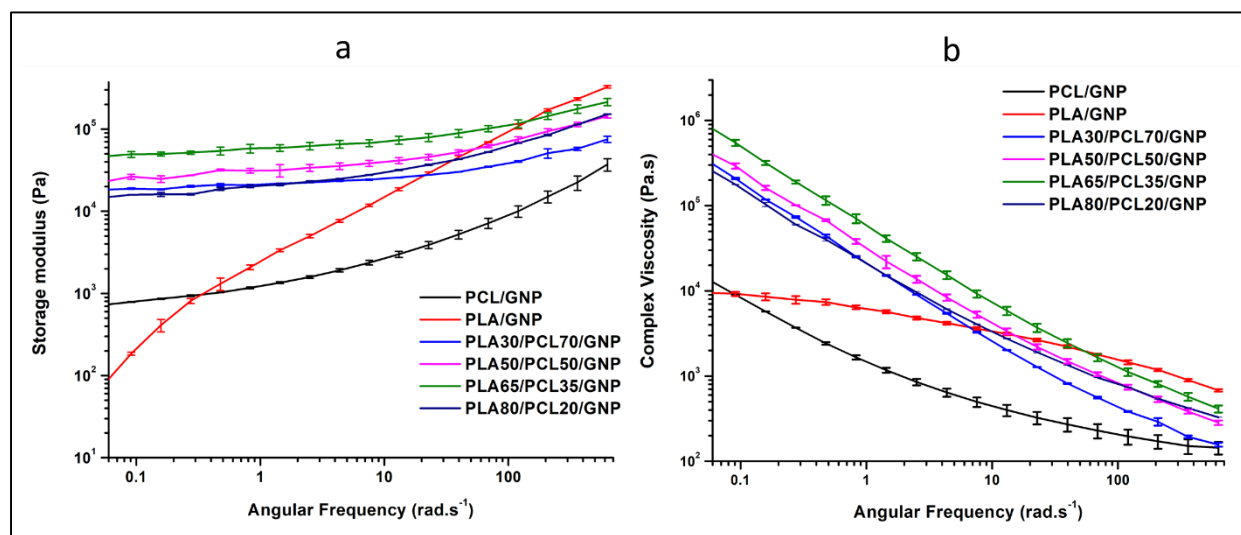


Figure 102: Storage modulus and complex viscosity versus angular frequency of compression moulded composites containing 10 wt.% of GNP

Thus, by combining the SEM, electrical volume resistivity, solvent extraction, and rheological conclusions, PLA65/PCL35/GNP shows the best properties that are linked to the more interesting co-continuous structure of this sample. When referring to the models demonstrated in table 22, Kitayama and Bourry-Favis models, which predict that PLA58/PCL48/GNP and PLA60/PCL40/GNP are the phase inversion points respectively at  $628 \text{ rad.s}^{-1}$ , are the closest to our experimental findings.

#### 6.3.4. DSC results

In an attempt of correlating the co-continuity with the degree of crystallinity of each polymer, DSC tests were carried out. The results are demonstrated in figure 103 and table 25. The percentage of crystallinity of PLA was improved in the case of the ternary composites as compared to the binary composite and the pure polymer that showed no exothermic peak

because of its slow crystallization [78]. This indicates that the presence of PCL acted as a nucleating agent for the PLA crystallites. This percentage was maximal in the sample that possesses a co-continuous structure (PLA65/PCL35/GNP) (7 %). As an explanation, the presence of selectively localised GNP at the continuous interface should have promoted the crystallization of this polymer through a heterogeneous nucleating effect [79][80]. The improvement of the PLA crystallization was obtained in another nanocomposite blend system that contained selectively localised CNT in poly butylene succinate (PBS) phase and at the interface between PLA and PBS [77]. In the present work, PCL crystallinity percentage was improved only in the case of the co-continuous composite (59 % as compared to 50 % of pure PCL). This can be due to the selectively localised dense continuous graphene network present in this phase that promoted its fractionated crystallization [80]. It has been mentioned that the melt crystallization of PCL component in the PLA/PCL blend composites can be strongly influenced by the carbon nanofiller selective localization which can trigger an evident nucleating effect. This can be the result of three roles played by the nanofiller: a heterogeneous substrate to facilitate nucleation, a physical barrier to retard the spherulite growth [79], and an inhibitor of the polymer chains mobility to increase their incorporation into the growing crystals [81]. Several studies have already highlighted that nucleation caused by nanoparticles is highly dependent on the quality of their dispersion and the surface area which in turn modifies the number of nucleation sites available to start the process [82][83].

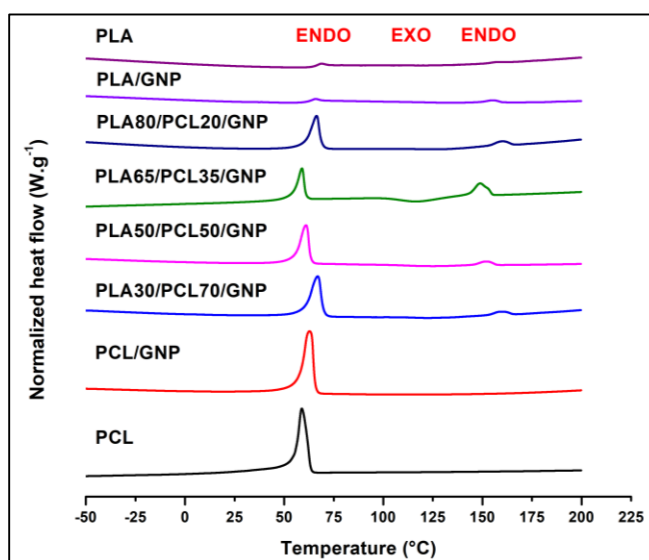


Figure 103: DSC second heating step curves of PLA, PCL, and their binary and ternary composites

Table 25; DSC results of PLA, PCL, and their composites

Sample name	T <sub>m</sub> (PLA) (°C)	T <sub>m</sub> (PCL) (°C)	T <sub>c</sub> (PLA) (°C)	T <sub>g</sub> (PLA) (°C)	X <sub>c</sub> (PLA) (%)	X <sub>c</sub> (PCL) (%)
PCL	-	58 ± 0	-	-	-	50 ± 0
PCL/GNP	-	62 ± 2	-	-	-	53 ± 0
PLA30/PCL70/GNP	156 ± 0	63 ± 2	124 ± 1	63 ± 0	2 ± 0	50 ± 0
PLA50/PCL50/GNP	153 ± 0	61 ± 1	124 ± 3	61 ± 1	2 ± 0	51 ± 0
PLA65/PCL35/GNP	148 ± 2	58 ± 2	115 ± 3	58 ± 3	7 ± 0	59 ± 0
PLA80/PCL20/GNP	155 ± 1	63 ± 2	132 ± 2	63 ± 2	1 ± 0	51 ± 0
PLA/GNP	155 ± 1	-	133 ± 2	61 ± 2	1 ± 0	-
PLA	156 ± 2	-	-	63 ± 1	1 ± 0	-

### 6.3.5. TGA results

To evaluate the thermal stability of the nanocomposites, thermogravimetric analyses were carried out under nitrogen atmosphere and the results are presented in figure 104 and table 26. Pure PCL shows greater thermal stability as compared to pure PLA due to its superior maximal degradation temperature (greater by 50 °C). Both polymers show single degradation step. Thus, their blend composites showed a double-staged degradation that corresponds to the individual degradation of PLA and PCL components. The thermal stability was not improved in the case of the composites as compared to the pure polymers due to the similar values of the onset and maximal degradation temperatures. When comparing the theoretical and experimental char yield at 600 °C, it can be noticed that there is char formation improvement only in the case of the PLA65/PCL35/GNP which can be attributed to the dense graphene network that protected the PCL phase, inhibited its mobility, and acted as a barrier to the mass transfer during thermal degradation [77][84]. The lowest char yield was obtained for PLA/GNP composite (lower than the theoretical char yield). This can be probably attributed to the GNP aggregates present in this sample (figure 97) that played no role in protecting the PLA chains against the thermal degradation.

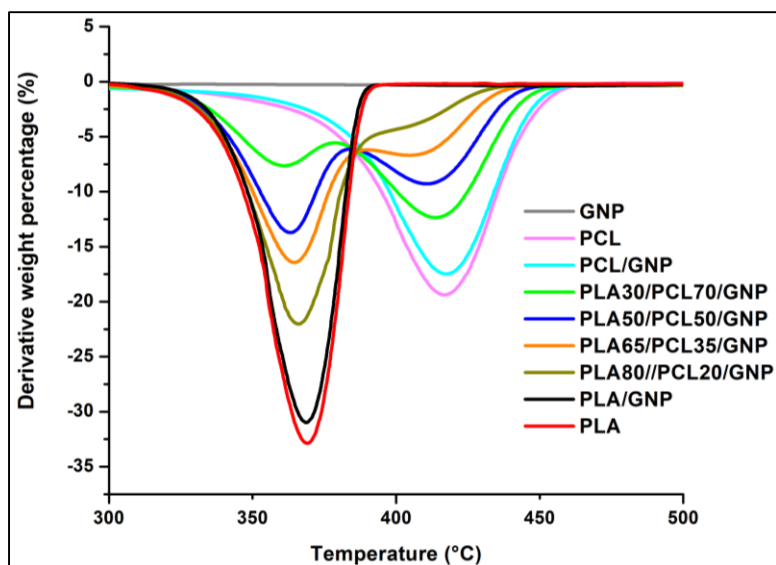


Figure 104: TGA curves of PLA, PCL, their binary and ternary composites

Table 26: TGA results of PLA, PCL, their binary, and ternary composites

Sample name	Maximal degradation temperature ( $T_{max}$ ) of each polymer		Total mass loss (%)	Experimental percentage of char yield (at 600 °C)	Theoretical percentage of char yield (at 600 °C)	Onset temperature ( $T_{onset}$ ) (°C)
	PLA	PCL				
PCL	-	416 ± 2	100 ± 0	0	-	383 ± 2
PCL/GNP	-	414 ± 2	97 ± 0	7 ± 0	9 ± 0	383 ± 1
PLA30/PC L70/GNP	361 ± 2	413 ± 4	97 ± 0	8 ± 1	9 ± 0	351 ± 1
PLA50/PC L50/GNP	363 ± 2	413 ± 2	98 ± 0	8 ± 0	9 ± 0	352 ± 0
PLA65/PC L35/GNP	364 ± 4	412 ± 2	95 ± 0	15 ± 1	9 ± 0	355 ± 1
PLA80/PC L20/GNP	365 ± 2	410 ± 5	97 ± 0	8 ± 0	9 ± 0	351 ± 2
PLA/GNP	368 ± 2	-	100 ± 0	4 ± 1	9 ± 0	351 ± 0
PLA	366 ± 5	-	100 ± 0	0	-	345 ± 1

All the previous results led to a conclusion that PLA65/PCL35/GNP is the best formulation in terms of microstructure and properties. As a result, PLA65/PCL35 composition was chosen for the following three various studies:

- 1) Influence of the annealing time on the co-continuity and therefore on the electrical conductivity
- 2) Influence of the twin-screw extrusion protocol on the co-continuity and the electrical conductivity
- 3) Effect of the graphene content on the co-continuity and the electrical conductivity

#### 6.4. Influence of annealing time during compression moulding on the co-continuity

The increase of the compression moulding duration effect on PLA65/PCL35/10 wt.% GNP composite co-continuous morphology was studied. Figure 105 shows that the increase of compression moulding time from 10 min (figure 105.a) to 35 min (figure 105.c) caused the increase of the size of both phases. The annealing effect that is more pronounced with the longer duration of thermo-compression is the reason behind this morphological evolution. For double percolated structures, thermal annealing can induce phase coarsening which can effectively improve the phase continuity of the co-continuous structure and reduce the interfacial area [85]. The coarsening of immiscible co-continuous polystyrene (PS)/poly (methyl methacrylate) (PMMA) blends during quiescent annealing was already studied in a previous work [41]. The volume average pore diameter was used to characterise the coarsening effect that was evidenced by the pore size growth. The mercury intrusion porosimetry (MIP) was used to estimate this diameter after the selective extraction of each polymer phase using a convenient solvent. Consequently, a direct relationship between the pore size ( $R$ ) and the annealing time ( $t$ ) was deduced ( $R \sim kt$ ). In another work [86], the electrical properties of PS/PMMA/MWCNT composites with double percolation structures were improved by thermal annealing. The greater coalescence of small phases caused the construction of more perfect co-continuous structure with greater conductive pathway continuity. Moreover, re-aggregation of loose MWCNT into a better network in the preferential PMMA phase during the thermal annealing process helped in

improving the electrical conductivity. The construction of conductive networks by thermal annealing treatment in polymer matrices was reported in a lot of works [85][87-93]. In the present work, the increase of the annealing time also leads to an increase in the electrical conductivity (table 27). This might be due to the greater time given to GNP to form a better-connected conductive pathway that was facilitated by the greater PLA continuity (increase of PLA continuity percentage with the annealing time, table 27).

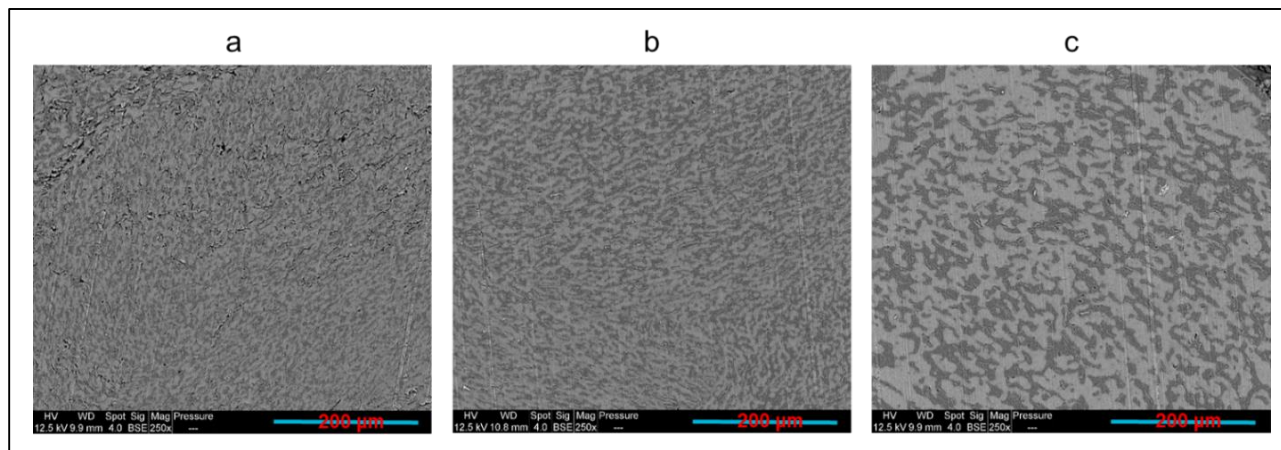


Figure 105: PLA65/PCL35/GNP compression moulded composite during 10 min (a), 20 min (b), and 35 min (c)

Table 27: Electrical volume resistivity, electric current and LED photos (at 5 V), and PLA continuity percentage of PLA65/PCL35/GNP samples manufactured during different compression moulding times (the PCL continuity was 100 % in these samples)

Time (min)	Electrical volume resistivity ( $\Omega \cdot \text{cm}$ )	Electric current (mA) (5 V)	LED (5 V)	Continuous PLA fraction (%) (solvent extraction method)
10	$38 \pm 8$	$9 \pm 0.08$		$85 \pm 2$
20	$34 \pm 9$	$9 \pm 0.02$		$91 \pm 2$
35	$26 \pm 5$	$9 \pm 0.04$		$99 \pm 1$

## 6.5. Influence of the extrusion protocol

It has been reported that the processing sequence is one of the important factors that influence the electrical properties of various binary blend composites [68]. To compare with PLA65/PCL35/10 wt.% GNP composite prepared by one extrusion step, the same composite prepared by two extrusion steps was prepared and evaluated. In the latter, GNP were first blended with PLA, then the resulting PLA/GNP pellets were added to PCL in a second step. Results showed a co-continuous structure regardless of the different preparation procedures (figures 106.a and 106.b). In the two steps extruded composite, GNP particles are only present in the PCL phase as indicated by the yellow arrows, whereas the PLA phase marked by the blue arrows seems GNP-free (figure 106.c). This observation highlights the migration of GNP from the PLA phase to PCL during extrusion. As a consequence, the viscosity of PCL phase increased to promote co-continuity of both polymer phases as explained by Tao et al. [94]. These authors observed the migration phenomenon of carbon nanotubes in co-continuous PLA/PCL blends. The successive phenomena of interfacial driving – separation – division – coalescence are responsible of the nanofiller migration from PLA to PCL based on their research. Figure 107 shows these phenomena in the PLA/PCL/GNP system of this study.

Similar PLA continuity percentage probably favoured by the GNP migration led to similar electrical resistivity in both composites (table 28). This can be attributed to the similar concentration of GNP in the PCL phase. The complete migration of the nanoparticles from one polymer phase to another during the melt blending is not always the case. Cui et al. [68], have obtained much greater electrical volume resistivity of the (PP+CB)/Novolac composite (PP and CB were melt blended together at first using an internal mixer and later mixed with Novolac) as compared to the simultaneously blended composite. In the latter, the CB particles are selectively localised in the Novolac phase. In the former, because of the greater affinity of the CB particles to the Novolac phase, these particles migrated from the PP phase but in a partial manner.

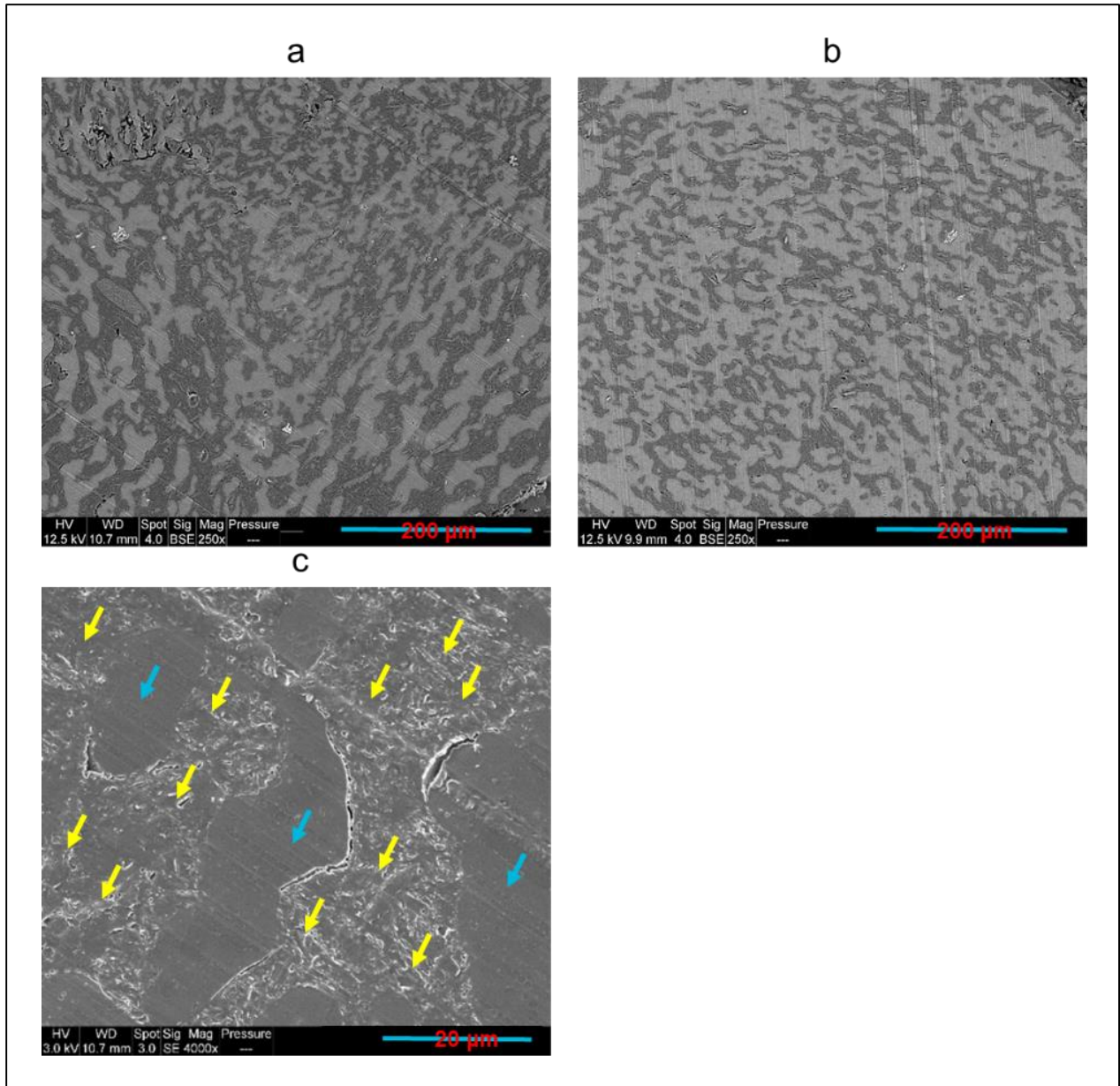


Figure 106: PLA65/PCL35/GNP compression moulded sample extruded in two steps (a,c) and in one step (b); the yellow and blue arrows indicate PCL/GNP and PLA phases respectively

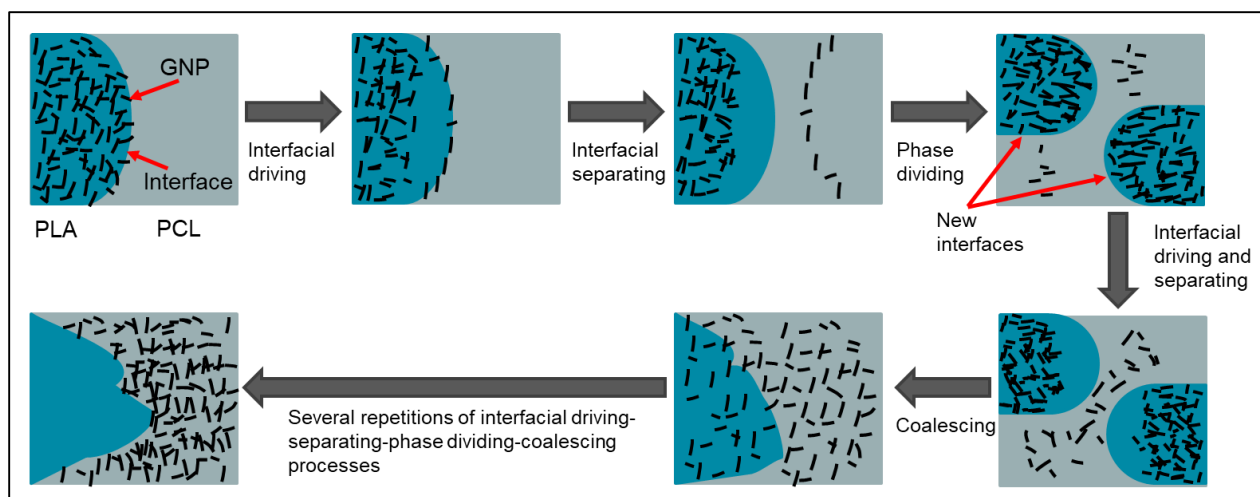
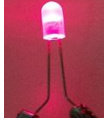


Figure 107: Scheme representing the migration mechanism of GNP from PLA to PCL during twin-screw extrusion (image adapted from reference [94] with GNP instead of CNT)

Table 28: Electrical volume resistivity, electric current and LED photos (at 5 V), and PLA continuity percentage of PLA65/PCL35/GNP samples manufactured using one and two extrusion steps (the PCL continuity was 100 % in these samples)

Number of twin screw extrusion steps	Electrical volume resistivity ( $\Omega \cdot \text{cm}$ )	Electric current (mA) (5 V)	LED (5 V)	Continuous fraction (%) (solvent extraction method)	PLA continuity percentage (%) (solvent extraction method)
One	$26 \pm 5$	$9 \pm 0.04$		$99 \pm 1$	
Two	$30 \pm 3$	$9 \pm 0.06$		$96 \pm 1$	

## 6.6. Influence of GNP content on the co-continuity

For the objective of verifying whether the variation in the graphene content would maintain the co-continuity, GNP percentage was varied from 5 wt.% to 20 wt.% in the PLA65/PCL35 blend composites. Figures 108 and 109 present the SEM observations of the different samples and their continuity fraction percentages respectively. Combining the results of both figures shows that the co-continuous morphology was maintained when the graphene percentage was equal to and

less than 10 wt.%. Beyond this percentage, the PLA continuity percentage decreased to around 50 % at 20 wt.% of graphene. The increase of the viscosity of PCL and the consecutive shearing entailed reduction in PLA domains size to therefore perturb their continuity. Consequently, the barrier to the coalescence of the PLA phase was increased. Although the presence of graphene nanoparticles inside the minor phase increases the elasticity and therefore could stabilise the elongated domains, a threshold of this stabilization could exist. In PA6/PEO system reinforced by graphene, the co-continuity was reduced with the increase of the graphene content due to the reduction of coalescence [70]. Also it was the case in PA6/ABS system, where with the increase of MWCNT content, the co-continuous structure is more refined [10]. Table 29 demonstrates the electrical volume resistivity of these composites. The increase of graphene percentage resulted in denser GNP network formation and therefore the electrical volume resistivity decreased to 0.002  $\Omega$ .cm at 20 wt.% of GNP. In conclusion, although it has greater resistivity, PLA65/PCL35/10 wt.% GNP composite represents a compromise between robust co-continuity and good electrical conductivity.

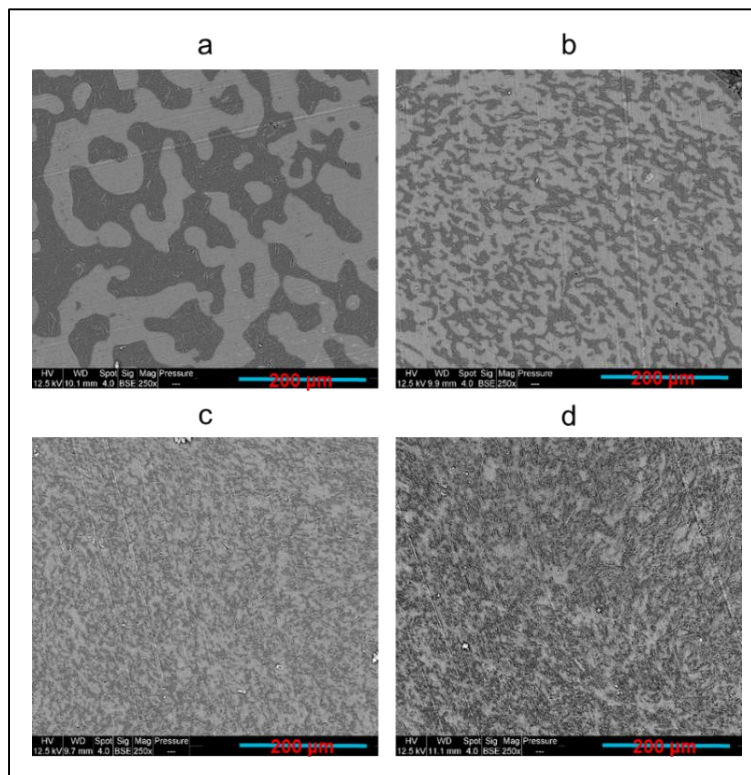


Figure 108: SEM images of compression moulded PLA65/PCL35 blend composites reinforced with 5 wt.% GNP (a), 10 wt.% GNP (b), 15 wt.% GNP (c), and 20 wt.% GNP (d) (white phase is PLA and grey phase is PCL)

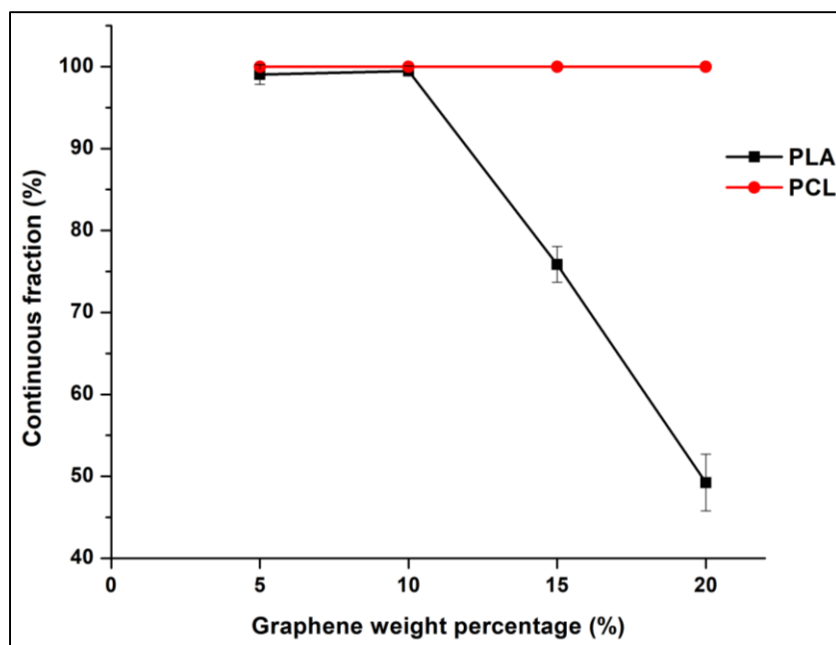


Figure 109: Variation of the continuity percentage of PLA and PCL fractions with the increase of graphene percentage in PLA65/PCL35/GNP composites

Table 29: Electrical volume resistivity and electric current results with the accompanied LED photos at 5 V of PLA65/PCL35/GNP composites (GNP content varies between 5 wt.% and 20 wt.%)

Weight percentage of graphene (%)	Electrical volume resistivity ( $\Omega \cdot \text{cm}$ )	Electric current (mA) (5 V)	LED (5 V)
5	$487 \pm 10$	$0.002 \pm 0.005$	
10	$26 \pm 5$	$9 \pm 0.04$	
15	$0.01 \pm 0.003$	$16 \pm 2$	
20	$0.002 \pm 0.0006$	$26 \pm 7$	

## 6.7. Influence of 3D printing on the co-continuity

The co-continuous structure can help in increasing the printing performance and the possibility to produce a conductive composites at low percolation thresholds [20][71][95]. Thus, several composites containing 10 wt.% of GNP and different proportions of PLA and PCL were prepared by fused filament fabrication (FFF). The electrical results of these samples along with the results of the compression moulded samples are demonstrated in table 30. The objective of these experiments is to investigate the possible conservation of the co-continuous structure after the additive manufacturing process. And therefore, to see the consequences on the electrical resistivity. The morphology of toluene etched 3D printed PLA65/PCL35/10 wt.% GNP is demonstrated in figure 110. The distinction between the PLA and the PCL phases was not possible for the 3D printed samples with high PLA content, therefore the surface etching technique was implemented prior to SEM. The presence of elongated pores that correspond to the absent PCL phase indicates that this sample is co-continuous. This can be confirmed by its lowest electrical resistivity, that was able to illuminate the LED, as compared to the other printed samples. But still, the co-continuous compression moulded sample shows lower electrical volume resistivity. This can be due to the presence of partial co-continuity that starts and ends in each deposited filament and that is not extended all over the volume as it is the case in the compression moulded samples. The high shear rate ( $125 \text{ s}^{-1}$ ) at the nozzle may also have an impact on the microstructure. Moreover, oriented GNP aggregates in the 3D printed sample can be another reason. Figures 111.a and 111.b show some oriented graphene aggregates, surrounded by blue ellipses, in PLA30/PCL70/GNP 3D printed composite possessing a sea-island morphology. These aggregates were absent in the compression moulded sample (figure 111.c) that shows good and random dispersion of graphene in the PCL phase. These microstructural differences are the reason behind the inferior electrical resistivity in all the compression moulded samples as compared to the printed ones. It is noteworthy that as the percentage of PCL increases from 35 wt.% to 70 wt.%, the electrical volume resistivity increases. The same trend was also observed for the compression moulded samples (table 30).

Table 30: Electrical volume resistivity and electric current results with the accompanied LED photos at 5 V of the 3D printed and compression moulded samples containing 10 wt.% GNP and PLA content varying between 80 wt.% and 30 wt.%

Sample	Electrical volume resistivity (3D printed) ( $\Omega\cdot\text{cm}$ )	Electric current (3D printed) (mA) (5 V)	LED (3D printed) (5 V)	Electrical volume resistivity (compression moulded) ( $\Omega\cdot\text{cm}$ )	Electric current (compression moulded) (mA) (5 V)	LED (compression moulded) (5 V)
PLA80/PCL20 /GNP	$> 10^7$	-	No light	$4900 \pm 90$	$0.000001 \pm 0.004$	No light
PLA65/PCL35 /GNP	$1001 \pm 30$	$0.001 \pm 0.01$		$26 \pm 5$	$9 \pm 0.04$	
PLA50/PCL50 /GNP	$3278 \pm 89$	$0.000009 \pm 0.00005$	No light	$76 \pm 15$	$3 \pm 0.05$	
PLA40/PCL60 /GNP	$5372 \pm 90$	$0.000006 \pm 0.00007$	No light	$126 \pm 21$	$1 \pm 0.02$	
PLA30/PCL70 /GNP	$7000 \pm 101$	$0.0000001 \pm 0.00009$	No light	$237 \pm 25$	$1 \pm 0.01$	

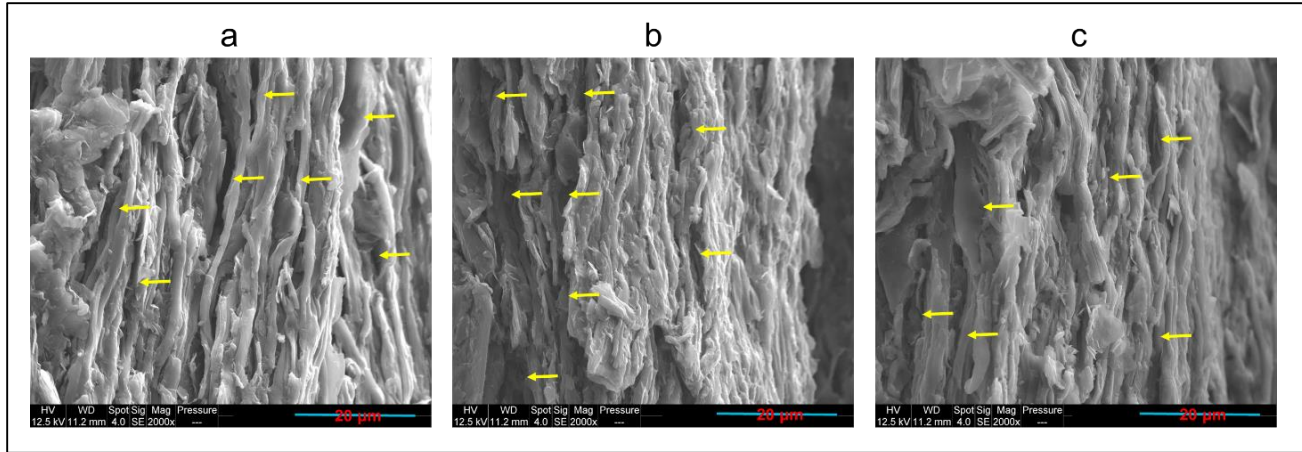


Figure 110 : SEM images of surface etched 3D printed PLA65/PCL35/GNP composite (the yellow arrows point to the pores where PCL elongated nodules were present) (the 3D printed filaments orientation is the same as the orientation of the PCL pores)

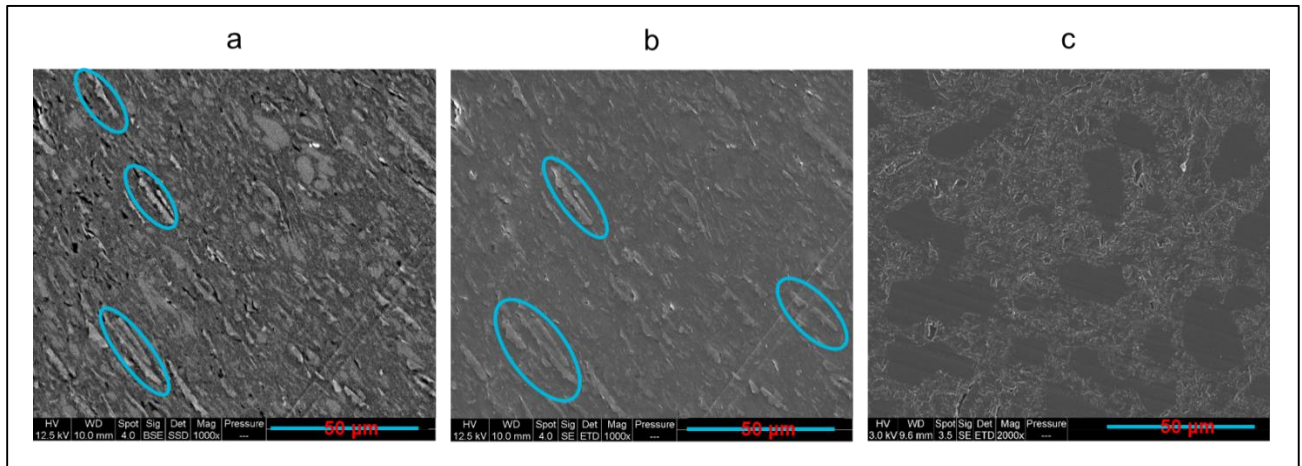


Figure 111: The SEM images of PLA30/PCL70/GNP 3D printed (a,b) and compression moulded (c) composites (the brighter phase is PLA in figure 111.a and the blue ellipses surround the graphene aggregates) (the 3D printed filaments have the same orientation as the GNP aggregates)

## 7. Conclusion

This study has shown for the first time the achievement of a double electrical percolation phenomenon in PLA/PCL/GNP nanocomposites. The influence of different processes on this phenomenon has been scrutinised. The weight percentage of graphene was initially fixed at 10 wt.% and the respective percentages of PLA and PCL were varied between 0 and 100 wt.%. The AFM and the SEM techniques showed selective localization of GNP in the PCL phase and the co-

continuity range was from PLA55/PCL45/GNP to PLA70/PCL30/GNP in the compression moulded samples as it was confirmed by the solvent extraction experiments. The electrical volume resistivity was the lowest in this range with the best results for the PLA65/PCL35/GNP. The melt shear rheological parameters such as the storage modulus and complex viscosity were the greatest for the PLA65/PCL35/GNP at the low angular frequency indicating the presence of the densest graphene percolated structure. The thermal analysis using TGA and DSC showed that PLA65/PCL35/GNP has greater char formation and percentage of crystallinity of both polymers. Various viscosity and storage modulus-based models were applied to predict the phase inversion point that represents the maximum of the co-continuity. Accordingly, Kitayama and Bourry-Favis models were the closest to our experimental findings since they predict at  $628 \text{ rad}\cdot\text{s}^{-1}$  that PLA58/PCL42/GNP and PLA60/PCL40/GNP are the phase inversion points respectively and we have obtained that PLA65/PCL35/GNP has the greatest co-continuity. Moreover, the influence of various processing parameters on the co-continuity was studied. As expected, the size of the co-continuous domains increased due to the annealing effect which led to the resistivity reduction. All the samples exhibited a co-continuous structure starting from 10 minutes of compression moulding with increase in PLA continuity percentage with the compression moulding time. The sample fabricated in two extrusion steps showed a phenomenon of complete migration of GNP from the PLA phase to the PCL phase with a co-continuous microstructure establishment. Furthermore, the increase of the graphene percentage led to decrease in the polymers network size and co-continuity due to the variation of the complex viscosity ratio of the two polymers and the barrier effect to coalescence. The 3D printed PLA65/PCL35/GNP composite showed the best electrical conductivity results due to partial co-continuous structure, conversely to the other compositions. Yet, the compression moulded samples still have superior electrical conductivity due to their co-continuous microstructure that is extended all over the surface. This is not the case for the 3D printed sample whose co-continuity size is restricted within the diameter of each deposited filament. Overall, the results demonstrate that the investigated PLA/PCL/GNP composites are promising materials for technological applications such as chemical sensors, flexible electronic devices, electrical circuit printing, and electromagnetic interference shielding (EMI).

## 8. Bibliography

- [1] P.-C. Ma, N. A. Siddiqui, G. Marom, and J.-K. Kim, "Dispersion and functionalization of carbon nanotubes for polymer-based nanocomposites: A review," *Compos. Part A Appl. Sci. Manuf.*, vol. 41, pp. 1345–1367, 2010, doi: <https://doi.org/10.1016/j.compositesa.2010.07.003>.
- [2] T. Villmow, S. Pegel, A. John, R. Rentenberger, and P. Pötschke, "Liquid sensing: smart polymer/CNT composites," *Mater. Today*, vol. 14, pp. 340–345, 2011, doi: [https://doi.org/10.1016/S1369-7021\(11\)70164-X](https://doi.org/10.1016/S1369-7021(11)70164-X).
- [3] R. A. Antunes, M. C. L. de Oliveira, G. Ett, and V. Ett, "Carbon materials in composite bipolar plates for polymer electrolyte membrane fuel cells: A review of the main challenges to improve electrical performance," *J. Power Sources*, vol. 196, pp. 2945–2961, 2011, doi: <https://doi.org/10.1016/j.jpowsour.2010.12.041>.
- [4] Z.-M. Dang, J.-K. Yuan, J.-W. Zha, T. Zhou, S.-T. Li, and G.-H. Hu, "Fundamentals, processes and applications of high-permittivity polymer–matrix composites," *Prog. Mater. Sci.*, vol. 57, pp. 660–723, 2012, doi: <https://doi.org/10.1016/j.pmatsci.2011.08.001>.
- [5] K. R. Ryan, M. P. Down, N. J. Hurst, E. M. Keefe, and C. E. Banks, "Additive manufacturing (3D printing) of electrically conductive polymers and polymer nanocomposites and their applications," *eScience*, vol. 2, pp. 365–381, 2022, doi: <https://doi.org/10.1016/j.esci.2022.07.003>.
- [6] Y. Liu, H. He, G. Tian, Y. Wang, J. Gao, C. Wang, L. Xu, and H. Zhang, "Morphology evolution to form double percolation polylactide/polycaprolactone/MWCNTs nanocomposites with ultralow percolation threshold and excellent EMI shielding," *Compos. Sci. Technol.*, vol. 214, p. 108956, 2021, doi: <https://doi.org/10.1016/j.compscitech.2021.108956>.
- [7] J. Huang, C. Mao, Y. Zhu, W. Jiang, and X. Yang, "Control of carbon nanotubes at the interface of a co-continuous immiscible polymer blend to fabricate conductive composites with ultralow percolation thresholds," *Carbon N. Y.*, vol. 73, pp. 267–274, 2014, doi: <https://doi.org/10.1016/j.carbon.2014.02.063>.
- [8] A. Sadeghi, R. Moeini, and J. K. Yeganeh, "Highly conductive PP/PET polymer blends with high electromagnetic interference shielding performances in the presence of thermally reduced graphene nanosheets prepared through melt compounding," *Polym. Compos.*, vol. 40, pp. E1461–E1469, 2019, doi: <https://doi.org/10.1002/pc.25051>.
- [9] S. Maiti, N. K. Shrivastava, and B. B. Khatua, "Reduction of percolation threshold through double percolation in melt-blended polycarbonate/acrylonitrile butadiene styrene/multiwall carbon nanotubes elastomer nanocomposites," *Polym. Compos.*, vol. 34, pp. 570–579, 2013, doi: <https://doi.org/10.1002/pc.22462>.
- [10] S. Bose, A. R. Bhattacharyya, A. P. Bondre, A. R. Kulkarni, and P. Pötschke, "Rheology, electrical conductivity, and the phase behavior of cocontinuous PA6/ABS blends with MWNT: Correlating the aspect ratio of MWNT with the percolation threshold," *J. Polym. Sci. Part B Polym. Phys.*, vol. 46, pp. 1619–1631, 2008, doi: <https://doi.org/10.1002/polb.21501>.

- [11] J. Chen, X. Cui, Y. Zhu, W. Jiang, and K. Sui, "Design of superior conductive polymer composite with precisely controlling carbon nanotubes at the interface of a co-continuous polymer blend via a balance of  $\pi$ - $\pi$  interactions and dipole-dipole interactions," *Carbon* N. Y., vol. 114, pp. 441–448, 2017, doi: <https://doi.org/10.1016/j.carbon.2016.12.048>.
- [12] D. Strugova, J. C. Ferreira Junior, É. David, and N. R. Demarquette, "Ultra-Low Percolation Threshold Induced by Thermal Treatments in Co-Continuous Blend-Based PP/PS/MWCNTs Nanocomposites," *Nanomaterials*, vol. 11, 2021, doi: [10.3390/nano11061620](https://doi.org/10.3390/nano11061620).
- [13] J. Chen, X. Cui, K. Sui, Y. Zhu, and W. Jiang, "Balance the electrical properties and mechanical properties of carbon black filled immiscible polymer blends with a double percolation structure," *Compos. Sci. Technol.*, vol. 140, pp. 99–105, 2017, doi: <https://doi.org/10.1016/j.compscitech.2016.12.029>.
- [14] F. Gubbels, S. Blacher, E. Vanlathem, R. Jerome, R. Deltour, F. Brouers, and P. Teyssie, "Design of Electrical Composites: Determining the Role of the Morphology on the Electrical Properties of Carbon Black Filled Polymer Blends," *Macromolecules*, vol. 28, pp. 1559–1566, 1995, doi: [10.1021/ma00109a030](https://doi.org/10.1021/ma00109a030).
- [15] Y. Pan, X. Liu, X. Hao, Z. Starý, and D. W. Schubert, "Enhancing the electrical conductivity of carbon black-filled immiscible polymer blends by tuning the morphology," *Eur. Polym. J.*, vol. 78, pp. 106–115, 2016, doi: <https://doi.org/10.1016/j.eurpolymj.2016.03.019>.
- [16] Y. Luo, S.-Y. Xiong, F. Zhang, X.-X. He, X. Lu, and R.-T. Peng, "Preparation of conductive polylactic acid/high density polyethylene/carbon black composites with low percolation threshold by locating the carbon black at the Interface of co-continuous blends," *J. Appl. Polym. Sci.*, vol. 138, p. 50291, 2021, doi: <https://doi.org/10.1002/app.50291>.
- [17] X. Lu, B. Kang, and S. Shi, "Selective Localization of Carbon Black in Bio-Based Poly (Lactic Acid)/Recycled High-Density Polyethylene Co-Continuous Blends to Design Electrical Conductive Composites with a Low Percolation Threshold," *Polymers (Basel)*, vol. 11, 2019, doi: [10.3390/polym11101583](https://doi.org/10.3390/polym11101583).
- [18] Y. Kou, A. T. Cote, J. Liu, X. Cheng, and C. W. Macosko, "Robust networks of interfacial localized graphene in cocontinuous polymer blends," *J. Rheol. (N. Y. N. Y.)*, vol. 65, pp. 1139–1153, 2021, doi: [10.1122/8.0000294](https://doi.org/10.1122/8.0000294).
- [19] L. Bai, R. Sharma, X. Cheng, and C. W. Macosko, "Kinetic Control of Graphene Localization in Co-continuous Polymer Blends via Melt Compounding," *Langmuir*, vol. 34, pp. 1073–1083, 2018, doi: [10.1021/acs.langmuir.7b03085](https://doi.org/10.1021/acs.langmuir.7b03085).
- [20] M. C. Bertolini, S. Dul, G. M. O. Barra, and A. Pegoretti, "Poly(vinylidene fluoride)/thermoplastic polyurethane flexible and 3D printable conductive composites," *J. Appl. Polym. Sci.*, vol. 138, p. 50305, 2021, doi: <https://doi.org/10.1002/app.50305>.
- [21] M. Kocun, A. Labuda, W. Meinhold, I. Revenko, and R. Proksch, "Fast, High Resolution, and Wide Modulus Range Nanomechanical Mapping with Bimodal Tapping Mode," *ACS Nano*, vol. 11, pp. 10097–10105, 2017, doi: [10.1021/acsnano.7b04530](https://doi.org/10.1021/acsnano.7b04530).

- [22] D. Bourry and B. D. Favis, "Cocontinuity and phase inversion in HDPE/PS blends: Influence of interfacial modification and elasticity," *J. Polym. Sci. Part B Polym. Phys.*, vol. 36, pp. 1889–1899, 1998, doi: 10.1002/(SICI)1099-0488(199808)36:11<1889::AID-POLB10>3.0.CO;2-3.
- [23] S. Mani, M. F. Malone, and H. H. Winter, "Influence of phase separation on the linear viscoelastic behavior of a miscible polymer blend," *J. Rheol. (N. Y. N. Y.)*, vol. 36, pp. 1625–1649, 1992, doi: 10.1122/1.550277.
- [24] A. Ajji, L. Choplin, and R. E. Prud'Homme, "Rheology of polystyrene/poly(vinyl methyl ether)blends near the phase transition," *J. Polym. Sci. Part B Polym. Phys.*, vol. 29, pp. 1573–1578, 1991, doi: <https://doi.org/10.1002/polb.1991.090291301>.
- [25] S. Steinmann, W. Gronski, and C. Friedrich, "Influence of selective filling on rheological properties and phase inversion of two-phase polymer blends," *Polymer (Guildf.)*, vol. 43, pp. 4467–4477, 2002, doi: [https://doi.org/10.1016/S0032-3861\(02\)00271-9](https://doi.org/10.1016/S0032-3861(02)00271-9).
- [26] J. Galloway, M. Montminy, and C. Macosko, "Image analysis for interfacial area and cocontinuity detection in polymer blends," *Polymer (Guildf.)*, vol. 43, pp. 4715–4722, 2002, doi: 10.1016/S0032-3861(02)00282-3.
- [27] S. Steinmann, W. Gronski, and C. Friedrich, "Cocontinuous polymer blends: influence of viscosity and elasticity ratios of the constituent polymers on phase inversion," *Polymer (Guildf.)*, vol. 42, pp. 6619–6629, 2001, doi: [https://doi.org/10.1016/S0032-3861\(01\)00100-8](https://doi.org/10.1016/S0032-3861(01)00100-8).
- [28] J. Galloway and C. Macosko, "Comparison of methods for the detection of cocontinuity in poly(ethylene oxide)/polystyrene blends," *Polym. Eng. Sci.*, vol. 44, pp. 714–727, 2004, doi: 10.1002/pen.20064.
- [29] N. Marin and B.D. Favis, "Co-continuous morphology development in partially miscible PMMA/PC blends," *Polymer (Guildf.)*, vol. 43, pp. 4723–4731, 2002, doi: 10.1016/S0032-3861(02)00280-X.
- [30] R. Willemse, A. Posthuma de Boer, J. van Dam, and A. Gotsis, "Co-continuous morphologies in polymer blends: a new model," *Polymer (Guildf.)*, vol. 39, pp. 5879–5887, 1998, doi: [doi.org/10.1016/S0032-3861\(97\)10200-2](https://doi.org/10.1016/S0032-3861(97)10200-2).
- [31] R. C. Willemse, A. Posthuma de Boer, J. van Dam, and A. D. Gotsis, "Co-continuous morphologies in polymer blends: the influence of the interfacial tension," *Polymer (Guildf.)*, vol. 40, pp. 827–834, 1999, doi: [https://doi.org/10.1016/S0032-3861\(98\)00307-3](https://doi.org/10.1016/S0032-3861(98)00307-3).
- [32] J. Li, P. L. Ma, and B. D. Favis, "The Role of the Blend Interface Type on Morphology in Cocontinuous Polymer Blends," *Macromolecules*, vol. 35, pp. 2005–2016, 2002, doi: 10.1021/ma010104+.
- [33] K. Dedecker and G. Groeninckx, "Reactive compatibilisation of A/(B/C) polymer blends. Part 2. Analysis of the phase inversion region and the co-continuous phase morphology," *Polymer (Guildf.)*, vol. 39, pp. 4993–5000, 1998, doi: [https://doi.org/10.1016/S0032-3861\(97\)10089-1](https://doi.org/10.1016/S0032-3861(97)10089-1).

- [34] G. Filippone, N. T. Dintcheva, F. P. La Mantia, and D. Acierno, "Using organoclay to promote morphology refinement and co-continuity in high-density polyethylene/polyamide 6 blends - Effect of filler content and polymer matrix composition," *Polymer (Guildf)*., vol. 51, pp. 3956–3965, 2010, doi: 10.1016/j.polymer.2010.06.044.
- [35] T. Omonov, C. Harrats, P. Moldenaers, and G. Groeninckx, "Phase continuity detection and phase inversion phenomena in immiscible polypropylene/polystyrene blends with different viscosity ratios," *Polymer (Guildf)*., vol. 48, pp. 5917–5927, 2007, doi: 10.1016/j.polymer.2007.08.012.
- [36] A. Mirzadeh, P. G. Lafleur, M. R. Kamal, and C. Dubois, "The effect of compatibilizer on the co-continuity and nanoclay dispersion level of tpe nanocomposites based on PP/EPDM," *Polym. Eng. & Sci.*, vol. 50, pp. 2131–2142, 2010, doi: <https://doi.org/10.1002/pen.21744>.
- [37] S. Chaput, C. Carrot, M. Castro, and F. Prochazka, "Co-continuity interval in immiscible polymer blends by dynamic mechanical spectroscopy in the molten and solid state," *Rheol. Acta*, vol. 43, pp. 417–426, 2004, doi: 10.1007/s00397-004-0369-4.
- [38] N. Mekhilef, B. D. Favis, and P. J. Carreau, "Morphological stability, interfacial tension, and dual-phase continuity in polystyrene-polyethylene blends," *J. Polym. Sci. Part B Polym. Phys.*, vol. 35, pp. 293–308, 1997, doi: [https://doi.org/10.1002/\(SICI\)1099-0488\(19970130\)35:2<293::AID-POLB7>3.0.CO;2-T](https://doi.org/10.1002/(SICI)1099-0488(19970130)35:2<293::AID-POLB7>3.0.CO;2-T).
- [39] E. Schwach and L. Avérous, "Starch-based biodegradable blends: morphology and interface properties," *Polym. Int.*, vol. 53, pp. 2115–2124, 2004, doi: <https://doi.org/10.1002/pi.1636>.
- [40] T. S. Omonov, C. Harrats, G. Groeninckx, and P. Moldenaers, "Anisotropy and instability of the co-continuous phase morphology in uncompatibilized and reactively compatibilized polypropylene/polystyrene blends," *Polymer (Guildf)*., vol. 48, pp. 5289–5302, 2007, doi: <https://doi.org/10.1016/j.polymer.2007.06.043>.
- [41] Z. Yuan and B. D. Favis, "Coarsening of immiscible co-continuous blends during quiescent annealing," *AIChE J.*, vol. 51, pp. 271–280, 2005, doi: <https://doi.org/10.1002/aic.10281>.
- [42] S. Hammani, N. Moulai-Mostefa, L. Benyahia, and J.-F. Tassin, "Effects of composition and extrusion parameters on the morphological development and rheological properties of PP/PC blends. Co-continuity investigation," *J. Polym. Res.*, vol. 19, p. 9940, 2012, doi: 10.1007/s10965-012-9940-3.
- [43] C. Calberg, S. Blacher, F. Gubbels, F. Brouers, R. Deltour, and R. Jérôme, "Electrical and dielectric properties of carbon black filled co-continuous two-phase polymer blends," *J. Phys. D. Appl. Phys.*, vol. 32, pp. 1517–1525, 1999, doi: 10.1088/0022-3727/32/13/313.
- [44] N.-A. Masarra, M. Batistella, J. C. Quantin, A. Regazzi, M. F. Pucci, R. El Hage, and J. M. Lopez- Cuesta, "Fabrication of PLA/PCL/Graphene Nanoplatelet (GNP) Electrically Conductive Circuit Using the Fused Filament Fabrication (FFF) 3D Printing Technique," *Materials (Basel)*., vol. 15, 2022, doi: 10.3390/ma15030762.

- [45] R. Patwa, A. Kumar, and V. Katiyar, "Crystallization kinetics, morphology, and hydrolytic degradation of novel bio-based poly(lactic acid)/crystalline silk nano-discs nanobiocomposites," *J. Appl. Polym. Sci.*, vol. 135, pp. 1–18, 2018, doi: 10.1002/app.46590.
- [46] H. Y. Kweon, M. K. Yoo, I. K. Park, T. H. Kim, H. C. Lee, H. S. Lee, J. S. Oh, T. Akaike, and C. S. Cho, "A novel degradable polycarbonate networks for tissue engineering," *Biomaterials*, vol. 24, pp. 801–808, 2003, doi: 10.1016/s0142-9612(02)00370-8.
- [47] A. Nuzzo, E. Bilotti, T. Peijs, D. Acierno, and G. Filippone, "Nanoparticle-induced co-continuity in immiscible polymer blends – A comparative study on bio-based PLA-PA11 blends filled with organoclay, sepiolite, and carbon nanotubes," *Polymer (Guildf.)*, vol. 55, pp. 4908–4919, 2014, doi: <https://doi.org/10.1016/j.polymer.2014.07.036>.
- [48] M. A. Kashfipour, M. Guo, L. Mu, N. Mehra, Z. Cheng, J. Olivio, S. Zhu, J. M. Maia, and J. Zhu, "Carbon nanofiber reinforced Co-continuous HDPE/PMMA composites: Exploring the role of viscosity ratio on filler distribution and electrical/thermal properties," *Compos. Sci. Technol.*, vol. 184, p. 107859, 2019, doi: <https://doi.org/10.1016/j.compscitech.2019.107859>.
- [49] "[https://www.natureworksllc.com/~media/Technical\\_Resources/Technical\\_Data\\_Sheets/TechnicalDataSheet\\_2003D\\_FFP-FSW\\_pdf.pdf](https://www.natureworksllc.com/~media/Technical_Resources/Technical_Data_Sheets/TechnicalDataSheet_2003D_FFP-FSW_pdf.pdf)," accessed on October 23<sup>rd</sup> 2022.
- [50] L. Jeantet, A. Regazzi, A. Taguet, M. Pucci, A.-S. Caro, and J.-C. Quantin, "Biopolymer blends for mechanical property gradient 3D printed parts," *Express Polym. Lett.*, vol. 15, pp. 137–152, 2021, doi: 10.3144/expresspolymlett.2021.13.
- [51] T. Zhong, J. Li, and K. Zhang, "A molecular dynamics study of Young's modulus of multilayer graphene," *J. Appl. Phys.*, vol. 125, p. 175110, 2019, doi: 10.1063/1.5091753.
- [52] J. de Aguiar, M. Decol, W. M. Pachekoski, and D. Becker, "Mixing-sequence controlled selective localization of carbon nanoparticles in PLA/PCL blends," *Polym. Eng. Sci.*, vol. 59, pp. 323–329, 2019, doi: 10.1002/pen.24908.
- [53] O. J. Botlhoko, S. S. Ray, and J. Ramontja, "Influence of functionalized exfoliated reduced graphene oxide nanoparticle localization on mechanical, thermal and electronic properties of nanobiocomposites," *Eur. Polym. J.*, vol. 102, pp. 130–140, 2018, doi: <https://doi.org/10.1016/j.eurpolymj.2018.03.012>.
- [54] I. S. Miles and A. Zurek, "Preparation, structure, and properties of two-phase co-continuous polymer blends," *Polym. Eng. Sci.*, vol. 28, pp. 796–805, 1988, doi: <https://doi.org/10.1002/pen.760281205>.
- [55] D. R. Paul and J. W. Barlow, "Polymer Blends," *J. Macromol. Sci. Part C*, vol. 18, pp. 109–168, 1980, doi: 10.1080/00222358008080917.
- [56] R. M. Ho, C. H. Wu, and A. C. Su, "Morphology of plastic/rubber blends," *Polym. Eng. Sci.*, vol. 30, pp. 511 – 518, 1990, doi: 10.1002/pen.760300903.

- [57] N. Kitayama, H. Keskkula, and D. R. Paul, "Reactive compatibilization of nylon 6/styrene-acrylonitrile copolymer blends: Part 1. Phase inversion behavior," *Polymer (Guildf)*., vol. 41, pp. 8041 – 8052, 2000, doi: 10.1016/S0032-3861(00)00156-7.
- [58] V. Everaert, L. Aerts, and G. Groeninckx, "Phase morphology development in immiscible PP/(PS/PPE) blends influence of the melt-viscosity ratio and blend composition," *Polymer (Guildf)*., vol. 40, pp. 6627 – 6644, 1999, doi: 10.1016/S0032-3861(99)00048-8.
- [59] "https://www.scopus.com/inward/record.uri?eid=2-s2.0-0021420709&partnerID=40&md5=bc4173f917ee673da2b80a12cc2079ee", accessed on October 20<sup>th</sup> 2022.
- [60] L. A. Utracki, "History of commercial polymer alloys and blends (from a perspective of the patent literature)," *Polym. Eng. Sci.*, vol. 35, pp. 2–17, 1995, doi: <https://doi.org/10.1002/pen.760350103>.
- [61] C. F. Antunes, M. van Duin, and A. V Machado, "Morphology and phase inversion of EPDM/PP blends – Effect of viscosity and elasticity," *Polym. Test.*, vol. 30, pp. 907–915, 2011, doi: <https://doi.org/10.1016/j.polymertesting.2011.08.013>.
- [62] N. Mekhilef and H. Verhoogt, "Phase inversion and dual-phase continuity in polymer blends: theoretical predictions and experimental results," *Polymer (Guildf)*., vol. 37, pp. 4069–4077, 1996, doi: [https://doi.org/10.1016/0032-3861\(96\)00254-6](https://doi.org/10.1016/0032-3861(96)00254-6).
- [63] P. Pötschke and D. R. Paul, "Formation of Co-continuous Structures in Melt-Mixed Immiscible Polymer Blends," *J. Macromol. Sci. Part C*, vol. 43, pp. 87–141, 2003, doi: 10.1081/MC-120018022.
- [64] L. Wang, C. Shi, Z.-X. Guo, and J. Yu, "Tailoring the morphology of polypropylene/polyamide 66 blend at an asymmetric composition by using organoclay and maleic anhydride grafted polypropylene," *J. Ind. Eng. Chem.*, vol. 20, pp. 259–267, 2014, doi: <https://doi.org/10.1016/j.jiec.2013.03.040>.
- [65] M. Kong, Y. Huang, G. Chen, Q. Yang, and G. Li, "Retarded relaxation and breakup of deformed PA6 droplets filled with nanosilica in PS matrix during annealing," *Polymer (Guildf)*., vol. 52, pp. 5231–5236, 2011, doi: <https://doi.org/10.1016/j.polymer.2011.08.052>.
- [66] M. Kontopoulou, Y. Liu, J. R. Austin, and J. S. Parent, "The dynamics of montmorillonite clay dispersion and morphology development in immiscible ethylene–propylene rubber/polypropylene blends," *Polymer (Guildf)*., vol. 48, pp. 4520–4528, 2007, doi: <https://doi.org/10.1016/j.polymer.2007.05.068>.
- [67] Y. Li and H. Shimizu, "Novel morphologies of poly(phenylene oxide) (PPO)/polyamide 6 (PA6) blend nanocomposites," *Polymer (Guildf)*., vol. 45, pp. 7381–7388, 2004, doi: <https://doi.org/10.1016/j.polymer.2004.09.018>.
- [68] L. Cui, Y. Zhang, Y. Zhang, X. Zhang, and W. Zhou, "Electrical properties and conductive mechanisms of immiscible polypropylene/Novolac blends filled with carbon black," *Eur. Polym. J.*, vol. 43, pp. 5097–5106, 2007, doi: <https://doi.org/10.1016/j.eurpolymj.2007.08.023>.

- [69] J. Zhao, X. Yin, J. Shi, X. Zhao, X. Wang, M. Chen, Z.-M. Dang, and G.-H. Hu, "Effect of the mixing on the dielectric constant of poly(vinylidene fluoride)/isotactic polypropylene blends," *Sci. Adv. Mater.*, vol. 5, pp. 505–511, 2013, doi: 10.1166/sam.2013.1481.
- [70] M. Hadaeghnia, S. Ahmadi, I. Ghasemi, and P. M. Wood-Adams, "Manipulating the morphology of PA6/POE blends using graphene to achieve balanced electrical and mechanical properties," *Compos. Sci. Technol.*, vol. 200, p. 108412, 2020, doi: <https://doi.org/10.1016/j.compscitech.2020.108412>.
- [71] Y. Lyu, J. Pang, Z. Gao, Q. Zhang, and X. Shi, "Characterization of the compatibility of PVC/PLA blends by Aid of Rheological Responses," *Polymer (Guildf.)*, vol. 176, pp. 20–29, 2019, doi: <https://doi.org/10.1016/j.polymer.2019.05.016>.
- [72] P. Pötschke, M. Abdel-Goad, I. Alig, S. Dudkin, and D. Lellinger, "Rheological and dielectrical characterization of melt mixed polycarbonate-multiwalled carbon nanotube composites," *Polymer (Guildf.)*, vol. 45, pp. 8863–8870, 2004, doi: <https://doi.org/10.1016/j.polymer.2004.10.040>.
- [73] D. Wu, Y. Zhang, M. Zhang, and W. Yu, "Selective Localization of Multiwalled Carbon Nanotubes in Poly( $\epsilon$ -caprolactone)/Polylactide Blend," *Biomacromolecules*, vol. 10, pp. 417–424, 2009, doi: 10.1021/bm801183f.
- [74] S. Bose, C. Özdilek, J. Leys, J. W. Seo, M. Wübberhorst, J. Vermant, and P. Moldenaers, "Phase Separation as a Tool to Control Dispersion of Multiwall Carbon Nanotubes in Polymeric Blends," *ACS Appl. Mater. Interfaces*, vol. 2, pp. 800–807, 2010, doi: 10.1021/am9008067.
- [75] Y. Zhu, R. Cardinaels, J. Mewis, and P. Moldenaers, "Rheological properties of PDMS/clay nanocomposites and their sensitivity to microstructure," *Rheol. Acta*, vol. 48, p. 1049, 2009, doi: 10.1007/s00397-009-0387-3.
- [76] Y. Meng, S. Sharma, J. S. Chung, W. Gan, S. H. Hur, and W. M. Choi, "Enhanced Electromagnetic Interference Shielding Properties of Immiscible Polyblends with Selective Localization of Reduced Graphene Oxide Networks," *Polymers (Basel)*, vol. 14, 2022, doi: 10.3390/polym14050967.
- [77] V. Sivanjineyulu, K. Behera, Y.-H. Chang, and F.-C. Chiu, "Selective localization of carbon nanotube and organoclay in biodegradable poly(butylene succinate)/polylactide blend-based nanocomposites with enhanced rigidity, toughness and electrical conductivity," *Compos. Part A Appl. Sci. Manuf.*, vol. 114, pp. 30–39, 2018, doi: <https://doi.org/10.1016/j.compositesa.2018.08.009>.
- [78] S. Laske, W. Ziegler, M. Kainer, J. Wuerfel, and C. Holzer, "Enhancing the temperature stability of PLA by compounding strategies," *Polym. Eng. & Sci.*, vol. 55, pp. 2849–2858, 2015, doi: <https://doi.org/10.1002/pen.24176>.
- [79] D. Wu, D. Lin, J. Zhang, W. Zhou, M. Zhang, Y. Zhang, Y. Zhang, D. Wang, and B. Lin, "Selective Localization of Nanofillers: Effect on Morphology and Crystallization of PLA/PCL Blends," *Macromol. Chem. Phys.*, vol. 212, pp. 613–626, 2011, doi: 10.1002/macp.201000579.

- [80] M. de Paula Cavalcante, L. R. de Menezes, E. J. da Rocha Rodrigues, and M. I. B. Tavares, "Selective localization of nanohydroxyapatite in poly(3-hydroxybutyrate)/polycaprolactone blends composites and its effects on crystallization and molecular dynamics," *J. Mater. Sci.*, vol. 56, pp. 3692–3712, 2021, doi: 10.1007/s10853-020-05492-8.
- [81] A. Cayla, C. Campagne, M. Rochery, and E. Devaux, "Melt spun multifilament yarns of carbon nanotubes-based polymeric blends: Electrical, mechanical and thermal properties," *Synth. Met.*, vol. 162, pp. 759–767, 2012, doi: <https://doi.org/10.1016/j.synthmet.2012.03.021>.
- [82] A. M. Díez-Pascual and A. L. Díez-Vicente, "Poly (3-hydroxybutyrate)/ZnO bionanocomposites with improved mechanical, barrier and antibacterial properties," *Int. J. Mol. Sci.*, vol. 15, pp. 10950–10973, 2014, doi: 10.3390/ijms150610950.
- [83] J. Ivorra-Martinez, L. Quiles-Carrillo, T. Boronat, S. Torres-Giner, and J. A. Covas, "Assessment of the mechanical and thermal properties of injection-molded poly (3-hydroxybutyrate-co-3-hydroxyhexanoate)/hydroxyapatite nanoparticles parts for use in bone tissue engineering," *Polymers (Basel)*, vol. 12, p. 1389, 2020, doi.org/10.3390/polym12061389.
- [84] C. Gao, S. Zhang, B. Han, H. Sun, G. Wang, and Z. Jiang, "Multi-walled carbon nanotube induced co-continuity of poly (ether ether ketone)/polyimide blends for high performance conductive materials," *Rsc Adv.*, vol. 4, pp. 42175–42182, 2014, doi.org/10.1039/C4RA07473D.
- [85] Y. Chen, Q. Yang, Y. Huang, X. Liao, and Y. Niu, "Influence of phase coarsening and filler agglomeration on electrical and rheological properties of MWNTs-filled PP/PMMA composites under annealing," *Polymer (Guildf)*, vol. 79, pp. 159–170, 2015, doi: <https://doi.org/10.1016/j.polymer.2015.10.027>.
- [86] H. Zhang, J. Chen, X. Cui, Y. Hu, L. Lei, Y. Zhu, and W. Jiang, "Thermal annealing induced enhancement of electrical properties of a co-continuous polymer blend filled with carbon nanotubes," *Compos. Sci. Technol.*, vol. 167, pp. 522–528, 2018, doi: <https://doi.org/10.1016/j.compscitech.2018.08.048>.
- [87] B. H. Cipriano, A. K. Kota, A. L. Gershon, C. J. Laskowski, T. Kashiwagi, H. A. Bruck, and S. R. Raghavan, "Conductivity enhancement of carbon nanotube and nanofiber-based polymer nanocomposites by melt annealing," *Polymer (Guildf)*, vol. 49, pp. 4846–4851, 2008, doi: <https://doi.org/10.1016/j.polymer.2008.08.057>.
- [88] I. Alig, T. Skipa, D. Lellinger, and P. Pötschke, "Destruction and formation of a carbon nanotube network in polymer melts: Rheology and conductivity spectroscopy," *Polymer (Guildf)*, vol. 49, pp. 3524–3532, 2008, doi: <https://doi.org/10.1016/j.polymer.2008.05.037>.
- [89] R. Zhang, A. Dowden, H. Deng, M. Baxendale, and T. Peijs, "Conductive network formation in the melt of carbon nanotube/thermoplastic polyurethane composite," *Compos. Sci. Technol.*, vol. 69, pp. 1499–1504, 2009, doi: <https://doi.org/10.1016/j.compscitech.2008.11.039>.
- [90] Y. Pan, H. K. F. Cheng, L. Li, S. H. Chan, J. Zhao, and Y. K. Juay, "Annealing induced electrical conductivity jump of multi-walled carbon nanotube/polypropylene composites and influence of

molecular weight of polypropylene,” *J. Polym. Sci. Part B Polym. Phys.*, vol. 48, pp. 2238–2247, 2010, doi: <https://doi.org/10.1002/polb.22106>.

[91] Q. Cao, Y. Song, Y. Tan, and Q. Zheng, “Thermal-induced percolation in high-density polyethylene/carbon black composites,” *Polymer (Guildf.)*, vol. 50, pp. 6350–6356, 2009, doi: <https://doi.org/10.1016/j.polymer.2009.10.059>.

[92] T. Skipa, D. Lellinger, W. Böhm, M. Saphiannikova, and I. Alig, “Influence of shear deformation on carbon nanotube networks in polycarbonate melts: Interplay between build-up and destruction of agglomerates,” *Polymer (Guildf.)*, vol. 51, pp. 201–210, 2010, doi: <https://doi.org/10.1016/j.polymer.2009.11.047>.

[93] W. Li, Y. Zhang, J. Yang, J. Zhang, Y. Niu, and Z. Wang, “Thermal Annealing Induced Enhancements of Electrical Conductivities and Mechanism for Multiwalled Carbon Nanotubes Filled Poly(Ethylene-co-Hexene) Composites,” *ACS Appl. Mater. Interfaces*, vol. 4, pp. 6468–6478, 2012, doi: [10.1021/am302597f](https://doi.org/10.1021/am302597f).

[94] J.-R. Tao, D. Yang, Y. Yang, Q.-M. He, B. Fei, and M. Wang, “Migration mechanism of carbon nanotubes and matching viscosity-dependent morphology in Co-continuous Poly(lactic acid)/Poly( $\epsilon$ -caprolactone) blend: Towards electromagnetic shielding enhancement,” *Polymer (Guildf.)*, vol. 252, p. 124963, 2022, doi: <https://doi.org/10.1016/j.polymer.2022.124963>.

[95] Y. Lyu, H. Yin, Y. Chen, Q. Zhang, and X. Shi, “Structure and evolution of multiphase composites for 3D printing,” *J. Mater. Sci.*, vol. 55, pp. 6861–6874, 2020, doi: [10.1007/s10853-020-04505-w](https://doi.org/10.1007/s10853-020-04505-w).

## 9. Supplementary information

Three types of tests were performed to study the complex viscosity evolution of PCL/GNP composites, containing different percentages of graphene, by varying different parameters. The PCL and GNP grades are the same as the ones mentioned in the materials section. The conditions of the linearity, frequency, and thermal stability tests are described in figure 112. The tests were carried out using the same device described in the characterizations part of this chapter. The linearity tests results are not demonstrated in this section and their aim is knowing the upper limits of the viscoelastic range. The thermal stability results showed that all the samples are stable during 1h and 22 minutes. Only the frequency tests results are shown in the following figures.

Linearity	Angular frequency: 628 rad.s <sup>-1</sup> Range of shear: 0.001%- 50%	Three temperatures were chosen for these tests: <b>180 °C</b> <b>200 °C</b> <b>220 °C</b>
Frequency	Frequency range: 0.01- 628 rad.s <sup>-1</sup> Duration of the test: 60 min	
Thermal stability	Duration of the test: 60 min Frequency: 1 Hz Percentage of shear: 1%	

Figure 112: The parameters of the linearity, frequency, and thermal stability tests

In figure 113, the complex viscosity curves versus the angular frequency of PCL/GNP composites containing different GNP contents at different temperatures are exhibited. Figures (a), (b), and (c) show the results at different temperatures, 180 °C, 200 °C, and 220 °C respectively. The complex viscosity results in the low frequency region start to show a shoulder with the increase of the temperature for the various composites.

Figure 114 shows the complex viscosity curves of the different PCL/GNP composites containing different GNP contents at different angular frequencies and different temperatures. With the

increase of the temperature from 180 °C (a) to 220 °C (c), the complex viscosity independence on the percentage of graphene increases for low frequencies.

Figures 115a, 115b, and 115c exhibit the complex viscosity results versus temperatures at different angular frequencies of PCL/10% GNP, PCL/15% GNP, and PCL/20% GNP respectively. With the increase of the percentage of graphene, the complex viscosity seems to be independent of the temperature at low frequencies. Figure 116 that shows the complex viscosity results versus angular frequency and at different temperatures of the different composites emphasizes this information.

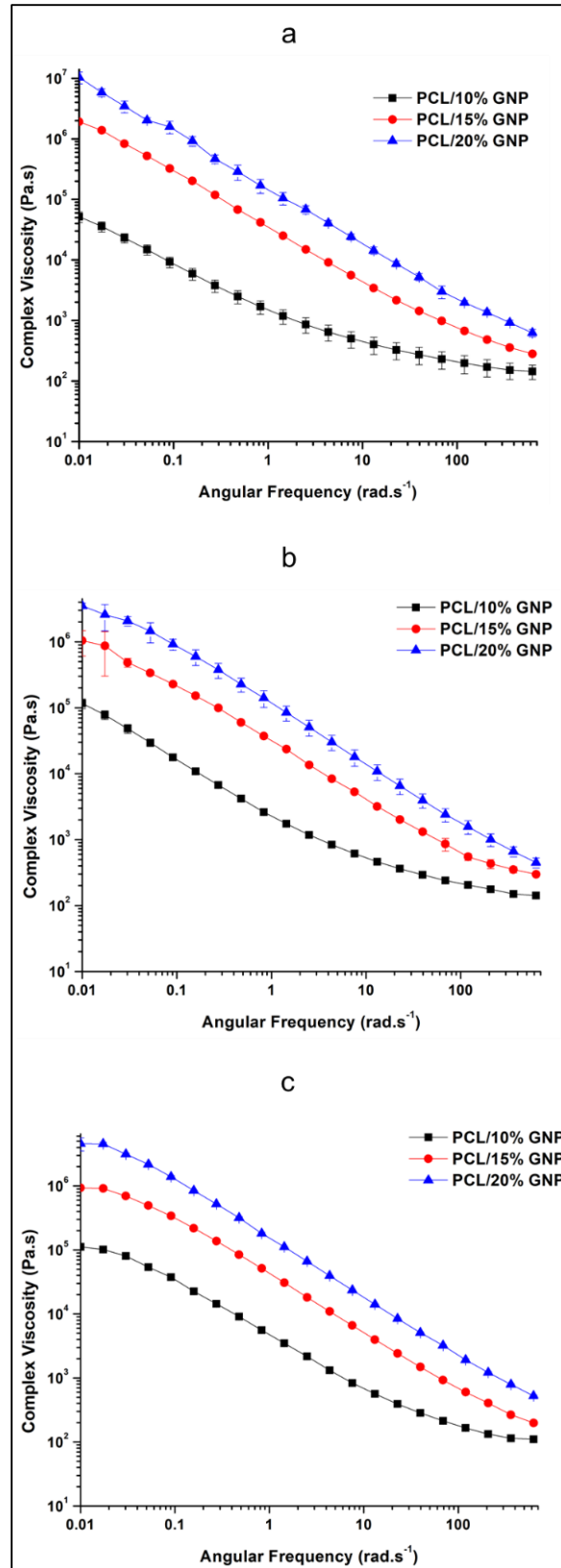


Figure 113: Complex viscosity versus angular frequency curves of PCL/GNP composites containing different GNP contents at different temperatures, (a) 180 °C, (b) 200 °C, (c) 220 °C

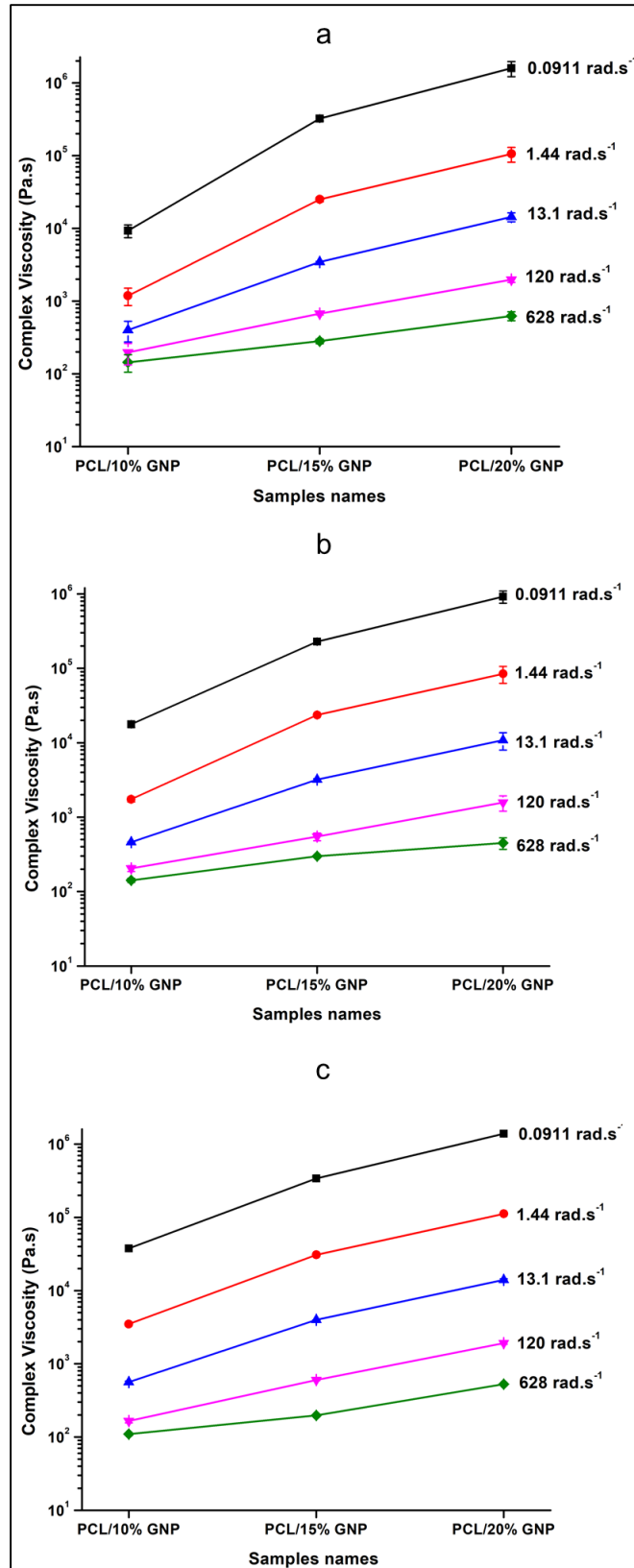


Figure 114: Complex viscosity of the different PCL/GNP composites containing different GNP percentages at different angular frequencies and different temperature, (a) 180 °C, (b) 200 °C, (c) 220 °C

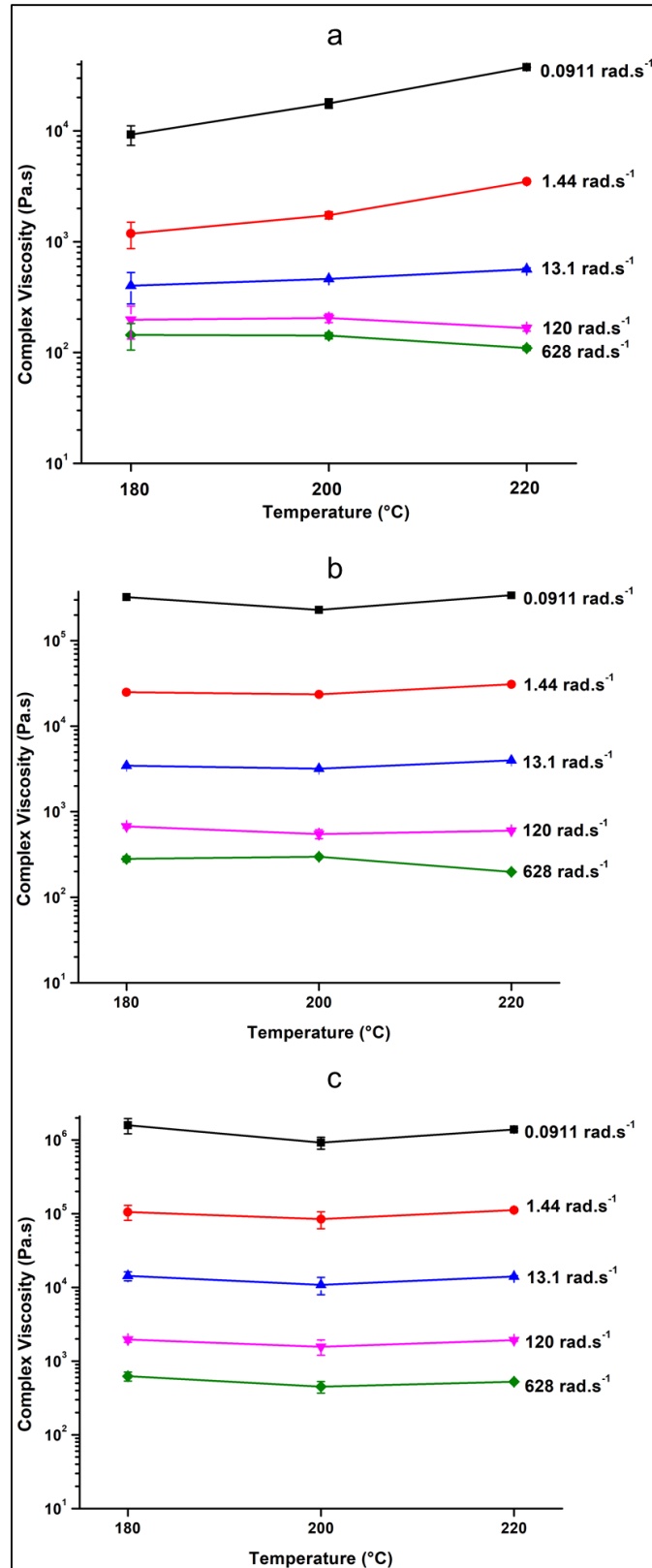


Figure 115: Complex viscosity curves versus temperatures and at different angular frequencies of (a) PCL/10% GNP, (b) PCL/15% GNP, (c) PCL/20% GNP

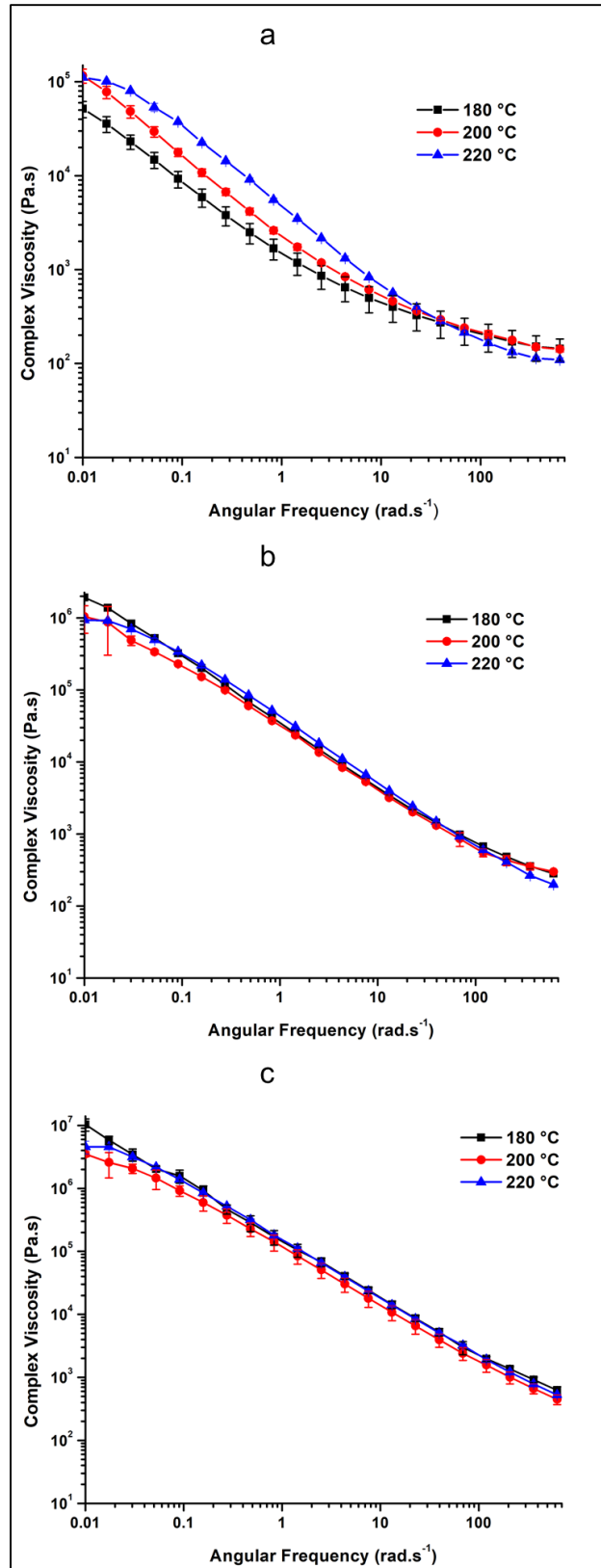
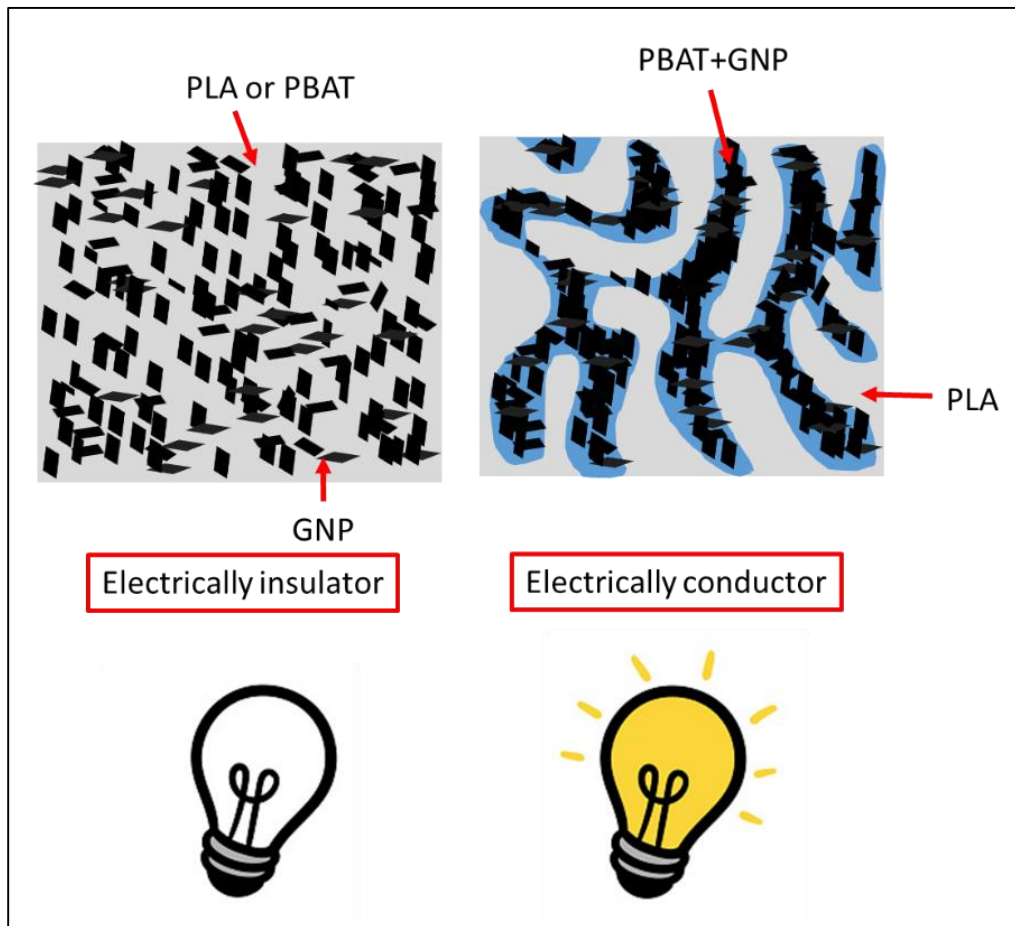


Figure 116: Complex viscosity curves versus angular frequency at different temperatures of (a) PCL/10% GNP, (b) PCL/15% GNP, (c) PCL/20% GNP

# Annex: Preliminary study of double electrical percolation in PLA/PBAT/GNP nanocomposite blends

## 1. Graphical abstract



## 2. Abstract

This work explores the possibility of obtaining double electrical percolation phenomenon in polylactic acid (PLA)/polybutylene adipate terephthalate (PBAT)/graphene nanoplatelets (GNP) composites prepared via compression moulding and fused filament fabrication (FFF) techniques. Contact angle measurements using a goniometer were carried out to theoretically predict,

according to thermodynamics, the localization of GNP in the blends. Experimentally, using the scanning electron microscopy (SEM) and atomic force microscopy (AFM), GNP were found in the PBAT phase which helped in the creation of a double percolation in PLA60/PBAT40/10 wt.% GNP composite as confirmed by the electrical resistivity results. Compression moulded samples showed superior electrical conductivity as compared to the 3D printed ones that probably possess a sea-island morphology instead of the co-continuous one. Although much better electrical conductivity results were obtained in the ternary compression moulded composites as compared to the binary ones, still the optimal morphology in terms of co-continuity and electrical properties needs to be discovered by manufacturing further formulations containing increased content of PBAT (45 to 55 wt.%). And maybe in this case, the 3D printed optimal formulation would be electrically conductive.

### **3. Introduction**

Electrically conductive polymer composites consisting of conductive fillers dispersed in a polymer system continue to grab increasing academic and industrial attention. These materials can be used in various applications such as static dissipation materials, electromagnetic interference shielding, radio frequency interference shielding, semiconducting layers in power cables, and supercapacitors [1-13].

Carbon-based nanoparticles have been used as reinforcing materials within the polymeric matrices in the last few years. For the development of electrically conductive composites, carbon nanoparticles such as graphite [14-16], carbon nanotubes (CNTs) [17-19], graphene-based [20-23], carbon fibers (CF) [24-26], and carbon black (CB) [27-31] have been implemented. The electrical percolation is an important parameter for the electrical conduction in the polymer composites. Numerous efforts have been exerted to study the relation of this value with various factors [32-36]. In general, many attempts have been made to reduce this threshold by varying the matrix type and filler size, aspect ratio, and conductivity [37]. One of the methods to decrease this threshold is by developing the concept of “double percolation” in immiscible polymer blends. This concept refers to the selective localization of the conductive fillers in one polymer

phase or at the interphase of a co-continuous polymer blend to form a percolated network in the host phase [38].

Double electrical percolation was obtained in several polymer blend systems. Regarding PLA/PBAT composites, three contributions that discuss the double electrical percolation using carbon nanotube (CNT) have been published. Urquijo et al. [39] have developed co-continuous PLA60/PBAT40/CNT nanocomposites using twin-screw extrusion followed by compression moulding. In this work, the nanofillers were found in the PBAT phase. The samples possessing a co-continuous microstructure had lower electrical percolation threshold of 1.28 wt.% of CNT as compared to 1.62 wt.% of CNT in the samples possessing a sea-island morphology. Jalali Dil et al. [40] manufactured PLA/PBAT/multi walled CNT (MWCNT) nanocomposites possessing the double electrical percolation at 50 wt.% of each polymer. The MWCNT presence at the interface has caused a bridging effect whose role was the perfection of the incomplete continuity of PBAT domains and the creation of additional conductive pathways. Dhakal et al. [41] succeeded to develop electrically conductive nanocomposites based on PLA45 wt.%/PBAT55 wt.% blends filled with MWCNT. A low electrical percolation threshold (around 1 wt.% of the fillers) compared to the literature works was achieved. To confirm the electrical conductivity results, the nanocomposite films were integrated into an electrical circuit. The MWCNT were selectively localized in PBAT and thus enhancing the formation of the co-continuous microstructure.

So far, there has been no research works concerned with the creation of the double electrical percolation in PLA/PBAT/graphene nanocomposites. Therefore, in this chapter we verified the possibility to obtain this phenomenon in PLA/PBAT/GNP composites prepared by compression moulding and FFF. PLA60/PBAT40 and PLA70/PBAT30 reinforced with 10 wt.% of GNP have been manufactured and their electrical properties were compared with those of PLA/10 wt.% GNP and PBAT/10 wt.% GNP binary composites. This chapter aims to open the doors towards fabricating electrically conductive biodegradable composite systems which still can be enhanced by increasing the PBAT percentage to get better co-continuous morphology and electrical performance.

## 4. Experimental procedure

### 4.1. Materials

PLA Ingeo™ 2003D (4% D-lactide, 96% L-lactide content) was purchased from NatureWorks (Minnetonka, MN, USA). It is characterized by MFR of 6 g/10 min (210 °C, 2.16 kg), density of 1.24 g.cm<sup>-3</sup>, glass transition temperature of 60 °C, and melting temperature of 150 °C.

PBAT is a commercial grade ecoflex® F Blend C1200 obtained from Cabamix (Cabannes, France) in a pellet form. This grade is featured by MFR of 2.7–4.9 g/10 min (190 °C, 2.16 kg), density of 1.25–1.27 g.cm<sup>-3</sup>, glass transition temperature of -31 °C, and melting temperature of 110-120 °C.

GNP M5 grade was acquired from XG Sciences (Lansing, USA). The manufacturer reports the following characteristics for this grade: average thickness of 6-8 nm, diameter of about 5 µm, and specific surface area between 120-150 m<sup>2</sup>.g<sup>-1</sup>. It has a density of 2.2 g.cm<sup>-3</sup> and electrical conductivity of 10<sup>7</sup> S.m<sup>-1</sup>. The production of these GNP is based on the exfoliation of sulphuric acid-based intercalated graphite by rapid microwave heating followed by ultrasonic treatment [42].

Diiodomethane (99 % purity) used in this study was purchased from Alfa Aesar and was used as received for the contact angle measurement tests.

### 4.2. Nanocomposites and blends preparation

#### 4.2.1. Compounding

PLA/PBAT pure blends (60 and 70 wt.% of PLA) and their graphene composites containing 10 wt.% of GNP were prepared using a co-rotating twin-screw extruder (Process 11, Thermo Scientific, Massachusetts, United States) at a temperature of 180 °C (cooling system was placed on the screw feeding zone), speed of 250 rpm, and flow rate of 0.94 kg.h<sup>-1</sup>. The screw diameter is 11 mm and the L/D ratio is 40. During the extrusion process, granules of the neat polymers (dried overnight at 60 °C) and the GNP (dried overnight at 80 °C) were added simultaneously into the extruder for the preparation of the nanocomposite blends. The neat blends (without GNP)

and the binary composites (PLA or PBAT/10 wt.% GNP) were prepared also using the same protocol.

#### **4.2.2. Compression moulding**

After vacuum drying the extruded blends and nanocomposites to prevent their degradation during processing, hot pressing using a laboratory compression press (LAB 800 PA, PINETTE PEI, France) was carried out. The conditions of these experiments are:

- cycle time of 10 minutes
- temperature of 180 °C (top and bottom)
- rate of 30 °C.min<sup>-1</sup>
- force of 500 kN

Using a water-cooling system, the temperature was decreased to 120 °C at a rate of 30 °C.min<sup>-1</sup> to demould the samples. For testing and characterizations, disks of 25 mm x 3 mm intended for the contact angle measurements, melt-shear rheological tests, SEM, and AFM were prepared. Moreover, square plates of 100 mm x 100 mm x 3 mm were also manufactured, from which bars of 30 mm x 5 mm x 3 mm were cut for the electrical resistance tests.

#### **4.2.3. Filament extrusion**

PLA60/PBAT40/10 wt.% GNP pellets were used to feed a mini single-screw extruder NEXT 1.0 (3devo, Netherlands) to obtain calibrated filaments. The processing temperature profile gradually increased from T1 = 165 °C to T2 = 180 °C, T3 = 181°C, and T4 = 183 °C. Note that T1 is the temperature of the zone that is closest to the feeder and the screw rotation speed was fixed at 5 rpm. The final diameter of the extruded filaments was approximately 2.85 ± 0.5 mm.

#### **4.2.4. Fused filament fabrication**

PLA60/PBAT40/10 wt.% GNP 3D-printed specimens were manufactured by feeding an A4v3 FFF printer (3ntr, Italy) with the filaments obtained as described in the previous paragraph. Bar-shaped samples were built up along the horizontal orientation. All samples were produced according to the following printing parameters:

- object infill of 100%
- nozzle diameter of 0.8 mm

- raster angle between +45° and -45°
- nozzle temperature of 180 °C
- bed temperature of 60 °C
- layer height of 0.2 mm
- infill speed of 40 mm.s<sup>-1</sup>

The 3D printed bar-shaped samples intended for the electrical resistance measurements have the same dimensions as the compression moulded ones for the purpose of comparison.

## 5. Characterization techniques

### 5.1. Contact angle measurements

The location of GNP in the immiscible PLA/PBAT blend can be predicted by thermodynamics using the wetting coefficient ( $\omega_\alpha$ ) [43] according to equation (1):

$$\omega_\alpha = \cos \theta = \frac{\gamma_{GNP/PBAT} - \gamma_{GNP/PLA}}{\gamma_{PLA/PBAT}} \quad (1)$$

Where,  $\gamma_{PLA/PBAT}$  is the interfacial tension between PLA and PBAT,  $\gamma_{GNP/PLA}$  is the interfacial tension between GNP and PLA, and  $\gamma_{GNP/PBAT}$  is the interfacial tension between GNP and PBAT.

Three cases occur depending on the value of  $\omega_\alpha$ :

- If  $\omega_\alpha$  is greater than one, then GNP should be in PLA (figure 117.a).
- If  $\omega_\alpha$  is smaller than -1, then GNP should be localized in PBAT (figure 117.b).
- If  $\omega_\alpha$  is between 1 and -1, then GNP should be located at the interface of the two polymers (figure 117.c).

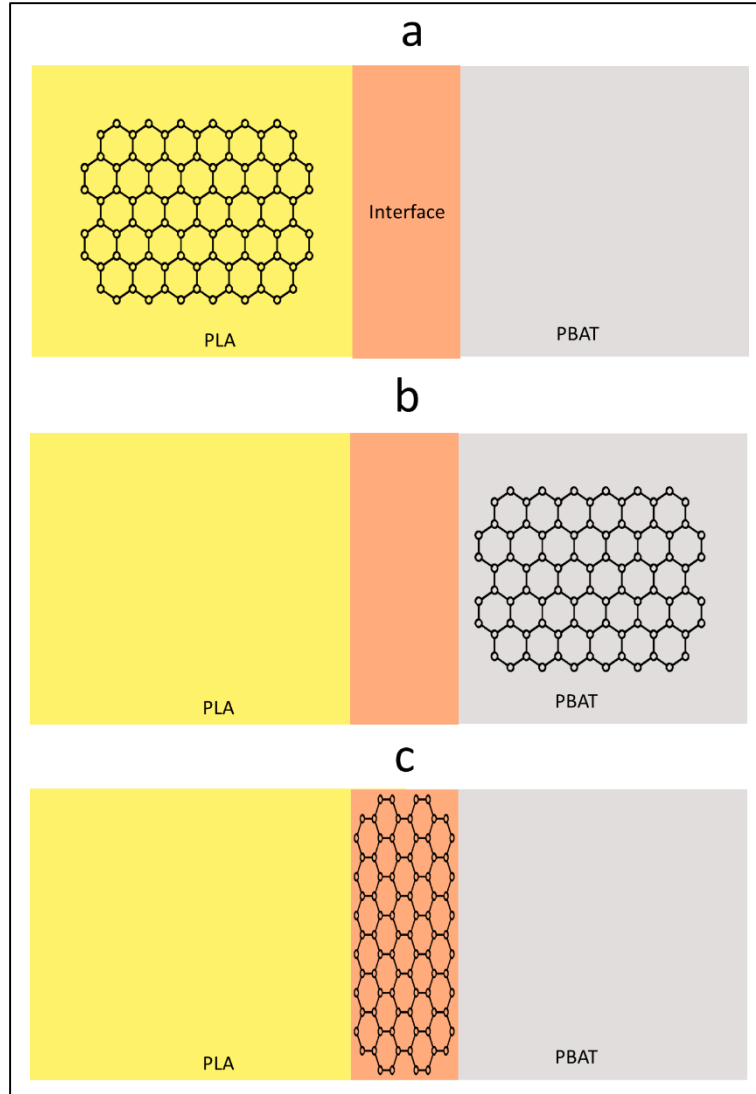


Figure 117: Scheme of the GNP distribution in the immiscible polymer blends based on the wetting coefficient

The harmonic mean equation can be used to calculate the interfacial tension  $\gamma_{ij}$  between PLA and PBAT using the polymers surface energies and their dispersive and polar components according to equation (2):

$$\gamma_{ij} = \gamma_i + \gamma_j - \frac{4\gamma_i^d \gamma_j^d}{\gamma_i^d + \gamma_j^d} - \frac{4\gamma_i^p \gamma_j^p}{\gamma_i^p + \gamma_j^p} \quad (2)$$

The geometric mean equation can be used for calculating the interfacial tension between GNP and PLA or PBAT using the polymer and filler surface energies and their dispersive and polar components according to equation (3):

$$\gamma_{ij} = \gamma_i + \gamma_j - 2\sqrt{\gamma_i^d \gamma_j^d} - 2\sqrt{\gamma_i^p \gamma_j^p} \quad (3)$$

In these equations,  $\gamma_i^d$  and  $\gamma_i^p$  are the dispersive and polar contributions to the total surface tension  $\gamma_i$  respectively.

To determine  $\gamma_i$ , its polar and dispersive components should be calculated first using Owens-Wendt model. This model represents a relationship between the contact angle ( $\theta$ ) and the total surface tension  $\gamma_i$  as shown in equation (4) [44]:

$$\frac{\gamma_l (1 + \cos \theta)}{2\sqrt{\gamma_l^d}} = \sqrt{\gamma_s^p} \times \frac{\sqrt{\gamma_l^p}}{\sqrt{\gamma_l^d}} + \sqrt{\gamma_s^d} \quad (4)$$

Where,  $\gamma_l^p$  is the liquid polar surface tension,  $\gamma_l^d$  is the liquid dispersive surface tension,  $\gamma_s^p$  is the solid polar surface energy, and  $\gamma_s^d$  is the solid dispersive surface energy. The total surface energy or tension is therefore the summation of the polar and dispersive surface energies or tensions. The test liquid surface tensions and their polar and dispersive components are presented in table 31 [45].

Table 31: The surface energy components of water and diiodomethane

Probe liquid	$\gamma_l$ (mJ.m <sup>-2</sup> )	$\gamma_l^p$ (mJ.m <sup>-2</sup> )	$\gamma_l^d$ (mJ.m <sup>-2</sup> )
Water	72.8	51.0	21.8
Diiodomethane	50.8	0.0	50.8

Contact angles were measured using a Krüss DSA30 goniometer. The contact angle ( $\theta$ ) is defined as the angle between the sample surface and the tangent line at the point of contact of the liquid droplet with the surface. Purified water and diiodomethane were used as probe liquids and the volumes of water and diiodomethane droplets were 3 and 1.5  $\mu$ l respectively. A drop of each probe liquid was ejected on the sample's surface and ten  $\theta$  values were taken consecutively and their average value was calculated. Six sessile drop tests were performed for each liquid and each formulation and two samples were tested per material. From these contact angles, the surface energies were calculated according to equation (4) and using the values in table 31. The

interfacial tensions between each of the two components were then calculated according to equations (2) and (3). Finally, the wetting coefficient of the PLA/PBAT blend filled with GNP was calculated according to equation (1).

### **5.1.1. Scanning electron microscopy (SEM)**

The micrographs were taken at 10 kV with a FEI Quanta 200 scanning electron microscope (SEM) (Fisher Thermo Scientific, Pittsburgh, USA). The compression moulded pure blends and nanocomposites were ultra-microtomed (Leica EM UC7) using a diamond knife and then carbon-sputtered prior to the investigations that took place along the sample transversal section. The objective of the ultra-microtomy is obtaining better contrast between the two polymer phases. Back scattered electron (BSE) and secondary electron (SE) images were collected and treated.

### **5.1.2. Atomic force microscopy (AFM)**

For verifying the selective localization of GNP in the blend composites, the microstructure of the compression moulded PLA60/PBAT40/10 wt.% GNP composite were investigated by AFM technique (MFP-3D infinity, Asylum Research AFM, Oxford instruments). The samples surfaces were cryogenically sectioned by diamond knives using an ultra-microtome (Leica EM UC7) to obtain flat and smooth surfaces. AFM characterisations were carried out along the transversal section of the disks. In addition, AFM images were obtained in a tapping mode at ambient conditions using AC160TSR3 tip at a scan rate of 1 Hz. Both the topographic (height) and phase images were recorded and analysed.

### **5.1.3. Rheological measurements**

Rheological properties of pure PLA and PBAT were investigated with a rotational rheometer (MCR 702, Anton Paar, Graz, Austria) in oscillatory shear mode using a parallel-plate (25 mm diameter) and a gap of 1 mm. The samples were analysed at 190 °C under nitrogen to avoid their thermal degradation. Frequencies ranging between 0.01 and 600 rad.s<sup>-1</sup> were tested with a strain of 1 %. Before the frequency tests, the upper limits of the viscoelastic range were determined by strain sweep tests at 200 rad.s<sup>-1</sup>. The samples were vacuum dried overnight at 60 °C before being tested at least two times.

#### 5.1.4. Electrical resistance measurements

Electrical resistance was measured using four probes method (described in details in the characterizations part of chapter 3). The measurements took place on 10 bar-shaped samples for each formulation. Each specimen was tested at a voltage of 5 V by using a direct current (DC) power supply (Topward, TPS-4000). The current flow on the samples was measured between two external electrodes using a multimeter (ITT instruments, MX 579 Metrix) and the voltage was measured between the internal electrodes using a digital multimeter (HAMEG Instruments, HM 8011). One surface of each sample was in contact with the four identical copper electrodes that were equidistant from each other. Using the resistance results, the electrical volume resistivity ( $\rho$ ) was calculated according to equation (5):

$$\rho = \frac{R \times S}{L} \quad (5)$$

Where, R is the electrical resistance ( $\Omega$ ), S is the cross-sectional area ( $m^2$ ) and it is equal to the width of the sample multiplied by its thickness, and L is the distance between the internal electrodes (3.7 mm).

An electric circuit was connected for each formulation by the in-series assembly of the voltage generator (5 V), LED, and the sample.

## 6. Results and discussion

### 6.1. Microstructure of pure PLA/PBAT blends

The microstructure of the unfilled blends containing different polymer contents and 10 wt.% of GNP was studied first using SEM. In this context, figures 118 and 119 show the morphology of PLA60/PBAT40 and PLA70/PBAT30 blends respectively. The PBAT darker phase (indicated by yellow arrows) is quasi-co-continuous in PLA60/PBAT40 (figure 118) blend, whereas it is dispersed in a nodular form in PLA70/PBAT30 blend (figure 119). Later, the impact of graphene on the microstructure of these blends will be investigated.

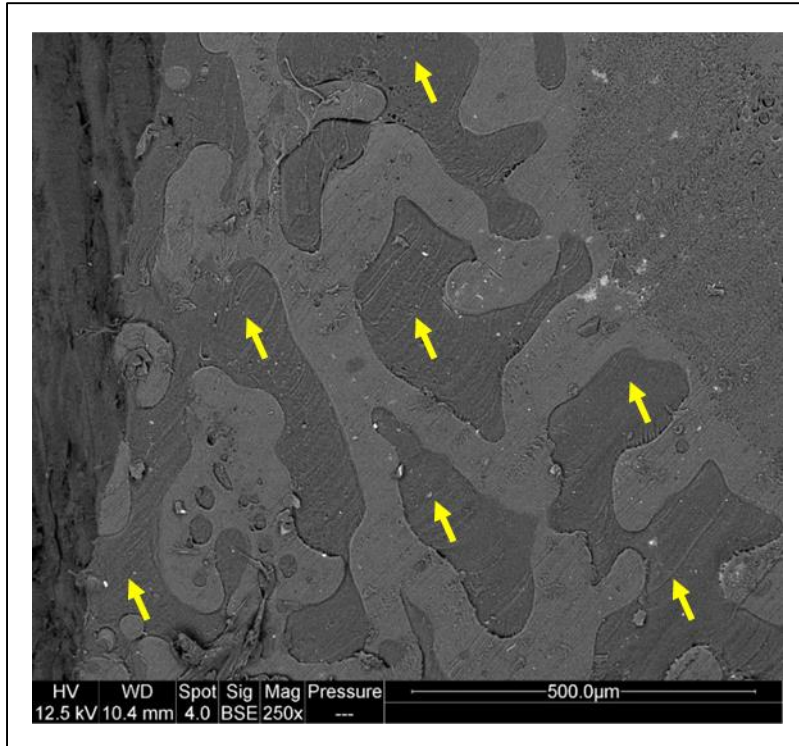


Figure 118: BSE SEM image of compression moulded PLA60/PBAT40 blend

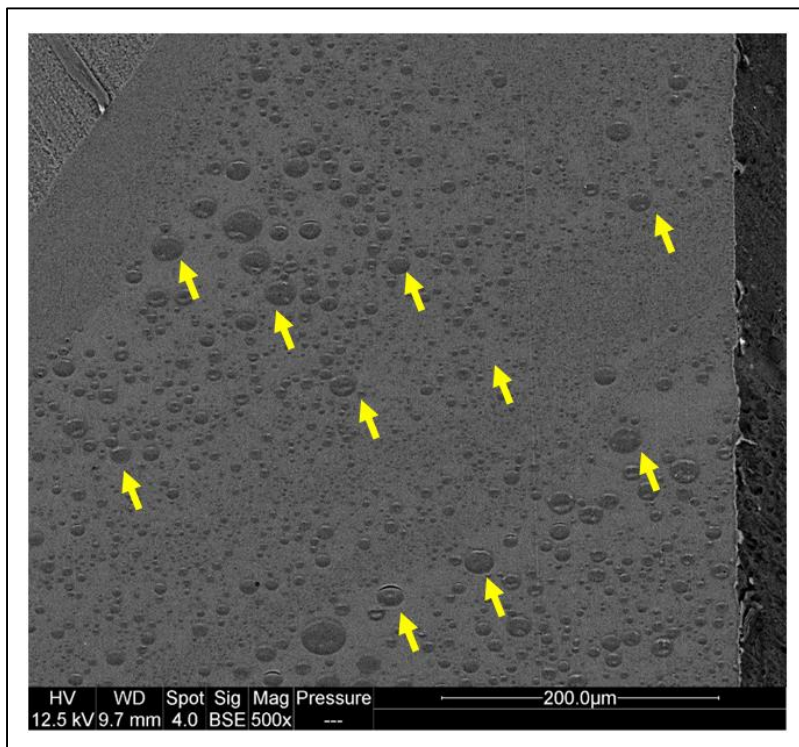


Figure 119: BSE SEM image of compression moulded PLA70/PBAT30 pure blend

## 6.2. Theoretical and experimental localization of GNP in PLA/PBAT blends

Based on the contact angle measurements performed in this study, PLA and PBAT possess solid surface energies equal to  $39.4 \pm 0.6 \text{ mJ.m}^{-2}$  and  $38.5 \pm 2.7 \text{ mJ.m}^{-2}$  respectively. These results are shown in table 32 along with the results of GNP ( $58.9 \pm 0.1 \text{ mJ.m}^{-2}$ ).

The calculations of the interfacial surface energies between PLA and PBAT, PLA and GNP, and PBAT and GNP based on equations (2) and (3) in the characterizations section gave the following results respectively:  $\gamma_{\text{PLA/PBAT}} = 134.3 \text{ mJ.m}^{-2}$ ,  $\gamma_{\text{GNP/PLA}} = 8.8 \text{ mJ.m}^{-2}$ , and  $\gamma_{\text{GNP/PBAT}} = 6.6 \text{ mJ.m}^{-2}$  (table 33). Consequently, the wetting coefficient based on these results and calculated according to equation (1) is -0.0164 (between 1 and -1) thus indicating that in principle GNP should be localized at the interface between PLA and PBAT. In the following section which discusses the experimental selective localization of the nanofiller in the blends, this result will be verified.

*Table 32: The solid surface energy, its dispersive and polar components of the pure polymers and the nanofiller*

Sample	Solid surface energy ( $\text{mJ.m}^{-2}$ )	Polar component ( $\text{mJ.m}^{-2}$ )	Dispersive component ( $\text{mJ.m}^{-2}$ )
PLA	$39.4 \pm 0.6$	$4.5 \pm 0.4$	$34.9 \pm 1$
PBAT	$38.5 \pm 2.7$	$6.3 \pm 1.4$	$32.1 \pm 1.3$
Graphene	$58.9 \pm 0.1$	$25.9 \pm 0.05$	$33 \pm 0.1$

*Table 33: The interfacial surface energies between PLA and PBAT, PLA and GNP, and PBAT and GNP*

Sample	Interfacial surface energy ( $\text{mJ.m}^{-2}$ )
PLA/PBAT	134.3
PLA/GNP	8.8
PBAT/GNP	6.6

Figure 120 shows the complex viscosity curves of the pure polymers. Over the entire angular frequency range, PLA has superior complex viscosity. This comparison between the rheological data was used later in this section for the interpretation of the selective localization of GNP in the blends. Figure 121 shows the topography (a) and the phase (b) images of PLA60/PBAT40/10 wt.% GNP compression moulded composite. The yellow indications (arrows and dotted line) refer to the graphene filled PBAT phase. The identification of the phases took place based on the colours and stiffness of the polymer components. For instance, the brightest colour in figure 121.b refers to the most flexible phase which is PBAT. But in this figure, PLA and graphene have similar colours, so the topography figure (121.a) was used to identify these materials. The roughest material (graphene) has the brightest color in the topography image. Thus, the combination of the information from both figures indicates the following: graphene particles are selectively localized in the PBAT phase (yellow indications) and the PLA matrix (orange arrows) seems not to contain any nanoparticles. For example, an interesting PBAT nodule that depicts this preferential localization is surrounded by the blue ellipse in which a graphene particle indicated by the red arrow is positioned. Figure 122 shows another zone on the same surface (the arrows, ellipses, and dotted lines in this figure have the same significance as those in figure 121).

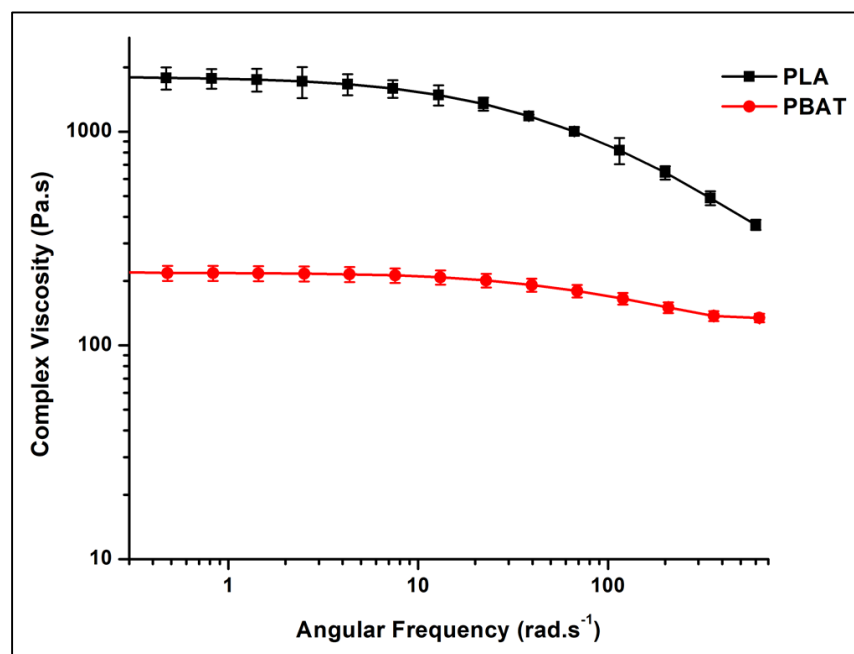


Figure 120: Complex viscosity curves of PLA and PBAT pure polymers

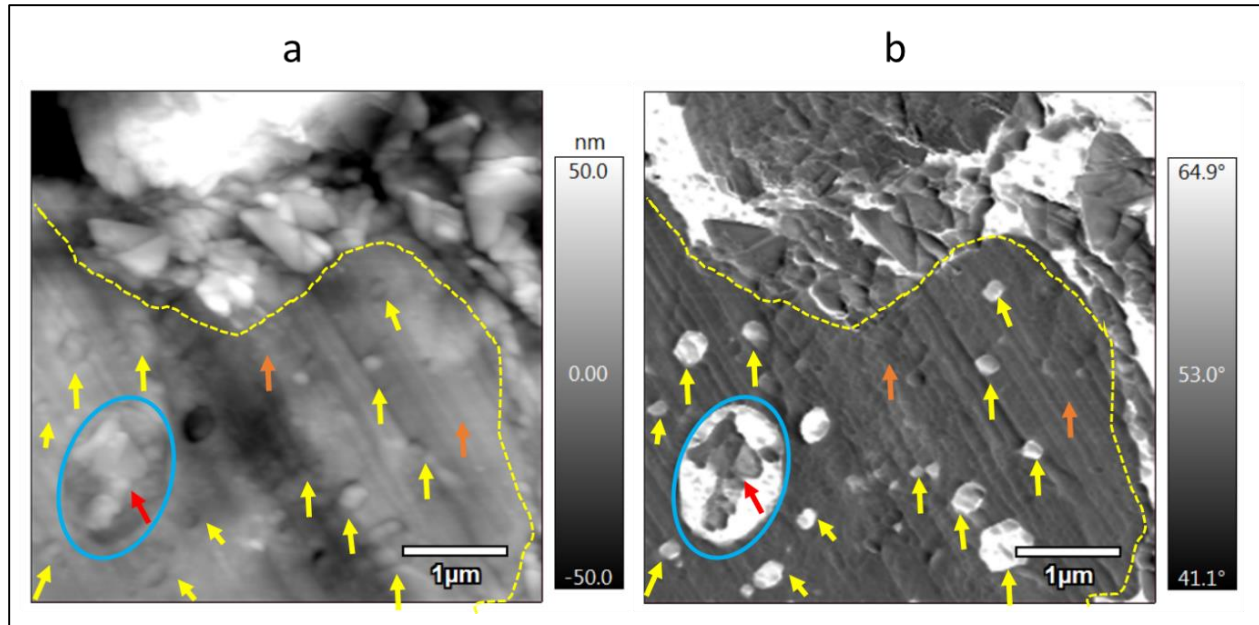


Figure 121: AFM topography (a) and phase (b) images of PLA60/PBAT40/10 wt.% GNP compression moulded composite (the yellow indications correspond to graphene filled PBAT, the orange arrows indicate PLA, and the blue ellipse including a red arrow shows a PBAT nodule containing a graphene nanoparticle respectively)

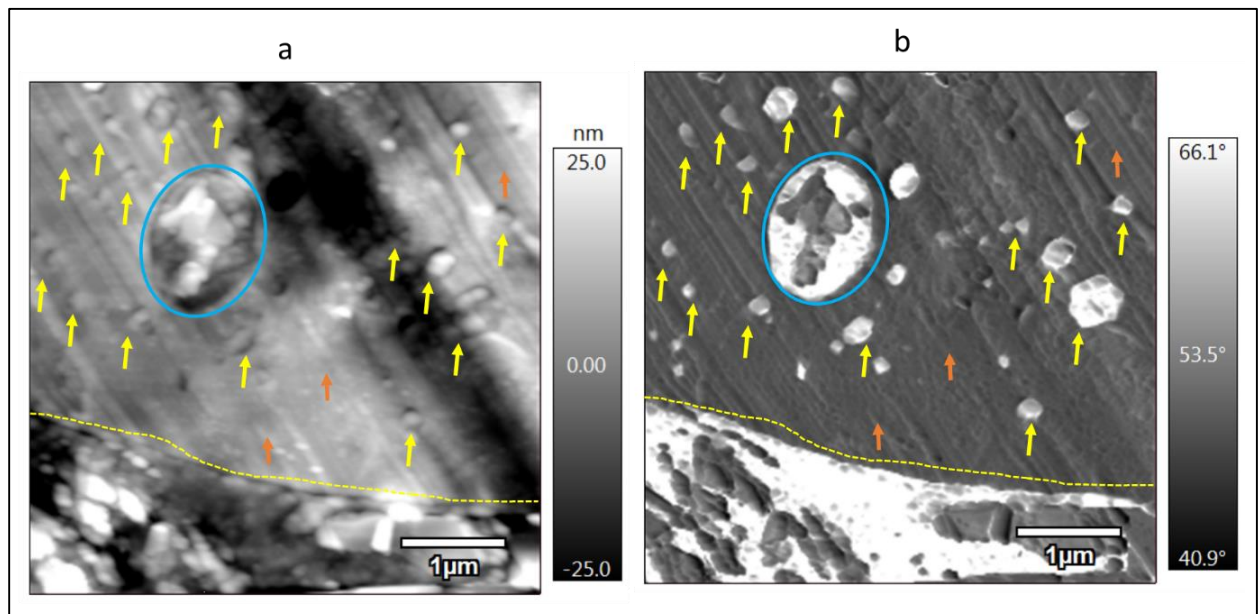


Figure 122: AFM topography (a) and phase (b) images of PLA60/PBAT40/10 wt.% GNP compression moulded composite

To ascertain the selective distribution of graphene in the PBAT phase, a profile (red line that starts from the blue point) was drawn on the profile image (figure 123.a) and detailed in figure 123.b.

The highest peak in this graph normally corresponds to the most flexible material (PBAT). And lower peaks correspond to PLA and graphene. The analysis of this profile shows that along the red line, the highest peaks are relevant to PBAT. When the line superposes with a graphene particle, the peak intensity decreases. And for the PLA zones, the peaks have also lower amplitude. Due to the big difference between the Young's modulus of graphene and PLA, there should be greater difference between their peak's amplitudes. But maybe in this case the location of graphene in a very flexible phase like PBAT gave similar phase peak as that of PLA. Figure 124 gives another example regarding another profile drawn on the same surface.

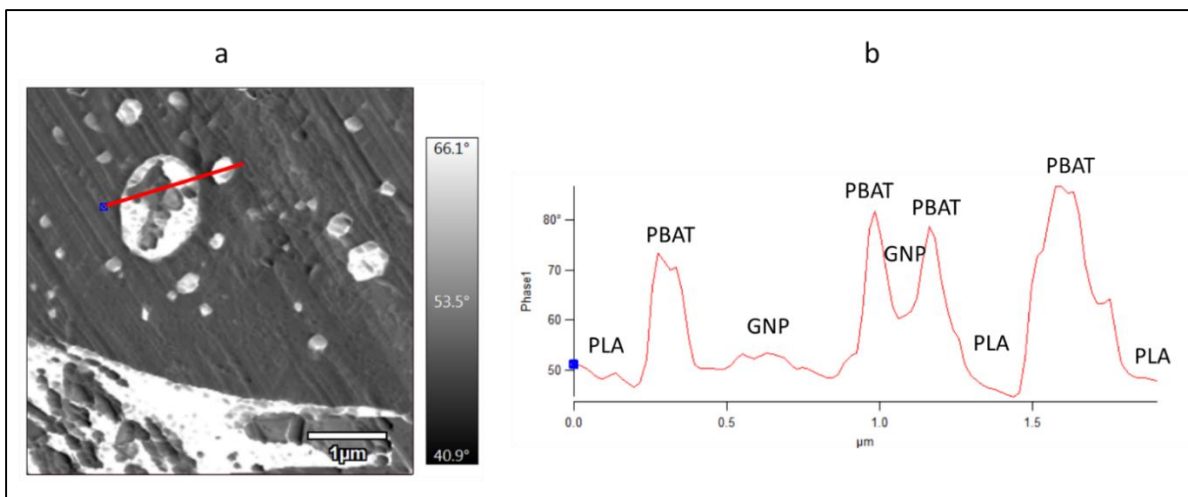


Figure 123: AFM phase image (a) of PLA60/PBAT40/10 wt.% GNP compression moulded composite (the red line in this image is related to the profile in figure (b))

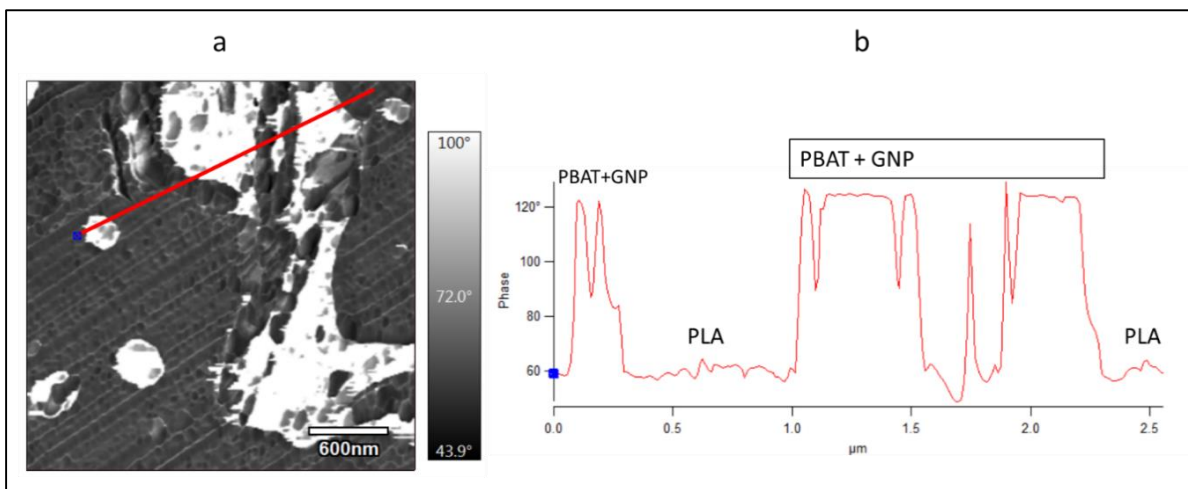


Figure 124: AFM phase image (a) of PLA60/PBAT40/10 wt.% GNP compression moulded composite (the red line in this image is related to the profile in figure (b))

Since AFM investigations treat very small zones of the surface, it was necessary to verify on the larger scale by using the SEM technique the selective localization of graphene in the PBAT phase. Figures 125 and 126 show the SEM images of PLA60/PCL40/10 wt.% GNP and PLA70/PBAT30/10 wt.% GNP compression moulded composites respectively. In the BSE images (figures 125.a and 126), the darker phase corresponds to PBAT (indicated by yellow arrows). This phase contains the graphene particles that can be clearly seen in the SE images (indicated by yellow arrows) (figures 125.b and 125.c). The GNP in these images seem to be aggregated in the PBAT phase as it was also observed in a previous work [46].

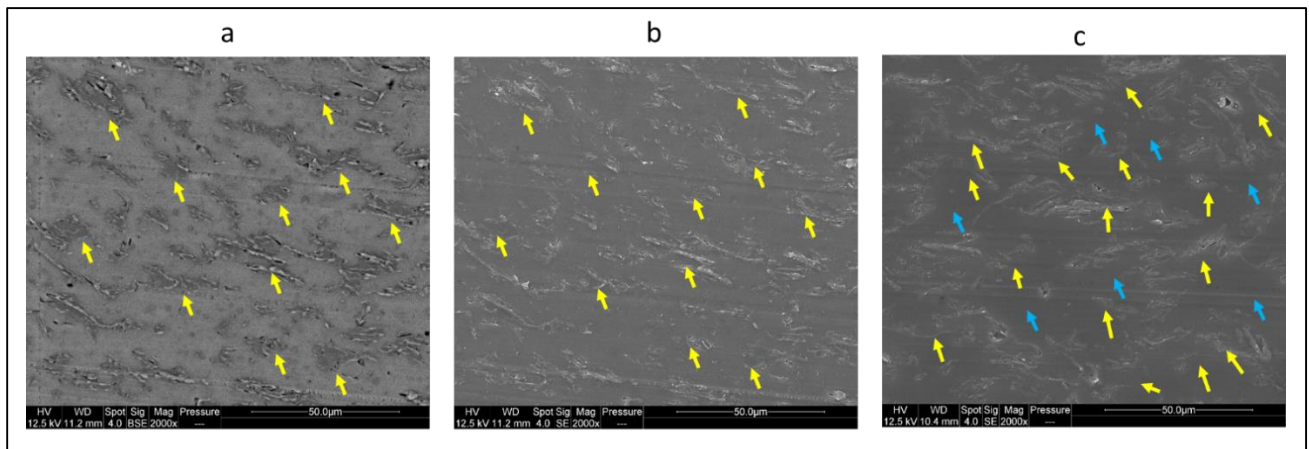


Figure 125: BSE (a) and SE (b,c) SEM images of compression moulded PLA60/PBAT40/10 wt.% GNP composite

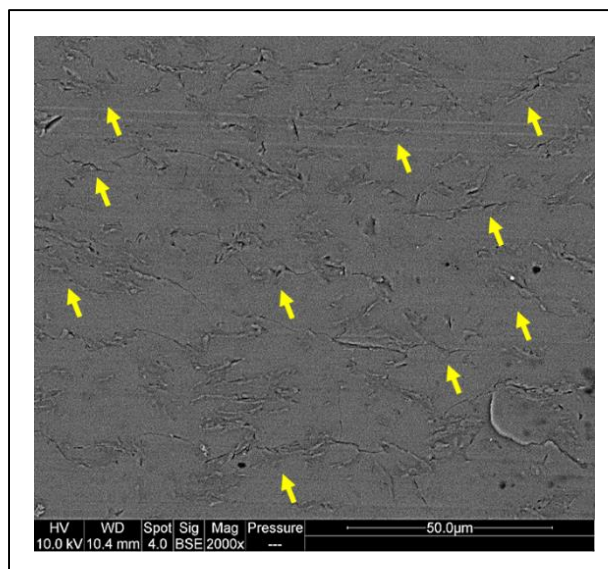


Figure 126: BSE SEM image of compression moulded PLA70/PBAT30/10 wt.% GNP composite

Based on the thermodynamic prediction using the wetting coefficient calculations, GNP should be at the interface, but experimentally these particles are localized in the PBAT phase. Similar result was obtained by Adrar et al. [46]. In their work and based on the wetting coefficient calculations after the contact angle measurements, graphene particles should be localized at the interface between PLA and PBAT. But transmission electron microscopy (TEM) images exhibited full localization of the graphene particles in the PBAT phase. The disability of the graphene particles to attain their thermodynamic equilibrium state was the reason behind the discrepancy between the theoretical and the experimental results. This phenomenon was related to the mixing strategy. In other words, when PLA, PBAT, and graphene were simultaneously mixed, graphene was encapsulated by PBAT which melted before PLA. Similar results were reported in other works [47-49], where the authors showed that the localization of the particles changed with the mixing strategy. This was especially the case for polymers that have large difference in their melting temperatures as PLA and PBAT.

Another explanation can be the greater compatibility of the carbon nanofillers with the aromatic groups of PBAT [50-52] rather than the aliphatic groups of PLA. Ko et al. [53] prepared PLA/PBAT/MWCNT composites using twin-screw extrusion followed by compression moulding. They have also obtained the selective localization of the nanofiller in the PBAT phase. According to them, several factors such as the viscosity ratio of the blend, the flexibility of the polymer chains, and the polymer chemical structure were found to have impact on this selective localization. For instance, the less viscous phase such as PBAT has more chance to contain the graphene nanoparticles during melt processing. In our work and by referring to the complex viscosity results in figure 120, the selective localization of GNP in the PBAT phase can be justified. Urquijo et al. [39] reached the same result in their PLA/PBAT/MWCNT composites and they attributed this finding to the lower viscosity of PBAT. Dhakal et al. [41] have explained this preferential localization by the facility of the flexible PBAT chains to adsorb on the CNT surface. This causes the alignment of the PBAT backbones along with the CNT particles during the adsorption process to finally fully include these particles.

### 6.3. PLA/PBAT/GNP nanocomposites electrical performance

Table 34 shows the electrical volume resistivity and the LED photos (at 5 V) of the binary and ternary composites. PLA/10 wt.% GNP possesses greater electrical volume resistivity ( $4866 \pm 65 \Omega\cdot\text{cm}$ ) as compared to PBAT/10 wt.% GNP ( $4000 \pm 81 \Omega\cdot\text{cm}$ ) and this can be attributed to the higher interfacial energy existing between PLA and GNP ( $8.8 \text{ mJ}\cdot\text{m}^{-2}$ ) as compared to that between PBAT and GNP ( $6.6 \text{ mJ}\cdot\text{m}^{-2}$ ). The greater interfacial energy probably caused greater agglomerations of GNP in the PLA matrix and therefore lower electrical conductivity was generated. The ternary composites with the same GNP content showed much lower electrical resistivity and lightening of the LED at 5 V with better results for the PLA60/PBAT40/10 wt.% GNP. Based on the SEM images in figure 127, the microstructures of both ternary composites seem similar. Both demonstrate elongated thin graphene containing PBAT nodules that are almost to be in contact with each other. This can be attributed to the selective positioning of the nanoparticles in this phase that increased its viscosity and therefore acted as barrier to its divisions [54]. The formation of elongated ellipsoidal PBAT droplets with the selective localization of the nanofillers in this phase in PLA/PBAT blends were reported elsewhere [54][55]. Based on the SEM images, we can have information about the 2D continuity of the phases. The 3D continuity cannot be known based on these images and it might be greater in the PLA60/PBAT40/10 wt.% GNP composite. The double electrical percolation threshold exists in both samples, but still better electrical conductivity results can be obtained by optimizing the PBAT nodules continuity through increasing the percentage of PBAT in the composites. This phenomenon was also created in PLA60 wt.%/PBAT40 wt.% filled with CNT in another research work. The selective localization of CNT in PBAT due to their greater compatibility produced larger elongated PBAT domains that are more characteristic of the co-continuous morphology [39]. Dhakal et al. succeeded also to obtain the same phenomenon [41]. These authors have connected an electric circuit with a bulb by applying an electrical voltage of 24 V. At and above 3 wt.% of CNT in the PLA/PBAT blend, the brightening of the bulb has become significant.

In table 34, the electrical resistivity results of PLA60/PBAT40/10 wt.% GNP 3D printed samples are also demonstrated. The huge electrical volume resistivity ( $> 10^7 \Omega\cdot\text{cm}$ ) of these samples

indicates their insulating nature. Additional processing steps (single screw extrusion and 3D printing) of PLA60/PBAT40/10 wt.% GNP probably caused the shredding of the graphene containing PBAT elongated nodules and therefore they were distant and separated by the insulating PLA chains to yield very low conductivity in these samples.

Table 34: Electrical volume resistivity and LED photos (at 5 V) of the binary and ternary composites containing 10 wt.% of GNP

Sample name	Electrical volume resistivity ( $\Omega \cdot \text{cm}$ )	LED (at 5 V)
PLA/GNP (compression moulded)	$4866 \pm 65$	No light
PLA70/PBAT30/GNP (compression moulded)	$890 \pm 50$	
PLA60/PBAT40/GNP (compression moulded)	$120 \pm 30$	
PLA60/PBAT40/GNP (3D printed)	$> 10^7$	No light
PBAT/GNP (compression moulded)	$4000 \pm 81$	No light

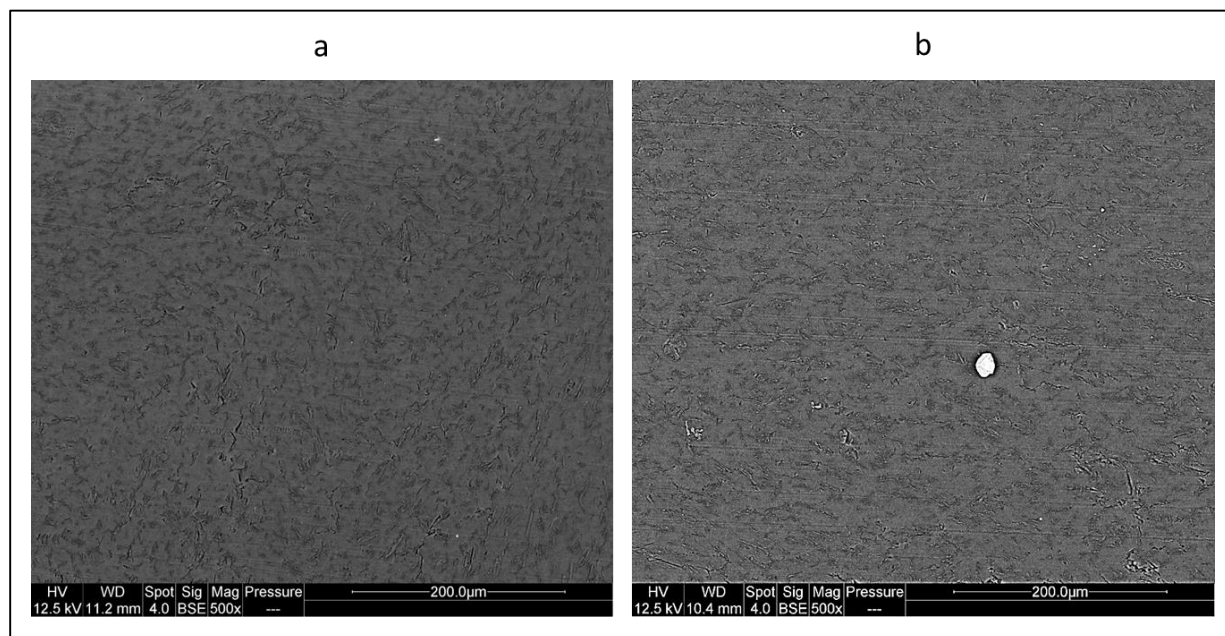


Figure 127: BSE SEM images of compression moulded PLA60/PBAT40/10 wt.% GNP (a) and PLA70/PBAT30/10 wt.% GNP (b) composites

## 7. Conclusion

This work was intended to check the possibility of creating double electrical percolation in PLA/PBAT/GNP composites. For this purpose, PLA60/PBAT40, PLA70/PBAT30, and their composites containing 10 wt.% of GNP were manufactured. The pure blends exhibited good contrast between PLA and PBAT, where PLA60/PBAT40 showed quasi-co-continuous structure whereas PLA70/PBAT30 showed sea-island morphology. The AFM and the SEM results showed the selective localization of GNP in the PBAT phase and this result was not in agreement with the thermodynamics which predicted the graphene localization at the interface. In the composites, thin PBAT elongated nodules resulted from the selective localization of graphene to give a semi-co-continuous structure in the ternary composites. The 3D printed PLA60/PBAT40/10 wt.% GNP possess an insulating nature to show that further processing of this formulation disrupted its co-continuity. This chapter thus concluded that it is possible to develop the double percolation in the PLA/PBAT blends using graphene nanoparticles. But still several experiments need to be performed in the future to determine the optimal morphology and electrical performance of the

compression moulded samples to be printed later and maybe in this case 3D printing can yield semi-conductive PLA/PBAT/GNP composites. Example of which experiments that can be carried out are:

- ❖ Fixing the graphene percentage (10 wt.%) and varying the percentages of the polymers to see a nice co-continuous structure (full continuity of the phases and especially the graphene containing PBAT phase)
- ❖ 3D printing of the best co-continuous structure
- ❖ Applying the viscosity-based models (discussed in chapter 4) to compare between the theoretical prediction of the co-continuity and the experimental findings
- ❖ Performing differential scanning calorimetry (DSC) tests of samples possessing sea-island and co-continuous morphologies to calculate the percentage of crystallinity of PBAT in the composites (to correlate the percentages of crystallinity with the co-continuity)

## 8. Bibliography

- [1] P. J. Brigandi, J. M. Cogen, and R. A. Pearson, "Electrically conductive multiphase polymer blend carbon-based composites," *Polym. Eng. & Sci.*, vol. 54, pp. 1–16, 2014, doi: <https://doi.org/10.1002/pen.23530>.
- [2] I. C. Finegan and G. G. Tibbetts, "Electrical conductivity of vapor-grown carbon fiber/thermoplastic composites," *J. Mater. Res.*, vol. 16, pp. 1668–1674, 2001, doi: [10.1557/JMR.2001.0231](https://doi.org/10.1557/JMR.2001.0231).
- [3] V. Panwar, J.-O. Park, S.-H. Park, S. Kumar, and R. M. Mehra, "Electrical, dielectric, and electromagnetic shielding properties of polypropylene-graphite composites," *J. Appl. Polym. Sci.*, vol. 115, pp. 1306–1314, 2010, doi: <https://doi.org/10.1002/app.29702>.
- [4] J. Li, H. Liu, J. Guo, Z. Hu, Z. Wang, B. Wang, L. Liu, Y. Huang, and Z. Guo, "Flexible, conductive, porous, fibrillar polymer–gold nanocomposites with enhanced electromagnetic interference shielding and mechanical properties," *J. Mater. Chem. C*, vol. 5, pp. 1095–1105, 2017, doi: [10.1039/C6TC04780G](https://doi.org/10.1039/C6TC04780G).
- [5] T. Villmow, S. Pegel, A. John, R. Rentenberger, and P. Pötschke, "Liquid sensing: smart polymer/CNT composites," *Mater. Today*, vol. 14, pp. 340–345, 2011, doi: [https://doi.org/10.1016/S1369-7021\(11\)70164-X](https://doi.org/10.1016/S1369-7021(11)70164-X).
- [6] S. Mondal, S. Ganguly, P. Das, D. Khastgir, and N. C. Das, "Low percolation threshold and electromagnetic shielding effectiveness of nano-structured carbon based ethylene methyl acrylate nanocomposites," *Compos. Part B Eng.*, vol. 119, pp. 41–56, 2017, doi: <https://doi.org/10.1016/j.compositesb.2017.03.022>.
- [7] P.-C. Ma, N. A. Siddiqui, G. Marom, and J.-K. Kim, "Dispersion and functionalization of carbon nanotubes for polymer-based nanocomposites: A review," *Compos. Part A Appl. Sci. Manuf.*, vol. 41, pp. 1345–1367, 2010, doi: <https://doi.org/10.1016/j.compositesa.2010.07.003>.
- [8] X. Liu, J. Krüchel, G. Zheng, and D. W. Schubert, "Mapping the Electrical Conductivity of Poly(methyl methacrylate)/Carbon Black Composites Prior to and after Shear," *ACS Appl. Mater. Interfaces*, vol. 5, pp. 8857–8860, 2013, doi: [10.1021/am4031517](https://doi.org/10.1021/am4031517).
- [9] A. Rahman, I. Ali, S. M. Al Zahrani, and R. H. Eleithy, "A Review of the applications of nanocarbon polymer composites," *Nano*, vol. 06, pp. 185–203, 2011, doi: [10.1142/S179329201100255X](https://doi.org/10.1142/S179329201100255X).
- [10] J. J. Vilatela and D. Eder, "Nanocarbon Composites and Hybrids in Sustainability: A Review," *ChemSusChem*, vol. 5, pp. 456–478, 2012, doi: <https://doi.org/10.1002/cssc.201100536>.
- [11] L. Liu, Z. Niu, and J. Chen, "Unconventional supercapacitors from nanocarbon-based electrode materials to device configurations," *Chem. Soc. Rev.*, vol. 45, pp. 4340–4363, 2016, doi: [10.1039/C6CS00041J](https://doi.org/10.1039/C6CS00041J).

- [12] G. Zhou, D. Wang, F. Li, L. Zhang, Z. Weng, and H.-M. Cheng, "The effect of carbon particle morphology on the electrochemical properties of nanocarbon/polyaniline composites in supercapacitors," *New Carbon Mater.*, vol. 26, pp. 180–186, 2011, doi: [https://doi.org/10.1016/S1872-5805\(11\)60075-9](https://doi.org/10.1016/S1872-5805(11)60075-9).
- [13] M. R. Lukatskaya, B. Dunn, and Y. Gogotsi, "Multidimensional materials and device architectures for future hybrid energy storage," *Nat. Commun.*, vol. 7, p. 12647, 2016, doi: [10.1038/ncomms12647](https://doi.org/10.1038/ncomms12647).
- [14] F. He, S. Lau, H. L. Chan, and J. Fan, "High Dielectric Permittivity and Low Percolation Threshold in Nanocomposites Based on Poly(vinylidene fluoride) and Exfoliated Graphite Nanoplates," *Adv. Mater.*, vol. 21, pp. 710–715, 2009, doi: <https://doi.org/10.1002/adma.200801758>.
- [15] A. Gupta and R. K. Goyal, "Electrical properties of polycarbonate/expanded graphite nanocomposites," *J. Appl. Polym. Sci.*, vol. 136, p. 47274, 2019, doi: <https://doi.org/10.1002/app.47274>.
- [16] H. min Kim, S. Lee, Y. S. Song, and D. Lee, "Synergistic improvement of electrical and thermal conductivities of carbon-based nanocomposites and its prediction by Mori-Tanaka scheme with interfacial resistances," *Compos. Struct.*, vol. 211, pp. 56–62, 2019, doi: <https://doi.org/10.1016/j.compstruct.2018.12.018>.
- [17] O. Kaynan, A. Yıldız, Y. E. Bozkurt, E. Ozden Yenigun, and H. Cebeci, "Electrically conductive high-performance thermoplastic filaments for fused filament fabrication," *Compos. Struct.*, vol. 237, p. 111930, 2020, doi: <https://doi.org/10.1016/j.compstruct.2020.111930>.
- [18] O.-K. Park, P. S. Owuor, Y. M. Jaques, D. S. Galvao, N. H. Kim, J. H. Lee, C. S. Tiwary, and P. M. Ajayan, "Hexagonal boron nitride-carbon nanotube hybrid network structure for enhanced thermal, mechanical and electrical properties of polyimide nanocomposites," *Compos. Sci. Technol.*, vol. 188, p. 107977, 2020, doi: <https://doi.org/10.1016/j.compscitech.2019.107977>.
- [19] F. Du, R. C. Scogna, W. Zhou, S. Brand, J. E. Fischer, and K. I. Winey, "Nanotube Networks in Polymer Nanocomposites: Rheology and Electrical Conductivity," *Macromolecules*, vol. 37, pp. 9048–9055, 2004, doi: [10.1021/ma049164g](https://doi.org/10.1021/ma049164g).
- [20] H. Kim, Y. Miura, and C. W. MacOsco, "Graphene/polyurethane nanocomposites for improved gas barrier and electrical conductivity," *Chem. Mater.*, vol. 22, pp. 3441–3450, 2010, doi: [10.1021/cm100477v](https://doi.org/10.1021/cm100477v).
- [21] P. Costa, S. Gonçalves, H. Mora, S. A. C. Carabineiro, J. C. Viana, and S. Lanceros-Mendez, "Highly Sensitive Piezoresistive Graphene-Based Stretchable Composites for Sensing Applications," *ACS Appl. Mater. Interfaces*, vol. 11, pp. 46286–46295, 2019, doi: [10.1021/acsami.9b19294](https://doi.org/10.1021/acsami.9b19294).
- [22] F. J. Okparaocha, A. R. Ipeaiyeda, M. E. Makhatha, and S. O. Alayande, "Morphology and functional properties of electrospun expanded polystyrene (EPS)/reduced graphene oxide (RGO)

nanofiber composite,” *Fullerenes, Nanotub. Carbon Nanostructures*, vol. 27, pp. 939–946, 2019, doi: 10.1080/1536383X.2019.1666365.

[23] L. Yang, W. Weng, X. Fei, L. Pan, X. Li, W. Xu, Z. Hu, and M. Zhu, “Revealing the interrelation between hydrogen bonds and interfaces in graphene/PVA composites towards highly electrical conductivity,” *Chem. Eng. J.*, vol. 383, p. 123126, 2020, doi: <https://doi.org/10.1016/j.cej.2019.123126>.

[24] K. Filik, G. Karnas, G. Masłowski, M. Oleksy, R. Oliwa, and K. Bulanda, “Testing of Conductive Carbon Fiber Reinforced Polymer Composites Using Current Impulses Simulating Lightning Effects,” *Energies*, vol. 14, 2021, doi: 10.3390/en14237899.

[25] J. Wen, Z. Xia, and F. Choy, “Damage detection of carbon fiber reinforced polymer composites via electrical resistance measurement,” *Compos. Part B Eng.*, vol. 42, pp. 77–86, 2011, doi: <https://doi.org/10.1016/j.compositesb.2010.08.005>.

[26] T. Kil, D. W. Jin, B. Yang, and H. K. Lee, “A comprehensive micromechanical and experimental study of the electrical conductivity of polymeric composites incorporating carbon nanotube and carbon fiber,” *Compos. Struct.*, vol. 268, p. 114002, 2021, doi: <https://doi.org/10.1016/j.compstruct.2021.114002>.

[27] F. Li, L. Qi, J. Yang, M. Xu, X. Luo, and D. Ma, “Polyurethane/conducting carbon black composites: Structure, electric conductivity, strain recovery behavior, and their relationships,” *J. Appl. Polym. Sci.*, vol. 75, pp. 68–77, 2000, doi: [https://doi.org/10.1002/\(SICI\)1097-4628\(20000103\)75:1<68::AID-APP8>3.0.CO;2-I](https://doi.org/10.1002/(SICI)1097-4628(20000103)75:1<68::AID-APP8>3.0.CO;2-I).

[28] K. Dai, X.-B. Xu, and Z.-M. Li, “Electrically conductive carbon black (CB) filled in situ microfibrillar poly(ethylene terephthalate) (PET)/polyethylene (PE) composite with a selective CB distribution,” *Polymer (Guildf.)*, vol. 48, pp. 849–859, 2007, doi: <https://doi.org/10.1016/j.polymer.2006.12.026>.

[29] L. Karásek and M. Sumita, “Characterization of dispersion state of filler and polymer-filler interactions in rubber-carbon black composites,” *J. Mater. Sci.*, vol. 31, pp. 281–289, 1996, doi: 10.1007/BF01139141.

[30] S. Matchawet, A. Kaesaman, P. Bomlai, and C. Nakason, “Electrical, dielectric, and dynamic mechanical properties of conductive carbon black/epoxidized natural rubber composites,” *J. Compos. Mater.*, vol. 50, pp. 2191–2202, 2016, doi: 10.1177/0021998315602941.

[31] Q. Zhang, J. Wang, B.-Y. Zhang, B.-H. Guo, J. Yu, and Z.-X. Guo, “Improved electrical conductivity of polymer/carbon black composites by simultaneous dispersion and interaction-induced network assembly,” *Compos. Sci. Technol.*, vol. 179, pp. 106–114, 2019, doi: <https://doi.org/10.1016/j.compscitech.2019.05.008>.

[32] G. D. Seidel and A.-S. Puydupin-Jamin, “Analysis of clustering, interphase region, and orientation effects on the electrical conductivity of carbon nanotube–polymer nanocomposites via computational micromechanics,” *Mech. Mater.*, vol. 43, pp. 755–774, 2011, doi: <https://doi.org/10.1016/j.mechmat.2011.08.010>.

- [33] T. Natsuki, M. Endo, and T. Takahashi, "Percolation study of orientated short-fiber composites by a continuum model," *Phys. A Stat. Mech. its Appl.*, vol. 352, pp. 498–508, 2005, doi: <https://doi.org/10.1016/j.physa.2004.12.059>.
- [34] H. M. Ma and X.-L. Gao, "A three-dimensional Monte Carlo model for electrically conductive polymer matrix composites filled with curved fibers," *Polymer (Guildf)*, vol. 49, pp. 4230–4238, 2008, doi: <https://doi.org/10.1016/j.polymer.2008.07.034>.
- [35] W. S. Bao, S. A. Meguid, Z. H. Zhu, Y. Pan, and G. J. Weng, "A novel approach to predict the electrical conductivity of multifunctional nanocomposites," *Mech. Mater.*, vol. 46, pp. 129–138, 2012, doi: <https://doi.org/10.1016/j.mechmat.2011.12.006>.
- [36] W. Wang and A. H. Jayatissa, "Computational and experimental study of electrical conductivity of graphene/poly(methyl methacrylate) nanocomposite using Monte Carlo method and percolation theory," *Synth. Met.*, vol. 204, pp. 141–147, 2015, doi: <https://doi.org/10.1016/j.synthmet.2015.03.022>.
- [37] A. Motaghi, A. Hrymak, and G. H. Motlagh, "Electrical conductivity and percolation threshold of hybrid carbon/polymer composites," *J. Appl. Polym. Sci.*, vol. 132, 2015, doi: <https://doi.org/10.1002/app.41744>.
- [38] J. Huang, C. Mao, Y. Zhu, W. Jiang, and X. Yang, "Control of carbon nanotubes at the interface of a co-continuous immiscible polymer blend to fabricate conductive composites with ultralow percolation thresholds," *Carbon N. Y.*, vol. 73, pp. 267–274, 2014, doi: <https://doi.org/10.1016/j.carbon.2014.02.063>.
- [39] J. Urquijo, N. Aranburu, S. Dagr eou, G. Guerrica-Echevarr a, and J. I. Eguiaz abal, "CNT-induced morphology and its effect on properties in PLA/PBAT-based nanocomposites," *Eur. Polym. J.*, vol. 93, pp. 545–555, 2017, doi: <https://doi.org/10.1016/j.eurpolymj.2017.06.035>.
- [40] E. Jalali Dil, M. Arjmand, I. Otero Navas, U. Sundararaj, and B. D. Favis, "Interface Bridging of Multiwalled Carbon Nanotubes in Polylactic Acid/Poly(butylene adipate-co-terephthalate): Morphology, Rheology, and Electrical Conductivity," *Macromolecules*, vol. 53, pp. 10267–10277, 2020, doi: [10.1021/acs.macromol.0c01525](https://doi.org/10.1021/acs.macromol.0c01525).
- [41] K. N. Dhakal, B. Krause, R. Lach, A. Wutzler, W. Grellmann, H. H. Le, A. Das, S. Wie bner, G. Heinrich, and R. Adhikari, "Electrically conductive nanocomposites based on poly(lactic acid)/flexible copolyester blends with multiwalled carbon nanotubes," *J. Appl. Polym. Sci.*, vol. 139, p. 51554, 2022, doi: <https://doi.org/10.1002/app.51554>.
- [42] K. Kalaitzidou, H. Fukushima, and L. T. Drzal, "Mechanical properties and morphological characterization of exfoliated graphite–polypropylene nanocomposites," *Compos. Part A Appl. Sci. Manuf.*, vol. 38, pp. 1675–1682, 2007, doi: <https://doi.org/10.1016/j.compositesa.2007.02.003>.
- [43] S. Steinmann, W. Gronski, and C. Friedrich, "Influence of selective filling on rheological properties and phase inversion of two-phase polymer blends," *Polymer (Guildf)*, vol. 43, pp. 4467–4477, 2002, doi: [https://doi.org/10.1016/S0032-3861\(02\)00271-9](https://doi.org/10.1016/S0032-3861(02)00271-9).

- [44] D. K. Owens and R. C. Wendt, "Estimation of the surface free energy of polymers," *J. Appl. Polym. Sci.*, vol. 13, pp. 1741–1747, 1969, doi: <https://doi.org/10.1002/app.1969.070130815>.
- [45] L. Jeantet, A. Regazzi, A. Taguet, M. Pucci, A.-S. Caro, and J.-C. Quantin, "Biopolymer blends for mechanical property gradient 3D printed parts," *Express Polym. Lett.*, vol. 15, pp. 137–152, 2021, doi: [10.3144/expresspolymlett.2021.13](https://doi.org/10.3144/expresspolymlett.2021.13).
- [46] S. Adrar, A. Habi, A. Ajji, and Y. Grohens, "Synergistic effects in epoxy functionalized graphene and modified organo-montmorillonite PLA/PBAT blends," *Appl. Clay Sci.*, vol. 157, pp. 65–75, 2018, doi: <https://doi.org/10.1016/j.clay.2018.02.028>.
- [47] L. Elias, F. Fenouillot, J.-C. Majesté, G. Martin, and P. Cassagnau, "Migration of nanosilica particles in polymer blends," *J. Polym. Sci. Part B Polym. Phys.*, vol. 46, pp. 1976–1983, 2008, doi: <https://doi.org/10.1002/polb.21534>.
- [48] E. Jalali Dil and B. D. Favis, "Localization of micro- and nano-silica particles in heterophase poly(lactic acid)/poly(butylene adipate-co-terephthalate) blends," *Polymer (Guildf.)*, vol. 76, pp. 295–306, 2015, doi: <https://doi.org/10.1016/j.polymer.2015.08.046>.
- [49] E. Jalali Dil and B. D. Favis, "Localization of micro and nano- silica particles in a high interfacial tension poly(lactic acid)/low density polyethylene system," *Polymer (Guildf.)*, vol. 77, pp. 156–166, 2015, doi: <https://doi.org/10.1016/j.polymer.2015.08.063>.
- [50] A. Nish, J.-Y. Hwang, J. Doig, and R. J. Nicholas, "Highly selective dispersion of single-walled carbon nanotubes using aromatic polymers," *Nat. Nanotechnol.*, vol. 2, pp. 640–646, 2007, doi: [10.1038/nnano.2007.290](https://doi.org/10.1038/nnano.2007.290).
- [51] G. J. Bahun, C. Wang, and A. Adronov, "Solubilizing single-walled carbon nanotubes with pyrene-functionalized block copolymers," *J. Polym. Sci. Part A Polym. Chem.*, vol. 44, pp. 1941–1951, 2006, doi: <https://doi.org/10.1002/pola.21308>.
- [52] P. Wang, S. Gao, X. Chen, L. Yang, X. Wu, S. Feng, X. Hu, J. Liu, P. Xu, and Y. Ding, "Effect of hydroxyl and carboxyl-functionalized carbon nanotubes on phase morphology, mechanical and dielectric properties of poly(lactide)/poly(butylene adipate-co-terephthalate) composites," *Int. J. Biol. Macromol.*, vol. 206, pp. 661–669, 2022, doi: <https://doi.org/10.1016/j.ijbiomac.2022.02.183>.
- [53] S. W. Ko, M. K. Hong, B. J. Park, R. K. Gupta, H. J. Choi, and S. N. Bhattacharya, "Morphological and rheological characterization of multi-walled carbon nanotube/PLA/PBAT blend nanocomposites," *Polym. Bull.*, vol. 63, pp. 125–134, 2009, doi: [10.1007/s00289-009-0072-9](https://doi.org/10.1007/s00289-009-0072-9).
- [54] R. Salehiyan, M. Nofar, K. Malkappa, and S. S. Ray, "Effect of nanofillers characteristics and their selective localization on morphology development and rheological properties of melt-processed polylactide/poly(butylene adipate-co-terephthalate) blend composites," *Polym. Eng. & Sci.*, vol. 60, pp. 2749–2760, 2020, doi: <https://doi.org/10.1002/pen.25505>.
- [55] E. Jalali Dil, N. Virgilio, and B. D. Favis, "The effect of the interfacial assembly of nano-silica in poly(lactic acid)/poly(butylene adipate-co-terephthalate) blends on morphology, rheology and

mechanical properties,” *Eur. Polym. J.*, vol. 85, pp. 635–646, 2016, doi:  
<https://doi.org/10.1016/j.eurpolymj.2016.07.022>.

## General conclusions and future perspectives

The objective of this work was to evaluate the potential of incorporating Graphene nanoplatelets (GNP) in biodegradable matrices such as polylactic acid (PLA), polycaprolactone (PCL), polybutylene adipate terephthalate (PBAT) and their blends to produce conductive materials.

At first, optimization tests were achieved using different GNP fillers namely M5, C300, C500, and C750 in PLA matrix based on solvent casting method, injection moulding, and fused filament extrusion (FFF). The main difference between these grades lies in their microstructural differences where M5 GNP has the greatest aspect ratio and lowest surface area. PLA/PCL ratio optimization and GNP grades addition into the optimized PLA/PCL formulation were carried out using twin-screw extrusion followed by injection moulding and 3D printing processes. It was found that M5 GNP grade is promising since it possesses the highest ordered crystalline structure and because it led to the highest mechanical performance in term of Young's modulus and the lowest electrical percolation threshold in the PLA matrix. Moreover, it seems that filling PLA80/PCL20 formulation with M5 GNP caused the greatest improvements in the PLA crystallinity, PCL thermal stability, PLA/PCL complex viscosity, storage modulus, and Young's modulus. Therefore, this grade was used throughout the entire PhD work.

Then, GNP were added into the PLA80/PCL20 matrix at different percentages using twin-screw extrusion followed by injection moulding and FFF. In these samples, PCL was dispersed as spherical nodules in the PLA matrix. The graphene nanoparticles were partially selectively localized in the PCL nodules when their size permitted. This selective localization was attributed to the lower viscosity and lower melting temperature of PCL. The electrical resistivity results showed that the injection moulded samples are insulators even at 25 wt.% of GNP. On contrary, the 3D printed samples are semiconductors starting from 15 wt.% of GNP with lightening of the LED at 5V starting from 20 wt.% of GNP. This behavior in terms of electrical performance can be related to the microstructural differences resulting from each process. 3D printed samples show stacking of GNP on the surface of the deposited filaments whose orientation fits the printing direction. On the other hand, the injection moulded samples show an insulating surface that is almost empty from GNP. The printing raster angle was found to impact the electrical results with

the best results for the samples printed in the longitudinal direction. The rheological results showed earlier threshold as compared to the electrical ones.

After discovering the possibility to obtain electrically conductive PLA/PCL/GNP composites using the FFF, a new purpose emerged which is lowering the electrical percolation threshold using FFF. Therefore, the development of the double electrical percolation threshold in this system was accomplished. For this, twin-screw extrusion followed by compression moulding and 3D printing to manufacture samples containing the same GNP percentage (10 wt.%) and different polymer percentages was performed. In all these samples, there was a phenomenon of complete graphene localization in the PCL phase that was independent from the polymer proportions and the mixing strategy. After predicting the phase inversion point using complex viscosity based models, the range of co-continuity was determined by means of solvent extraction and SEM which was found between 55 and 70 wt.% of PLA in the compression moulded samples. The electrical volume resistivity was the lowest in this range thanks to the phenomenon of the double percolation with the best results for PLA65/PCL35/10 wt.% GNP. This composite possessed the highest storage modulus and complex viscosity and the greatest char formation and polymers percentages of crystallinity when it was compared to the binary composites and ternary composites possessing sea-island morphology. The impact of several parameters on the PLA65/PCL35/GNP microstructure was investigated. For example, the increase of annealing effect accompanied with the increase of the compression moulding time caused the increase of the PLA continuity and the electrical conductivity with the existence of the co-continuous morphology even after 10 minutes of annealing. Second, fabricating samples in two-extrusion steps showed no impact on the establishment of the co-continuous microstructure and the electrical properties and a phenomenon of complete migration of graphene from the PLA phase to the PCL phase took place. Third, increasing the graphene content exhibited disruption of the co-continuity starting from 15 wt.% of graphene. The 3D printed PLA65/PCL35/GNP composites, although showed lower electrical conductivity when compared to the compression moulded ones, but demonstrated the lightening of the LED due to the presence of a co-continuous structure. The superior electrical conductivity of the co-continuous compression moulded

samples can be due to the extension of the co-continuity all over the surface whereas it is restricted within the diameter of each deposited filament in the 3D printed ones.

After succeeding in establishing the double electrical percolation for the 3D printed PLA/PCL/GNP composites, trials to accomplish the same phenomenon in PLA/PBAT/GNP composites were carried out in samples prepared by twin-screw extrusion followed by compression moulding and FFF. Some samples containing fixed content of GNP (10 wt.%) and different proportions of polymers were manufactured and studied. The results showed complete selective localization of GNP in the PBAT phase rendered to the chemical structure of this polymer and its lower viscosity. This was not in agreement with the thermodynamics that predicted the GNP localization at the blend interface. The PLA60/PCL40 blend and its composites showed quasi-co-continuous structure with finer PBAT elongated nodules in the composite. The ternary composites (PLA60/PBAT40/GNP and PLA70/PBAT30/GNP) exhibited lightening of the LED at 5V indicating the existence of double electrical percolation threshold that was absent in the 3D printed samples. The insulating nature of the 3D printed samples can be changed into a semi-conductive one by performing further investigations such as applying the viscosity-based models to predict the phase inversion point. Also, the PBAT percentage can be increased to see a desired co-continuous structure in the compression moulded samples. This step can be followed by 3D printing of the best co-continuous structure and investigations concerning its electrical properties.

Overall, this PhD work demonstrates that the investigated PLA/GNP blend composite systems are promising biodegradable materials for technological applications such as chemical sensors, flexible electronic devices, electrical circuit printing, and electromagnetic interference shielding (EMI).



## List of Figures

FIGURE 1: CLASSIFICATION OF BIODEGRADABILITY OF COMMON BIOPLASTICS (READAPTED FROM REFERENCE [14]) .....	13
FIGURE 2: THE LIFE CYCLE OF PLA (REPRODUCED FROM REFERENCE [22]) .....	15
FIGURE 3: VARIOUS APPLICATIONS OF PLA (READAPTED FROM REFERENCE [19]) .....	15
FIGURE 4: STEREOISOMERS OF LACTIDE [24].....	16
FIGURE 5: THE CHEMICAL STRUCTURES OF E-CAPROLACTONE AND PCL .....	17
FIGURE 6: SYNTHESIS OF PCL FROM E-CAPROLACTONE AND 6-HYDROXYHEXANOIC (6-HYDROXYCAPROIC) ACID [38] .....	18
FIGURE 7: THE MAIN APPLICATIONS OF PCL (REPRODUCED FROM REFERENCE [46]) .....	19
FIGURE 8: SYNTHESIS OF PBAT [47].....	20
FIGURE 9: SOME PBAT BASED PRODUCTS (REPRODUCED FROM REFERENCE [54]).....	21
FIGURE 10: GRAPHENE, GO, AND R-GO CHEMICAL STRUCTURES [57].....	22
FIGURE 11: LIQUID PHASE EXFOLIATION OF GRAPHITE TO GNP [61].....	23
FIGURE 12: SOME APPLICATIONS OF GNP BASED COMPOSITES (READAPTED FROM REFERENCE [62]).....	24
FIGURE 13: VARIOUS TYPES OF NANOFILLERS [68] .....	25
FIGURE 14: THE VARIOUS MICROSTRUCTURES THAT CAN EXIST IN THE CASE OF POLYMER BLENDS (READAPTED FROM REFERENCE [69]) ...	26
FIGURE 15: THE VARIOUS MICROSTRUCTURES THAT CAN EXIST AFTER MIXING THE POLYMER BLEND WITH NANOPARTICLES (READAPTED FROM REFERENCE [70]).....	27
FIGURE 16: THE IMPACT OF ANNEALING ON THE MICROSTRUCTURE OF SOME FILLED IMMISCIBLE POLYMER BLENDS (READAPTED FROM REFERENCE [71]).....	27
FIGURE 17: THE MAIN STEPS OF 3D PRINTING (REPRODUCED FROM REFERENCE [75]) .....	28
FIGURE 18: SCHEMATIC REPRESENTATION OF THE FFF TECHNIQUE (REPRODUCED FROM REFERENCE [80]) .....	29
FIGURE 19: SCHEMATIC IMAGE SIMULATING THE AFM IMAGE OF THE CO-CONTINUOUS MICROSTRUCTURE OF PLA60/PCL40 CALIBRATED FILAMENT (READAPTED FROM REFERENCE [83]) .....	30
FIGURE 20: SCHEMATIC IMAGE SIMULATING THE SEM IMAGE OF PLA80/PCL20 WITH THE OPTIMIZED MORPHOLOGY (READAPTED FROM REFERENCE [88]).....	32
FIGURE 21: THE MANUFACTURING PROCESS OF THE PLA/PCL/HNT 3D PRINTED SCAFFOLDS (SCHEMATIC REPRESENTATION READAPTED FROM REFERENCE [97]) .....	33
FIGURE 22: THE MANUFACTURING PROCESS OF THE PLA/PCL/HA/BT 3D PRINTED SCAFFOLDS (SCHEMATIC REPRESENTATION READAPTED FROM REFERENCE [98]) .....	34
FIGURE 23: A SIMULATION OF THE TEM IMAGE THAT SHOWS THE AGGREGATIONS OF TiO <sub>2</sub> IN THE PLA/PCL MATRIX (REPRODUCED FROM REFERENCE [84]).....	35
FIGURE 24: A SCHEMATIC REPRESENTATION OF THE SELECTIVE LOCALIZATION OF THE CNT AND OMMT IN THE PLA/PCL BLEND (REPRODUCED FROM REFERENCE [93]) .....	36
FIGURE 25: A SIMULATION OF THE TEM IMAGE THAT SHOWS THE SELECTIVE LOCALIZATION OF THE CNT IN THE PCL PHASE IN THE PLA/PCL BLEND (REPRODUCED FROM REFERENCE [100]).....	37

FIGURE 26: EFFECT OF CNT LOCALIZATION ON THE BLEND MORPHOLOGY (IMAGE REPRODUCED FROM REFERENCE [100]) .....37

FIGURE 27: THE MANUFACTURING PROCESS OF PLA/PCL/WOOD POWDER COMPOSITES (IMAGE REPRODUCED FROM REFERENCE [90]) .38

FIGURE 28: THE EFFECT OF THE COMPATIBILIZER ON THE MICROSTRUCTURE OF PLA/PBAT BLENDS (IMAGE REPRODUCED FROM REFERENCE [103]) .....39

FIGURE 29: THE LOCATION OF THE COMPATIBILIZER AT THE INTERFACE OF PLA/PBAT BLENDS (IMAGE REPRODUCED FROM REFERENCE [104]) .....40

FIGURE 30: THE IMPACT OF SHEARING ON THE MICROSTRUCTURE OF PLA/PBAT BLENDS (IMAGE REPRODUCED FROM REFERENCE [107]) .....41

FIGURE 31: THE MANUFACTURING PROCESS OF THE PLA/PBAT COMPATIBILIZED COMPOSITES (IMAGE REPRODUCED FROM REFERENCE [110]) .....42

FIGURE 32: SCHEMATIC REPRESENTATION OF CONDUCTIVE FILLER PARTICLES AND INSULATING POLYMER IN INSULATING (A) AND CONDUCTIVE (B) COMPOSITES .....44

FIGURE 33: ELECTRICAL CONDUCTIVITY VARIATION AS FUNCTION OF THE FILLER VOLUME FRACTION (IN THIS FIGURE, THE FILLER PARTICLES ARE FIBER-SHAPED BUT OTHER SHAPES ALSO EXIST LIKE THE SPHERICAL (CB) AND PLANAR (GRAPHENE) FORMS) .....45

FIGURE 34: SCHEMATIC REPRESENTATION OF THE TUNNELLING AND DIRECT CONTACT ELECTRICAL CONDUCTIVITY MECHANISMS.....46

FIGURE 35: POSSIBLE MORPHOLOGIES OF FILLER LOCALIZATION IN CO-CONTINUOUS POLYMER BLENDS [132] .....47

FIGURE 36: DOUBLE ELECTRICAL PERCOLATION IN ABS/PC/MWCNT COMPOSITES (READAPTED FROM REFERENCE [139]) .....48

FIGURE 37: SCHEMATIC REPRESENTATION OF THE EXPERIMENTAL PROCEDURE USED TO PREPARE 3D PRINTED PLA/CB COMPOSITES (READAPTED FROM REFERENCE [154]) .....52

FIGURE 38: SCHEMATIC PRESENTATION OF THE EXPERIMENTAL PROCEDURE USED TO PREPARE 3D PRINTED PLA/MWCNT COMPOSITES (READAPTED FROM REFERENCE [157]) .....53

FIGURE 39: SEM FEI QUANTA 200 FEG (FISHER THERMO SCIENTIFIC) MACHINE .....70

FIGURE 40: X-RAY BRUKER D8 ADVANCE DIFFRACTOMETER .....71

FIGURE 41: SETSYS EVOLUTION EQUIPMENT SETARAM TGA EQUIPMENT.....71

FIGURE 42: SEM IMAGES AT TWO DIFFERENT MAGNIFICATIONS OF THE DIFFERENT GNP GRADES, (A,B) M5 GNP, (C,D) C300 GNP, (E,F) C500 GNP, AND (G,H) C750 GNP .....74

FIGURE 43: EDX GRAPHS OF THE DIFFERENT C-GNP GRADES, (A) C300 GNP, (B) C500 GNP, AND (C) C750 GNP .....75

FIGURE 44: XPS DATA OF THE OXYGEN CONTENT OF EACH GNP GRADE (READAPTED FROM THE MANUFACTURER DATA [9]) .....76

FIGURE 45: XRD CURVES OF THE FOUR GNP GRADES.....76

FIGURE 46: TGA (A) AND DTG (B) CURVES OF THE DIFFERENT GNP GRADES UNDER O<sub>2</sub> ATMOSPHERE.....77

FIGURE 47: BC21 CLEXTRAL 900 MM TWIN-SCREW EXTRUDER.....78

FIGURE 48: SCHEME REPRESENTING THE DIFFERENT STEPS OF SOLVENT CASTING METHOD .....79

FIGURE 49: KRAUSSMAFFEI INJECTION MOULDING MACHINE .....80

FIGURE 50: YVROUD LINE .....80

FIGURE 51: A4v3 FFF 3D PRINTER .....81

FIGURE 52: AC-CUPYC 1330 (MICROMETRICS) HELIUM PYCNOMETER .....	82
FIGURE 53:ZWICK ROELL BZ2 MACHINE .....	83
FIGURE 54: TWO-PROBES ELECTRICAL MEASUREMENT ASSEMBLY.....	83
FIGURE 55: SEM IMAGES OF PLA/1 WT.% GNP INJECTION MOULDED COMPOSITES AT TWO DIFFERENT MAGNIFICATIONS: (A,B) CONTAIN M5 GNP, (C,D) CONTAIN C300 GNP, (E,F) CONTAIN C500 GNP, AND (G,H) CONTAIN C750 GNP (THE YELLOW ARROWS INDICATE THE GNP AGGREGATES, ALL THE SHINY SILVER PARTICLES CORRESPOND TO GRAPHENE) .....	85
FIGURE 56: SEM IMAGES OF PLA/3 WT.% GNP INJECTION MOULDED COMPOSITES AT TWO DIFFERENT MAGNIFICATIONS: (A,B) CONTAIN M5 GNP AND (C,D) CONTAIN C750 GNP (THE YELLOW ARROWS INDICATE THE GNP AGGREGATES OR PARTICLES, ALL THE SHINY SILVER PARTICLES CORRESPOND TO GRAPHENE) .....	86
FIGURE 57: XRD GRAPHS OF PLA AND PLA/3% GNP COMPOSITES .....	87
FIGURE 58: YOUNG’S MODULUS OF INJECTION MOULDED AND 3D PRINTED PURE PLA AND ITS COMPOSITES.....	89
FIGURE 59: TENSILE STRENGTH OF INJECTION MOULDED AND 3D PRINTED PURE PLA AND ITS COMPOSITE.....	90
FIGURE 60: ELONGATION AT BREAK OF INJECTION MOULDED AND 3D PRINTED PURE PLA AND ITS COMPOSITES.....	91
FIGURE 61: SEM IMAGES OF PLA/5 WT.% M5 (A), PLA/10 WT.% M5 (B), PLA/5 WT.% C500 (C), AND PLA/10 WT.% C500 (D) (THE YELLOW INDICATIONS SHOW THE GNP).....	92
FIGURE 62: PROCESS 11 TWIN-SCREW EXTRUDER.....	93
FIGURE 63: MINI-PRESS ZAMAK MERCATOR .....	94
FIGURE 64: 3DEVO MINI SINGLE-SCREW EXTRUDER .....	94
FIGURE 65: TENSILE PROPERTIES OF 3D PRINTED PLA/PCL BLENDS .....	96
FIGURE 66: SEM IMAGES OF INJECTION MOULDED (A) AND 3D PRINTED (B) PLA80/PCL20 BLENDS.....	97
FIGURE 67: SEM IMAGES OF INJECTION MOULDED (A) AND 3D PRINTED (B) PLA70/PCL30 BLENDS.....	97
FIGURE 68: PERKIN-ELMER DIAMOND DSC DEVICE .....	99
FIGURE 69: PCFC DEVICE .....	100
FIGURE 70: RHEOMETER (ANTON PAAR) .....	100
FIGURE 71: DSC CURVES OF INJECTION MOULDED PURE POLYMERS, THEIR BLEND (PLA80/PCL20), AND THEIR COMPOSITES (PLA80/PCL20/10 WT.% GNP).....	102
FIGURE 72: DSC CURVES OF 3D PRINTED PURE POLYMERS, THEIR BLEND, AND THEIR COMPOSITES .....	103
FIGURE 73: PCFC CURVES OF INJECTION MOULDED PURE POLYMERS, THEIR BLEND (PLA80/PCL20), AND THEIR COMPOSITES (PLA80/PCL20/10 WT.% GNP).....	105
FIGURE 74: PCFC CURVES OF 3D PRINTED PURE POLYMERS, THEIR BLEND, AND THEIR COMPOSITES .....	106
FIGURE 75: COMPLEX VISCOSITY CURVES OF THE PURE POLYMERS, THEIR BLEND, AND THEIR COMPOSITES.....	107
FIGURE 76: STORAGE MODULUS CURVES OF THE PURE POLYMERS, THEIR BLEND, AND THEIR COMPOSITES.....	108
FIGURE 77: YOUNG’S MODULUS DATA OF INJECTION MOULDED AND 3D PRINTED BLEND AND COMPOSITES .....	109
FIGURE 78: TENSILE STRENGTH DATA OF INJECTION MOULDED AND 3D PRINTED BLEND AND COMPOSITES .....	110
FIGURE 79: ELONGATION AT BREAK DATA OF INJECTION MOULDED AND 3D PRINTED BLEND AND COMPOSITES .....	110

FIGURE 80: THE DIFFERENT 3D PRINTING PATTERNS ACCORDING TO THE THREE DIFFERENT RASTER ANGLES: A)  $+45^{\circ}/-45^{\circ}$ , B)  $0^{\circ}$ , AND C)  $90^{\circ}$  .....126

FIGURE 81: THE SETUP OF THE ELECTRICAL RESISTANCE MEASUREMENT USING THE FOUR PROBES METHOD .....132

FIGURE 82: (A) AND (B) SEM IMAGES OF M5 GNP AT DIFFERENT MAGNIFICATIONS; (C) EDX GRAPH; (D) THE PART OF THE SURFACE THAT IS SURROUNDED BY A RECTANGLE AND WHOSE SURFACE ELEMENTS ARE SHOWN IN THE EDX GRAPH (C).....135

FIGURE 83: (A) AFM TOPOGRAPHY; (B) AFM PHASE IMAGES OF THE PLA/PCL/10 WT.% M5 INJECTION MOULDED SAMPLE; (C) TOPOGRAPHY AND PHASE PROFILES IN A DRAWN RED LINE THAT IS TRACED IN (A) AND (B) (THE ARROWS IN THE IMAGES POINT TOWARDS THE DIFFERENT COMPONENTS OF THE COMPONENTS OF THE COMPOSITE AND THEIR COLORS MATCH THE DESIGNATION OF THE PEAKS IN THE PROFILES).....136

FIGURE 84: (A), (C), AND (E) AFM TOPOGRAPHY; (B), (D), AND (F) THE CORRESPONDING PHASE IMAGES OF (A), (C), AND (E) RESPECTIVELY OF THE INJECTION MOULDED PLA/PCL/10 WT.% M5 (THE YELLOW CIRCLES SURROUND THE PCL PARTICLES CONTAINING GNPs AND THE BLUE CIRCLES SURROUND THE PURE PCL NODULES) .....138

FIGURE 85: (A) AFM TOPOGRAPHY; (B) AFM PHASE, (C) ZOOMED IMAGE OF (A); (D) ZOOMED IMAGE OF (B), OF 3D PRINTED PLA/PCL/10 WT.% M5 (THE YELLOW CIRCLES SURROUND FEW GNPs) .....139

FIGURE 86: (A) AND (C) SEM IMAGES OF TOLUENE ETCHED INJECTION MOULDED PLA/PCL/10 WT.% M5 COMPOSITE; (B) SEM IMAGES OF TOLUENE ETCHED 3D PRINTED PLA/PCL/10 WT.% M5 COMPOSITE (THE YELLOW CIRCLES SURROUND THE GNPs POSITIONED IN THE PORES WHERE THE PCL NODULES WERE SUPPOSED TO BE AND THE YELLOW ARROWS ARE POINTED TOWARDS THESE PORES).....140

FIGURE 87: (A) SEM IMAGE OF 3D PRINTED PLA/PCL/15 WT% M5; (B), (C), AND (D) SEM IMAGES OF INJECTION MOULDED PLA/PCL/15 WT.% M5 COMPOSITE (THE YELLOW ELLIPSES SURROUND SOME GRAPHENE FLAKES AND THE DOTTED LINES INDICATE THE SIMILAR ORIENTATION OF THE GRAPHENE PLATELETS IN THE INJECTION MOULDED SAMPLES) .....141

FIGURE 88: (A) SEM IMAGE OF THE INJECTION MOULDED PLA/PCL/15 WT.% M5 COMPOSITE AND ITS EDX (D); (B) SEM IMAGE OF 3D PRINTED PLA/PCL/15 WT.% M5 COMPOSITE AND ITS EDX (E); (C) THE ZONE OF OBSERVATION WHERE (A) AND (B) WERE TAKEN AND INDICATED BY THE SMALL BLACK CIRCLE (THE YELLOW CIRCLES SURROUND SOME GRAPHENE FLAKES) .....142

FIGURE 89: (A), (C), AND (E) SEM IMAGES AT THE INTERFACE OF TWO 3D PRINTED FILAMENTS OF PLA/PCL/15 WT.% M5 COMPOSITES; (B), (D), AND (F) THE ZOOMED IMAGES OF (A), (C), AND (E) RESPECTIVELY (THE YELLOW ARROWS ARE POINTED TOWARDS SOME GRAPHENE NANOPATELETS) .....143

FIGURE 90: THE STORAGE MODULUS CURVES OF PLA, PCL, PLA/PCL BLEND AND ITS COMPOSITES .....144

FIGURE 91: THE COMPLEX VISCOSITY CURVES OF PURE PLA AND PCL POLYMERS IN ADDITION TO THEIR BLEND AND COMPOSITES .....145

FIGURE 92: DTG CURVES ( $N_2$  ATMOSPHERE,  $10^{\circ}C.MIN^{-1}$ ) OF GNP, PLA, PCL, PLA/PCL BLENDS, AND THEIR COMPOSITES.....147

FIGURE 93: DSC CURVES OF PLA, PCL, THEIR BLEND, AND THEIR COMPOSITES .....148

FIGURE 94: THE VARIATION OF THE ELECTRICAL VOLUME RESISTIVITY OF THE COMPOSITES AS FUNCTION OF THE PERCENTAGE OF M5 GNP .....154

FIGURE 95: THE ELECTRICAL CIRCUIT CONNECTED USING THE 3D PRINTED PLA/PCL/25 WT.% M5 COMPOSITE .....155

FIGURE 96: SCREW PROFILE AND CONDITIONS SET DURING PLA/PCL/GNP NANOCOMPOSITES PROCESSING (PICTURE FROM LUDOVIC® SOFTWARE) .....170

FIGURE 97: SEM BSE AND SE IMAGES OF PCL/10 WT.% GNP (A,B) AND PLA/10 WT.% GNP (C,D) COMPRESSION MOULDED COMPOSITES (THE YELLOW ARROWS INDICATE THE PRESENCE OF GNP).....177

FIGURE 98: AFM IMAGES OF PLA60/PCL40/GNP, WHERE (B) SHOWS THE COMPONENTS OF THE PROFILE DRAWN ON (A) AND (C), (D), AND (E) REPRESENT THE TOPOGRAPHY, PHASE, AND ELASTIC MODULUS IMAGES OF ANOTHER OBSERVED ZONE ON THE SAME SURFACE (THE YELLOW ELLIPSES SURROUND THE GNP, THE BLUE STARS DENOTE THE PLA PHASE, AND THE RED TRIANGLES INDICATE THE GRAPHENE CONTAINING PCL PHASE) .....178

FIGURE 99: SEM IMAGES OF PLA60/PCL40/GNP, BSE (A) AND SE (B) AND SE IMAGES AT LOWER MAGNIFICATION OF PLA65/PCL35/GNP (c), PLA60/PCL40/GNP (d), PLA50/PCL50/GNP (e), PLA40/PCL60/GNP (f), AND PLA30/PCL70/GNP (g) COMPRESSION MOULDED COMPOSITES (THE YELLOW ARROWS INDICATE THE GNP RICH PCL PHASE AND THE BLUE ONES INDICATE THE PLA PHASE).....180

FIGURE 100: SEM BSE IMAGES OF PLA70/PCL30/GNP (A), PLA65/PCL35/GNP (B), PCL60/PCL40/GNP (C), PLA55/PCL45/GNP (D), PLA50/PCL50/GNP (E), PLA45/PCL55/GNP (F), PLA40/PCL60/GNP (G), PLA30/PCL70/GNP (H) (PLA IS THE WHITE PHASE AND PCL IS THE GREY PHASE).....185

FIGURE 101: CONTINUOUS FRACTION PERCENTAGE PLOT OF PLA AND PCL PHASES OF EACH COMPRESSION MOULDED COMPOSITE CONTAINING 10 WT.% OF GNP VERSUS THE PLA WEIGHT PERCENTAGE (THESE RESULTS WERE OBTAINED FROM THE SOLVENT EXTRACTION METHOD).....187

FIGURE 102: STORAGE MODULUS AND COMPLEX VISCOSITY VERSUS ANGULAR FREQUENCY OF COMPRESSION MOULDED COMPOSITES CONTAINING 10 WT.% OF GNP .....190

FIGURE 103: DSC SECOND HEATING STEP CURVES OF PLA, PCL, AND THEIR BINARY AND TERNARY COMPOSITES .....191

FIGURE 104: TGA CURVES OF PLA, PCL, THEIR BINARY AND TERNARY COMPOSITES .....193

FIGURE 105: PLA65/PCL35/GNP COMPRESSION MOULDED COMPOSITE DURING 10 MIN (A), 20 MIN (B), AND 35 MIN (C) .....195

FIGURE 106: PLA65/PCL35/GNP COMPRESSION MOULDED SAMPLE EXTRUDED IN TWO STEPS (A,C) AND IN ONE STEP (B); THE YELLOW AND BLUE ARROWS INDICATE PCL/GNP AND PLA PHASES RESPECTIVELY .....197

FIGURE 107: SCHEME REPRESENTING THE MIGRATION MECHANISM OF GNP FROM PLA TO PCL DURING TWIN-SCREW EXTRUSION (IMAGE REPRODUCED FROM REFERENCE [94]) .....198

FIGURE 108: SEM IMAGES OF COMPRESSION MOULDED PLA65/PCL35 BLEND COMPOSITES REINFORCED WITH 5 WT.% GNP (A), 10 WT.% GNP (B), 15 WT.% GNP (C), AND 20 WT.% GNP (D) (WHITE PHASE IS PLA AND GREY PHASE IS PCL) .....199

FIGURE 109: VARIATION OF THE CONTINUITY PERCENTAGE OF PLA AND PCL FRACTIONS WITH THE INCREASE OF GRAPHENE PERCENTAGE IN PLA65/PCL35/GNP COMPOSITES .....200

FIGURE 110 : SEM IMAGES OF SURFACE ETCHED 3D PRINTED PLA65/PCL35/GNP COMPOSITE (THE YELLOW ARROWS POINT TO THE PORES WHERE PCL ELONGATED NODULES WERE PRESENT) (THE 3D PRINTED FILAMENTS ORIENTATION IS THE SAME AS THE ORIENTATION OF THE PCL PORES).....203

FIGURE 111: THE SEM IMAGES OF PLA30/PCL70/GNP 3D PRINTED (A,B) AND COMPRESSION MOULDED (C) COMPOSITES (THE BRIGHTER PHASE IS PLA IN FIGURE 111.A AND THE BLUE ELLIPSES SURROUND THE GRAPHENE AGGREGATES) (THE 3D PRINTED FILAMENTS HAVE THE SAME ORIENTATION AS THE GNP AGGREGATES).....203

FIGURE 112: THE PARAMETERS OF THE LINEARITY, FREQUENCY, AND THERMAL STABILITY TESTS.....214

FIGURE 113: COMPLEX VISCOSITY VERSUS ANGULAR FREQUENCY CURVES OF PCL/GNP COMPOSITES CONTAINING DIFFERENT GNP CONTENTS AT DIFFERENT TEMPERATURES, (A) 180 °C, (B) 200 °C, (C) 220 °C .....216

FIGURE 114: COMPLEX VISCOSITY OF THE DIFFERENT PCL/GNP COMPOSITES CONTAINING DIFFERENT GNP PERCENTAGES AT DIFFERENT ANGULAR FREQUENCIES AND DIFFERENT TEMPERATURE, (A) 180 °C, (B) 200 °C, (C) 220 °C.....217

FIGURE 115: COMPLEX VISCOSITY CURVES VERSUS TEMPERATURES AND AT DIFFERENT ANGULAR FREQUENCIES OF (A) PCL/10% GNP, (B) PCL/15% GNP, (C) PCL/20% GNP .....218

FIGURE 116: COMPLEX VISCOSITY CURVES VERSUS ANGULAR FREQUENCY AT DIFFERENT TEMPERATURES OF (A) PCL/10% GNP, (B) PCL/15% GNP, (C) PCL/20% GNP .....219

FIGURE 117: SCHEME OF THE GNP DISTRIBUTION IN THE IMMISCIBLE POLYMER BLENDS BASED ON THE WETTING COEFFICIENT .....226

FIGURE 118: BSE SEM IMAGE OF COMPRESSION MOULDED PLA60/PBAT40 BLEND .....230

FIGURE 119: BSE SEM IMAGE OF COMPRESSION MOULDED PLA70/PBAT30 PURE BLEND.....230

FIGURE 120: COMPLEX VISCOSITY CURVES OF PLA AND PBAT PURE POLYMERS .....232

FIGURE 121: AFM TOPOGRAPHY (A) AND PHASE (B) IMAGES OF PLA60/PBAT40/10 WT.% GNP COMPRESSION MOULDED COMPOSITE (THE YELLOW INDICATIONS CORRESPOND TO GRAPHENE FILLED PBAT, THE ORANGE ARROWS INDICATE PLA, AND THE BLUE ELLIPSE INCLUDING A RED ARROW SHOWS A PBAT NODULE CONTAINING A GRAPHENE NANOPARTICLE RESPECTIVELY).....233

FIGURE 122: AFM TOPOGRAPHY (A) AND PHASE (B) IMAGES OF PLA60/PBAT40/10 WT.% GNP COMPRESSION MOULDED COMPOSITE .....233

FIGURE 123: AFM PHASE IMAGE (A) OF PLA60/PBAT40/10 WT.% GNP COMPRESSION MOULDED COMPOSITE (THE RED LINE IN THIS IMAGE IS RELATED TO THE PROFILE IN FIGURE (B)) .....234

FIGURE 124: AFM PHASE IMAGE (A) OF PLA60/PBAT40/10 WT.% GNP COMPRESSION MOULDED COMPOSITE (THE RED LINE IN THIS IMAGE IS RELATED TO THE PROFILE IN FIGURE (B)) .....234

FIGURE 125: BSE (A) AND SE (B,C) SEM IMAGES OF COMPRESSION MOULDED PLA60/PBAT40/10 WT.% GNP COMPOSITE .....235

FIGURE 126: BSE SEM IMAGE OF COMPRESSION MOULDED PLA70/PBAT30/10 WT.% GNP COMPOSITE .....235

FIGURE 127: BSE SEM IMAGES OF COMPRESSION MOULDED PLA60/PBAT40/10 WT.% GNP (A) AND PLA70/PBAT30/10 WT.% GNP (B) COMPOSITES .....239

## List of Tables

TABLE 1: PROPERTIES OF PCL [43] .....	18
TABLE 2: PROPERTIES OF PBAT (BASF ECOFLEX® C1200 F BLEND) [48-52] .....	21
TABLE 3 : THE LATERAL DIMENSION, THICKNESS, AND DENSITY OF THE DIFFERENT GNP GRADES.....	70
TABLE 4: THE PROPERTIES OF THE FOUR GNP GRADES .....	70
TABLE 5: TGA DATA OF THE DIFFERENT GNP GRADES (UNDER O <sub>2</sub> ATMOSPHERE) .....	77
TABLE 6: THE POROSITY VALUES OF 3D PRINTED PLA POLYMER AND ITS COMPOSITES .....	88
TABLE 7: ELECTRICAL PERCOLATION THRESHOLDS OF THE PLA/GNP SOLVENT CASTED SAMPLES (MEASURED BY TWO-PROBES METHOD) ..	92
TABLE 8: POROSITY RESULTS OF THE 3D PRINTED PLA/PCL BLENDS.....	96
TABLE 9: DSC DATA OF INJECTION MOULDED PURE POLYMERS, THEIR BLEND (PLA80/PCL20), AND THEIR COMPOSITES (PLA80/PCL20/10 WT.% GNP).....	101
TABLE 10: DSC DATA OF 3D PRINTED PURE POLYMERS, THEIR BLEND, AND THEIR COMPOSITES.....	102
TABLE 11: PCFC DATA OF INJECTION MOULDED PURE POLYMERS, THEIR BLEND (PLA80/PCL20), AND THEIR COMPOSITES (PLA80/PCL20/10 WT.% GNP) .....	104
TABLE 12: PCFC DATA OF 3D PRINTED SAMPLES .....	105
TABLE 13: POROSITY DATA OF 3D PRINTED BLEND AND COMPOSITES.....	109
TABLE 14: THE SURFACE ENERGY COMPONENTS OF WATER AND DIODOMETHANE.....	129
TABLE 15: THE SOLID SURFACE ENERGY, ITS DISPERSIVE AND POLAR COMPONENTS, THE TEST LIQUIDS, AND THE MODELS USED FOR SOLID SURFACE ENERGY CALCULATIONS OF THE PLA, PCL, AND GNP .....	134
TABLE 16: THE TGA RESULTS OF PLA, PCL, THEIR BLEND, AND THEIR COMPOSITES .....	147
TABLE 17: THE MELTING TEMPERATURES OF PLA AND PCL, CRYSTALLIZATION TEMPERATURE OF PLA, AND THE DEGREE OF CRYSTALLINITY OF PLA IN THE PLA PURE POLYMER, THE BLEND, AND THE COMPOSITES .....	149
TABLE 18: THE TENSILE PROPERTIES OF THE 3D PRINTED PLA, PLA/PCL BLEND, AND ITS COMPOSITES .....	151
TABLE 19: ELECTRICAL VOLUME RESISTIVITY OF 3D PRINTED COMPOSITES HAVING GRAPHENE PERCENTAGES STARTING FROM 10 WT.% TO 25 WT.% (THE RASTER ANGLE OF THESE SAMPLES IS +45°/-45°, FIGURE 80.A) .....	151
TABLE 20: THE ELECTRICAL VOLUME RESISTIVITY RESULTS OF THE PLA/PCL/20 WT.% M5 COMPOSITES ACCORDING TO THREE DIFFERENT PATTERNS BY CHANGING THE PRINTING RASTER ANGLES.....	155
TABLE 21: THE THREE MAIN SERIES OF EXTRUDED COMPOSITES AND THE OBJECTIVE BEHIND PREPARING EACH COMPOSITION.....	170
TABLE 22: COMPLEX VISCOSITY AND STORAGE MODULUS RESULTS OF PLA AND PCL/GNP COMPOSITES AT 180 °C AND 120 RAD. S <sup>-1</sup> AND 628 RAD. S <sup>-1</sup> .....	182
TABLE 23: DIFFERENT PHASE INVERSION MODELS AND THEIR RESULTS IN PLA/PCL/10WT.% GNP COMPOSITES AT 180 °C AND 120 RAD. S <sup>-1</sup> AND 628 RAD. S <sup>-1</sup> .....	182
TABLE 24: ELECTRICAL VOLUME RESISTIVITY AND ELECTRIC CURRENT RESULTS WITH THE ACCOMPANIED LED PHOTOS AT 5 V OF THE COMPRESSION MOULDED SAMPLES CONTAINING 10 WT.% OF GNP AND PLA CONTENT BETWEEN 0 WT.% TO 100 WT.% .....	188
TABLE 25; DSC RESULTS OF PLA, PCL, AND THEIR COMPOSITES.....	192

TABLE 26: TGA RESULTS OF PLA, PCL, THEIR BINARY, AND TERNARY COMPOSITES .....	193
TABLE 27: ELECTRICAL VOLUME RESISTIVITY, ELECTRIC CURRENT AND LED PHOTOS (AT 5 V), AND PLA CONTINUITY PERCENTAGE OF PLA65/PCL35/GNP SAMPLES MANUFACTURED DURING DIFFERENT COMPRESSION MOULDING TIMES (THE PCL CONTINUITY WAS 100 % IN THESE SAMPLES) .....	195
TABLE 28: ELECTRICAL VOLUME RESISTIVITY, ELECTRIC CURRENT AND LED PHOTOS (AT 5 V), AND PLA CONTINUITY PERCENTAGE OF PLA65/PCL35/GNP SAMPLES MANUFACTURED USING ONE AND TWO EXTRUSION STEPS (THE PCL CONTINUITY WAS 100 % IN THESE SAMPLES).....	198
TABLE 29: ELECTRICAL VOLUME RESISTIVITY AND ELECTRIC CURRENT RESULTS WITH THE ACCOMPANIED LED PHOTOS AT 5 V OF PLA65/PCL35/GNP COMPOSITES (GNP CONTENT VARIES BETWEEN 5 WT.% AND 20 WT.%) .....	200
TABLE 30: ELECTRICAL VOLUME RESISTIVITY AND ELECTRIC CURRENT RESULTS WITH THE ACCOMPANIED LED PHOTOS AT 5 V OF THE 3D PRINTED AND COMPRESSION MOULDED SAMPLES CONTAINING 10 WT.% GNP AND PLA CONTENT VARYING BETWEEN 80 WT.% AND 30 WT.%.....	202
TABLE 31: THE SURFACE ENERGY COMPONENTS OF WATER AND DIIDOMETHANE.....	227
TABLE 32: THE SOLID SURFACE ENERGY, ITS DISPERSIVE AND POLAR COMPONENTS OF THE PURE POLYMERS AND THE NANOFILLER .....	231
TABLE 33: THE INTERFACIAL SURFACE ENERGIES BETWEEN PLA AND PBAT, PLA AND GNP, AND PBAT AND GNP .....	231
TABLE 34: ELECTRICAL VOLUME RESISTIVITY AND LED PHOTOS (AT 5 V) OF THE BINARY AND TERNARY COMPOSITES CONTAINING 10 WT.% OF GNP.....	238

## Abstract

The demand on conductive polymers possessing both functionality and biodegradability is increasing rapidly due to environmental constraints. In this regard, the objective of this PhD project is devoted to the development of novel polymer nanocomposites with the final aim to improve the performance of the 3D printed parts obtained by fused filament fabrication (FFF). The attention has been focused on graphene nanoplatelets (GNP) nanofillers incorporated into polylactic acid (PLA) and its blends PLA/polycaprolactone (PCL) and PLA/polybutylene adipate terephthalate (PBAT). Optimization studies on PLA and PLA/PCL blend composites by solvent casting, injection moulding, and 3D printing showed promising performance for PLA80/PCL20 filled with M5 GNP. The addition of M5 GNP at different proportions to PLA80/PCL20 matrix using twin-screw extrusion followed by injection moulding and FFF highlighted a sea-island microstructure with selective localization of the GNP particles in the PCL nodules. Due to microstructural differences, the 3D printed samples showed a semi-conductive character at and above 15 wt.% of graphene, whereas the injection moulded samples possessed an insulating nature even at 25 wt.% of the nanofiller. Afterwards, a double electrical percolation threshold was achieved in compression moulded and 3D printed PLA/PCL/GNP composites whose percentage of graphene was fixed at 10 wt.%. The electrical and rheological properties, polymers crystallinity percentage, and char formation improvement were found optimal for PLA65/PCL35/GNP. Compression moulded samples had superior electrical conductivity on the 3D printed samples due to their co-continuous microstructure that is extended all over the whole volume. Preliminary results of PLA/PBAT/GNP composites showed that graphene was fully selectively localized in the PBAT phase and had better electrical performance for samples prepared by compression moulding compared to 3D printing. Further investigations are envisioned to improve the electrical performance of these 3D printed systems.

**Keywords :** PLA, PCL, PBAT, GNP, 3D printing, FFF, injection moulding, compression moulding, electrical conductivity, electrical percolation, double electrical percolation

## Résumé

La demande en polymères conducteurs biodégradables possédant à la fois des propriétés de conductivité électrique et de biodégradabilité connaît une augmentation rapide ces dernières années en raison des contraintes environnementales et du développement durable des écosystèmes. Par conséquent, l'objectif de ce projet de thèse est consacré au développement de nouveaux polymères nanocomposites dans le but d'améliorer les performances des pièces imprimées en 3D obtenues par fabrication de filaments fondus (FFF). L'attention a été portée sur les nanocharges de nanoplaquettes de graphène (GNP) incorporées dans l'acide polylactique (PLA) et ses mélanges tels que PLA/polycaprolactone (PCL) et PLA/polybutylène adipate téréphtalate (PBAT). Les études d'optimisation du PLA et PLA/PCL par dissolution/évaporation de solvant, injection et impression 3D ont montré des performances prometteuses pour le PLA80/PCL20 et le M5 GNP. L'ajout de M5 GNP à différentes proportions dans la matrice PLA80/ PCL20 obtenue par extrusion suivie d'un moulage par injection et FFF a mis en évidence une microstructure de type nodulaire avec une localisation sélective des particules de GNP dans les nodules de PCL. A cause de leurs différences microstructurales, les échantillons imprimés en 3D ont montré un caractère semi-conducteur à partir de de 15 % en masse de graphène alors que les échantillons obtenus par injection ont eu un comportement isolant, même à 25 % en masse de GNP. Par la suite, le seuil de double percolation électrique a été déterminé dans des composites PLA/PCL/GNP obtenus par thermocompression et imprimés en 3D dont le pourcentage de graphène était fixé à 10 %. Les propriétés électriques, rhéologiques, le taux de cristallinité des polymères et l'amélioration de la formation de char ont été jugées optimales pour le PLA65/PCL35/GNP. Les échantillons obtenus par thermocompression ont montré une conductivité électrique supérieure à celle des échantillons imprimés en 3D en raison de leur microstructure co-continue qui s'étend sur toute leur volume. Des résultats préliminaires sur les composites PLA/PBAT/GNP ont mis en évidence une localisation préférentielle du graphène dans la phase PBAT avec de meilleures performances électriques pour les échantillons préparés par compression à chaud par rapport à l'impression 3D. Des investigations approfondies sont envisagées pour améliorer les performances électriques des échantillons imprimés en 3D.

**Mots-clés :** PLA, PCL, PBAT, GNP, impression 3D, FFF, injection, thermocompression, conductivité électrique, percolation électrique, double percolation électrique